Development of the Theoretical and Experimental Framework of a Heliostat Field Calibration Method

Entwicklung der theoretischen und experimentellen Ansätze einer Heliostatenfeld-Kalibriermethode

Von der Fakultät für Maschinenwesen der Rheinisch-Westfälischen Technischen Hochschule Aachen zur Erlangung des akademischen Grades eines Doktors der Ingenieurwissenschaften genehmigte Dissertation

vorgelegt von

Johannes Christoph Sattler

Berichter: Univ.-Prof. Dr.-Ing. Bernhard Hoffschmidt
Univ.-Prof. Dr. rer. nat. Constantin Leon Häfner

Tag der mündlichen Prüfung: 10.11.2023

Acknowledgements

First and foremost I would like to gratefully thank Univ.-Prof. Dr.-Ing. Bernhard Hoffschmidt, director of the Institute of Solar Research from the German Aerospace Center (DLR) and Chair of Solar Components at the RWTH Aachen, for his tremendous support and for being the principle PhD supervisor. I would also like to express my sincere gratitude to Univ.-Prof. Dr. rer. nat. Constantin Leon Häfner (Fraunhofer ILT and Chair of Laser Technology at the RWTH Aachen) for his kind support as second examiner.
I am very grateful and thankful to Dr. rer. nat. Joachim Göttsche, Head of Department of Efficient Building and Systems Technology at the Solar-Institut Jülich of the FH Aachen University of Applied Sciences, for his excellent guidance and encouragement as mentor of this PhD thesis.
I would also like to thank Dr. Marc Röger (DLR), Peter Schwarzbözl (DLR), Dr.-Ing. Reiner Buck (DLR) and Ansgar Macke (CSP Services) for the interesting and productive discussions during the time of the preparation of a journal paper within the research project HeliBo (funded by the German federal state of North Rhine-Westphalia). I very much appreciate the kind support from Prof. Dr.-Ing. Dekorsy, Dr. Frank Duschek, Dr. Andreas Peckhaus and Prof. Dr. Carsten Pargmann (DLR) on the topic of lasers. Furthermore, I am very grateful to Dr. Hannes Vogelmann and Johannes Speidel from Karlsruhe Institute of Technology (KIT) for kindly granting me to use their laser equipment that was temporarily in use at the site of the German Meteorological Service (DWD) within the measurement campaign FESSTVaL (Field Experiment on Sub-mesoscale Spatio-Temporal Variability in Lindenberg). Many thanks also to Dr. Lehmann (DWD-Lindenberg) for granting me access to the site. I would like to thank Dr. Thomas Trickl (KIT) and Prof. Dr. Andreas Petzold (Forschungszentrum Jülich), Dr. rer. nat. Natalie Hanrieder (DLR), Dr.-Ing. Florian Sutter (DLR) and Dr.-Ing. Björn Schiricke (DLR) for information and data that was very useful for the thesis work. Much appreciation is also extended to Mr. Biermann and Mr. Bornschlegel (Fraunhofer ILT) for kindly lending technical equipment. I would also very much like to thank the team from project partner Radiant Dyes.
From the colleagues of my workplace, the Solar-Institut Jülich, I have received a lot of encouragement during the time of the preparation of this dissertation. I would like to express my gratitude to Prof. Dr.-Ing. Ulf Herrmann (Executive Director), Cristiano Teixeira Boura (Head of Department of Solar Thermal Systems), Dr. rer. nat Markus Sauerborn and Iesse Schneider for their kind encouragement.
Very importantly, I would like to also thank my dear wife Andrea and daughter Liliana for their strong support and patience. As a token of appreciation I am dedicating this PhD thesis to them. I would also like to extend my very special thanks to my family in England, Colombia and Germany.

Abstract

Central receiver systems (CRS) deploy thousands to more than a hundred thousand individually, biaxially sun-tracking heliostats to reflect direct solar irradiance onto a central absorber structure called receiver atop of a tower. Due to the resulting high solar irradiance flux density on the receiver, CRS are able to achieve high operating temperatures. This is highly useful for realising high overall efficiencies when operating a Rankine cycle or for solar chemical processes for the production of solar fuels, among other. However, CRS have the disadvantage that each heliostat must have its own drives for dual-axis tracking of the sun's path in the sky at a high accuracy. Ideally, the tracking accuracy should be $\leq$1 mrad (Sattler et al. 2020). This, though, still poses a problem nowadays as the tracking accuracy is influenced by several error sources. To measure the orientation of heliostats, it is necessary to deploy a calibration system. Most CRS deploy the state-of-the-art camera-target method, but it has disadvantages including that the calibration process for an entire heliostat field is very slow.

In this work, the focus was on the research and development of a calibration method which foresees the deployment of a dual-axis tracking central laser system and two cameras. This calibration method is referred to as central laser and camera system (CLCS). The aim was to achieve an accuracy of 0.1 mrad for measuring the orientation of a heliostat. Choosing an optimal configuration of the laser and camera system is complex. To confirm the theory of the CLCS, a simulation model was developed and validated as well as several indoor laboratory tests and an outdoor test were carried out. These experiments and theory showed that with a specific configuration of the laser and camera system it is feasible that the CLCS can, in principle, work as a real application in the future. For the assessment of the measurement accuracy of the CLCS, a simulation study using images of laser beams from an outdoor test campaign was carried out, which concluded that with the used camera, a mean measurement accuracy of 0.37 mrad is realistic, which is sufficiently good. For the CLCS, a measurement rate of 10 Hz is seen to be feasible. Compared with the state-of-the-art camera-target method, the CLCS can potentially be operated at a far higher measurement speed of up to 300 times faster when the orientation of a heliostat is measured using only a single mirror facet. Measuring multiple mirror facets per heliostat for determining the overall heliostat normal is also possible. In addition, the CLCS can also be deployed during the night.

Kurzfassung

Solarturmkraftwerke verwenden tausende bis mehr als hundertausend individuell, zweiachsig der Sonne nachgeführte Heliostaten, um direkte Solarstrahlung auf eine als Receiver bezeichnete zentrale Absorberstruktur oben auf einem Turm zu reflektieren. Aufgrund der daraus resultierenden hohen Solarstrahlungsflussdichte auf dem Receiver sind Solarturmkraftwerke in der Lage, hohe Betriebstemperaturen zu erreichen. Dies ist besonders nützlich unter anderem zur Realisierung von hohen Gesamtwirkungsgraden bei Betrieb eines Clausius-Rankine-Kreisprozesses oder für solarchemische Verfahren zur Herstellung von solaren Kraftstoffen. Solarturmkraftwerke haben jedoch den Nachteil, dass jeder Heliostat die Sonnenbahn mit eigenen zweiachsigen Antrieben mit hoher Genauigkeit nachführen muss. Idealerweise sollte die Nachführgenauigkeit $\leq$1 mrad betragen (Sattler et al. 2020). Dies stellt jedoch auch heutzutage noch immer ein Problem dar, da die Nachführgenauigkeit von mehreren Fehlerquellen beeinflusst wird. Um die Ausrichtung der Heliostaten zu vermessen, ist es notwendig, ein Kalibriersystem einzusetzen. Die meisten Solarturmkraftwerke verwenden die dem aktuellen Stand der Technik entsprechende Kamera-Target-Methode, die jedoch Nachteile hat, beispielsweise dass der Kalibrierprozess für ein gesamtes Heliostatfeld sehr langsam ist. In der vorliegenden Arbeit lag der Fokus auf der Erforschung und Entwicklung einer Kalibriermethode, die den Einsatz eines zweiachsig nachgeführten zentralen Lasersystems und zweier Kameras vorsieht. Diese Kalibriermethode wird als zentrales Laser-Kamera-System (CLCS) bezeichnet. Das Ziel war, eine Genauigkeit von 0.1 mrad für die Messung der Ausrichtung eines Heliostaten zu erreichen. Die Auswahl einer optimalen Konfiguration des Laser- und Kamerasystems ist komplex. Um die Theorie des CLCS zu bestätigen, wurde ein Simulationsmodell entwickelt und validiert sowie mehrere Laborversuche und ein Außenversuch durchgeführt. Die Experimente und die Theorie zeigten, dass es mit einer spezifischen Konfiguration des Laser- und Kamerasystems realistisch ist, dass das CLCS prinzipiell in einer realen Anwendung in der Zukunft funktionieren kann. Zur Bewertung der Messgenauigkeit des CLCS wurde eine Simulationsstudie unter Verwendung von Bildaufnahmen von Laserstrahlen vom Außenversuch durchgeführt, die zu dem Ergebnis kam, dass mit der verwendeten Kamera eine mittlere Messgenauigkeit von 0.37 mrad realistisch ist, was ausreichend gut ist. Für das CLCS ist eine Messrate von 10 Hz realistisch. Verglichen mit der aktuellen Kamera-Target-Methode kann das CLCS potentiell mit einer weit höheren Messgeschwindigkeit betrieben werden und zwar bis zu 300-mal schneller, wenn bei der Vermessung der Ausrichtung eines Heliostaten lediglich eine einzelne Spiegelfacette verwendet wird. Die Vermessung mehrerer Spiegelfacetten pro Heliostat, um daraus die Gesamt-Heliostatennormale zu bestimmen, ist ebenfalls möglich. Darüber hinaus kann das Laser-Kamera-Verfahren auch nachts eingesetzt werden.

Table of Contents

List of Figures

List of Tables

List of Symbols

Greek Symbols

Symbol	Description	Unit
α	Absorption coefficient.	1/m
α	Angle, angular field of view (AFOV).	°
ϕ	Azimuth view angle.	°
Δ	Change in a quantity.	-
$\Delta\nu$	Frequency.	Hz
∂	Partial derivative.	-
$\eta(\lambda)$	Quantum efficiency of image sensor.	-
$\eta_{\mathrm{pc}}(\lambda)$	Efficiency of photocathode.	-
γ	Angle of incidence.	°
γ	Angle of reflection.	°
γ	Angle.	°
λ	Wavelength.	m
λ_0	Centre transmission wavelength at normal incidence angle.	m
λ_θ	New centre transmission wavelength at the angle of incidence.	m
$\mu_{\mathrm{abs,m}}(\lambda)$	Molecular absorption coefficient.	m^{-1}
$\mu_{\mathrm{abs,p}}(\lambda)$	Absorption coefficient of a particle.	m^{-1}
$\mu_{\mathrm{ext}}(\lambda)$	Total extinction coefficient.	m^{-1}
μ_{p}	Number of photons.	-
$\mu_{\mathrm{sca,p}}(\lambda)$	Scattering coefficient of a particle.	m^{-1}
$\mu_{\mathrm{y,dark}}$	Grey value of a pixel of a dark image.	-
$\mu_{\mathrm{electrons,L,p}}$	Mean number of electrons produced from photons per pixel.	-
$\mu_{\mathrm{sca,m}}(\lambda)$	Molecular Rayleigh scattering coefficient.	m^{-1}
$\mu_{\mathrm{y,p}}$	Mean digital number (grey value) of a pixel.	-
$\mu_{\mathrm{photons,BGD},\lambda,\mathrm{p}}$	Mean number of photons per pixel from background irradiance after passing the filter.	-
$\mu_{\mathrm{e,p}}$	Total number of electrons from the scattered laser beam as well as background signal.	-
$\mu_{\mathrm{photons,L,p}}$	Mean number of photons from the scattered laser beam impinging on an image sensor's pixel.	-

$\mu_{\text{electrons,BGD},\lambda,\text{p}}$	Mean number of electrons per pixel produced from photons from background irradiance.	-
Ω	Resistance.	Ω
Ω_1	Solid angle.	sr
Ω_2	Solid angle.	sr
φ	Divergence of a laser beam.	rad
π	Circumference of a circle divided by its diameter.	m^2
$\pi_n(\cos\theta)$	Function describing angular scattering patterns of the spherical harmonics.	-
ρ	Angle of incidence.	$^\circ$
$\rho_\text{m}(\lambda)$	Mirror reflectivity.	%
σ_e^2	Poisson distribution.	-
$\sigma_{\text{scat,mR}}$	Rayleigh scattering cross-section.	m^2
σ_d^2	Normal distributed noise source due to read-out and amplifier circuits.	-
σ_y^2	Total temporal variance of the digital signal y.	-
σ_q^2	Uniformly distributed noise source due to conversion from analogue to digital signal.	-
τ_ext	Optical depth.	-
$\tau_\text{F}(\lambda)$	Transmissivity of spectral filter.	-
$\tau_\text{lens}(\lambda)$	Transmissivity of lens.	-
θ	Angle of incidence.	$^\circ$
θ	Scattering angle.	$^\circ$
$\tau_n(\cos\theta)$	Function describing angular scattering patterns of the spherical harmonics.	-
$\xi_\text{Image Space}$	System's image space resolution.	lp/mm
ξ_Sensor	Sensor resolution.	lp/mm
ζ	Portion of charge carriers contributing to photo current and did not recombine at the semiconductor surface.	-

Roman Symbols

Symbol	Description	Unit
A	Area.	m^2
A	Cross-sectional area.	m^2
$A_\text{b,cs}$	Initial laser beam cross-sectional area.	m^2
A_lens	Camera lens aperture.	m^2
a_n	Scattering coefficient.	-

A_{p}	Cross-sectional area of a particle.	m^2
$A_{\mathrm{b,cs,m}}$	Cross-sectional area of a laser beam when it impinges on a mirror.	m^2
b	Image distance.	m
b_{n}	Scattering coefficient.	-
b	Ratio involving object distance R and focal length of camera lens f.	-
c	Speed of light.	m/s
c	Value of y at the interception of the line with the y-axis.	-
c	Change in a quantity.	-
d	Diameter.	m
d	Penetration depth.	m
D_{p}	Particle diameter.	m
d_{p}	Particle diameter.	m
D_{AB}	Distance between the laser source and a heliostat.	m
D_{CD}	Length of laser beam in the AFOV of the camera.	m
E	Exposure flux.	$\mathrm{W/m}^2$
e	Exponential constant.	-
E_{L}	Pulse energy of a pulsed laser.	J
$E_{\mathrm{photon}}(\lambda)$	Energy of a single photon at a specific wavelength.	J
f	Focal length of camera lens.	m
$f(\delta)$, f	Correction factor.	-
F(air	King's factor.	m/s
F'	Point/coordinate where a focal point forms.	%
$\mathrm{Gain}_{\mathrm{MCP}}$	Amplification of the signal inside an microchannel plate (MCP).	-
H	Exposure (or energy density).	$\mathrm{J/m}^2$
h	Height of scenery.	m
h	Height.	m
h	Planck's constant.	$\mathrm{kg \cdot m^2 \cdot s^{-1}}$
h_{s}	Height of image sensor.	m
h_{p}	Height of scenery viewed by single pixel.	m
i	Imaginary number.	-
$I_{\mathrm{L},0}$	Initial laser beam intensity.	$\mathrm{W/m}^2$
I_{scat}	Scattering intensity.	$\mathrm{W/m}^2$
$I_{\mathrm{BGDF},\lambda}$	Background irradiance.	$\mathrm{W/m}^2$
$I_{\mathrm{L},D_{\mathrm{B}}}$	Laser beam intensity at heliostat.	$\mathrm{W/m}^2$
$I_{\mathrm{reflected},F'}$	Intensity of a reflected laser beam at focal point F'.	$\mathrm{W/m}^2$

i_1	Intensity parameter for perpendicular polarisation.	-
i_2	Intensity parameter for parallel polarisation.	-
$I_{\mathrm{b,m}}$	Intensity of a laser beam when it impinges on a mirror.	$\mathrm{W/m^2}$
$I_0\,(\lambda)$	Intensity of the monochromatic light source.	$\mathrm{W/m^2}$
$I_{\mathrm{transmitted}}\,(\lambda)$	Intensity of transmitted monochromatic light.	$\mathrm{W/m^2}$
i_1	Intensity parameter for perpendicular polarisation.	-
i_2	Intensity parameter for parallel polarisation.	-
$I_{\mathrm{b,s}}(\lambda)$	Laser beam's intensity after attenuation.	$\mathrm{W/m^2}$
$I_{\mathrm{DHI}}(\lambda)$	Diffuse horizontal irradiance from the sky.	$\mathrm{W/m^2}$
$I_{\mathrm{scat,pR}}\,(\theta)$	Rayleigh scattering intensity for a specified particle with single diameter.	$\mathrm{W/m^2}$
$I_{\mathrm{scat,total}}\,(\theta)$	Total scattering intensity from Mie and Rayleigh scattering.	$\mathrm{W/m^2}$
$I_{\mathrm{scat,mR}}(\theta)$	Scattering intensity at a specified scattering angle for a single molecule at a distance R from the scatterer source.	$\mathrm{W/m^2}$
$I_{\mathrm{scat,Mie,total}}\,(\theta)$	Total Mie scattering at specified scattering angle for a defined particle concentration and distribution.	$\mathrm{W/m^2}$
$I_{\mathrm{scat,pR,total}}\,(\theta)$	Rayleigh scattering intensity for a specified particle number and size distribution.	$\mathrm{W/m^2}$
$I_{\mathrm{scat,mR,total}}(\theta)$	Total scattering intensity at a specified scattering angle at a distance R from the scatterer source.	$\mathrm{W/m^2}$
$I_{\mathrm{scat,Mie}}(\theta)$	Scattering intensity at a specified scattering angle for a single particle with a specified diameter at a distance R from the scatterer source.	$\mathrm{W/m^2}$
K	Overall system gain for the analogue-to-digital conversion (ADC).	-
k	Imaginary part of the complex refractive index.	-
L	Length.	m
L	Luminance.	$\mathrm{cd/m^2}$
m	Gradient or slope of a straight line.	-
m	Complex refractive index containing the real and imaginary part.	-

$\overrightarrow{n}$	Normal vector.	-
n_{eff}	Refractive index of the optical filter.	-
N_{m}	Concentration of absorbing molecules.	m^{-3}
$n_{\mathrm{p,b}}$	Width of beam in pixels.	-
$N_{\mathrm{photons,L}}$	Number of photons emitted by a laser.	-
N_{p}	Particle concentration.	m^{-3}
$N_{\mathrm{photons},\lambda}$	Number of photons entering camera.	-
$N_{\mathrm{p,d}}$	Particle concentration at a specific diameter.	m^{-3}
n	Real part of the complex refractive index.	-
n_{air}	Number of air molecules per unit volume.	m^{-3}
$n_{\mathrm{p,h}}$	Number of vertical pixels of image sensor.	-
$N_{\mathrm{p,vol,d}}$	Number of particles of a specified diameter.	-
$n_{\mathrm{p,w}}$	Number of horizontal pixels of image sensor.	-
n_0	Refractive index of the incident medium.	-
$N_{\mathrm{air,vol}}$	Number of air molecules in the volume of the laser beam within the angular field of view (AFOV) of the camera.	m^{-3}
P	Peak power.	W
$P(\theta)$	Phase function.	-
P_{m}	Mean power.	W
P_{L}	Initial laser peak power.	W
$P_{\mathrm{n}}^{(1)}$	Legendre polynomial of order n and first degree.	-
P_{scat}	Power of scattered light.	W
Q	Pulse energy.	J
Q_{ext}	Single particle extinction efficiency.	-
q	Pre-factor dependent on a laser's pulse form.	-
R	Distance.	m
R	Reflection of the surface of the pixel.	-
r	Curvature radius.	m
r	Radius.	m
$R'(\theta)$	Boundary count value.	-
$R(\theta)$	Vector of Radon transform with the maximum θ count values.	-
$R(\theta,x')$	Radon output matrix with the bin count values of θ and x'.	-
SR	Scattering ratio.	%

$\left\|S_1\left(\theta\right)\right\|^2$	Intensity parameter for perpendicular polarisation.	-
$\left\|S_2\left(\theta\right)\right\|^2$	Intensity parameter for parallel polarisation.	-
$S_1\left(\theta\right)$	Scattering amplitudes of the electric fields $E_\perp$ (perpendicular).	-
$S_2\left(\theta\right)$	Scattering amplitudes of the electric fields $E_\parallel$ (parallel).	-
Δt_{pc}	Pockels cell delay.	s
$\Delta t_{\mathrm{pulse}}$	Pulse width.	s
T	Transmission.	%
V_{b}	Beam volume within the angular field of view of the camera.	m^3
w	Width of scenery.	m
w_{s}	Width of image sensor.	m
wf	Boundary count value for weighing function.	-
w_{p}	Width of scenery viewed by single pixel.	m
W	Product of scattering ratio and reflectance normalised to the wavelength $\lambda = 320\,\mathrm{nm}$.	m^{-3}
W_{DHI}	Product of scattering ratio and reflectance normalised to the wavelength $\lambda = 320\,\mathrm{nm}$, multiplied by a normalised DHI ratio.	m^{-3}
Δx	Distance.	m
x	Coordinate.	-
x	Size parameter.	-
x_{p}	Height of single pixel.	m
y	Coordinate.	-
y	Distance.	m
y_{p}	Width of single pixel.	m
z	Coordinate.	-

Subscripts

Symbol	Description	Unit
b	background	-
ext	extinction	-
e	electric	-
i	index	-
L	laser	-
l	lower	-

max	maximum	-
min	minimum	-
normed	normed value	-
p	lower bound of summation	-
p	particle	-
j	index of summation	-
p	upper bound of summation	-
t	target	-
u	upper	-

Superscript

Symbol	Description	Unit
α	absorption	-
d	thickness	m

Acronyms

ADC	analogue to digital conversion, 40, 71, 72, 105, 121
AFOV	angular field of view, xii, 16, 18, 29, 37–40, 42, 83–85, 89–91, 111, 122, 125, 142, 164, 166, XLVII, LXI–LXIV
AM	auxiliary mirror, 12
AOI	angle of incidence, viii, 89–92
B&W	black and white, XLII
BNC	Bayonet Neill-Concelman, 86, 103, 115, 116, 138
BPP	beam parameter product, 20
CCD	charge-coupled device, ix, 71–73, 114, 119, 120, 122, 132, XXXIX
CD	compact disk, 98
CLCS	central laser and camera system, iii, iv, vi, vii, xii, 3–7, 14, 18, 20, 21, 26, 28–30, 33, 35, 38, 39, 41–44, 46, 47, 50, 52, 54–56, 58–61, 64–66, 69, 70, 73–75, 84, 88–92, 95–106, 109–115, 118, 125–127, 129, 132–135, 137, 138, 148, 149, 153, 156–169, XXXI, XXXII, XXXIV, XXXVIII, XLV
CMOS	complementary metal oxide semiconductor, 71–73, 115, XXXIX
COM	Communication port, ix, 118
CRS	central receiver systems, iii, xii, 1–3, 8, 15, 58, 61, 66, 112, 152, 156, 159, 160
CSP	Concentrated Solar Power, 1, 55, 66, 111, 134
cw	continuous wave, 74, 93–95, 97, 98
CWL	central wavelength, viii, 88–92, 97, 111, 114, 115, 158
DHI	Diffuse Horizontal Irradiance, 30, 42, 47, 48, 50, 54–56, 109, 162, 163, XXXI
DN	Digital number, 40
DNI	Direct Normal Irradiance, 42, 44, 45, 47
DSNU	dark signal non-uniformity, XXXIX
DWD	Deutscher Wetterdienst, 45, 51, 137, 138, 146–149, 158, 165
EM radiation	electromagnetic, 42, 44, 56, 103, 138
EMVA	European Machine Vision Association, 41
FL	flashlamp, 103
FOV	field of view, 30, 31, 33, 83, 84, 96, 111, 166, XLVI

FWHM	full width at half maximum, 88, 90–92, 99, 111, 112, 115, 126, 127, 141, 142, 158, 162, 164, 165, XXXII, LXV, LXVI
GHI	Global Horizontal Irradiance, 42, 47
GigE	Gigabit Ethernet, 86
GTI	Global Tilted Irradiance, 47–49
GV	greyscale value, 120–122, XLII
HITRAN	High-Resolution Transmission Molecular Absorption (HITRAN) Database, XXXIII
HR	high reflection, 129, 130
HT	high transmission, 129, 130
HTF	heat transfer fluid, 2
IR	infrared, x, 28, 43, 53–56, 73, 78, 79, 84, 96, 100, 110, XXXI–XXXIII
ISS	International Space Station, 47
KIT	Karlsruhe Institute of Technology, 137, 138
LED	light-emitting diode, 13, 152, 166
LiDAR	Light Detection and Ranging, 51, 88, 94
MCP	microchannel plate, xv, 41, 77–81, 115
MIR	mid infrared, 99
MODTRAN	MODTRAN (MODerate resolution atmospheric TRANsmission), XXXIII
MPE	maximum permissible exposure, LII
MTF	modulation transfer function, xi, 81, 163, XLII, XLIV, XLV
Nd:Yag	neodymium-doped yttrium aluminum garnet, XXXVII
NIR	near infrared, 99
OCS	online calibration system, 8, 154, 156
OD	optical depth, 92
OPC	optical particle counter, 61
OPO	optical parametric oscillator, 98–100, 111, 163
PC	Pockels cell, 103
PDF	probability density function, LIII
PMAG	primary magnification, XLVI, XLVII
PRNU	pixel response non-uniformity, XXXIX
PTC	parabolic trough collector, 1

QE	quantum efficiency, 73
R&D	Research and development, 3, 111, 158, 161–165, 167
RC	regular calibration, 8
sCMOS	scientific complementary metal oxide semiconductor, 71
SD	slope deviation, 105, 106
SEM	scanning electron microscopy, 59
SIJ	Solar-Institut Jülich, 137, 158
SMA	SubMiniature version A, 86
SMB	SubMiniature version B, 86
SOLSPEC	*SOLar SPECtrometer*, 47
SSI	spectral solar irradiance, vii, x, 42, 43, 45–47, 50, XXXI, XXXII
TTL	Transistor-Transistor Logic, 116
UAV	unmanned aerial vehicle, 13, 152, 153
UV	ultra violet, vii, viii, 28, 42–44, 48, 50, 52, 53, 66, 73, 78, 84, 85, 96, 99, 100, 109–111, 114, 115, 137, 157, 158, 165, 166, XXXI

1 Introduction and Motivation

Concentrated Solar Power (CSP) plants exist since several decades. The majority of the installed CSP plants are parabolic trough collector (PTC) plants followed by central receiver systems (CRS). PTC plants used to mainly be deployed for generating electricity, but nowadays the focus is also on the production of process heat. CRS deploy thousands to more than a hundred thousand individually, biaxially sun-tracking heliostats to reflect direct solar irradiance onto a central absorber structure called receiver atop of a tower. Due to the resulting high solar irradiance flux density on the receiver, CRS are able to achieve high operating temperatures. This is highly useful for realising high overall efficiencies when operating a Rankine cycle or for solar chemical processes for the production of solar fuels, among other.

For a PTC the tracking of the sun's position is non-complex and can be realised at a low-cost. Tagle-Salazar et al. (2020) state that PTCs typically operate with closed-loop tracking for which a sensor (either a pair of light-sensitive diodes or PV cells) is used. For PTCs the advantage is that a single sensor can be used for the tracking control of a collector row. For CRS, tracking the sun's position accurately is a far more complex task. Heliostats of today's larger-scale CRS plants are placed as far as around 1 km or even further from the tower whereby they have only marginal tracking error tolerances. For instance, a heliostat tracking misalignment of 1 mrad (equivalent to 0.057°) results in an offset from the desired aim point by around 2 m for a heliostat at a horizontal distance of 1 km north of the tower (Sattler et al. 2020). The tolerance of the misalignment of a heliostat depends on the requirements defined by the plant developer, which is individual for each CRS system. To define the tolerance one must consider, for example, the following:

- Complexity of aim point strategy for the receiver.
- Receiver's material temperature tolerance regarding hot spots as well as receiver overheating protection.
- Receiver dimension, the size of the sun's image (depending on heliostat facet size, number of facets, facet canting as well as the projected sun spot size, distances of the heliostats, etc.).
- Decreasing bisector angle with the distances of the heliostats from the tower leading to a lower misalignment tolerance for distant heliostats.

Figure 1.1 shows a visualisation of the effect when a heliostat on the north-south axis has a vertical misalignment at solar noon. The result is a vertical shift of the reflected sun image on the receiver. Considering a heliostat as origin, a vertical angular deviation of the mirror normal by $\partial\gamma$ leads to a vertical angular deviation

of $\partial\alpha$ for the reflected sun rays whereby $-\partial\alpha = 2 \cdot \partial\gamma$ due to the bisector of the angle between the sun and the aim point.

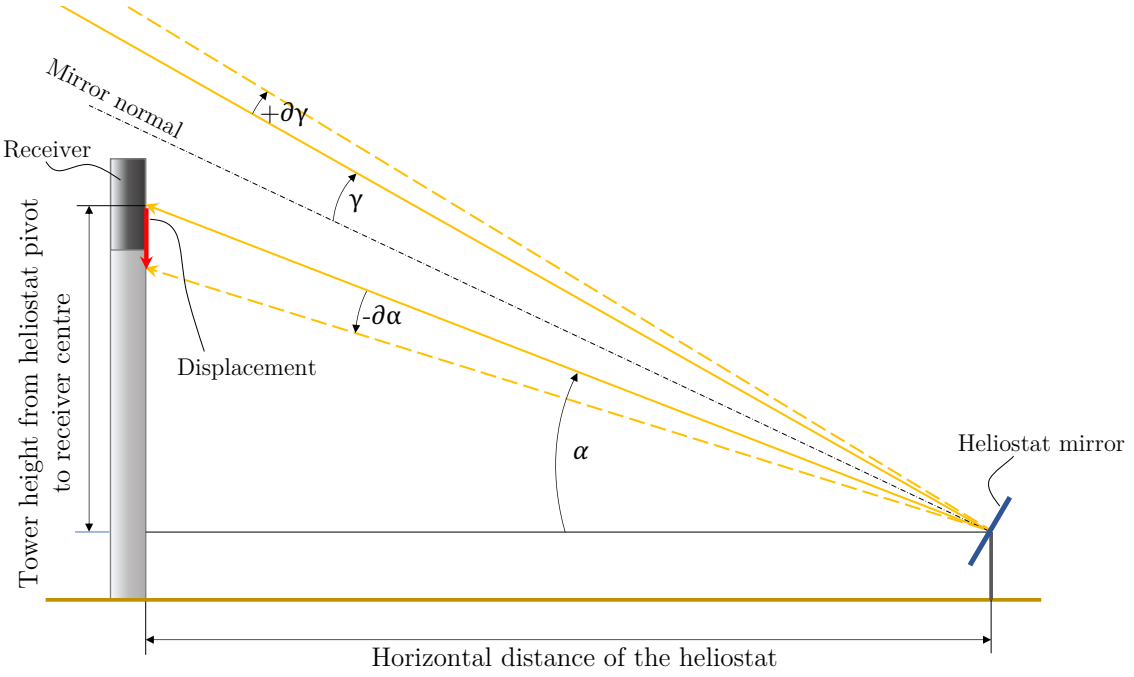

Figure 1.1: Displacement of heliostat aim point when tracking error occurs.

There are various types of receivers which are designed to deploy a specific heat transfer fluid (HTF). Most of the operating CRS use molten salt or water/steam as HTF for their receivers, but also receivers using air as HTF are available. Receivers using solid particles as HTF have also been investigated or are in development. Other HTF have also been investigated in the past but did not have a break through. In the past decades, the CRS technology (also referred to as solar power tower plant, power tower or solar tower) has been subject to several technological advances which include not only the further development of individual system components.

Table 1.1 lists the key data of 11 commercial CRS plants of relevant electrical power output above 50 MW_e. It can be observed in the data that there is no clear trend regarding the heliostat size. While some developers choose small mirror sizes with e.g. 15 m^2 mirror area, others prefer very large mirror areas such as 116 m^2, 140 m^2 or even 178.5 m^2, while again others developed heliostats with a medium size of e.g. 50 m^2 mirror area. Moreover, when examining the heliostat field technology, a great diversity can be identified regarding the heliostat frame design, heliostat shape (square, pentagonal, hexagonal), number of facets, azimuth and zenith drive system, communication technology as well as the heliostat field layout (circular rows, straight rows, irregular patterns).

Table 1.1: Examples of CRS with electrical output > 50 MW_e (NREL 2021a), source denoted by ◇ is (SENER 2018). The short names for CRS are *Ashalim Plot B (Megalim), **Power China Qinghai Gonghe, ***Shouhang Dunhuang 100 MW Phase II, ****SUPCON Delingha 50 MW Tower.

Name of CRS	Electr. output [MW]	Tower height [m]	Heliostat mirror area [m^2]	Number of heliostats [pieces]	Heliostat field mirror area [m^2]	Country	Operational since
Ashalim *	121	250	21	50,600	1,052,480	Israel	2019
Atacama-1	110	243	140	10,600	1,484,000	Chile	2021
CEEC Hami	50	220	50	14,000	696,751	China	2019
Crescent Dunes	110	195	116	10,347	1,197,148	USA	2015
Ivanpah	377	139.9	15	173,500	2,600,000	USA	2014
Khi Solar One	50	200	140	4,120	576,800	S. Africa	2016
LuNeng Haixi	50	188	138	4,400	610,000	China	2019
NOOR III	150	247	178.5 ◇	7,400	1,312,000	Morocco	2018
Qinghai **	50	210	20	25,795	516,000	China	2019
Shouhang ***	100	263	116	12,121	1,400,000	China	2018
SUPCON ****	50	200	20	27,135	542,700	China	2018

The CRS technology uses a vast number of heliostats which must individually track the sun's path in the sky with a high accuracy and precision over the course of the day and year. Accurate and precise tracking is necessary in order for the solar irradiance flux density distribution on the receiver to be optimal, to maximise the energy yield from concentrated solar irradiance from the heliostat field and to avoid hot spots on the receiver. Moreover, inaccurate aiming of the heliostat field directly leads to a loss in revenue and must be avoided. However, several effects lead to inaccurate tracking. To measure and correct the orientation of heliostats, CRS deploy a heliostat field calibration system (Sattler et al. 2020). Various calibration systems that have been developed over the past decades are presented in chapter 2.

The focus of this PhD thesis is on a heliostat calibration method called central laser and camera system (CLCS), which was investigated in the research and development (R&D) project HeliBo at the Solar-Institut Jülich of the FH Aachen University of Applied Sciences.

The working principle of the CLCS, which is described by Sattler & Göttsche (2022) and is shown in Figure 1.2, is as follows:

- A laser with a dual-axis tracking system is positioned at an elevation such as position A on the tower (1). A suitable location could be, for example, below the receiver (2).
- For a measurement of the orientation of a heliostat or a heliostat's mirror facet, the laser is first aligned with the respective mirror.
- Then, a laser beam is emitted from the laser's position at A. The beam impinges on the heliostat's mirror facet (3) and is subsequently reflected into the atmosphere. The beam's path after the reflection is B→C.
- The laser beam scatters photons while traversing through the atmosphere.
- For the CLCS concept to work, two cameras (4a and 4b) must simultaneously photograph the beam's scattered photons from two positions with different viewing angles onto the beam.
- In a final step of the measurement process, the orientation of the laser beam is computed from the two individual images of the beam within the field of view of the camera (5) and (6). For the computation, a computer system with image processing software (7) is required.
- For a new measurement, the laser is then aligned with another mirror facet.

Only the reflected beam (path B→C) is of interest. If the cameras photograph both the beam of the paths A→B as well as B→C, then it is necessary to be able to distinguish between the two beams. This can be done, for example, by means of precalculating the expected path A→B, followed by a calculation of the beam's vector in the image, such that it can then be excluded in the image analysis. The aim is to achieve a calibration accuracy of about 0.1 mrad (Sattler & Göttsche 2022).

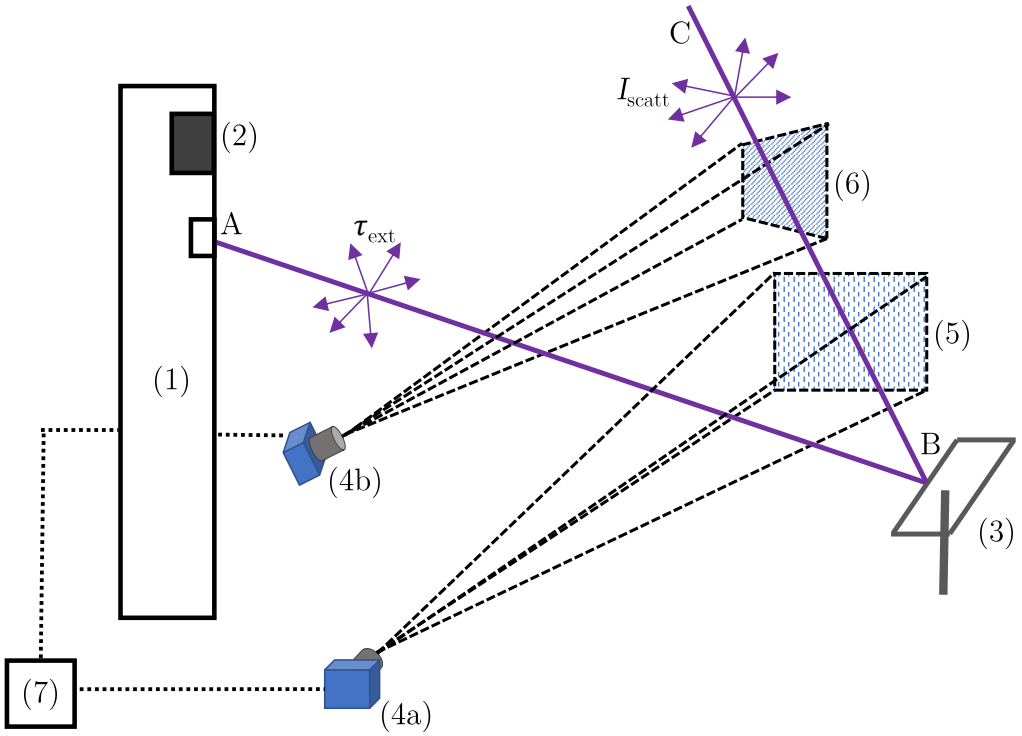

Figure 1.2: Schematic of the CLCS (based on illustration from Dabrowksi et al. (2014), amended to show more details). Reproduced from Sattler & Göttsche (2022), with the permission of AIP Publishing.

A different, easier conception of how a camera of the CLCS shall photograph a laser beam is shown in Figure 1.3. Here, an example of a green laser beam with a wavelength of 532 nm (green colour) is shown. Photons from the laser beam are scattered by air molecules and particles in the atmosphere. Some of the scattered photons impinge on an optical filter of a camera system. If the optical filter allows only the wavelength bandwidth around the laser wavelength (i.e. in this example at around 532 nm) to pass through, then it will block or reflect all other wavelengths within the transmission properties of the optical filter. The impinging and reflected wavelengths represented by the rainbow colours in Figure 1.3 is the diffuse irradiance from the "blue" sky. It should be noted that in actual fact the sky is only perceived as being blue whereas in reality it contains all wavelengths of the spectrum (Bohren 2007, p. 58). From the diffuse irradiance, light wavelengths at around 532 nm will pass through the optical filter together with the scattered photons from the laser beam. Furthermore, the photons passing through the optical filter must also pass through a camera lens before they impinge of the camera's image sensor. The image sensor converts the photons to electrons and - in the case of a monochrome sensor - into greyscale pixel values.

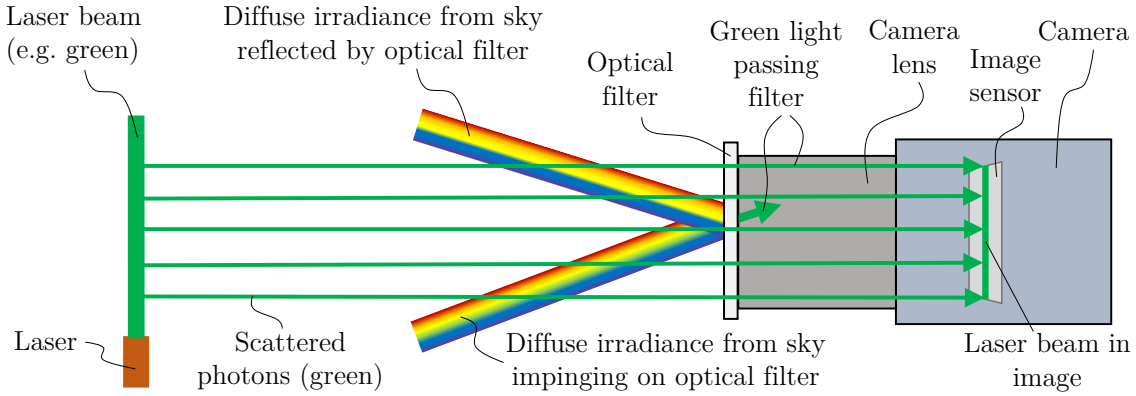

Figure 1.3: Conception of CLCS showing how the scattered light from the laser beam reaches the camera's image sensor.

When photographing a laser beam from the side in clear-sky atmospheric outdoors conditions, it can only be visible when a sufficient number of scattered photons of the beam impinge on the eye or a camera's image sensor. Achieving this at night or in hazy ambient conditions is far less challenging than during broad daylight in clear, sunny weather. Firstly, during the day, the contrast between the diffuse solar irradiance from the sky and the scattered laser beam is far lower than during the night. Secondly, it must always be ensured that the deployed laser is safe with respect to not damaging the (human) eye when accidentally viewed directly and that skin damage cannot occur. Thirdly, during the day, an appropriate optical filter must be used that reflects or blocks all diffuse solar irradiance with the exception of allowing only a small irradiance band around the central laser wavelength to transmit.

Chapters 3 provides an insight into the theory of the CLCS. To find the optimal configuration of the laser and camera system, it was necessary to study in detail the eight topics shown in Figure 1.4. These topics are mainly discussed in chapters 3 and 4, but partly also in other chapters. As will be evident in this work, every one of these topics depends on at least one other topic. From all these fields, laser safety is of utmost priority and presents a limit to the laser parameters that can be used. The study of laser safety was carried out using technical rules for laser safety that apply for Germany, which includes TROS Laserstrahlung (see BAuA (2018a), BAuA (2018b), BAuA (2018c), BAuA (2018d)) and DIN EN 60825-1, among others.

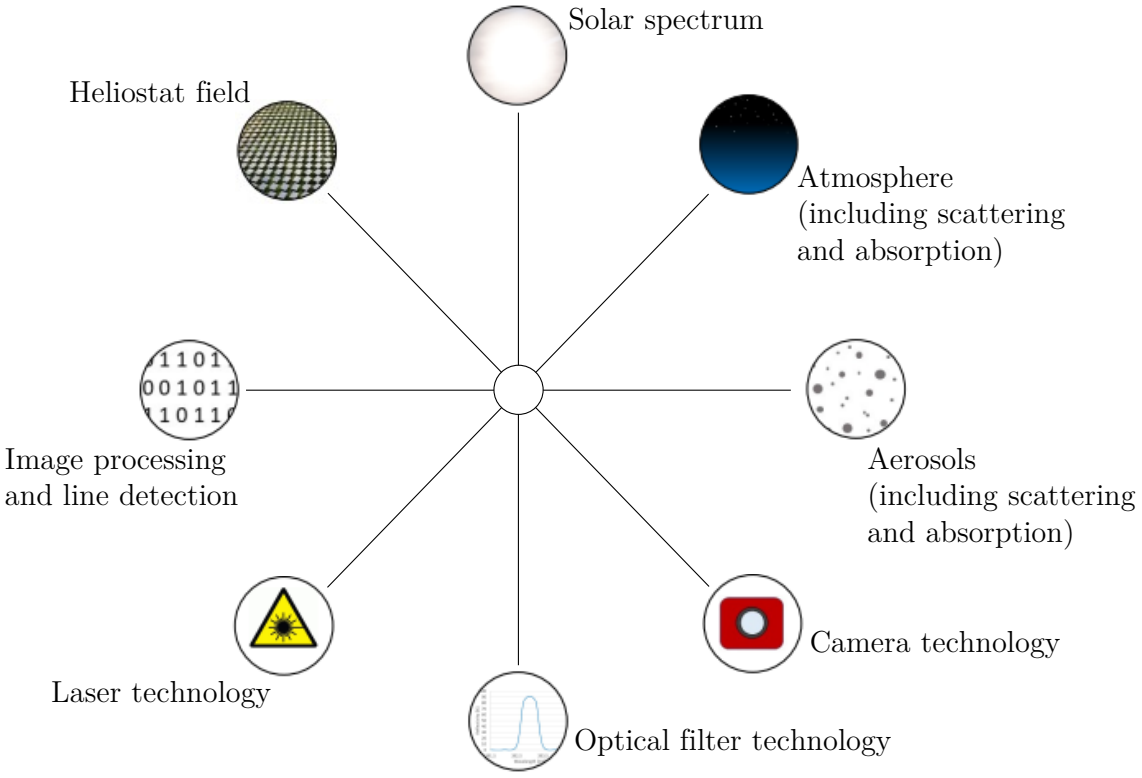

Figure 1.4: Topics of relevance for the CLCS.

In chapter 5, the selection of the laser and camera system components is made. Simulation studies and comparisons with results from laboratory and outdoor tests are part of chapter 6. In chapter 7, a comparison of the CLCS with other calibration methods is given. Finally, a conclusion and an outlook for the CLCS are presented in chapter 8.

2 Heliostat Field Calibration Technology

This chapter explores the terms and definitions used to describe heliostat field calibration methods and gives details on existing calibration methods and those which are under development. Chapter 2 is a summary of several topics pre-published by Sattler et al. (2020).

2.1 Heliostat field calibration – terms and definitions

The calibration of heliostats is a necessity in order to maintain a required tracking accuracy when operating a CRS such that the solar irradiance flux density on the receiver has the desired distribution. Moreover, spillage can be reduced to a minimum. There are several types of error sources of which some are major and others are minor. Major error sources are linked to design issues such as sensor and actuator errors as well as installation errors (Freeman et al. 2015). Sensor and actuator errors can be the gear ratio choice, a backdrive of the heliostat and low encoder resolution, while installation errors include pedestal tilt, azimuth and elevation reference angle and non-level terrain (Freeman et al. 2015). Further errors are described in Sattler et al. (2020). One can distinguish between three different types of calibration processes:

- Pre-calibration: A pre-calibration (also referred to as coarse calibration) is the very first calibration of heliostats during the commissioning phase of a heliostat field in which a coarse alignment of heliostats at an accuracy of between around 3 to 10 mrad is realised. (Sattler et al. 2020)
- Regular calibration: A regular calibration (RC) (also referred to as fine calibration) during the operation of a CRS is a very accurate calibration process where a calibration is repeated in defined time intervals (between a few seconds up to several weeks) whereby it is necessary to measure the alignment of heliostats at an accuracy of about 0.1 to 0.3 mrad (this accuracy is important such that the global tracking error is still acceptable). Small calibration intervals lead to better heliostat tracking accuracies. When a calibration interval within a few dozen of seconds is realised then one can refer to the calibration method as an online calibration system (OCS) due to the reason that it has closed-loop tracking control capability. (Sattler et al. 2020)
- Recurring calibration of devices: The third type of calibration refers to the recurring calibration of measurement devices that are mounted to a heliostat. A measurement device can be, for example, a camera. (Sattler et al. 2020)

When a heliostat is in operation, then it tracks the sun's position based on one of two types of tracking control, namely open-loop and closed-loop tracking control. But first it must be clarified what tracking control refers to. In Sattler et al. (2020) it is described that "tracking control (or heliostat control) is the (automated) operation of setting certain indicators (e.g. motor angles or drive positions) such that a desired heliostat orientation is obtained that is necessary to reflect the sun onto the aim point on a target or receiver. The accuracy, signal frequency, and the location where the feedback signal is created, define the type of tracking control" (p. 113). Two types of tracking control exist (for a more detailed description see Sattler et al. (2020)):

- Open-loop tracking control refers to a type of tracking of a heliostat where the alignment is realised based on feedback from (a) the controller or the encoder, (b) the theoretical sun position as well as (c) parameters obtained from calibrations. This control type can only be realised for heliostats which meet certain criteria such as maintaining the geometry. (Sattler et al. 2020)
- Closed-loop tracking control requires very fast feedback for all heliostats such that tracking can be realised in the seconds range in order to adequately respond to the fast-changing sun position as well as to stay within the defined allowable tracking error. The advantage of closed-loop tracking control is that the heliostat can have non-predictable and non-rigid kinematics. (Sattler et al. 2020)

Furthermore, there are two types of tracking motion, namely continuous tracking and stepwise tracking. The common tracking motion that is applied is stepwise tracking. With stepwise tracking, the heliostats' alignment is changed by a small amount every few seconds (e.g. in a 20 seconds interval) and is kept stationary between the movement intervals. While stationary, the focal spot on the receiver (or target) will drift towards or away from the desired aim point. The subsequent step movement then corrects the heliostat alignment. (Sattler et al. 2020)

Typically, calibration methods are described as being open-loop or closed-loop control capable. This, however, should be distinguished in more detail as many calibration methods realise a tracking control operation that is in-between open-loop and closed-loop control, i.e. a partial closed-cloop. This is due to the fact that depending on the type of calibration method, the level or quality of information or measurement data that is available for aligning a heliostat strongly varies. First it must be clear as to what the components of a signal or effect chain are. In Sattler et al. (2020) it is described that "the signal or effect (e.g. mirror surface normal, or solar focus) flows along various typical components (C)" (p. 113). The signal or effect flow along these components is illustrated in Figure 2.1 (a).

Regarding the quality of the alignment, several factors must be considered. For instance, a camera mounted on a heliostat will give, as feedback, the concentrator normal that represents the orientation of an entire heliostat. Therefore, if the heliostat has multiple mirror facets, the camera or sensor must represent the mirror facets' normals very well in order for the solar focus to hit its target as required. Upstream parameters such as the kinematics of the actuator and the heliostat axes also influence the measurement by the camera or sensor.

Having identified the components of the signal or effect chain, Sattler et al. (2020) also considered "the different monitoring or measuring devices (M) that indicate or measure along the signal or effect chain" (pp. 113–114), which are shown and listed in Figure 2.1 (b). The following paragraph describes these monitoring or measuring devices (M). The monitoring device M1 (computer screen indicating orientation setpoint values to be sent to a heliostat) applies for all devices. The heliostat controller (M2) gives set values to the controller. The encoder (M3a) measures the rotational and angular position. Using only the monitoring device M1 as well as data from the controller (M2) and the drive axes via the encoder (M3a) as feedback information can be regarded as being a more open-loop control system (even if technically M1, M2 and M3a in combination represent a closed-loop). Higher quality feedback is achieved with measurement techniques which can be referred to as M3b, M3c and M3d. A camera or sensor mounted on a heliostat (M3b) will give a higher quality measurement than a decoder (M3a), but a lower quality measurement than a deflectometric measurement technique (M3c) as with deflectometry it is possible to measure the normal vectors distributed over the total heliostat mirror surface. A calibration method regarded as M3d calculates a single heliostat normal vector. It should be noted that as the data from technique M3c can be used to calculate a single heliostat normal vector from the deflectometric measurement data from the individual facets' normal vectors, technique M3c has the potential to be even more accurate than technique M3d. Technique M4 should be interpreted as solar focus characterisation system. (Sattler et al. 2020)

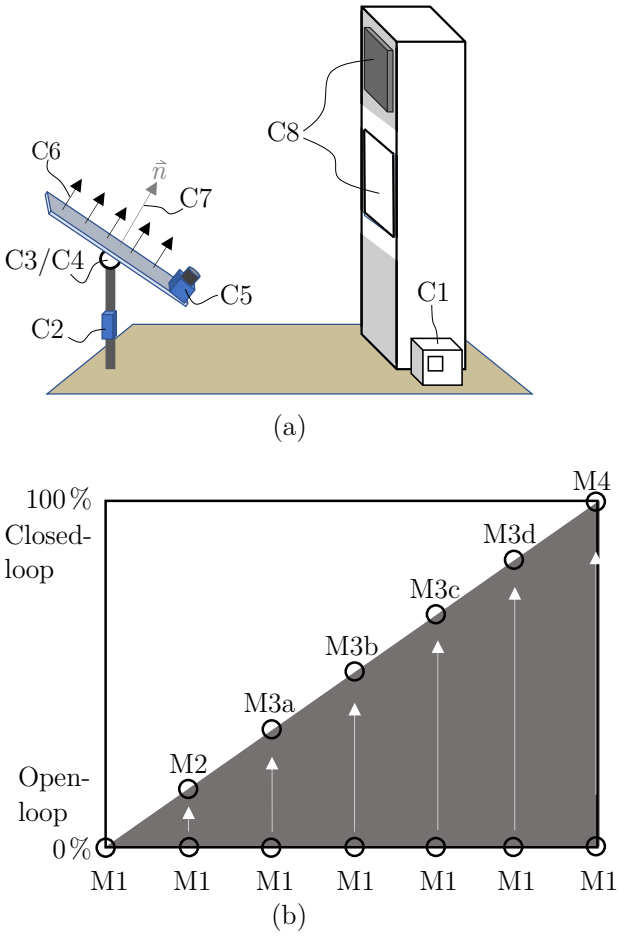

Components (C)
C1: CPU in control room
C2: Controller
C3: Actuator
C4: Encoder
C5: Mounted camera or sensor
C6: Mirror surface normals
C7: Concentrator normal
C8: Solar focus on receiver or target

Monitoring / measurement device (M)
M1: Monitor in control room
M2: Controller
M3a: Encoder
M3b: Camera or sensor
M3c: Other (mirror surface normals)
M3d: Other (normal vector of heliostat)
M4: Beam characterisation system

Figure 2.1: Drawings illustrating (a) components belonging to the signal or effect chain and (b) monitoring or measuring devices (based on illustrations from Sattler et al. (2020)).

2.2 Existing or proposed calibration technologies

Various methods for calibrating heliostats have been developed in the past decades which have different capabilities. Classifying calibration methods is useful such that the calibration methods can be grouped in order to improve the overview and to allow an easier comparison between them. In Sattler et al. (2020) several classification criteria were explored and a new classification criterium proposed, namely classifying calibration methods based on the "location, type and number of measuring devices or sensors" (p. 115). This classification resulted in the four classes named below:

- **Class A:** Central camera(s) or sensor(s)
- **Class B:** Central laser or radar based measurement methods
- **Class C:** Central solar focus position detection with cameras or sensors on tower
- **Class D:** Cameras or sensors on each heliostat

In the following, the classes A to D are described in more detail and one or more examples of calibration methods is given for each class. For selected calibration methods, advantages and disadvantages are described. The below details on classes A to D are based on Sattler et al. (2020), but fewer details and examples are given here compared to the extended content of the paper.

Class A
Class A, with the calibration methods shown in Figure 2.2, is further divided into two subclasses, namely A1 (cameras on ground) and A2 (Camera(s) on tower or UAV).

- Subclass A1 comprises two types of calibration methods, namely class A1a (camera-target method using the sun) and A1b (camera-target method using a signal beam or excitation). Examples of calibration methods are given below:
  - A1a: The camera-target method is the state-of-the-art calibration method which is widely applied worldwide. It was developed by King & Arvizu (1981). This method requires a Lambertian calibration target usually beneath the receiver onto which the heliostats' reflected beams are sequentially aimed at. When the heliostats reflect the sunlight onto the calibration target, a solar focus is formed which is photographed by a camera on the ground. The shape of the solar focus and the overall heliostat orientation can be identified through image processing. When repeating this procedure for a heliostat at different times during a day and the year, then the kinematics of a heliostat can be calibrated. This calibration method covers the signal chain M1–M4 and is estimated to measure with an accuracy of 0.1 mrad.
  - A1b: Signal beam or excitation methods have been proposed, which also use a camera and a target. A very promising development is investigated by Bern et al. (2016) who tested a signalisation method whereby one or more heliostats is set into an excitation (periodic movement). The heliostats keep tracking normally and reflect the solar irradiance onto the receiver during the calibration process. A camera (e.g. on the ground) is oriented to view the receiver and records images at a high frame rate. Using computer vision based software, the aim points from the individual heliostats can be identified. This calibration method covers the signal chain M1–M4.
  - A1b (cont'd): Flesch et al. (2012) and Gross (2016) suggested methods whereby a small, slightly tilted auxiliary mirror (AM) is attached to a heliostat, which reflects a low-energetic, secondary light beam onto a target beneath the receiver while the heliostats continue operating in tracking mode. To differentiate between the various auxiliary mirrors in the heliostat field, it is foreseen to use temporal shadowing, a colour code or the

use of various shapes. Images of the solar focus created by the auxiliary mirror are captured by a camera located on the ground. These calibration methods cover the signal chain M1–M3d.

- Subclass A2 comprises two types of calibration methods, namely class A2a (Single or multiple photos (photogrammetry)) and A2b (Reflected image of object (e.g. star, light-emitting diode (LED), sun/sun's brightness distribution) in a heliostat).
  - A2a: The calibration methods of class A2a foresee that an image from an actual heliostat is taken and processed. One method has a central camera positioned on a tower or a mast to acquire images of a heliostat, whereby the orientation of the heliostat is derived via automatic edge detection as described by Röger et al. (2010). Another method takes series of photos of a moving heliostat (Prahl et al. 2009), while another method uses an unmanned aerial vehicle (UAV) for taking a series of photos from a stationary heliostat (Jessen et al. 2020). The calibration methods of class A2a cover the signal chain M1–M3c/M3d. These calibration methods have a measuring accuracy in the range of several mrad and are suitable for coarse calibration.
  - A2b: The methods of class A2b foresee that cameras take images of an object that is seen in the mirror(s) of a heliostat. Such objects can, for example, be stars and LEDs. A method using an UAV was presented by Prahl et al. (2015). Schell (2011) describes a method whereby cameras mounted on several masts directly view the reflected sun beams of dozens heliostats that are aimed towards the cameras during a single calibration interval. The calibration methods of class A2b cover the signal chain M1–M3c and are estimated to be suitable for a fine calibration of heliostats.

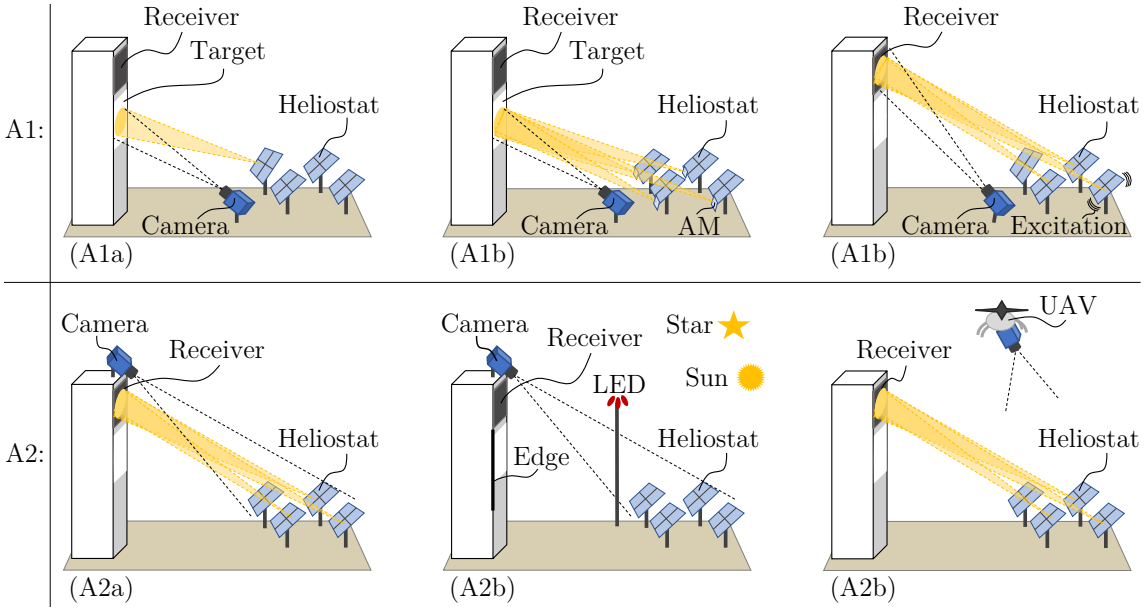

Figure 2.2: Calibration methods of classes A1 and A2 sorted by the classification criterium "location, type and number of measuring devices or sensors" (based on illustrations from Röger et al. (2018) and Sattler et al. (2020)).

Class B

Class B comprises the methods: (i) Central laser and cameras (i.e. the topic of this thesis), (ii) Central total station, (iii) Central radar, and (iv) Central laser scanner. The methods (i) to (iii) are shown in Figure 2.3. The methods cover the signal chain M1–M3d and are described below:

- (i): The central laser and camera system (CLCS) is investigated in this thesis. For a description of the working principle of the CLCS see chapter 1.
- (ii): The concept method with central total station foresees at least three standard glass triple prisms mounted on heliostats which reflect the laser light sent out by be central total station. Using post-processing software, a plane can be calculated from the coordinates of the prisms such that a normal vector can be computed. The potential accuracy of this method depends on the heliostat size and can be around 0.42 mrad for a heliostat with a mirror area of 100 m^2.
- (iii): A central radar method described by Sauerborn et al. (2012) uses a high-frequency, high-resolution millimetre wave radar to scan the heliostat field whereby each heliostat must be equipped with at least three corner reflectors. The overall heliostat frame normal is calculated from the plane deduced from the three corner reflectors. The central radar method was tested on 100 heliostats at the Solar Tower Jülich with heliostat distances between 50 and 300 m. This method is estimated to have an accuracy of around 2 mrad.

- (iv): A central laser method proposed by Sauerborn et al. (2013) measures the orientation of mirror facets from scanning the backside of the heliostats. This method is estimated to have a precision of around 2 mrad.

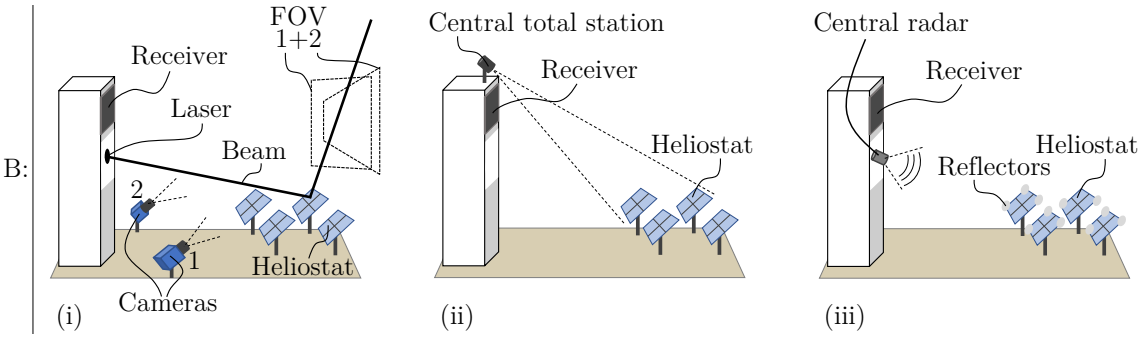

Figure 2.3: Calibration methods of class B sorted by the classification criterium "location, type and number of measuring devices or sensors" (based on illustrations from Röger et al. (2018) and Sattler et al. (2020)).

Class C

Class C, as shown in Figure 2.4, includes methods using: (i) Several cameras or non-optical sensors around the receiver, (ii) Several cameras embedded in the receiver, (iii) Camera array on moving bar moved along the receiver, and a (iv) Camera array or sensor array as target.

These calibration methods cover the signal chain M1–M4 and are estimated to measure within an accuracy of about 0.3 mrad. Examples are given below:

- (i) A calibration method with four cameras installed around the receiver is described by Yogev & Krupkin (1999). This method compares the brightness difference of the light in four simultaneously taken images of a heliostat using the four cameras. Convery (2011) devised a method using photosensors mounted around the receiver which can detect the focal spots of heliostats if they are set to vibrate.
- (ii) In a method described by Goldberg et al. (2015), pin-hole cameras are placed in a gap between receiver pipes.
- (iii) In a calibration system proposed by Collins et al. (2017), a moving bar with a camera array is moved sideways along the receiver. The cameras are subjected to a high solar irradiance flux density and take images of the heliostats during the sweep.
- (iv) Several methods foreseeing an array of digital cameras, optical sensors or photodetectors as target (e.g. below the receiver) were patented by Gross (2016). During the operation of the CRS, signal beams from small mirrors attached to each of the heliostats impinge on the target from which the orientation of each heliostat can be deduced.

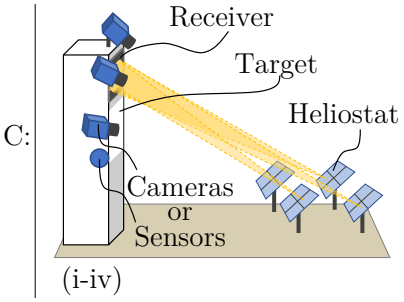

Figure 2.4: Calibration methods of class C sorted by the classification criterium "location, type and number of measuring devices or sensors" (based on illustrations from Röger et al. (2018) and Sattler et al. (2020)).

Class D

Class D methods, as shown in Figure 2.5, have cameras or sensors mounted on the reflector (e.g. the frame) of each heliostat. Several possibilities have been proposed for mounting cameras as illustrated in Figure 2.5 (i) or sensors as illustrated in Figure 2.5 (iia) and Figure 2.5 (iib). These calibration methods cover the signal chain M1–M3b. Some of these methods are estimated to measure with an accuracy of below 1 mrad. Examples are given below:

- (i) When mounting a camera on each heliostat in forward-facing direction, there are several options regarding the use of reference objects. Reference objects can be the position of the sun in the sky (which can be calculated to a high accuracy), the tower, the receiver or a target. A target can also be, for example, one or more artificial light sources. For example, Pfahl et al. (2009) use the sun and a second object (e.g. the receiver). Fairman et al. (2019) use retroreflectors placed near (or in front of) the receiver which are seen by cameras mounted on each individual heliostat. The retroreflectors reflect light impinging from each heliostat whereby the reflected light is captured in the images of each heliostat's associated camera. With an array of retroreflectors installed, the orientation of a heliostat can be deduced by their relative brightness of the reflections. Burisch et al. (2018) use light sources (e.g. artificial light sources, the sun or moon) as target. Each heliostat is equipped with a camera. In the images taken by each camera of each heliostat, the light source is identified in the images and used for calibrating a heliostat.
- (iia) Regarding the use of sensors, Swart (2017) describes a method whereby three or more small signal receivers are attached to each heliostat's mirror surface forming a plane that receive radio-frequency signals from transmitter towers installed around the heliostat field. The orientation is calculated using the principle of phase delay and the distances between the transmitter towers and signal receivers.
- (iib) A camera can also be mounted on the reflector backside if there are several or at least two identifiable objects in the angular field of view (AFOV) that can be taken as reference (for the definition of the AFOV see section 4.3.4 and

equation 4.9). Another method using sensors attached to heliostats is described by Sauerborn et al. (2013) who attached inclinometers and magnetic encoded sensors to heliostats.

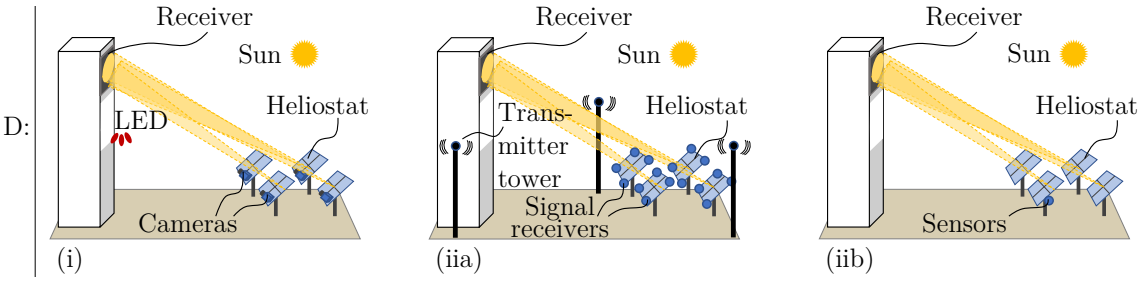

Figure 2.5: Calibration methods of class D sorted by the classification criterium "location, type and number of measuring devices or sensors" (based on illustrations from Röger et al. (2018) and Sattler et al. (2020)).

Comparison of the calibration systems:
In chapter 7, a comparison of the calibration systems (i.e. calibration methods) described in chapter 2 is given. This includes a description of the advantages and disadvantages for each of the classes A to D.

3 Theory of the Central Laser and Camera System

3.1 General physical model of laser and camera system

The basic working principle of the CLCS can be visualised with just a few main parameters and illustrations as shown in Figure 3.1. A brief description of Figure 3.1 is given in the list below:

- Position A: Laser source
- Path A to B: Laser beam's extinction losses $\tau_{\text{ext,AB}}$
- Position B: Reflection of the beam by a mirror facet of a heliostat with reflectance $\rho_{\text{m}}(\lambda)$
- Path B to C: Laser beam's extinction losses $\tau_{\text{ext,BC}}$
- Path C to D: The laser beam is in the AFOV of the cameras
- Position E: Scattered light within the AFOV reaches the camera
- The photographed scenery in the image has a height h and width w for a given distance.

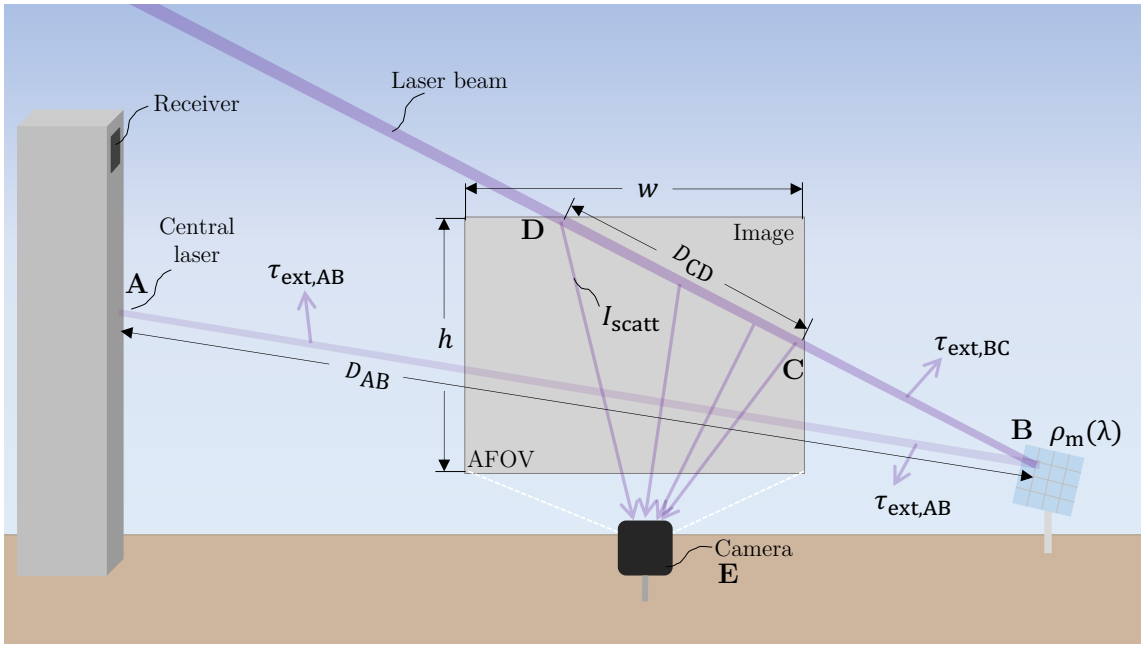

Figure 3.1: Visualisation of parameters of the central laser and camera system.

A general physical model of the CLCS is presented in this section. The principle workflow of the general physical model is shown in Figure 3.2. In a first step, which

is the code initialisation, the input parameters need to be loaded. The input is the technical data of (a) the camera (sensor dimensions, pixel dimensions, number of pixels vertically and horizontally, quantum efficiency at wavelength of laser), (b) the lens (focal distance, inlet window cross-sectional area), (c) the optical filter's spectral transmission characteristics, (d) the laser system (beam emission power or energy, beam emission duration, beam diameter, beam divergence), (e) the distance of the camera from laser beam, a particle concentration and size distribution, (f) the scattering and absorption characteristics of the particles as well as (g) solar spectral data. The calculation steps A to E listed in Figure 3.2 are presented on the following pages.

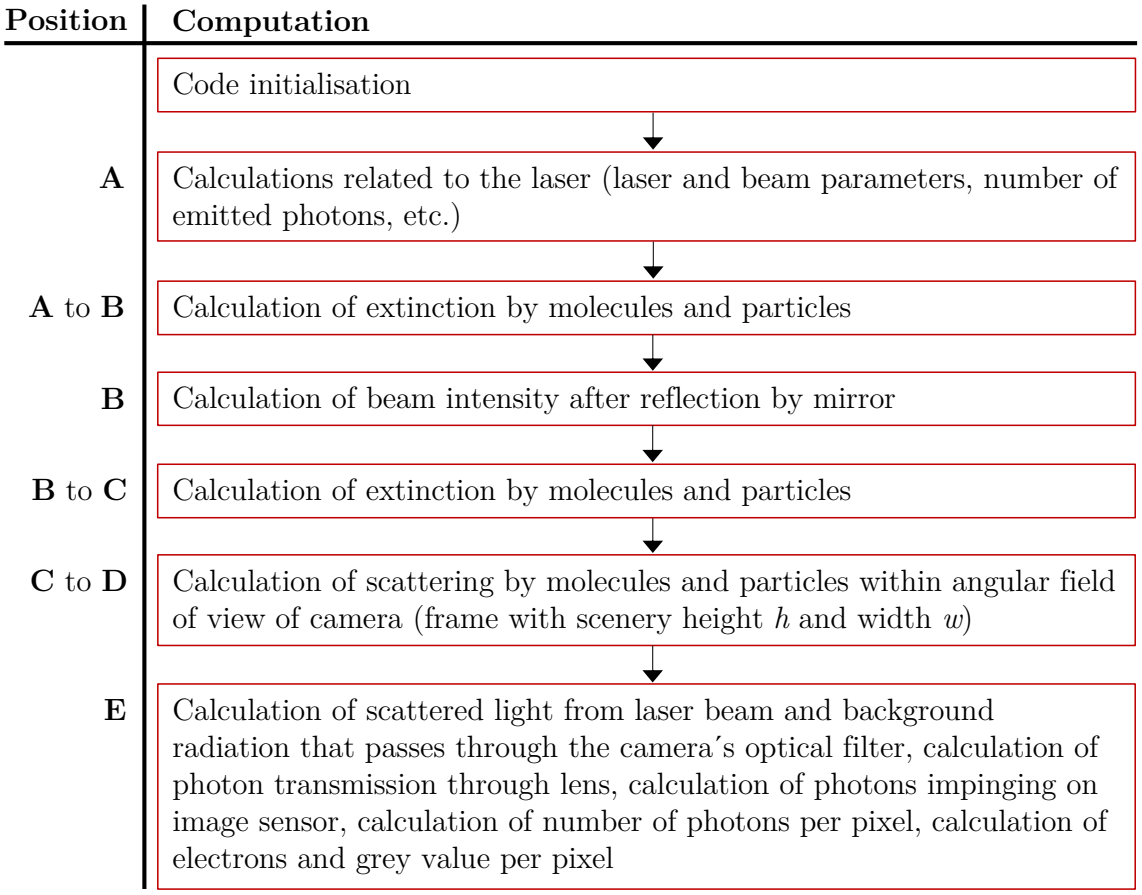

Figure 3.2: Functions of physical model calculating all relevant effects from the emitted laser beam to the grey value of a sensor's pixel.

3.1.1 Laser specific calculations (Position A)

The code initialisation is followed by calculations for the laser system located at position A (cf. Figure 3.1). In this section, only a few of many laser characteristics are considered (for more details on laser characteristics refer to section 4.5). If a laser is used that emits pulses (i.e. a so-called pulsed laser), then the initial laser peak

power P_{L} of a pulsed laser is derived from the pulse energy of a single pulse E_{L}, the pulse width $\Delta t_{\mathrm{pulse}}$ and q (a pre-factor which is dependent on the pulse form), using equation 3.1:

$$P_{\mathrm{L}} = q \cdot \frac{E_{\mathrm{L}}}{\Delta t_{\mathrm{pulse}}} \quad [\mathrm{W}] \tag{3.1}$$

The initial laser beam intensity $I_{\mathrm{L},0}$ is calculated from the laser peak power P_{L} and the initial laser beam cross-sectional area $A_{\mathrm{b,cs}}$ via equation 3.2:

$$I_{\mathrm{L},0} = \frac{P_{\mathrm{L}}}{A_{\mathrm{b,cs}}} \quad [\mathrm{W/m^2}] \tag{3.2}$$

As a laser beam typically expands over the distance due to beam divergence (φ), the drop in beam intensity needs to be accounted for as the cross-sectional area of the beam will increase. Taking into account that for the CLCS the distance between the laser source and the individual heliostats varies, it is possible to calculate the extent of this effect and use the results when specifying the laser system. For a given distance between the laser source and a heliostat, D_{AB}, the beam intensity $I_{\mathrm{L},D_{\mathrm{B}}}$ at the respective heliostat is approximated with equation 3.3:

$$I_{\mathrm{L},D_{\mathrm{B}}} = \frac{P_{\mathrm{L}}}{\pi \cdot (r_{\mathrm{L}} + D_{\mathrm{AB}} \cdot \tan(\varphi))^2} \quad [\mathrm{W/m^2}] \tag{3.3}$$

Equation 3.3 is only an approximation which was used in this work. For a detailed and more exact calculation, parameters such as M^2 or the beam's divergence and the beam parameter product (BPP) should also be included using another equation. The BPP is the product of the radius of the beam waist and the beam divergence half angle ($\varphi/2$) (Schneeweiss et al. 2017). The mentioned parameters are described in various literature such as Schneeweiss et al. (2017).

The number of photons that are emitted by a single laser impulse are calculated via equations 3.4 and 3.5. With equation 3.4 the energy of a single photon, $E_{\mathrm{photon}}(\lambda)$, is calculated from the Planck's constant h, the speed of light c and wavelength λ. The number of photons emitted by a laser, $N_{\mathrm{photons,L}}$, is obtained from dividing the pulse energy of a single pulse, E_{L}, by the energy of a single photon, $E_{\mathrm{photon}}(\lambda)$.

$$E_{\mathrm{photon}}(\lambda) = \frac{hc}{\lambda} \quad [\mathrm{J}] \tag{3.4}$$

$$N_{\text{photons,L}} = \frac{E_{\text{L}}}{E_{\text{photon}}(\lambda)} \quad [\text{-}] \tag{3.5}$$

3.1.2 Extinction of laser beam during travel to heliostat mirror (Path A → B)

Beam extinction (i.e. attenuation) occurs due to two processes in the atmosphere: electromagnetic scattering and absorption of light, i.e. photons interacting with various types of molecules, atomic gases, aerosol particles, haze, smoke, cloud droplets and drizzle etc. suspended in the atmosphere. Depending on the type of scatterer, scattering can occur in the form of reflection, refraction or diffraction (Lelli 2014), but also as reradiation after absorption. The different types of scattering are shown in Figure 3.3. The term "scattering" can be broadly defined as the "redirection of radiation out of the original direction of propagation, usually due to interactions with molecules and particles" (Lelli 2014). Light, which is an oscillating electromagnetic field, excites charges from molecules and particles that then radiate electromagnetic waves, i.e. scattered waves (Lelli 2014). Moosmüller & Arnott (2009) define the scattering of light as follows: "If light is incident on the particle, a dipole moment is induced in each scatterer by the applied oscillating field. These induced dipole moments oscillate at the frequency of the incident light, thereby radiating (i.e., scattering) in many directions. The light scattered by the particle is due to the superposition of the radiation of the individual scatterers, taking phase differences and the resulting interferences into account." (pp. 1028–1029).

Atmospheric scattering occurs due to two types of scattering which are defined below:

- "*Rayleigh scattering* refers primarily to the elastic scattering of light from atomic and molecular particles whose diameter is less than about one-tenth the wavelength of the incident light" (Lockwood 2015).
- "*Mie scattering* refers primarily to the elastic scattering of light from atomic and molecular particles whose diameter is larger than about the wavelength of the incident light" (Lockwood 2015).

Rayleigh scattering from air molecules and Rayleigh scattering from aerosol particles are treated separately. For Mie theory, only scattering from aerosol particles suspended in the near-ground atmosphere is relevant for the CLCS. The scattering theories are summarised in the following subsections. All theories assume spherical molecules and aerosol particles. Scattering can be categorised in elastic and inelastic scattering. This work only covers elastic scattering which is the scattering of electromagnetic radiation (i.e. light) whereby the scattered light retains the frequency

of the incident light (Hinds 1999, p. 349). More details about the boundaries of Rayleigh and Mie scattering, which depend on the light's wavelength as well as the scatterers type and size, are given at the beginning of section 4.2 and refer to Figure 4.10.

The magnitude of the scattering and absorption effect depends on the wavelength of light, the type of molecules, aerosol particles etc. the light interacts with as well as the composition, number and size distribution and physical properties of particles. Moosmüller & Arnott (2009) defines absorption to be "due to the damping of the oscillating dipoles and the incoherent process that transfers electromagnetic energy into thermal energy" (p. 1029). Details on the relevant scattering and absorption theories are given in section 3.1.4.

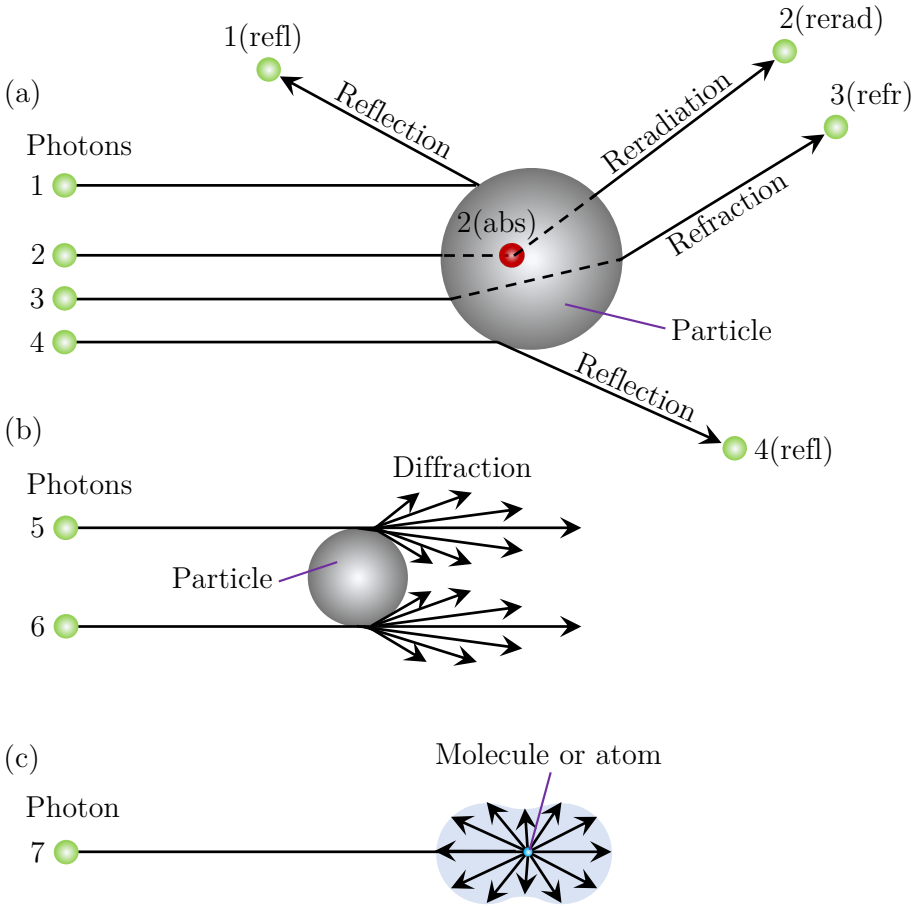

Figure 3.3: Scattering by refraction, diffraction, reflection and reradiation. (a) Photons (1, 2, 3 & 4) interacting with a macroscopic particle. Photons 1 & 4 are scattered by reflection 1(refl) & 4(refl), photon 2 is absorbed 2(abs) and possibly also reradiated after partial absorption 2(rerad), photon 3 is scattered by refraction 3(refr). (b) Photons 5 & 6 scattered by a particle via diffraction when the particle skims the edges of the particle. (c) Photon 7 is scattered by a molecule or atom (example is for unpolarised light). The drawing is based on illustrations from Mishchenko (2009), HORIBA (2021) and Sympatec (2021).

The remaining laser beam intensity after attenuation between the laser source at position A and the heliostat at position B, $I_{\mathrm{b,s}}(\lambda)$, is calculated using the Beer-Lambert-Bouguer law, which describes the transmission of monochromatic light through the atmosphere, as presented in equation 3.6:

$$I_{\mathrm{b,s}}(\lambda) = I_{\mathrm{L,0}}(\lambda) \cdot e^{-\tau_{\mathrm{ext},\lambda}(\Delta x)} = I_{\mathrm{L,0}}(\lambda) \cdot e^{-\mu_{\mathrm{ext},\lambda} \cdot \Delta x} = \frac{P_{\mathrm{L}}}{A_{\mathrm{b,cs}}} \cdot e^{-\mu_{\mathrm{ext},\lambda} \cdot \Delta x} \quad [\mathrm{W/m^2}] \quad (3.6)$$

where $\tau_{\mathrm{ext},\lambda}(\Delta x)$ is the total optical depth for a specified distance Δx (here, $\Delta \mathrm{x} = D_{\mathrm{AB}}$) and $\mu_{\mathrm{ext}(\lambda)}$ the total extinction coefficient (in $\mathrm{m^{-1}}$). The total extinction co-

efficient $\mu_{\text{ext}(\lambda)}$ is defined as "a measure of the rate of diminution of transmitted light via scattering and absorption for a medium" (Merriam-Webster 2021a). As per the equation 3.6, $\tau_{\text{ext},\lambda}(\Delta x) = \mu_{\text{ext}(\lambda)} \cdot \Delta x$. The vector path A→B is the equivalent to Δx. The total extinction coefficient $\mu_{\text{ext}(\lambda)}$ consists of four individual coefficients that are listed below:

- Molecular Rayleigh scattering coefficient, $\mu_{\text{sca,m}}(\lambda)$
- Molecular absorption coefficient, $\mu_{\text{abs,m}}(\lambda)$
- Scattering coefficient of particles, $\mu_{\text{sca,p}}(\lambda)$
- Absorption coefficient of particles, $\mu_{\text{abs,p}}(\lambda)$

Equation 3.7 shows all four individual coefficients:

$$\mu_{\text{ext}}(\lambda) = \Big(\mu_{\text{sca,m}}(\lambda) + \mu_{\text{abs,m}}(\lambda)\Big) + \Big(\mu_{\text{sca,p}}(\lambda) + \mu_{\text{abs,p}}(\lambda)\Big) \quad [\text{m}^{-1}] \tag{3.7}$$

Molecular scattering coefficient $\mu_{\text{sca,m}}(\lambda)$
The scattering coefficient can broadly be defined as "the fractional rate in the transmission of radiation through a scattering medium [...] at which the flux density of radiation decreases by scattering in respect to the thickness of the medium traversed" (Merriam-Webster 2021b). More generally, the scattering coefficient can be defined as the fraction of incident light scattered per unit length when traversing a medium ($dP_{\text{L}}/dL = -\mu P_{\text{L}}$).
The molecular scattering coefficient $\mu_{\text{sca,m}}(\lambda)$ should be understood as the sum of individual scattering coefficients for the various type of molecules and atomic gases the photons at a specified wavelength or specified wavelengths interact with. The molecular Rayleigh scattering coefficient, $\mu_{\text{sca,m}}(\lambda)$, can be calculated from the Rayleigh scattering cross-section, $\sigma_{\text{scat,mR}}$, (in m^2) and the number of air molecules per unit volume, n_{air}, (in the unit m^{-3}) using the below equation 3.8 (Bucholtz 1995):

$$\mu_{\text{sca,m}}(\lambda) = \sigma_{\text{R,m}}(\lambda) \cdot n_{\text{air}} \quad [\text{m}^{-1}] \tag{3.8}$$

For ambient air near the ground, the scattering coefficient at the wavelength of, for example, 400 nm is $\mu_{\text{sca,m}} = 4.26 \cdot 10^{-5}\,\text{m}^{-1}$ which means that in a beam of light a fraction of $4.26 \cdot 10^{-5}$ of the photons is scattered for every metre the light travels. More values for the scattering coefficient are given in section 4.1 in Table 4.2.

To obtain values of the Rayleigh scattering cross-section, the publication of Bodhaine et al. (1999) describes in detail equations and also presents detailed tables for the wavelengths of $\lambda = 0.25 - 1.00\,\mu\text{m}$ at sea level and latitude of 45° as well as other parameters such as the composition of the air molecules. The air composition, for which the Rayleigh scattering cross-sections were computed by Bodhaine et al. (1999), consists of the gases N_2, O_2, Ar, Ne, He, Kr, H_2, Xe and CO_2. As

an example, the Rayleigh scattering cross-section for the wavelength of 400 nm is $1.6738{\cdot}10^{-26}\,\mathrm{m}^2$ and for 600 nm it is $3.1640{\cdot}10^{-27}\,\mathrm{m}^2$. The Rayleigh scattering cross-section, $\sigma_{\mathrm{scat,mR}}(\lambda)$, for standard air can be calculated from the below equation 3.9 given in Bodhaine et al. (1999) (based on Penndorf (1957)):

$$\sigma_{\mathrm{scat,mR}}(\lambda) = \frac{24\pi^3(m^2-1)^2}{\lambda^4 \cdot n_{\mathrm{air}}^2 \cdot (m^2+2)^2} \cdot F(\mathrm{air}) \quad [\mathrm{m}^2] \tag{3.9}$$

where m is the wavelength-dependent refractive index of air (see equations given in Bodhaine et al. (1999) for exact computation and note that the approximate value of m is 1.00028), the number of air molecules per cubic metre of air is $n_{\mathrm{air}} = 2.546899 \cdot 10^{25}/\mathrm{m}^3$ near the ground and the parameter $F(\mathrm{air})$ is a depolarisation term called King's factor which is calculated from several equations proposed by and given in Bodhaine et al. (1999). Furthermore, Bodhaine et al. (1999) present a table with Rayleigh scattering cross-sections for wavelengths between 250 and 1,000 nm. Typically, data tables of the Rayleigh scattering cross-section are given in the unit cm^2, which must be converted to m^2 if SI units are used, as is the case in this thesis. In equation 3.9 it is evident that the Rayleigh scattering cross-section of light is inversely proportional to the fourth power of the wavelength ($\mu_{\mathrm{sca,m}} \propto \frac{1}{\lambda^4}$). Therefore the scattering effectiveness of ultraviolet, visible and infrared wavelengths varies strongly.

For a calculation of $\mu_{\mathrm{sca,m}}(\lambda)$, equation 3.10 below shown in (Hinds 1999) can also be used:

$$\mu_{\mathrm{sca,m}}(\lambda) = \frac{32\pi^3 (m-1)^2 \cdot f}{3{\cdot}\lambda^4 \cdot n_{\mathrm{air}}} \quad [\mathrm{m}^{-1}] \tag{3.10}$$

where, for air molecules at standard conditions, $f = 1.054$ (Hinds 1999). Parts of the above descriptions are already pre-published by Sattler & Göttsche (2022) in a similar way (Reproduced from Sattler & Göttsche (2022), with the permission of AIP Publishing).

Molecular absorption coefficient $\mu_{\mathbf{abs,m}}(\lambda)$

The molecular absorption coefficient $\mu_{\mathrm{abs,m}}(\lambda)$ can be defined as the fraction of incident light absorbed per unit length when traversing a medium. It should be understood as the sum of individual absorption coefficients for the various types of molecules and atomic gases the photons at a specified wavelength or specified wavelengths interact with. The molecular absorption coefficient $\mu_{\mathrm{abs,m}}(\lambda)$ can be calculated using equation 3.11:

$$\mu_{\mathrm{abs,m}}(\lambda) = \sigma_{\mathrm{abs,m}}(\lambda) \cdot N_{\mathrm{m}} \quad [\mathrm{m}^{-1}] \tag{3.11}$$

where $\sigma_{\mathrm{abs,m}}$ is the absorption cross-section of a gas and N_{m} is the concentration of absorbing molecules. Some molecules in the atmosphere absorb specific wavelength ranges but the effectiveness of absorption is dependent on the wavelength. The absorption of light also occurs at various altitudes in the atmosphere depending on the presence and density of the various gases. The probability that a molecule in the atmosphere absorbs a photon at a specific wavelength depends on the magnitude of the wavelength-dependent absorption cross-section (Roedel & Wagner 2018, p. 405) and is typically given in the unit (cm^2/molecule) which needs to be converted to the unit (m) if one works in SI units. In the ultraviolet wavelength range of the solar radiation, for example, the absorption in Earth's atmosphere occurs due to the molecules O_3, NO_2, NO, BrO, OClO, SO_2 and H_2CO (Bovensmann et al. 1999). The wavelength-dependent absorption cross-sections for various molecules can be obtained from databases such as IGACO (2016) or HITRAN (cf. Gordon et al. (2021)).

Scattering coefficient $\mu_{\mathbf{sca,p}}(\lambda)$ and absorption coefficient $\mu_{\mathbf{abs,p}}(\lambda)$ for particles

Particle scattering specifically in the context of relevance for the CLCS is the sum of Rayleigh scattering from aerosol particles and Mie scattering from aerosol particles and is described by the scattering coefficient $\mu_{\mathrm{sca,p}}(\lambda)$. For small particles of diameters d<0.05 µm, Rayleigh scattering equations apply whereas for diameters d>0.05 µm Mie scattering equations are used (Hinds 1999). The absorption of light by particles as a damping factor must also be considered which is described by the absorption coefficient $\mu_{\mathrm{abs,p}}(\lambda)$. The amount of light scattered or absorbed by a particle depends on the particle diameter, the wavelength and the complex refractive index of the particle whereby the complex refractive index has a real and an imaginary part. The real part is associated to the scattering and the imaginary part to the absorption ability. Values of refractive indices are discussed in section 3.1.4 in the topic on Mie scattering.

The individual losses due to scattering and absorption by particles can be combined to $\mu_{\mathrm{ext,p}}(\lambda) = \Big(\mu_{\mathrm{sca,p}}(\lambda) + \mu_{\mathrm{abs,p}}(\lambda)\Big)$. For monodisperse particles, i.e. particles of the same diameter, the extinction coefficient $\mu_{\mathrm{ext,p}}$ is expressed as given in equation 3.12 (Hinds 1999, p. 353):

$$\mu_{\mathrm{ext,p}} = N_{\mathrm{p}} \cdot A_{\mathrm{p}} \cdot Q_{\mathrm{ext}} = \frac{\pi \cdot N \cdot d^2 \cdot Q_{\mathrm{ext}}}{4} \quad [\mathrm{m}^{-1}] \tag{3.12}$$

where N_p is the particle concentration (number per unit volume), A_p the cross-sectional area of a particle, d the particle diameter (assuming spherical particles) and Q_ext the single particle extinction efficiency with values of Q_ext ranging from 0 to about 5. For polydisperse particles, i.e. for particles with a range of diameters, equation 3.13 is used for calculating the extinction coefficient $\mu_\mathrm{ext,p}$ (Hinds 1999, pp. 353–354):

$$\mu_\mathrm{ext,p} = \sum_{i=d_\mathrm{min}}^{d_\mathrm{max}} \frac{\pi \cdot N_i \cdot d_i^2 \cdot Q_\mathrm{ext,}i}{4} \qquad [\mathrm{m}^{-1}] \tag{3.13}$$

For particle sizes of d <0.05 µm, calculating Q_ext is straightforward using equation 3.14 (Hinds 1999, p. 354):

$$Q_\mathrm{ext} = \frac{8}{3}\left(\frac{\pi \cdot d}{\lambda}\right)^4 \left(\frac{m^2-1}{m^2+2}\right)^2 \qquad [-] \tag{3.14}$$

For particle diameters between 0.05 and 4 µm, equation 3.14 is no longer valid. For particles in the diameter range of 0.3 to 1 µm, the maximum value of Q_ext that can be expected from a non-absorbing particle is about 4, whilst for absorbing or irregular particles the maximum value of Q_ext is about 2 without oscillations (Hinds 1999, p. 354). The single particle extinction efficiency Q_ext must be computed. For the computation, for example, the code from Wilson & Reist (1994), or the software MiePlot by Philip Laven (see MiePlot (2018)) can be used.

The scattered light from the laser beam in path A→B is not needed to be photographed for the operation of the central laser and camera system as only the reflected beam is used for determining the orientation of a mirror facet. It should be noted though that if a beam from path A→B is also visible in an image of the camera system, then the line detection algorithm must be able to automatically disregard this line.

3.1.3 Reflectivity loss of the heliostat mirror (Position B)

Just before the laser beam impinges on the heliostat at position B, the laser beam will have an intensity of $I_\mathrm{b,s}(\lambda)$, reduced by extinction between position A and position B and the beam divergence. A further loss in beam intensity occurs due to reflection losses from the heliostat mirrors, whereby the mirror reflectance $\rho_\mathrm{m}\,(\lambda)$ is, among other, wavelength dependent. When considering that the laser beam is being reflected by a mirror facet of a heliostat, the beam intensity will be reduced

by the mirror's reflectance $\rho_{\mathrm{m}}(\lambda)$ at the laser's wavelength. A wavelength-dependent reflectance curve for a typical silvered-glass mirror of 4 mm thickness used in CSP applications is shown in Figure 3.4. At wavelengths in the visible and IR range the reflectance of a typical silvered-glass mirror is very high. At 400 nm, the reflectance is about 90 % and from around 525 to 1,500 nm the reflectance is above 95 %. In the UV range the reflectance decreases. At the wavelength of $\lambda = 350$ nm the reflectance is around 77 %, which is still relatively high but below this wavelength the spectral mirror reflectance sharply drops down. At $\lambda = 340$ nm the reflectance is still about 66 %, while at $\lambda = 330$ nm the reflectance is only around 45 %. The reflectance at $\lambda = 325$ nm is relatively low (28 %). At $\lambda = 320$ nm the reflectance is about 11 %. In section 4.1, an analysis is given (see Figure 4.9) to assess which laser wavelengths are the most suitable for the CLCS when taking the spectral mirror reflectance as well as the scattering effectiveness of light at various wavelengths into account (however, the optimal laser wavelength also depends on other factors, especially laser safety, availability of a suitable laser, the camera technology and the choice of optical filter).
It should be noted that in this work the reflectance is denoted as $\rho_{\mathrm{m}}(\lambda)$, but in the publication of Sutter et al. (2018) the reflectance is denoted more accurately as $\rho_{\lambda,\mathrm{h}}(\lambda,\theta,h)$. Moreover, at an angle of incidence between 0 and 70°, the reflectance of silvered-glass mirrors remains almost unchanged (Sutter et al. 2018).

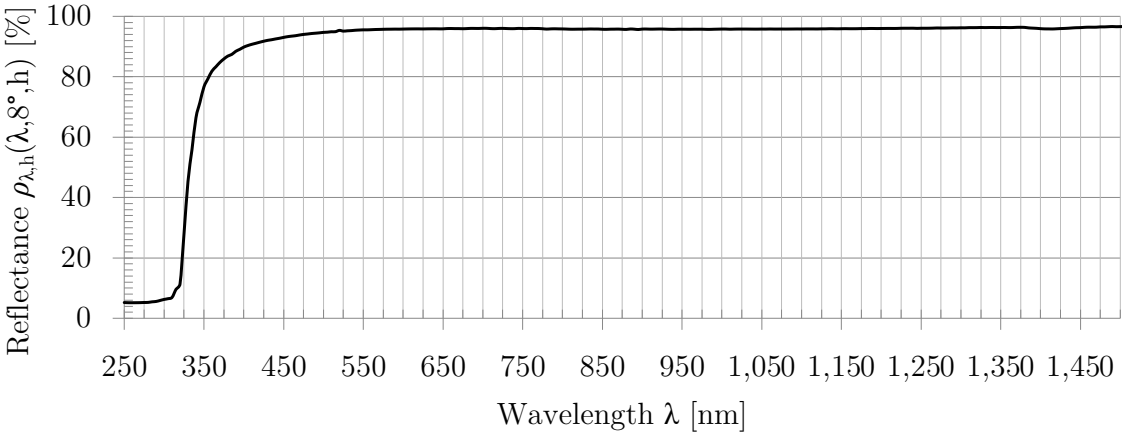

Figure 3.4: Typical hemispherical reflectance of a 4 mm thick silvered-glass mirror in the wavelength range from 250 to 1,500 nm (Sutter et al. 2018).

3.1.4 Calculation of scattering of the laser beam as seen by the camera (Path C → D)

The basic calculation procedure is to first calculate the scattering intensity due to Rayleigh and Mie scattering at distance R, which is presented in the current section 3.1.4. This calculation considers only the number of scattered photons due to the scattering from molecules and from particles within a beam volume within

the angular field of view AFOV of the camera (the AFOV describes the viewing angle of a camera system, more details are given in section 4.3.4). In the upcoming section 3.1.5, a calculation method is shown describing how the scattering intensity is converted into the total number of photons that enter the camera system. Moreover, it is shown how the total number of photons is distributed on pixels of the image sensor according to the equivalent beam width. An illustration corresponding to the above basic depiction of the main calculations for the CLCS is shown in Figure 3.5 (the detailed descriptions of the parameters are given in sections 3.1.4 and 3.1.5).

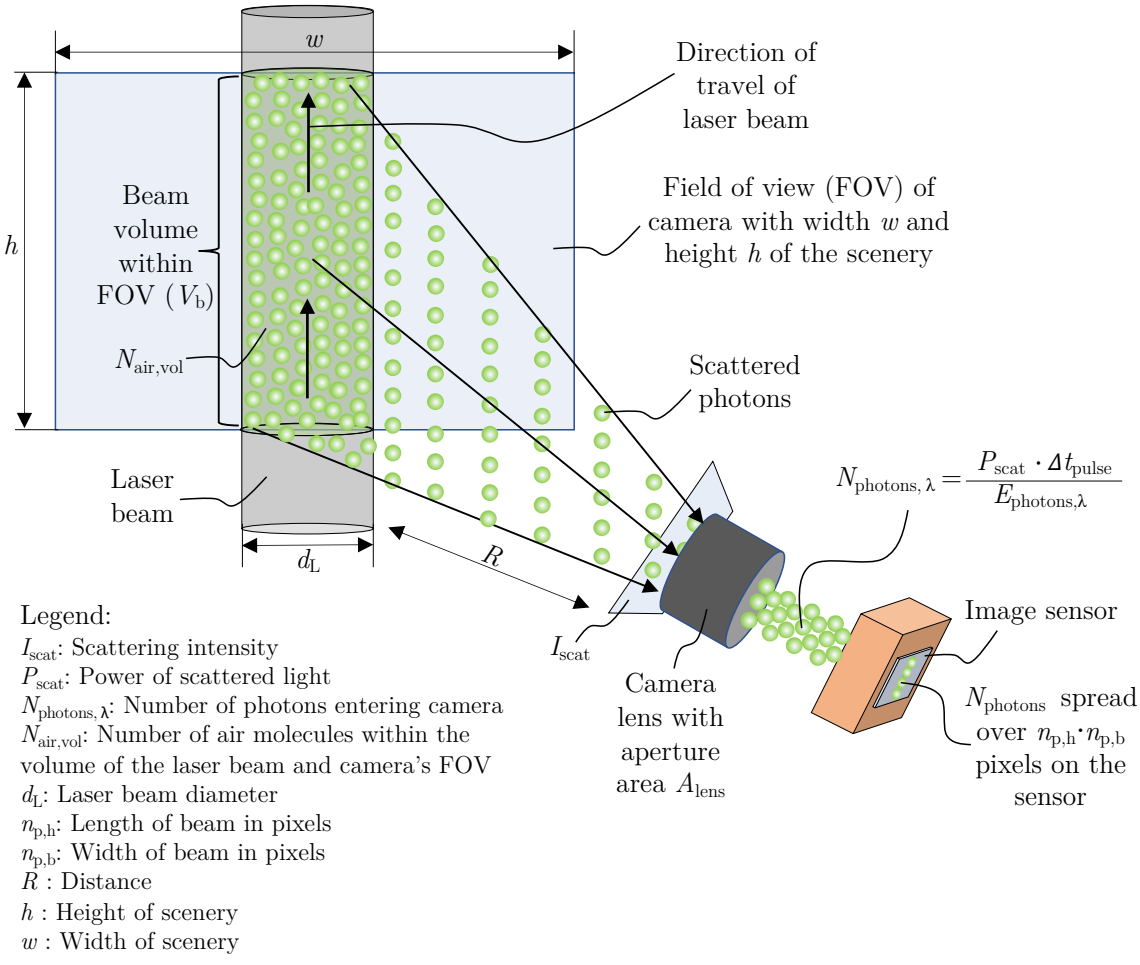

Figure 3.5: Visualisation of scattered photons from laser beam and the beam becoming visible in a greyscale image (the camera lens and the camera are shown detached from another for illustration purposes).

Equations describing Rayleigh scattering from air molecules

Parts of following descriptions are already pre-published by Sattler & Göttsche (2022) in a similar way (Reproduced from Sattler & Göttsche (2022), with the permission of AIP Publishing).

Rayleigh scattering from air molecules and atomic gases leads to a scattering effect which is clearly visible in nature: the blue sky during the day and the red sky during sunset (Young 1982). The diffuse irradiance from the sky (measured as Diffuse Horizontal Irradiance (DHI)) is therefore a result of Rayleigh scattering. The association of Rayleigh scattering with the blue sky is most widely spread (Moosmüller & Arnott 2009). The theory of particle scattering was formulated by Lord Rayleigh (John William Strutt) in publications such as Strutt (1871a), Strutt (1871b) and Strutt (1871c), but the explanation as to why the sky is blue during the day and red during sunsets was given by John Tyndall (Tyndall 1869). Without the vast amounts of molecules and atomic gases suspended in Earth's atmosphere, the sky when viewed from the Earth's surface would simply look black and stars would be visible even during the day (similar to when observing the open black space and stars directly from the moon). In Earth's atmosphere, each molecule that interacts with the unpolarised sunlight contributes to scattering. For unpolarised light "the traverse oscillations of the electric vector occur in all directions perpendicular to the direction of propagation" (Hinds 1999, p. 352). Light from a laser, however, is polarised and can be resolved into two perpendicularly polarised components that are referred to as vertical and horizontal polarisation (Hinds 1999, p. 352). Liou (2002) describes that the scattering cross-section $\sigma_{\text{scat,mR}}$ can be used as per equation 3.15 to calculate the scattering intensity $I_{\text{scat,mR}}(\theta)$ at a specified scattering angle for a single molecule at a distance R from the scatterer source with scattering intensity $I_0(\lambda)$ (the parameters in the equation are partly renamed according to the CLCS):

$$I_{\text{scat,mR}}(\theta) = I_0(\lambda) \cdot \frac{\sigma_{\text{scat,mR}}}{R^2} \cdot \frac{P(\theta)}{4\pi} \quad [\text{W/m}^2] \tag{3.15}$$

where I_0 is the intensity of the monochromatic light source. For details on the scattering cross-section $\sigma_{\text{scat,mR}}$ see equation 3.9 in the part on *Molecular scattering coefficient* in the previous section 3.1.2. The phase function $P(\theta)$ (i.e. angular distribution) adjusts the intensity according to the scattering direction and is described in more detail further below.

For the CLCS, the scattering of laser light for multiple molecules must be calculated and therefore equation 3.15 needs to be adjusted. By multiplying equation 3.15 with the number of air molecules in the volume of the laser beam within the field of view (FOV) of the camera, $N_{\text{air,vol}}$, the total scattering intensity $I_{\text{scat,mR,total}}(\theta)$ can be calculated according to equation 3.16. The parameter $N_{\text{air,vol}}$ is therefore a function

of the beam diameter d_{L} and the height of the scenery h in an image (i.e. the beam volume within the FOV of the camera as shown in Figure 3.5).

$$I_{\mathrm{scat,mR,total}}\left(\theta\right) = I_{\mathrm{b,s}}(\lambda) \cdot \frac{\sigma_{\mathrm{sca,mR}}}{R^2} \cdot \frac{P\left(\theta\right)}{4\pi} \cdot N_{\mathrm{air,vol}} \quad [\mathrm{W/m^2}] \tag{3.16}$$

When considering that the laser beam is being reflected by a mirror facet of a heliostat, equation 3.16 must be multiplied by the mirror's reflectivity $\rho_{\mathrm{m}}\left(\lambda\right)$ which is wavelength-dependent. Figure 3.6 shows the phase function of scattered light for perpendicular and parallel polarisation as well as unpolarised scattering shown in 2-D in polar coordinates (0 to 360°) (a similar representation is shown by Bohren & Huffman (1983, 2008)[p. 134]).

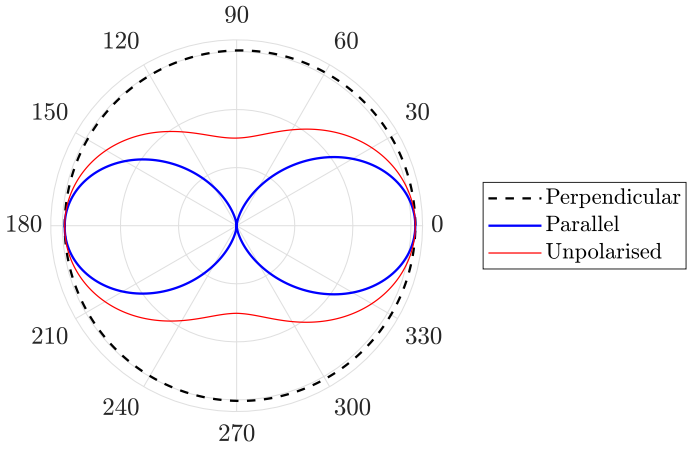

Figure 3.6: Phase function of scattered light for perpendicular and parallel polarisation as well as unpolarised scattering shown in 2-D in polar coordinates (0 to 360°) (Bohren & Huffman 1983, 2008).

Figure 3.7 shows a 3-D representation of the scattering intensity distribution of polarised light. If, for example, a laser beam travels in the direction along the y-axis, whereby the electric field is vertical along the z-axis, scattered light will have a homogeneous scattering intensity around the z-axis along angle ϕ on the x-y plane, but the scattering intensity reduces with increasing scattering angle θ. As per equation 3.17 and as can be seen in Figure 3.7, there is no scattering along the z-axis, i.e. in the direction of the electric field. Depending on the scattering angle θ, the scattering intensity is therefore strongly influenced by the phase function. The intensity of the scattered light of the laser visible to a camera can be optimised by means of adjusting the laser's polarisation plane. Equation 3.17 can be used to calculate the phase function for polarised light:

$$P\left(\theta\right) = \cos^2(\theta) \quad [-] \tag{3.17}$$

where the phase function $P(\theta)$ is at a maximum of 1 (i.e. on the x-axis and on the y-axis) when $\cos^2(\theta) = 0°$ and $P(\theta)$ is at a minimum of 0 when $\cos^2(\theta) = 90°$ (i.e. in the direction of the electric field along the z-axis). A selection of values of the phase function for different scattering angles is given in the following. $P(80°) = 0.03$, $P(70°) = 0.12$, $P(60°) = 0.25$, $P(45°) = 0.5$ and $P(25°) = 0.82$. The contribution of Rayleigh scattering will therefore vary depending on the scattering angle θ.

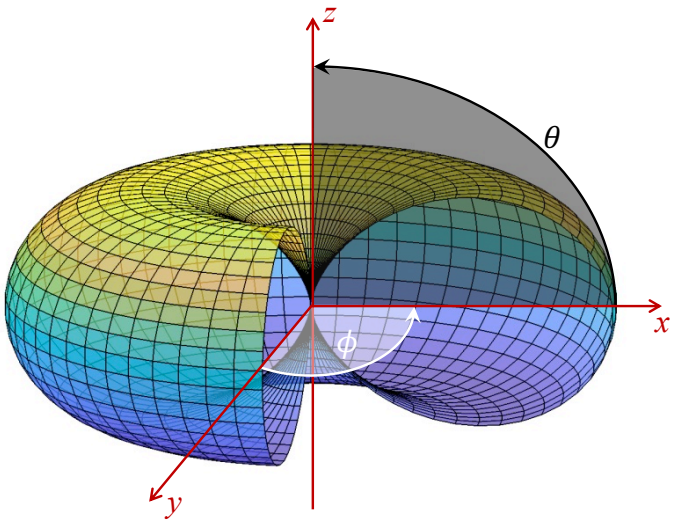

Figure 3.7: 3-D representation of the scattering intensity distribution for polarised light (based on illustration from Long (1977), see also Miles et al. (2001)). The electric field is along the z-axis and the laser beam travels on the y-axis. The phase function gives the scattering intensity in dependence of the scattering angle θ and azimuth view angle ϕ. The graphical presentation of the surface in colours is for enhancing visual legibility. Reproduced from Sattler & Göttsche (2022), with the permission of AIP Publishing.

Equations describing Mie scattering

The Mie theory for scattering, formulated by Gustav Mie (Mie 1908), is applied for particles with diameters greater than approximately 50 nm (Hinds 1999, p. 361). The Mie theory is very complicated and is covered extensively in the literature by van de Hulst (1957, 2012) and Kerker & Loebl (1969) as well as publications such as by Wiscombe (1980) and Dave (1968). Hinds (1999) [p. 361], or Kerker & Loebl (1969) [p. 62] in a similar way, describe the Mie scattering intensity as shown in equation 3.18:

$$I_{\text{scat,Mie}}(\theta) = \frac{I_0 \cdot \lambda^2 \cdot (i_1 + i_2)}{8 \cdot \pi^2 \cdot R^2} \qquad \left[\text{W/m}^2\right] \tag{3.18}$$

where for a single particle of a certain diameter and refractive properties, $I_{\text{scat,Mie}}(\theta)$ is the scattering intensity for a specified direction θ at distance R, I_0 is the intensity of the monochromatic light source, and i_1 and i_2 are intensity parameters for perpendicular and parallel polarisation, respectively. Depending on the light source's polarisation, only one of the two intensity parameters is used, e.g. for perpendicular polarisation, i_1 must be calculated and $i_2 = 0$. For unpolarised light, the average of both intensity parameters is taken, i.e. $0.5(i_1 + i_2)$ (Bohren & Huffman 1983, 2008, p. 133). van de Hulst (1957, 2012) uses the notation $i_1 = |S_1(\theta)|^2$ and $i_2 = |S_2(\theta)|^2$, where $S_1(\theta)$ and $S_2(\theta)$ are scattering amplitudes of the electric fields $E_\perp$ (perpendicular) and $E_\parallel$ (parallel), respectively, for a scattering angle θ. The polarisation has a significant effect on the scattering intensity. Obtaining the intensity functions requires complex calculations using a Mie computer code. The Mie intensity parameters i_1 and i_2 (i.e. $|S_1(\theta)|^2$ and $|S_2(\theta)|^2$, respectively) are functions of the complex refractive index of the particle m, the size parameter x, and the scattering angle θ. The parameters m, x and θ are included in the equations for calculating the scattering amplitudes $S_1(\theta)$ and $S_2(\theta)$ (see equations A.1 and A.2 in the appendix) as well as the equations for calculating the scattering coefficients a_n and b_n (see equations A.5 and A.6 in the appendix). Moreover infinite series involving Legendre polynomials and Bessel functions are used. The complex refractive index describes the scattering and absorption characteristics of particles for which details are given in section 4.2.3. The size parameter is described further below.

To calculate the Mie scattering intensity parameters for the use in equation 3.18 or coefficients, it is necessary to use a computer code. Dave (1968) created the well-known FORTRAN codes called DBMIE and DAMIE. Bohren & Huffman (1983, 2008) created a FORTRAN code called BHMIE that has similar capabilities compared with the code by Dave (1968). Wiscombe (1979) and Wiscombe (1980) published the FORTRAN Mie codes MIEV0 and MIEV1 which led Bohren & Huffman (1983, 2008) to implement modifications in the BHMIE code. A more modern, menu-driven program is described by Wilson & Reist (1994). An easy-to-use MATLAB® computer code by Mätzler (2002) and the software MiePlot by Philip Laven (see MiePlot (2018)), which are both based on the BHMIE algorithm from Bohren & Huffman (1983, 2008), are available and were both used in this work. For further reading, if of particular interest, equations for calculating coefficients of the Legendre and Fourier Series are described in Dave (1969).

Equation 3.18 needs to be further adapted for using it for the CLCS by means of expanding it with additional parameters. First, for a known particle concentration and size distribution data as well as the beam volume, equation 3.19 is needed for calculating the number of particles of a specified single diameter in the beam volume within the FOV of the camera, $N_{\text{p,vol,d}}$, i.e. the particle concentration at a specified diameter, $N_{\text{p,d}}$, and the beam volume V_{b} are used. The beam volume V_{b} is a function

of the beam diameter d_{L} and the height of the scenery h in an image (cf. Figure 3.5).

$$N_{\mathrm{p,vol,d}} = N_{\mathrm{p,d}} \cdot V_{\mathrm{b}} \qquad [-] \tag{3.19}$$

The extended Mie equation is shown in equation 3.20 below which includes equation 3.19 such that the scattering intensity can be calculated taking into account the different particles diameters. The parameter $I_{\mathrm{scat,Mie,total}}(\theta)$ is the total, integrated scattering intensity of a laser beam that traverses a volume of air with a defined particle concentration and size distribution, scattering along the scattering angle θ.

$$I_{\mathrm{scat,Mie,total}}(\theta) = \sum_{d_{\mathrm{p}}=\mathrm{min}}^{\mathrm{max}} \frac{I_{\mathrm{b,s}} \cdot \lambda^2 \cdot (i_1 + i_2) \cdot N_{\mathrm{p,vol,d}}(d_{\mathrm{p}})}{8 \cdot \pi^2 \cdot R^2} \qquad \left[\mathrm{W/m^2}\right] \tag{3.20}$$

For a particle with specified complex refractive index and diameter at a given wavelength, the amplitude or phase function resolved over an angle 2π provides the angular distribution of scattered light intensity (Lelli 2014). The previously described scattering amplitudes $S_1(\theta)$ and $S_2(\theta)$ are described by equations A.1 and A.2 (Kerker & Loebl 1969, p. 62) in the appendix along other details on Mie scattering.

The size parameter x, in some literature also referred to as α, is calculated using equation 3.21 and links the general scattering magnitude to the particle size via the circumference πd_{p} and the light source's wavelength λ (Hinds 1999, p. 351). From this equation it is clear that the smaller the light wavelength and larger the particle diameter is, the stronger is the scattering intensity.

$$x = \frac{\pi \cdot d_{\mathrm{p}}}{\lambda} \qquad [-] \tag{3.21}$$

Mie scattering is strongly forward directed with increasing size diameter, which can be shown in diagrams as phase function against the scattering angle between 0 and 180 ° or in a polar plot. Figure A.4 in the appendix shows several graphs of the phase function against the scattering angle for the size parameters $x = 1$, $x = 3$, $x = 6$ and $x = 12$ (the arbitrarily chosen wavelength for the size parameter calculation was kept at 300 nm and only the particle diameter was changed). The phase function amplitude varies depending on whether the light has a perpendicular or a parallel polarisation. Figure A.5 in the appendix shows the corresponding phase functions in a polar plot. The top half of the plot from 0 to 180° is for perpendicular and the

bottom half of the plot from 180 to 360° is for parallel polarised light. More details about the size parameter x is given at the beginning of section 4.2.

Rayleigh scattering by aerosol particles in the Rayleigh regime

Rayleigh scattering is also commonly related to the scattering of light by small particles (Moosmüller & Arnott 2009). The diameter of particles associated with Rayleigh scattering is below 50 nm, as previously described. The type of particles associated with Rayleigh scattering are Aitken nuclei. Depending on the literature, particles with diameter $\leq$50 nm are defined to belong to the so-called nucleation mode (AQEG 2005). Rayleigh scattering occurs by definition for $x << 1$, known as "Rayleigh regime" or "Rayleigh limit" (Moosmüller & Arnott 2009).

The following equation 3.22 is used for calculating the Rayleigh scattering intensity for particles with diameters much smaller than the wavelength of light, i.e. d_p<50 nm. Equation 3.22 also applies to gas molecules. Alternatively, it is also possible to use Mie theory calculations for the Rayleigh regime. Moosmüller & Arnott (2009) compared the Rayleigh approximation with Mie theory calculations for a specified refractive index which resulted in a close agreement for size parameters $x << 1$.

$$I_{\mathrm{scat,pR}}(\theta) = \frac{I_0 \cdot \pi^4 \cdot d_\mathrm{p}^6}{8 \cdot R^2 \cdot \lambda^4} \cdot \left(\frac{m^2-1}{m^2+2}\right)^2 \cdot B \qquad \left[\mathrm{W/m^2}\right] \tag{3.22}$$

where m is the complex refractive index of a scattering particle with small absorbing properties (i.e. small imaginary part) (Kerker & Loebl 1969, p. 33), $B = 1$ for perpendicular polarised light, $B = \cos^2\theta$ for parallel polarised light and $B = (1 + \cos^2\theta)$ for unpolarised light. If the imaginary part $k = 0$, $m = n + ik = n$ such that equation 3.22 can be written with n instead of m as is also found in (Kerker & Loebl 1969). For particles diameters d_p<50 nm (which includes gas molecules), the incident light induces an instantaneous electromagnetic field encompassing the entire particle or molecule forming a dipole whereby the dipole then adopts a state of oscillation in synchronisation with the incident electromagnetic field and reradiates electromagnetic energy in all directions (Hinds 1999, p. 359-360).

Equation 3.22 is valid only for a single spherical particle of a specific diameter. To calculate the scattering effect for the CLCS application with a specified particle concentration and size distribution of particles with diameters d_p<50 nm, it is necessary to extend equation 3.22. The extended Rayleigh scattering equation for calculating

the total scattering intensity of particles in a volume with specified particle concentration and size distribution is according to equation 3.23:

$$I_{\mathrm{scat,pR,total}}(\theta) = \sum_{d_\mathrm{p}=\mathrm{min}}^{\mathrm{max}} \frac{I_0 \cdot \pi^4 \cdot d_\mathrm{p}^6 \cdot N_{\mathrm{p,vol,d}}(d_\mathrm{p})}{8 \cdot R^2 \cdot \lambda^4} \cdot \left(\frac{m^2-1}{m^2+2}\right)^2 \cdot B \qquad \left[\mathrm{W/m^2}\right] \quad (3.23)$$

It should be noted that Hinds (1999) [p. 361] states that for particle diameters in the Rayleigh region, Mie theory and Rayleigh theory are identical. Similarly, Träger (2007) describes that for very small non-absorbing particles associated with Rayleigh scattering, Mie scattering theory yields the same result as Rayleigh scattering theory.

3.1.5 Calculation of scattered photons on a single pixel of an image sensor (Position E)

The basic theory of calculating the number of photons on a single pixel of a camera's image sensor and to calculate from that the pixel's greyscale value is described on the following pages. The presented equations are valid for typical industrial and scientific cameras. A variation of one equation to also describe so-called image intensifier cameras is also shown (for more details on camera technology, see section 4.3).

Figure 3.8 depicts how a scenery is seen by a digital camera. The height and width of the image sensor correspond to a certain height (h) and width (w) of the scenery which is photographed. The image sensor's dimensions are h_s and w_s.

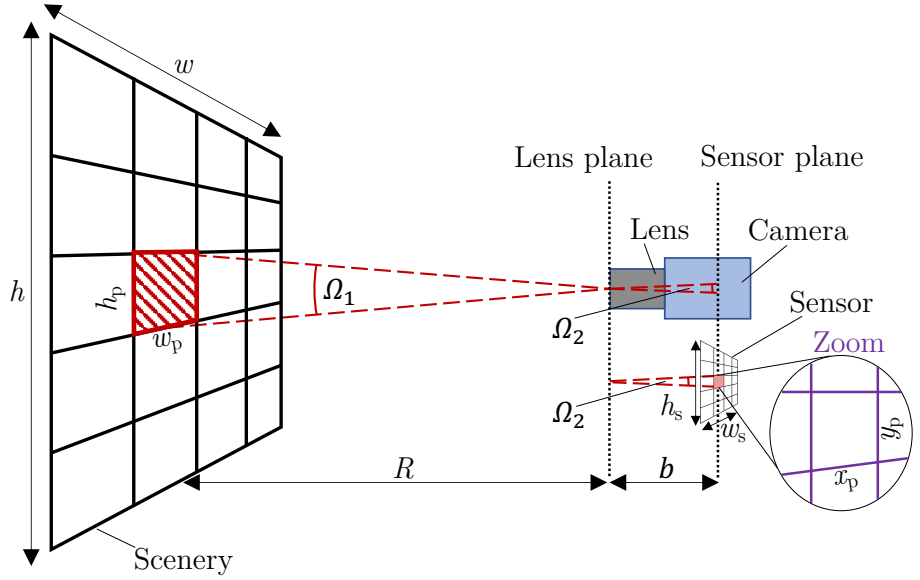

Figure 3.8: Scenery viewed by a single pixel and corresponding solid angles.

The corresponding height and width of the scenery in an image (h and w, respectively) can be calculated from the image sensor's dimensions, the focal distance f, the image distance b as well as the objects or scenery distance R as will be shown in subsequent equations (see also Figure 4.17 for further details). First, the image distance b is calculated using equations 3.24 (Demant et al. 2011):

$$b = \frac{R \cdot f}{R - f} \quad [\text{m}] \tag{3.24}$$

The height of the scenery, h, in the AFOV of a specified camera sensor and lens can now be calculated using equation 3.25 (Demant et al. 2011):

$$h = \frac{R}{b} \cdot h_s \quad [\text{m}] \tag{3.25}$$

Correspondingly, the width of the scenery, w, in the AFOV of a specified camera sensor and lens can be calculated using equation 3.26 (Demant et al. 2011):

$$w = \frac{R}{b} \cdot w_s \quad [\text{m}] \tag{3.26}$$

The solid angles Ω_1 and Ω_2 are identical and do not need to be considered in the equations as they cancel each other out.

The height h_p and width w_p of the scenery viewed by a single pixel is approximated by equations 3.27 and 3.28 by dividing by the number of vertical and horizontal pixels, i.e. $n_\mathrm{p,h}$ and $n_\mathrm{p,w}$, respectively. As image sensor's pixels are usually a square, h_p and w_p are identical.

$$h_\mathrm{p} = \frac{h}{n_\mathrm{p,h}} \qquad [\mathrm{m}] \tag{3.27}$$

$$w_\mathrm{p} = \frac{w}{n_\mathrm{p,w}} \qquad [\mathrm{m}] \tag{3.28}$$

The total scattering intensity of the beam within the AFOV of the camera, $I_\mathrm{scat,total}(\theta)$, is calculated as per equation 3.29, which is the sum of molecular Rayleigh scattering intensity, Rayleigh scattering intensity by very small particles and Mie scattering intensity by particles, i.e the sum of equations 3.16, 3.20 and 3.23. It should be noted that $I_\mathrm{scat,total}(\theta)$ calculates the scattering intensity in a specified direction for a laser beam which traverses a volume of air (calculated via the beam diameter and the length of the beam) within the AFOV of the camera.

$$I_\mathrm{scat,total}(\theta) = I_\mathrm{scat,mR,total}(\theta) + I_\mathrm{scat,pR,total}(\theta) + I_\mathrm{scat,Mie,total}(\theta) \qquad \left[\mathrm{W/m^2}\right] \tag{3.29}$$

Next it is considered that the scattered light impinges on the camera system and the grey value of the pixels on which the beam is visible is calculated. The following descriptions are already pre-published by Sattler & Göttsche (2022) in a similar way (Reproduced from Sattler & Göttsche (2022), with the permission of AIP Publishing). In a simplification, it is assumed that a laser beam is emitted vertically as was shown previously in Figure 3.5. The camera model used here is described for a scientific or industrial camera. The camera model needs a minor modification if an image intensifier camera is used. Moreover, it should be noted that it is considered that an optical filter is used as it is required for the CLCS to work whereby the optical filter is placed in front of the entrance window of the camera lens.

To calculate the power of the scattered light, P_scat, that enters an optical filter in front of a lens, equation 3.30 is used, whereby it is considered that the cross-sectional area of the optical filter and the camera lens are identical:

$$P_\mathrm{scat} = I_\mathrm{scat,total}(\theta) \cdot A_\mathrm{lens} \qquad [\mathrm{W}] \tag{3.30}$$

where A_{lens} is the camera lens aperture (i.e. the cross-sectional area of the lens). The number of scattered photons that enter the camera lens, $N_{\text{photons},\lambda}$, is calculated via equation 3.31:

$$N_{\text{photons},\lambda} = \frac{P_{\text{scat}} \cdot \Delta t_{\text{pulse}}}{E_{\text{photon},\lambda}} \quad [-] \tag{3.31}$$

where $E_{\text{photon},\lambda}$ is the energy of a single photon at a monochromatic wavelength λ. The energy of a single photon is calculated from the Planck's constant, h, and the speed of light, c, using equation 3.32:

$$E_{\text{photon},\lambda} = \frac{hc}{\lambda} \quad [\text{J}] \tag{3.32}$$

The mean number of photons from the scattered laser beam impinging on a sensor's pixel, $\mu_{\text{photons,L,p}}$, can be calculated using equation 3.33 below (for the equation it is assumed – in a simplification – that a laser beam is being emitted in vertical direction while it is further assumed that for a small distance (e.g. below around 50 m) the laser beam's intensity and its diameter remain uniform even with increasing distance):

$$\mu_{\text{photons,L,p}} = \frac{N_{\text{photons},\lambda} \cdot \tau_{\text{F}}(\lambda) \cdot \tau_{\text{lens}}(\lambda)}{n_{\text{p,w}} \cdot n_{\text{p,b}}} \quad [-] \tag{3.33}$$

where Δt_{pulse} is the beam emission duration of a laser, $\tau_{\text{F}}(\lambda)$ is the spectral transmissivity of the optical filter and $\tau_{\text{lens}}(\lambda)$ is the spectral transmissivity of the lens at the laser's central wavelength, $n_{\text{p,w}}$ is the total number of horizontal pixels of the image sensor and $n_{\text{p,b}}$ is the width of the beam in pixels. For a horizontally emitted laser beam, $n_{\text{p,h}}$ would be used instead of $n_{\text{p,w}}$. In reality the beam would neither be vertical nor horizontal in the CLCS application.

The mean number of photons converted to electrons for each pixel, $\mu_{\text{electrons,L,p}}$, is calculated from equation 3.34:

$$\mu_{\text{electrons,L,p}} = \eta(\lambda) \cdot \mu_{\text{photons,L,p}} \quad [-] \tag{3.34}$$

where $\eta(\lambda)$ is the quantum efficiency of the camera's image sensor.

When photographing a laser beam during the day in an outdoor environment, not only the photons from a scattered laser beam will impinge on the image sensor. In addition, also photons from the background's diffuse irradiance from the sky will impinge on the image sensor from within the AFOV of the camera's lens. The more

photons from the background irradiance impinge on the image sensor, the worse will become the contrast between the laser beam and the background. To calculate the background irradiance $I_{\mathrm{BGDF},\lambda}$ that transmits through the optical filter with transmissivity τ_{F}, equation 3.35 is applied:

$$I_{\mathrm{BGDF},\lambda} = \left(\int_{\lambda} I_{\mathrm{DHI}}\left(\lambda\right) \cdot \tau_{\mathrm{F}}\left(\lambda\right) \; d\lambda \right) \cdot \sin^2(\alpha) \qquad [\mathrm{W/m^2}] \tag{3.35}$$

where $I_{\mathrm{DHI}}\left(\lambda\right)$ is the diffuse horizontal irradiance from the sky and α is the AFOV of the camera's lens (assumed as narrow cone). For calculations in this thesis the ASTM G173-03 standard tables for reference solar spectral irradiance can be used. Using equation 3.36 below, in a next step, the calculation of the mean number of photons per pixel from the background irradiance, $\mu_{\mathrm{photons,BGD},\lambda,\mathrm{p}}$, after having passed through the optical filter can be carried out:

$$\mu_{\mathrm{photons,BGD},\lambda,\mathrm{p}} = \frac{I_{\mathrm{BGDF},\lambda} \cdot A_{\mathrm{lens}} \cdot \Delta t_{\mathrm{exp}} \cdot \tau_{\mathrm{lens}}\left(\lambda\right)}{E_{\mathrm{photon},\lambda} \cdot n_{\mathrm{p,h}} \cdot n_{\mathrm{p,w}}} \qquad [-] \tag{3.36}$$

where Δt_{exp} is the camera's exposure time, and $n_{\mathrm{p,h}}$ and $n_{\mathrm{p,w}}$ are the total number of vertical and horizontal pixels of the image sensor. For a single pixel, the mean number of electrons that are produced from the impinging photons from the background irradiance, $\mu_{\mathrm{electrons,BGD},\lambda,\mathrm{p}}$, is calculated from equation 3.37:

$$\mu_{\mathrm{electrons,BGD},\lambda,\mathrm{p}} = \eta\left(\lambda\right) \cdot \mu_{\mathrm{photons,BGD},\lambda,\mathrm{p}} \qquad [-] \tag{3.37}$$

Finally, equation 3.38 is used to calculate the mean digital number (i.e. grey value) of a pixel, $\mu_{\mathrm{y,p}}$:

$$\mu_{\mathrm{y,p}} = \left(\mu_{\mathrm{e,p}} + \mu_{\mathrm{y.dark,p}}\right) \cdot K \qquad [-] \tag{3.38}$$

where $\mu_{\mathrm{y.dark,p}}$ is the mean dark signal in the absence of light on the sensor, and K is the overall system gain for the analogue to digital conversion (ADC) which specifies the grey count rise (or Digital Number (DN)) per electron [DN/e$^-$]. The total number of electrons from the scattered laser beam as well as background signal is $\mu_{\mathrm{e,p}} = \mu_{\mathrm{electrons,L,p}} + \mu_{\mathrm{electrons,BGD},\lambda,\mathrm{p}}$. In the absence of the signal from the laser beam or solar irradiance, $\mu_{\mathrm{electrons,L,p}}$ or $\mu_{\mathrm{electrons,BGD},\lambda,\mathrm{p}}$ are equal to zero. In addition, noise must be considered (see topic *Noise* in section 4.3 for more details).

The equations given above for calculating the number of electrons and grey value of a pixel are similar and some of them identical to the European Machine Vision Association (EMVA) Standard 1288 (refer to EMVA (2016) for details on the EMVA Standard 1288). Some of the above presented equations, however, were adapted by the author of this thesis for the following reasons:

- The equations from the EMVA Standard 1288 only consider the image sensor, but not a lens and optical filter.
- As per the understanding from the author of this thesis, the EMVA Standard 1288 equations consider that the irradiance on the sensor is uniformly distributed on the image sensor, but this approach, however, is not applicable for calculating how a laser beam is captured in an image.

While many of the parameter symbols are kept the same as in the EMVA Standard 1288, some indices have been renamed for a better readability with respect to the context of the CLCS.

Image intensifier cameras are specialised cameras that can amplify very weak light signals into strong light signals (more details on this camera type are given in section 4.3.2). When considering an image intensifier camera, equations 3.33 and 3.34 need to be rewritten as image intensifier cameras work very differently from industrial and scientific cameras. The adaption of equation 3.33 for image intensifier cameras is equation 3.39:

$$\mu_{\text{photons,L,p}} = \frac{P_{\text{scat}} \cdot \Delta t_{\text{pulse}} \cdot \tau_{\text{F}}(\lambda) \cdot \tau_{\text{lens}} \cdot \eta_{\text{pc}}(\lambda)}{E_{\text{photon},\lambda} \cdot n_{\text{p,h}} \cdot n_{\text{p,v,b}}} \quad [-] \tag{3.39}$$

where, as only additional parameter compared to equation 3.33, the efficiency of the photocathode is given with $\eta_{\text{pc}}(\lambda)$ (for details on the photocathode, see section 4.3.2). For an image intensifier, the light signal amplification must be considered. The previous equation 3.34 is adapted to become equation 3.40.

$$\mu_{\text{electrons,L,p}} = \text{Gain}_{\text{MCP}} \cdot \eta(\lambda) \cdot \mu_{\text{photons,L,p}} \quad [-] \tag{3.40}$$

where Gain_{MCP} is the amplification of the signal inside the so-called microchannel plate (MCP) given as a number e.g. 10,000 (for details on the MCP, see section 4.3.2).

4 Main Investigated Topics of the Central Laser and Camera System

This chapter gives details on the investigated topics (cf. Figure 1.4) that are of central importance for allowing an objective selection of the main components of the CLCS, i.e. a suitable laser system, laser wavelength and camera system. Subsequently the specification of the CLCS is made in chapter 5 after an in-depth scrutiny of all relevant parameters and their inter-dependencies between the investigated topics.

4.1 Solar spectrum and atmosphere

This section explores the solar spectrum, wavelength-dependent scattering and absorption by molecules in the atmosphere as well as the attenuation of light wavelengths in the atmosphere. Conclusions on suitable and non-suitable laser wavelengths are also presented.

Molecular absorption of spectral irradiance in the Sun's and Earth's atmosphere plays a highly important role. Gases (i.e. molecules) have very selective electromagnetic (EM) wavelength absorption characteristics and therefore the attenuation of spectral irradiance by absorption strongly depends on the type(s) of molecule(s) as well as the number of molecules that have an absorbing effect on a specific wavelength. We distinguish between various types of irradiance. Commonly known types of irradiance are extraterrestrial spectral solar irradiance (SSI), terrestrial Global Horizontal Irradiance (GHI), terrestrial Direct Normal Irradiance (DNI) and terrestrial Diffuse Horizontal Irradiance (DHI). The question arises which of these types of irradiance plays the main role for the CLCS. The CLCS foresees that a laser beam reflected by a heliostat into the sky is photographed with two cameras. The cameras must therefore be oriented such that the sky is in the AFOV. In order to have as little background irradiance as possible, it is necessary to ensure that the sun is never in the AFOV of the cameras. Therefore, only the DHI must be considered for the CLCS. However, for a comprehensive review, this subsection also discusses the extraterrestrial SSI and direct irradiance. To explore which wavelength bands are particularly strongly absorbed by molecules, the low-resolution solar spectrum of the ASTM G173-03 Reference Spectra (derived from SMARTS v. 2.9.2) can be used. Figure 4.1 shows a graph with the curves of the extraterrestrial SSI as well as the sum of direct and circumsolar (terrestrial) irradiance. For the UV wavelengths from 280 to 399.5 nm, the resolution of the data is 0.5 nm and from 400 nm onwards, the resolution is 1 nm. When analysing the reference extraterrestrial SSI from ASTM G-

173 (blue curve), several local minima of irradiance intensity can be observed, which are Fraunhofer lines. These will be discussed at a later stage in this chapter. The spectral intensity of the sum of direct and circumsolar irradiance is shown by the red curve. The sum of direct and circumsolar irradiance is significantly lower than the extraterrestrial SSI. This is due to absorption and scattering processes in Earth's atmosphere. Some of the extinction is very strong and occurs with small and larger bandwidths, including the total extinction of irradiance. The major contributors to spectral wavelength absorption are ozone (O_3), water vapour (H_2O), oxygen (O_2) and carbon dioxide (CO_2). In the UV wavelength range, the ozone molecule is the major absorbing gas and in the IR wavelength range from around 900 nm, the main absorbing gas is water vapour.

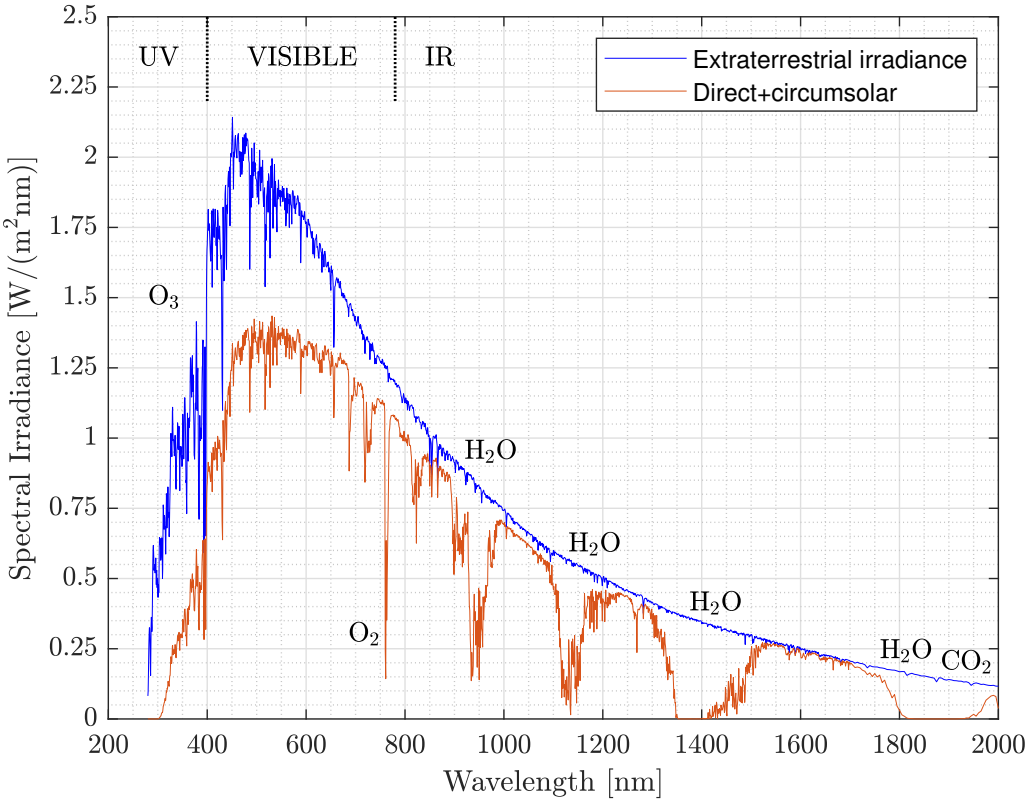

Figure 4.1: Low-resolution spectral extraterrestrial and terrestrial irradiance (Graph created with data from ASTM G173-03 Reference Spectra obtained from NREL (2021b). Credit: U.S. Department of Energy (DOE)/NREL/ALLIANCE).

In the atmosphere more than 18 types of gases exist in various concentrations at different altitudes (Bovensmann et al. 1999). An overview of the gases in the atmosphere is given by Bovensmann et al. (1999) who present a satellite spectrometer called *Scanning Imaging Absorption Spectrometer for Atmospheric Chartography* (SCIAMACHY) that measures in the wavelength range from 230 to 2,380 nm. The absorption of light by a single type molecule depends on its concentration, the wavelength range it typically absorbs and its altitude. Therefore, for the CLCS the poten-

tial absorption by a molecule type at or near ground altitude needs to be considered when choosing a laser wavelength.

The absorption effect of EM radiation in Earth's atmosphere due to the atmospheric gases ozone (O_3), water vapour (H_2O) and oxygen (O_2), is shown in Figure 4.2. The wavelength-dependent Rayleigh scattering is also shown. The magnitude of extinction through absorption and scattering is presented for the solar spectrum between wavelengths of 200 and 1,500 nm. In the UV range between 200 and 300 nm, 100 % of the EM radiation is extinct by the atmosphere. For this wavelength range, the extinction is due to molecular absorption through O_3 as well as Rayleigh scattering. From 300 to 350 nm, extinction due to molecular absorption by O_3 reduces from around 100 % down to 0 %. There is also a significant amount of Rayleigh scattering in this wavelength range. From 350 to 400 nm, extinction occurs only due to Rayleigh scattering. In the visible spectrum between 400 and 700 nm, extinction due to Rayleigh scattering reduces from around 30 % down to about 5 %. There are also small amounts of absorption by O_3, O_2 and H_2O. Between 700 and 1,000 nm, there is absorption through O_2 and O_3 absorption bands as well water vapour and CO_2 (not shown). There is a very strong absorption band of O_2 in the so-called A-band region at around 761 nm which stands out. From 1,000 to 1,100 nm, the extinction of EM radiation is insignificant. Beyond 1,100 nm, the extinction is only due to the absorption from water vapour and CO_2 (not shown). The spectral irradiance data (black and blue lines in bottom graph) is from the ASTM G173-03 reference spectra (terrestrial comprises direct and circumsolar irradiance). An approximation of the terrestrial DNI, shown by the red line, was computed by the author of this thesis. It should be noted that the relevant atmospheric thickness is around 80 km, although the thickest molecular density is found in the first 9 km. For the CLCS, short distances of laser beam travel are considered (e.g. 1 km) for which the effect of extinction through absorption is less strong. Also, for the CLCS, one must consider the molecular concentration of the absorbing gases near the ground and not at high altitudes.

The scattering of light in the atmosphere is Rayleigh scattering from the interaction of light with air molecules. The molecules of the air mainly consist of nitrogen (N_2) and oxygen (O_2) which make up 78.084 and 20.946 % volume (altogether about 99.03 %) in the dry atmosphere (Bodhaine et al. 1999). In addition, the gases Argon (Ar) and carbon dioxide (CO_2) add another about 0.97 % volume (Bodhaine et al. 1999). Other gases that are also present in air have extremely low concentrations. The wavelength-dependent Rayleigh scattering cross-sections for air presented by Bodhaine et al. (1999) were already discussed in section 3.1.2.

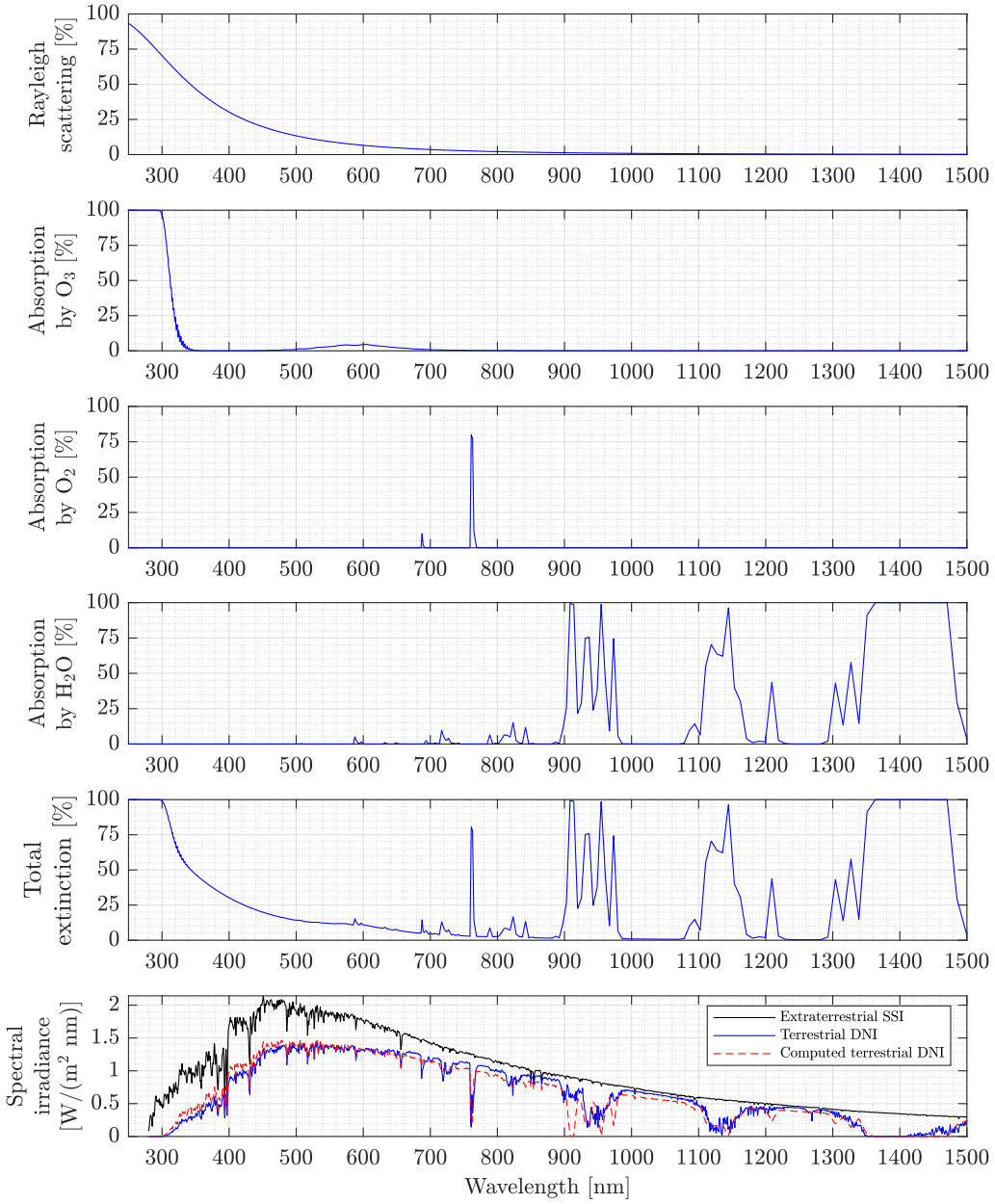

Figure 4.2: Approximate total extinction of solar irradiance through about 10 km of atmosphere. Rayleigh scattering cross-sections and calculations based on Bodhaine et al. (1999). Calculation of the absorption by O_3 with SCIAMACHY (Version 4.1) absorption cross-sections data. Calculation of absorption by O_3 with gas concentration data from Dr. Wolfgang Steinbrecht (DWD). Calculation of the absorption by O_2 from data from Bogumil et al. (2003) and Keller-Rudek et al. (2013). Spectral irradiance data (black and blue lines in bottom graph) is from the ASTM G173-03 reference spectra (terrestrial comprises direct and circumsolar irradiance) from NREL (2021b) (Credit: U.S. Department of Energy (DOE)/NREL/ALLIANCE). The approximated *computed terrestrial DNI* was calculated by the author of this thesis via the extraterrestrial SSI multiplied by the fraction of Rayleigh scattering and absorption from the above named gases for all wavelengths.

In the extraterrestrial SSI shown in Figure 4.1, local minima occur due to the absorption of wavelengths by various chemical elements in the sun's photosphere. Gases of different elements such as ionised calcium, hydrogen, neutral sodium and neutral iron are responsible for absorbing extraterrestrial SSI. These absorption lines are called Fraunhofer lines. Shapiro et al. (2015) state that above the wavelength of 170 nm, millions of Fraunhofer lines exist. While many are very fine in wavelength bandwidth, others are relatively broad. The widths of well-known bands vary between 0.0135 to 2.0253 nm. Two Fraunhofer lines with line widths greater than 1 nm are shown in Table 4.1 below, which are potentially relevant for the CLCS. Line widths smaller than about 1 nm cannot be considered for the CLCS due to limitations that arise from the characteristics of optical filters, as is shown in section 4.4.

Table 4.1: List of Fraunhofer lines with line widths potentially relevant for the CLCS. Data from Lang (2013), also available from Coseti (2006).

Wavelength (nm)	Line width (nm)
393.3682	2.0253
396.8492	1.5467

As per Table 4.1, the Fraunhofer lines with wide bandwidths are found at $\lambda = 393.3682\,\text{nm}$ and $\lambda = 396.8492\,\text{nm}$, with bandwidths of about 2 and 1.5 nm, respectively. The extraterrestrial SSI at these Fraunhofer lines is about 0.60 and $0.65\,\text{W}\,\text{m}^{-2}\,\text{nm}^{-1}$, respectively, as shown in Figure 4.3. When comparing the direct irradiance (including circumsolar irradiance) of the terrestrial spectrum measured at the ground with the extraterrestrial SSI, then – as is expected – the values of the direct irradiance are lower. This is due to the weakening of the extraterrestrial SSI caused by atmospheric scattering and absorption processes (i.e. attenuation) in Earth's atmosphere. The extinction of the wavelengths around the two described Fraunhofer lines is mainly due to Rayleigh scattering as shown in the first plot of Figure 4.2.

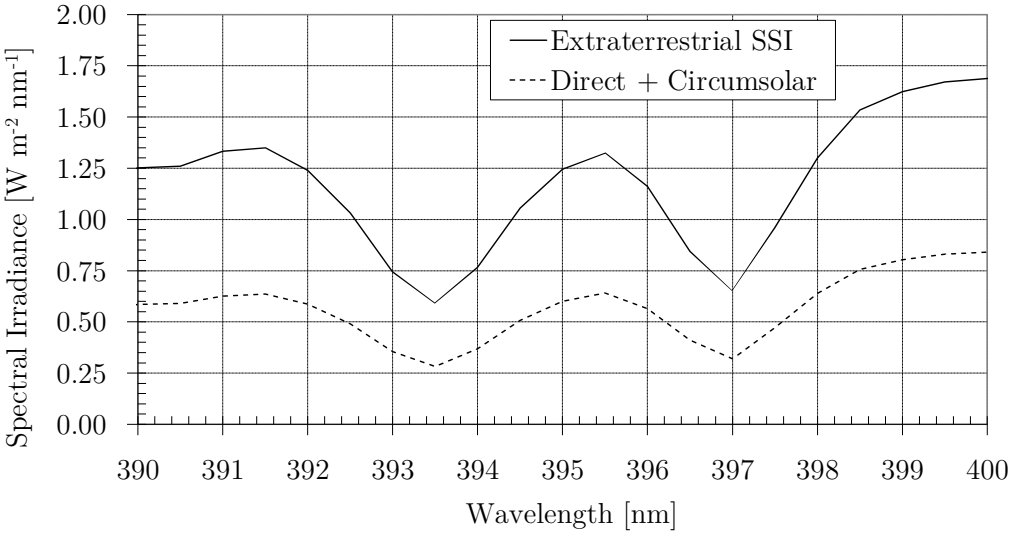

Figure 4.3: Extraterrestrial solar spectral irradiance (SSI) and terrestrial direct + circumsolar irradiance after atmospheric losses for the wavelength range 390 to 400 nm. Graph created using data from the ASTM G173-03 reference spectra (terrestrial comprises direct and circumsolar irradiance) from NREL (2021b) (Credit: U.S. Department of Energy (DOE)/NREL/ALLIANCE).

It should be noted that the ASTM G173-03 data has a low resolution. Meftah et al. (2018) present extraterrestrial SSI data measured with the spectrometer instrument *SOLar SPECtrometer* (SOLSPEC) on board of the International Space Station (ISS) which has a far higher resolution of better than 0.1 nm for wavelengths below 1,000 nm. In this data it can be observed that with values of about 0.42 and $0.51\,\mathrm{W\,m^{-2}\,nm^{-1}}$ at the two stated Fraunhofer lines, respectively, the minimum values of the extraterrestrial SSI are lower than those given by the ASTM G173-03 reference spectrum for SSI. The minimum values for the Fraunhofer lines in the SOLSPEC data are at the wavelengths $\lambda = 393.5\,\mathrm{nm}$ and $\lambda = 396.95\,\mathrm{nm}$.

As previously stated, only the DHI is considered as radiation background for the CLCS. Figure 4.4 shows, in an approximation, the DHI for the wavelengths from 280 to 1,500 nm. Normally, the DHI is calculated from substracting the DNI from the GHI. In the case of the ASTM G173-03 Reference Spectra, instead of GHI the Global Tilted Irradiance (GTI) is used which is valid for a surface tilted at 37°. Whereas global horizontal irradiance is defined as $GHI = DNI + DHI$, the global tilted irradiance is defined as GTI=direct irradiance+diffuse irradiance+reflected irradiance. However, at low tilt angles, the GHI and GTI do not vary much. At high tilt angles such as 37°, the GTI is expected to be higher than the GHI. Measured values presented by Marion & Smith (2017) suggest that the GTI with 40° tilt angle and south orientation is approximately 14 % higher than the GHI.
As an approximation in the work in the present thesis, the DHI was calculated from

the ASTM G173-03 Reference Spectra by subtracting the sum of direct and circumsolar irradiance from the GTI without correction. As per Figure 4.4, the highest value of the DHI is about $0.3\,\mathrm{W/(m^2nm)}$. The Fraunhofer lines at $\lambda = 393.3682\,\mathrm{nm}$ and $\lambda = 396.8492\,\mathrm{nm}$ have DHI values as low as about $0.1\,\mathrm{W/(m^2nm)}$. In the UV range, with exception of the above two Fraunhofer lines, the DHI values are about $0.2\,\mathrm{W/(m^2nm)}$ and are only exceeded slightly in the visible wavelength range between 400 and 500 nm. Beyond the wavelength of 500 nm, the DHI is decreasing gradually. In the O_2 absorption band around the wavelength of 760.5 nm, the DHI value is as low as about $0.01 - 0.05\,\mathrm{W/(m^2nm)}$. Next to the O_2 absorption A-band around the wavelength 760.5 nm shown in Figure 4.4, another absorption minimum is visible at around 763 nm. Wider absorption bands of H_2O and CO_2 in the wavelengths around 1,170, 1,400 and 1,900 nm are also clearly visible in the DHI curve and the spectral intensities are even lower than the described O_2 absorption band.

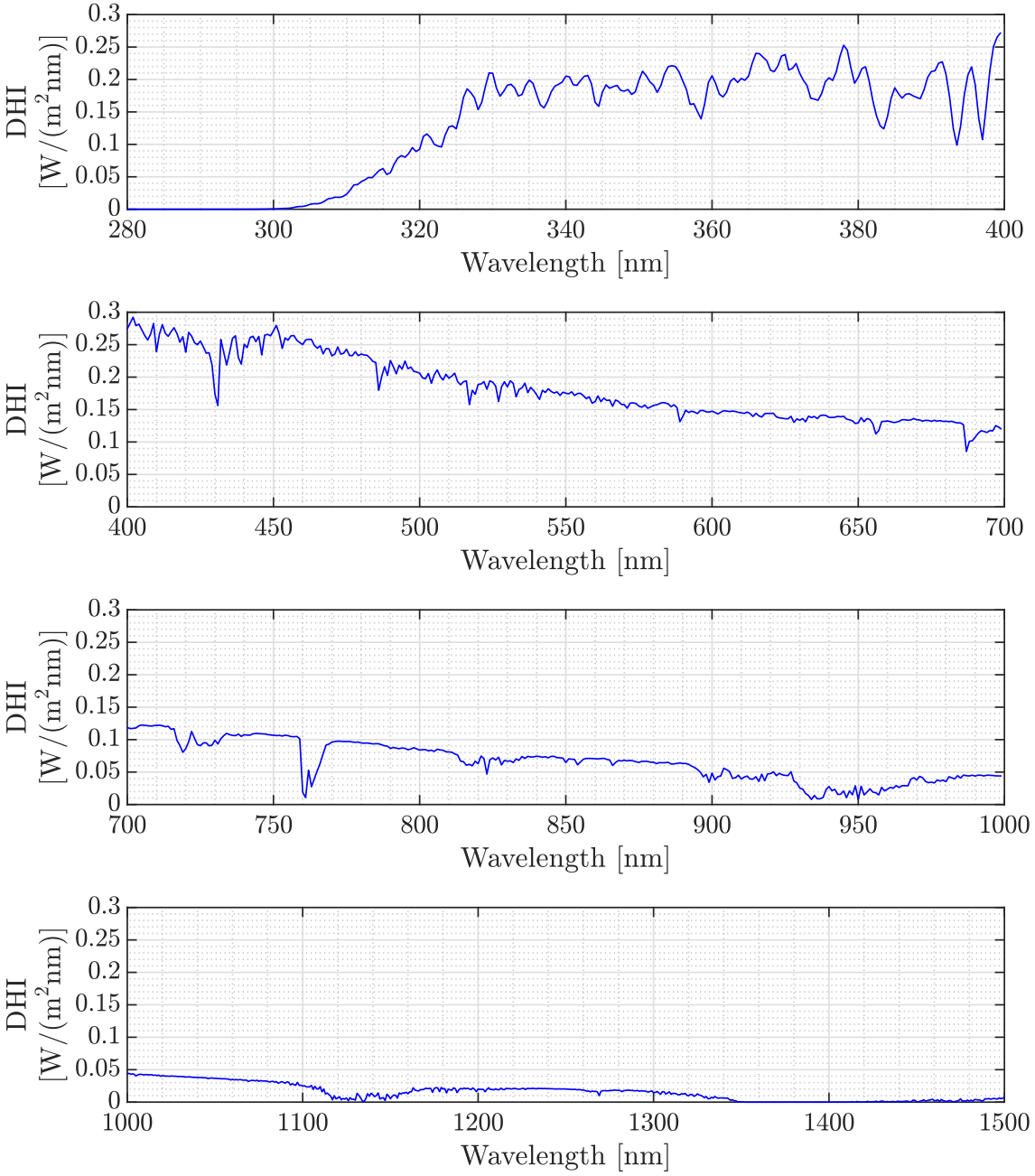

Figure 4.4: Diffuse solar spectral irradiance from 280 to 1,500 nm calculated from the GTI and direct + circumsolar irradiance ASTM G173-03 reference spectra data from NREL (2021b) (Credit: U.S. Department of Energy (DOE)/NREL/ALLIANCE).

In the UV and visible wavelength range, the direct irradiance is, in reality, fluctuating far more than shown in Figure 4.1. Subsequently, also the DHI fluctuates more strongly. However, this is not due to atmospheric molecular absorption, but due to the already highly fluctuating extraterrestrial SSI. Synthetic SSI data from Kurucz (1992) at a high resolution of 0.0004 nm can be obtained from libRadtran (2020). Figure 4.5 shows the UV wavelength range from 300 to 400 nm using the data from Kurucz (1992). The two Fraunhofer lines at around $\lambda = 393.5$ nm and $\lambda = 396.95$ nm are clearly visible in the bottom graph.

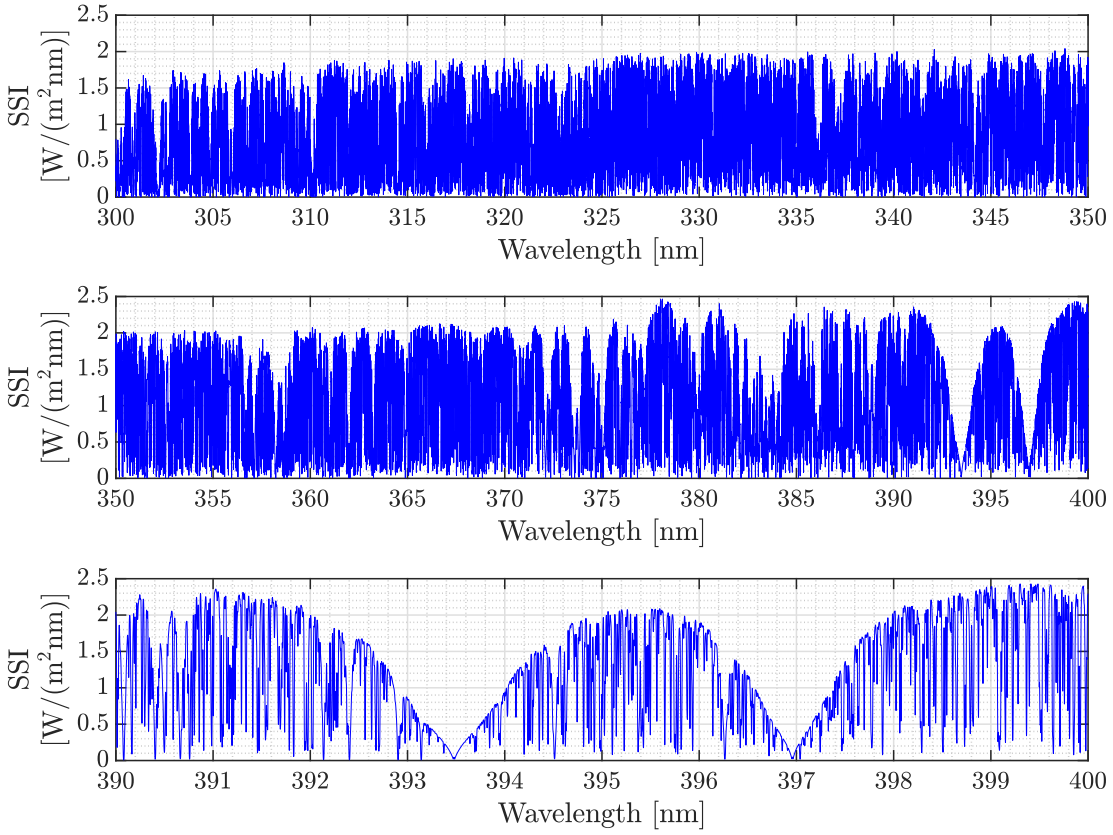

Figure 4.5: Extraterrestrial SSI for the UV wavelength range from 300 to 400 nm. Data is from Kurucz (1992), obtained from libRadtran (2020).

Parts of the following description are already pre-published by Sattler & Göttsche (2022) in a similar way (Reproduced from Sattler & Göttsche (2022), with the permission of AIP Publishing).

To determine whether or not a laser wavelength is being strongly absorbed by molecules present in the atmosphere, it is necessary to calculate the beam extinction from molecular absorption. However, as the CLCS is designed to work in the near-ground atmosphere, the concentration of the molecules of interest near the ground level must be used. The molecular absorption or attenuation of monochromatic light by molecules present in the atmosphere can play a significant role and the magnitude of absorption is highly dependent on the wavelength of the monochromatic light as well as the altitude. The concentration can vary strongly along the altitude,

especially for the ozone (O_3) molecule. As shown in Figure 4.6, the ozone concentration near the ground is approximately 80 ppb at an altitude of about 1 km. On the Zugspitze, Germany's highest mountain, the average annual ozone concentration is 55 ppb, which is equivalent to about $1.36 \cdot 10^{18}$ O_3 molecules/m^3 or $136 \cdot 10^{10}$ O_3 molecules/cm^3 (Trickl 2018). When UV light passes through Earth's atmosphere, a large proportion of it is absorbed by the ozone molecules.

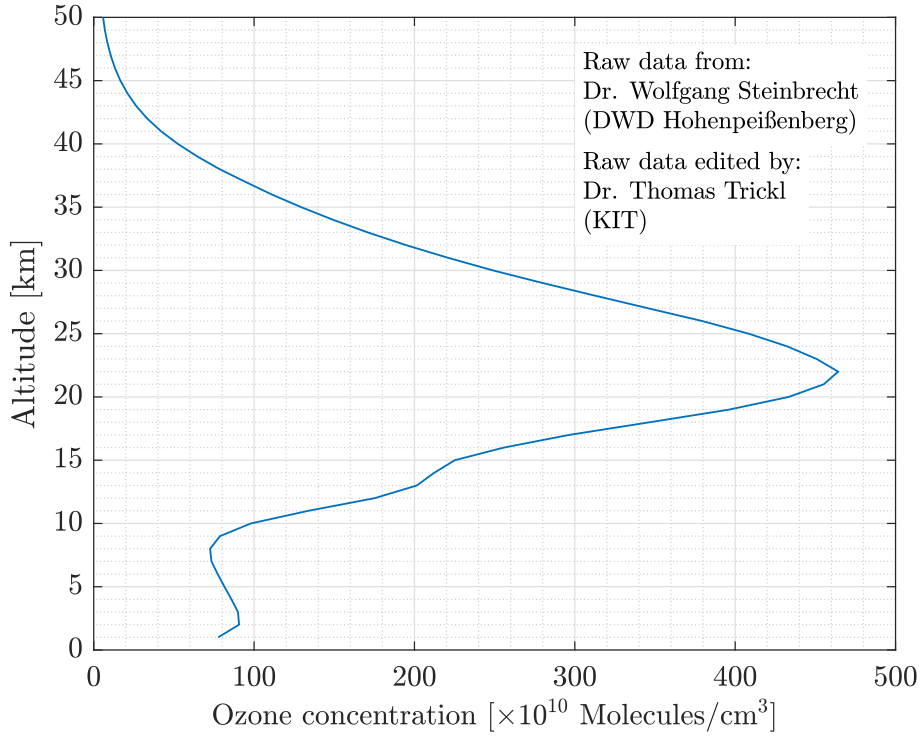

Figure 4.6: Annual mean measured ozone concentration up to an altitude of 50 km from the Meteorological Observatory Hohenpeißenberg operated by the Deutscher Wetterdienst (DWD). The annual data plot is based on climatological monthly average data from balloon sensors and LiDAR measurements (Data provided by Dr. Wolfgang Steinbrecht from DWD Hohenpeißenberg, data obtained from Trickl (2018)).

To calculate the fraction of transmitted monochromatic light, the Beer-Lambert-Bouguer law can be used which is given by equation 4.1 below:

$$\frac{I_{\text{transmitted}}(\lambda)}{I_0(\lambda)} = e^{-\mu_{\text{abs,m}}(\lambda)\cdot\Delta x} \quad [\text{W/m}^2] \tag{4.1}$$

where $I_{\text{transmitted}}(\lambda)$ is the intensity of transmitted monochromatic light, $I_0(\lambda)$ is the intensity of the monochromatic light source, Δx is the path distance of the light and $\mu_{\text{abs,m}}(\lambda)$ is the molecular absorption coefficient that was previously introduced in equation 3.11.

For the CLCS, only short laser path distances of around 1 to 1.5 km in the near-ground atmosphere need to be considered. It is therefore necessary to investigate how strong the absorption effect of the O_3 molecule is near the ground. To be able to calculate the transmission of light for a distance Δx, equation 4.1 is used in combination with absorption cross-section data for the wavelengths of interest. Absorption cross-section spectral data for O_3 measured with the SCIAMACHY spectrometer was obtained from (IGACO 2016). The absorption cross-section data file that was used is "SCIA_O3_Temp_cross-section_V4.1.DAT" with data for the temperature $T=295\,K$. Figure 4.7, which was created using this file, shows that the absorption cross-section is strongest at around $\lambda=256\,\text{nm}$. The relevant publications regarding the data are by Chehade et al. (2013) and Bogumil et al. (2003). Data from the SCIAMACHY spectrometer can also be downloaded from IUP (2021). Similar O_3 absorption cross-section data measured with the spectrometers *Echelle Spectrometer ESA 4000* and *Bruker HR 120 FTS* was presented by Gorshelev et al. (2014) and Serdyuchenko et al. (2014). The O_3 absorption cross-section data can be obtained from IUP (2021) using the hyperlink "Download the ASCII data, version 25.07.2012, zip, total size 12Mb" to download the file "serdyuchenkogorshelev5digits.dat".

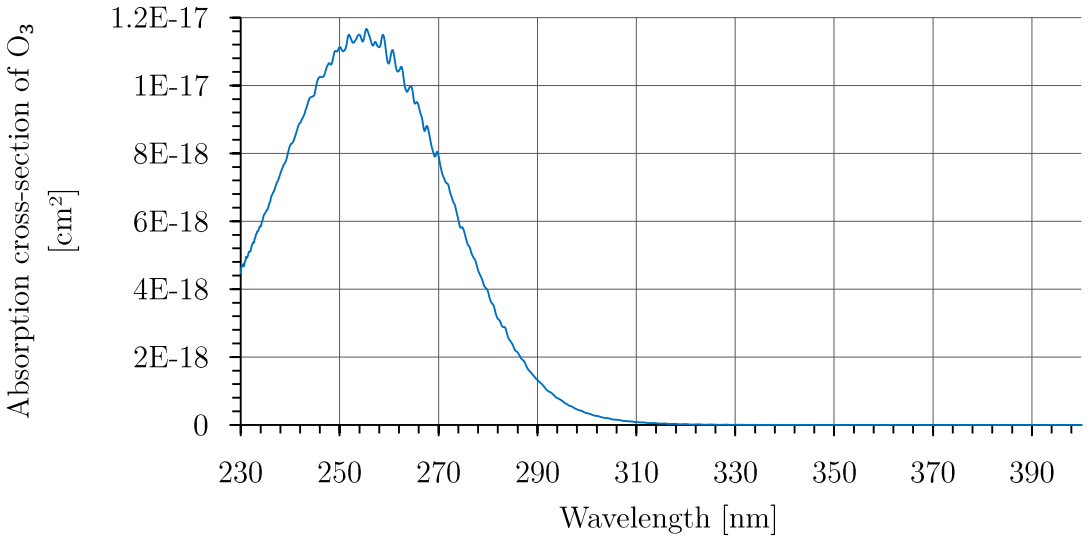

Figure 4.7: Absorption cross-sections for UV wavelengths between about 230 and 399 nm.

As shown in Figure 4.8, for short path lengths near the ground, the absorption or attenuation of UV light by O_3 molecules has a significant effect only for wavelengths that are smaller than about 315 nm, whereby the absorption effect has a maximum at around $\lambda=256\,\text{nm}$. As a minimum feasible wavelength for the CLCS a value of about $\lambda=320\,\text{nm}$ is feasible, as is stated in more detail in section 3.1.3. Therefore, the absorption of UV light by O_3 molecules does not play a significant role as long as the wavelength is above around $\lambda=320\,\text{nm}$.

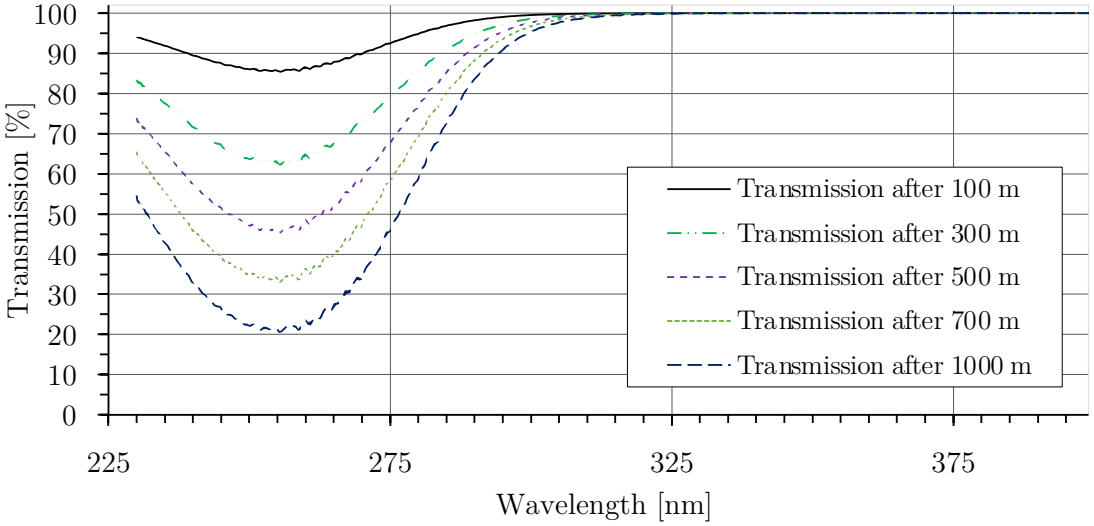

Figure 4.8: Transmission of UV wavelengths between about 230 and 399 nm through atmosphere near the ground for distances between 100 and 1,000 m for an O_3 concentration of 55 ppm.

Effectiveness of scattering by air molecules for different wavelengths

Parts of the description and results presented in the below section are already pre-published by Sattler & Göttsche (2022) in a similar way (Reproduced from Sattler & Göttsche (2022), with the permission of AIP Publishing).

The effectiveness of the scattering of light by air molecules for any specific wavelength can be determined with the scattering coefficient using equations 3.8 and 3.9 or equation 3.10. As shown in the previous Figure 4.2 (top), the scattering effectiveness of light from Rayleigh scattering by air molecules varies strongly and depends on the wavelength. Table 4.2 shows the scattering cross-section for air ($\sigma_{\mathrm{sca,m}}(\lambda)$) as well as the molecular scattering coefficient for air ($\mu_{\mathrm{sca,m}}(\lambda)$) for 15 wavelengths between λ=320 nm and λ=1,500 nm. In addition, the scattering ratio (SR) for these wavelengths compared to the molecular scattering coefficient, $\mu_{\mathrm{sca,m}}(\lambda)$, at λ=320 nm is given. The scattering ratio, SR, is calculated via equation 4.2 below:

$$SR(\lambda) = \frac{\mu_{\mathrm{sca,m}}(\lambda)}{\mu_{\mathrm{sca,m}}(\lambda = 320\,\mathrm{nm})} \quad [\%] \tag{4.2}$$

The equations 3.8 and 3.9 were used for calculating the scattering cross-sections and scattering coefficients. Scattering is strongest for the UV wavelength range and becomes very weak in the IR wavelength range. In comparison to $\lambda = 320$ nm, the scattering coefficients at, for example, $\lambda = 400$ nm, $\lambda = 500$ nm, $\lambda = 1{,}000$ nm and λ=1,500 nm are about 39.07 %, 15.55 %, 0.94 % and 0.18 %, respectively. This means that a laser wavelength in the UV wavelength range above λ=320 nm or in the visible range at around 400 nm would lead to the strongest scattering result with respect

to molecular scattering while wavelengths in the IR range only have comparatively little scattering effectiveness. A wavelength beyond λ=1,500 nm is not considered in this work as already at the wavelength of around 1,345 nm the DHI is below around 0.01 W/(m^{2}nm) and therefore extremely weak such that a good image contrast between a photographed laser beam and the background radiation could be obtained. However, it should be noted that the emitted laser beam at around $\lambda \geq$ 1,345 nm would need to emit light at a far higher pulse energy or power compared to a laser at the wavelength of λ=320 nm (this could lead to a potentially very expensive laser system with a high power consumption, while, of course, the laser safety must also be within the desired eye-safe laser class considered in this work).

Table 4.2: Values of scattering cross-sections and scattering coefficients for air as well as scattering ratios *SR* for selected wavelengths between λ=320 and 1,500 nm compared to 320 nm.

Wavelength, λ [nm]	Scattering cross-section for air, $\sigma_{sca,m}$ [m^2]	Scattering coefficient for air, $\mu_{sca,m}$ [m^{-1}]	Scattering ratio, SR [%]
320	4.284549×10^{-26}	1.091232×10^{-4}	100.00
335	3.525395×10^{-26}	8.978828×10^{-5}	82.28
350	2.928902×10^{-26}	7.459621×10^{-5}	68.36
400	1.673827×10^{-26}	4.263069×10^{-5}	39.07
500	6.661356×10^{-27}	1.696581×10^{-5}	15.55
600	3.164034×10^{-27}	8.058479×10^{-6}	7.38
700	1.692550×10^{-27}	4.310756×10^{-6}	3.95
800	9.864160×10^{-28}	2.512303×10^{-6}	2.30
900	6.133921×10^{-28}	1.562248×10^{-6}	1.43
1,000	4.013188×10^{-28}	1.022119×10^{-6}	0.94
1,100	2.735395×10^{-28}	6.966777×10^{-7}	0.64
1,200	1.928342×10^{-28}	4.911293×10^{-7}	0.45
1,300	1.398318×10^{-28}	3.561376×10^{-7}	0.33
1,400	1.038599×10^{-28}	2.645207×10^{-7}	0.24
1,500	7.875112×10^{-29}	2.005712×10^{-7}	0.18

Referring back to Figure 3.4, the reflectance of a typical CSP mirror below the wavelength λ=350 nm reduces with a steep gradient. At wavelengths above λ=350 nm, the reflectance is greater than 76 %. To be able to choose a suitable laser wavelength for the CLCS, the effective scattering compared to the wavelength λ=320 nm needs to also include the reduction in laser beam intensity after the reflectance of a laser

beam from a typical CSP mirror. As such, Figure 4.9 shows the product of the mirror reflectance and the scattering ratio (normalised to $\lambda = 320\,\text{nm}$), W, allowing the effective scattering to be compared for wavelengths between λ=320 nm and 1,500 nm. The corresponding equation 4.3 for calculating $W(\lambda)$ is given below:

$$W(\lambda) = \rho_{\text{m}}(\lambda) \cdot SR(\lambda) \quad [\%] \tag{4.3}$$

For creating Figure 4.9, the mirror reflectance values from Figure 3.4 were used as input and for reasons of comparison, it is assumed that the laser parameters would be identical for all wavelengths. It can be observed that at around λ=350 nm the highest scattering effectiveness is achieved when the mirror reflectance is also considered. If for reasons of laser safety or due to the unavailability of suitable components (e.g. camera) at around $\lambda = 350\,\text{nm}$, then another wavelength must be chosen for the CLCS. Relatively good effective scattering ratios are also found between λ=325 nm (26 %) and around λ=425 nm (28 %). An advantage of a laser wavelength at around λ=325 nm is that the DHI is only around 0.125 W/(m^{2}nm) and thus about a third lower than the DHI between λ=330 nm and 425 nm (about 0.18 W/(m^{2}nm) as can be observed in Figure 4.4). As previously stated, a lower DHI, as is, for example, found in the IR wavelength range, leads to a better contrast between a laser beam and the diffuse irradiance from the sky in an image. The scattering effectiveness of air for wavelengths in the IR wavelength range, however, is very low. If a laser wavelength at, for example, λ=1,000 nm were chosen for the CLCS, then compared to a laser at 350 nm the pulse energy or power of the laser would need to be about 59 times stronger in order to produce the same scattering effect while the DHI=0.05 W/(m^{2}nm) is about a factor 4 less. As another example, the pulse energy or power of a laser at $\lambda = 1{,}500\,\text{nm}$ would need to be 291 times stronger in order to produce the same scattering effect as a laser with a wavelength of 350 nm. In section 4.4, details are given regarding the requirements of optical filters for the CLCS. Suitable optical filter bandwidths are highlighted as well as that the laser must have a narrower bandwidth than the optical filter.

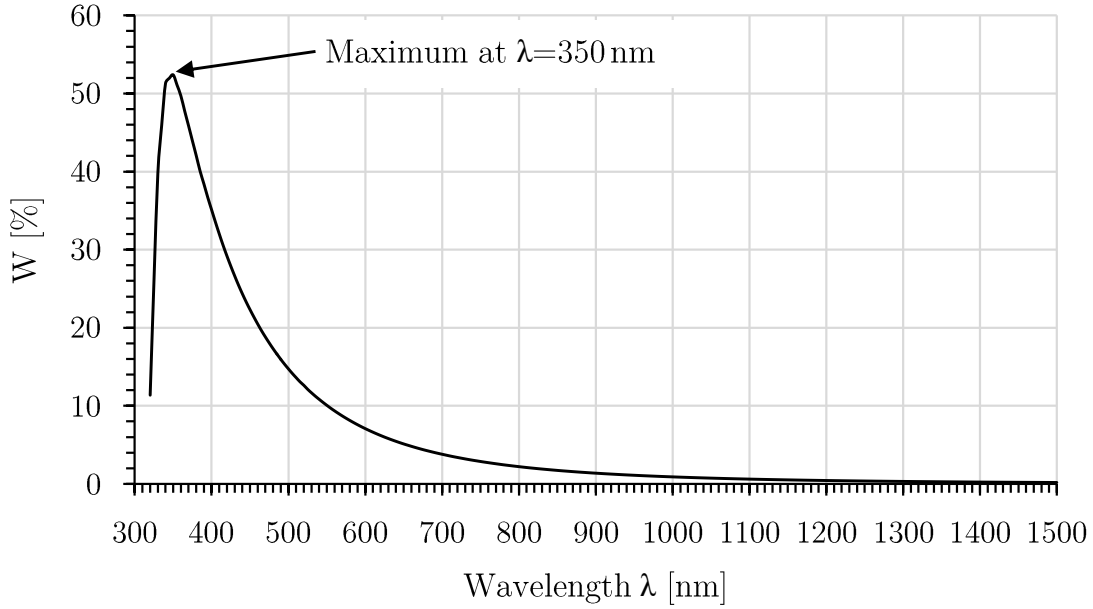

Figure 4.9: Graph showing W [%], which is the product of the mirror reflectance and the scattering ratio (normalised to the wavelength $\lambda = 320\,\text{nm}$).

Excursus: Exploration of low DHI in the O_2 absorption A-band
The theory around the CLCS was first focused on a wavelength at around 760.5 nm within the so-called O_2 absorption A-band in the IR range. The interest in this wavelength was based on the very low background irradiance of only around DHI=0.01 to $0.03\,\text{W/(m}^2\text{nm)}$ as shown in Figure 4.4. A low DHI value has the advantage that the contrast between a laser beam and the diffuse irradiance from the sky in an image improves compared to higher DHI values. The O_2 absorption A-band is explored in detail in the appendix whereby the disadvantages of using a laser for the CLCS with a wavelength within the A-band are discussed.

4.2 Aerosols

As per the Mie scattering theory, the scattering of EM radiation occurs from the interaction with aerosols, i.e. solid particles that are suspended in the air of the atmosphere. In order to be able to accurately calculate the intensity of Mie scattering and to determine its contributing factor for the CLCS, the prevailing particle concentration and size distribution as well as the wavelength-dependent complex refractive indices must be known. This section will also explore, which wavelengths are scattered by particles most efficiently. Before exploring these topics, more details about the size parameter x, which was first introduced in section 3.1.4, are given below.

Figure 4.10 shows the size parameter x for a wide range of particle radii and wavelengths as well as the various types of scatterers from air molecules up to raindrops

and hail. Also shown are the boundaries for Rayleigh scattering, Mie scattering, geometric optics as well as a region of negligible scattering.

As per Figure 4.10, Mie scattering is confined by the boundaries of the size parameter between $x = 0.2$ and $x = 2{,}000$ (valid only for single scattering and spherical particles). Rayleigh scattering is confined by the boundaries of the size parameter between $x = 0.002$ and $x = 0.2$ (valid only for single scattering and spherical particles). It should be noted that the Rayleigh regime for Aitken and nucleation nuclei (i.e. ultrafine particles) includes particle radii as small as about 0.5 nm. The particle radius of 0.5 nm marks the current lowest measurable radius that some high-standard, modern condensation particle counters are able to measure, such as some products from TSI (2018). Air molecules have radii below 0.5 nm. The radius of air molecules is about 0.15 nm and is therefore much smaller than particles in the nucleation nuclei range.

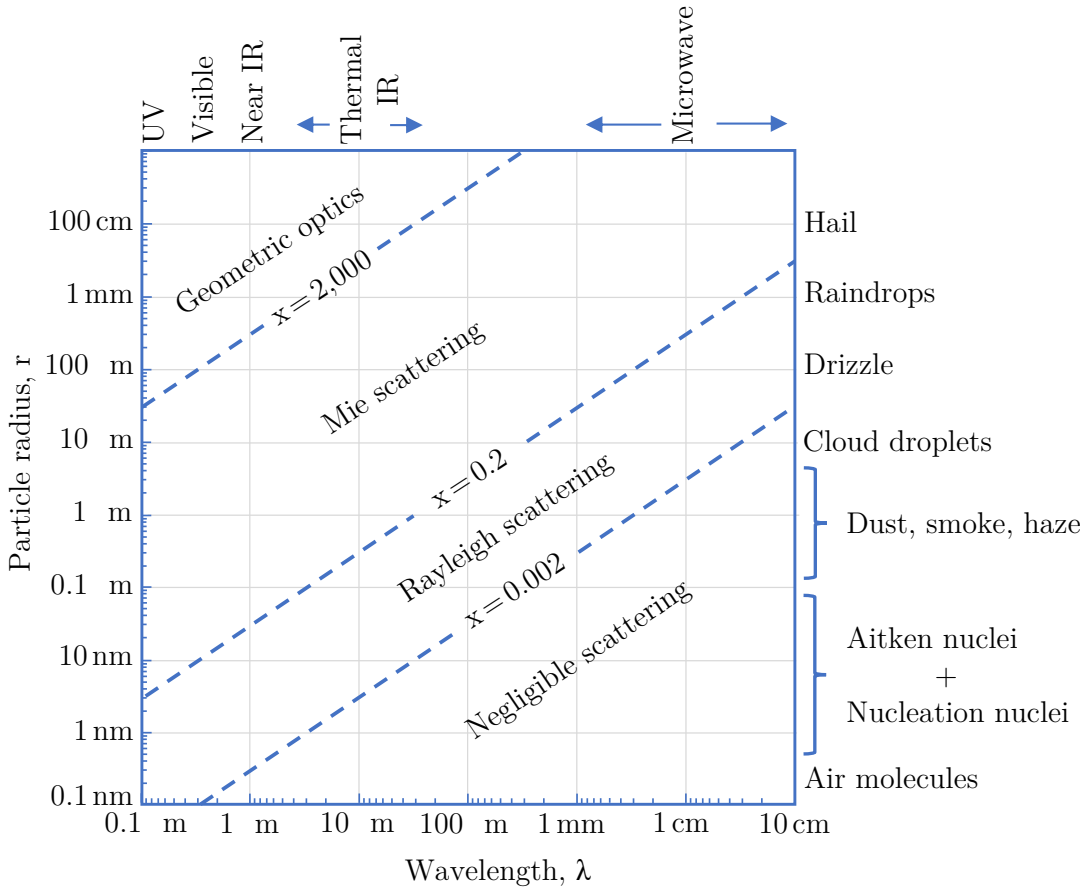

Figure 4.10: Size parameter x for a wide range of particle radii and wavelengths as well as scatterers (based on illustration from Petty (2006), with minor modifications).

4.2.1 Aerosols: types, emission, composition and origin

Aerosol types and global emission

Aerosol sources are both of natural as well as anthropogenic origin. The so-called primary particles are naturally occuring aerosols that are directly dissipated into the atmosphere (Andreae & Rosenfeld 2008). Primary particles are mineral dust, biogenic aerosols, sea salt, tropospheric volcanic dust as well as aerosols produced from forest fires and the natural burning of biomass (Tomasi & Lupi 2017). Primary particles from anthropogenic sources (i.e. from human origin) occur due to industrial dust (from the cement industry, transportation etc.), combustion of fossil fuels as well as incineration of waste and biomass (Tomasi & Lupi 2017). In addition, solid and liquid particles are produced from house heating and road transportation in the form of road surface abrasion, breaking as well as tyre wear off (Penkała et al. 2018). Furthermore, particles are defined to be secondary particles when gaseous precursors in the atmosphere are converted into aerosols (an example of this is the process of oxidation of SO_2 to H_2SO_4) (Andreae & Rosenfeld 2008).

For the CLCS in desert regions, only naturally occurring solid aerosols are considered, i.e. mineral dust, biogenic primary organic as well as sea salt. Sea salt could potentially be a relevant contributing scatterer alongside mineral dust if the CRS is located near the coast. Table 4.3 shows some general information on the global emissions of these aerosols with estimated best guess values from Andreae & Rosenfeld (2008) as well as ranges of global annual emissions of aerosol types. Sea salt has far higher emissions than mineral dust.

Table 4.3: Global annual emission data of three aerosol types that are relevant to the CLCS, considering only emissions from natural sources. Data shows ranges and average values measured in teragram per year (1 Tg yr^{-1} = 10^6 ton yr^{-1}). Data mainly taken from Andreae & Rosenfeld (2008) and partly from Tomasi & Lupi (2017).

Aerosol particle type	Natural sources	
	Estimated value	Range
Mineral dust		
$d < 1$ µm	165	
$d = 1$ to 2.5 µm	496	
$d = 2.5$ to 10 µm	992	
Total	1,600	1,000 to 2,150
Sea salt		
$d < 1$ µm	180	60 to 500
$d = 1$ to 16 µm	9,940	3,000 to 20,000
Total	10,130	3,000 to 20,000
Biogenic primary organic		
Total	35	15 to 70

Origin, shapes and composition of mineral dust

The atmosphere transports various aerosol types from various locations over far distances of up to thousands of kilometres across land, seas and oceans to other countries (Tomasi & Lupi 2017). Furthermore, Tomasi & Lupi (2017) state that mineral dust occurs due to wind erosion predominantly in desert and semi-arid regions. The Sahara desert but also other desert regions in North Africa, South Africa, the Middle East Asia, China and South America are the main sources for dust; the relevant arid and semi-arid dust source regions comprise about one-third of the Earth's land (Tomasi & Lupi 2017).

Detailed information on aerosols with respect to the origin, shapes and composition from the Sahara region are found in publications such as Knippertz & Stuut (2014), Tomasi & Lupi (2017) and Petzold et al. (2009). The travel paths of aerosols measured at a location in Germany were investigated by Ebert et al. (2004). Depending on their type and composition, dust particles have very different shapes. Various scanning electron microscopy (SEM) images of mineral (aeolian) dust particles are shown by Tomasi & Lupi (2017) including images of quartz, dolomite, kaolinite, palygorskite of Saharan origin, smectite, illite and gypsum.

Tomasi & Lupi (2017) describe that when dust particles are in contact with water,

they barely change their shape and morphological characteristics but highly moist air masses in the atmosphere at high altitudes can encompass the aerosol as water or ice shell. In this case, the aerosol will have a change in its radiative properties leading to lower scattering characteristics (Tomasi & Lupi 2017), i.e. the real part of the complex refractive index reduces. Trochkine et al. (2003) describe that particles can also merge or react with other particles while suspended in the air and when travelling long distances. Further it is described that when this happens the original particle becomes modified when merging with other particles such as sulphate or sea salt.

Origin, shape and composition of biogenic aerosols
Found abundantly in nature, plants and animals are another source of aerosols, the so-called biogenic aerosols, emitted in solid and liquid form (Tomasi & Lupi 2017). Aerosols from plants are, for example, macroscopic-sized debris and microbial particles such as seeds and pollens (Tomasi & Lupi 2017). Another example classified as biogenic aerosols are airborne insects such as flies, bugs and mosquitoes flying in the atmosphere (Tomasi & Lupi 2017).

Origin, shape and composition of sea salt
The emission of particles from the sea or ocean water surface is referred to as sea spray function or spume generation (depending on the wind speed) (Lundgren 2006). When waves of a sea or ocean break at the shore, air is enclosed in the water forming bubbles which burst at the water surface, release sea salt particles into the atmosphere and additionally release particles in a jet (Tomasi & Lupi 2017). Regarding spume generation at higher wind speeds, wind directly blows off spume droplets containing sea salt particles from the crests of the waves into the atmosphere (Lundgren 2006). The transport distance of sea salt particles depends on the wind speed. The windier it is, the farther sea salt particles are transported (Tsunogai 1975). In order to evaluate whether or not sea salt particles are of importance for the CLCS with respect to Mie scattering, the transport and concentration of sea salt from the coast towards into the inland needs to be assessed. Andreae & Rosenfeld (2008) state that sea salt particles are transported by the atmosphere only over short distances and then fall to the ground due to their weight. For example, Hoogerbrugge et al. (2012) present a map with sea salt concentrations of PM_{10} size particulate matter across the Netherlands (PM_{10} stands for particulate matter suspended in the air with diameters of less than 10 µm). The presented data shows that with 7 µg/m^3, the sea salt concentration at the coast is strongest and then steadily decreases further inland down to 3 µg/m^3 at the border with Germany (approx. 150 km from the coast). The main constituents of seal salt are Cl and Na (i.e. NaCl) with mass fractions of 55.4% and 30.8%, respectively. Other constituents of sea salt and their mass fractions are Mg (3.8%), S (2.6%), K (1.1%), Ca (1.1%), other elements (5.2%) (Hoogerbrugge

et al. 2012). Therefore, it can be expected that for a CRS located near a coast, salt suspended in the air will contribute to Mie scattering for the CLCS.

4.2.2 Particle size statistics, number concentrations and particle size distributions

In the following, particle size statistics, number concentrations and particle size distributions are discussed for mineral dust, biogenic aerosols and sea salt.

Mineral dust
As the CLCS is designed and tested in Jülich, Germany, a representative particle concentration and size distribution for this location shall be considered. In this work, historical particle data measured with a PALAS® Fidas 200 optical particle counter (OPC) at the location of the Solar-Institut Jülich (placed outdoors on the rooftop with a height above the ground of approximately 10 m) was examined. The PALAS® Fidas 200 OPC is a light-scattering aerosol spectrometer. The measured particle size range of this OPC is between about 0.19 and 18 µm. The measurement data from the PALAS® Fidas 200 particle counter also lists the lower and upper size intervals of the bins as well as a mean diameter for each bin, among other. The mean diameter with the corresponding particle count for each bin was used in this work. The working principle of the OPC is that a stream of air is sucked through the device whereby it passes a laser beam which scatters light whenever it strikes a particle. The size of a particle is determined from the intensity of the scattered light.

Figure A.9 in the appendix shows the particle concentration for the location Jülich for 143 selected sunny days. For these days, a data analysis was carried out whereby, for each day, the percentiles from 10 to 100 % in 10 % intervals were calculated for the total number of particles per litre and a median value was calculated. The median value of all 143 selected days was 46.7 particles/cm^3 (i.e. 46,700 particles/L). Generally, the data clearly showed that the number concentrations for particles are highly fluctuating. This means that there is no such thing as a typical number concentration for particles.

In order to validate that the particle count measurement data shown in Figure A.9 are in the right magnitude, parts of the data from the year 2017 was compared with measurement data at the location of the research institute Forschungszentrum Jülich for the same year presented by Perim de Faria et al. (2018). Although the used particle counters were not identical, the total particle count was the same order of magnitude. The own data measured with the PALAS® Fidas 200 particle counter is expected to be higher, as it already counts particles with diameters starting from 0.19 µm, whereas the particle counter from the Forschungszentrum Jülich measured

from 0.25 µm. Perim de Faria et al. (2018) write that there is a "great spatial and temporal variability" and "high variability in composition, size, shape and vertical distribution". Accordingly, the data presented by Perim de Faria et al. (2018) shows a strong variation of measured particle concentrations and it can be observed that the particle concentrations are higher in cold months (November to April) than in warm months (May to mid-October). In the following, the data from Perim de Faria et al. (2018) are described in more detail. Extreme recorded particle concentrations with diameters >0.25 µm were in the order of around 200 to 350 particles per cm^3 while low concentrations were around 20 to 30 particles per cm^3. The median concentrations in summer were around 40 to 75 particles per cm^3. Another particle counter that measured particles with diameters >10 nm recorded mean concentrations between around 2,200 and 3,000 particles per cm^3 in warm months. The highest recorded concentration was around 7,000 particles per cm^3. It should be noted that Jülich is located in the vicinity of three open pit coal mines which contributes to the particle concentration in the atmosphere.

A particle counter not only counts the particles, it also groups the particle sizes into size ranges as each particle counter has a finite number of so-called bins or channels for grouping the particles. Particle counters with a high resolution have, for example, 32 or 64 channels. As an example, Table A.1 in the appendix shows grouped particle data with random values for 11 bins (size ranges) and the counted particles for each of the bins. Additionally shown is the count as a portion from all particles as well as the cumulative portion. Hinds (1999) describes that each size interval has a lower and an upper size limit. It is further described that for each of the size intervals going from small to large particles size intervals, the upper size limit is identical to the lower limit of the subsequent interval. In the event that a particle's measured size is precisely at the upper limit, then this particle is sorted into the higher interval (Hinds 1999).

Regarding graphs for showing the particle number concentration against the particle diameter, data presented in publications is usually in the form of a so-called lognormal distribution graph. TSI (2012) describes that this is done to be able to compare data from different measurement instruments with different channel or bin resolutions. For plotting such a graph, the particle number data is adjusted such that it is normalised with the bin width on the vertical axis, leading to a normalised particle number value independent of the bin width. The particle size, which is shown on the x-axis, is also shown in a logarithmic scale. Clarke et al. (2003) describe that the representation of $dN/d\log D_p$ against $\log D_p$ allows to read off the particle number concentration from calculating the area under the curve. Moreover, particle concentration data for a greater range of particle sizes from small to large can be shown in a single graph. An example of such a graph is shown in Figure 4.11. The y-axis usually has the unit of cm^{-3}.

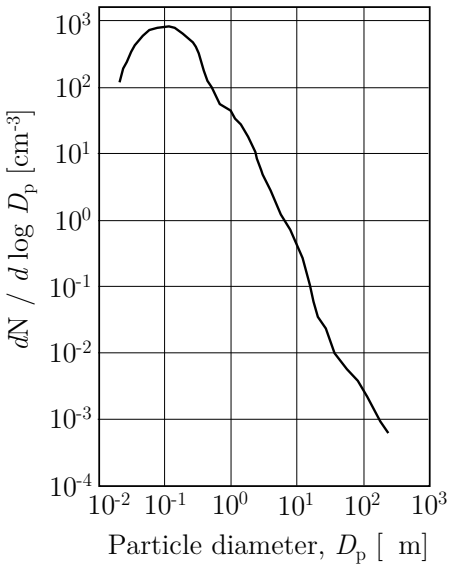

Figure 4.11: Example of a logarithmic graph of type $dN/d\log D_p$ against $\log D_p$ used for showing particle number concentrations.

The corresponding equation for calculating $dN/d\log D_p$ of the y-axis stated by TSI (2012) is shown in equation 4.4:

$$dN/d\log D_p = \frac{dN}{d\log D_p} = \frac{dN}{\log D_{p,u} - \log D_{p,l}} \tag{4.4}$$

where dN is the particle concentration, D_p is the midpoint particle diameter, $D_{p,u}$ is the upper channel diameter and $D_{p,l}$ is the lower channel diameter.

Regarding a representable particle number concentration and size distribution from the location Jülich to be used for Mie scattering calculations, a particle concentration of 65 particles/cm^3 was chosen from the available particle data. In the statistical analysis of the particle data, each size interval for a period of several days was ordered in descending order. The median count was then determined for each particle size column. Additionally, percentiles between 10 and 90 % were calculated to also determine very high and very low dust concentrations during the selected time period, respectively. The particle size distribution is shown as $dN/d\log D_p$ against the particle diameter in Figure 4.12 for days with available data between March and August 2017. For this data, the 10 % percentile of the time period with a high dust concentration contains also larger particles with diameters up to about 5.1 µm, while the median distribution contains particles with diameters up to about 1 µm and the 90 % percentile of the time period with a very low dust concentration contains only smaller particle diameters up to about 0.55 µm. Figure 4.12 additionally shows the particle number concentration and size distribution from Saharan regions from Kaaden et al. (2009), Müller et al. (2009) (ground-based measurements) and

Saharan dust measured airborne over the western Mediterranean basin by Denjean et al. (2016) in order to roughly estimate if higher scattering effects can be expected in the regions where a CLCS can typically be installed compared to Jülich. It is clear that the largest particles in the Saharan number and size distributions exceed the diameters measured in Jülich and have up to 30 µm is size, but the occurrence of these large particles is low (only up to 10^{-1} particle per cm^3).

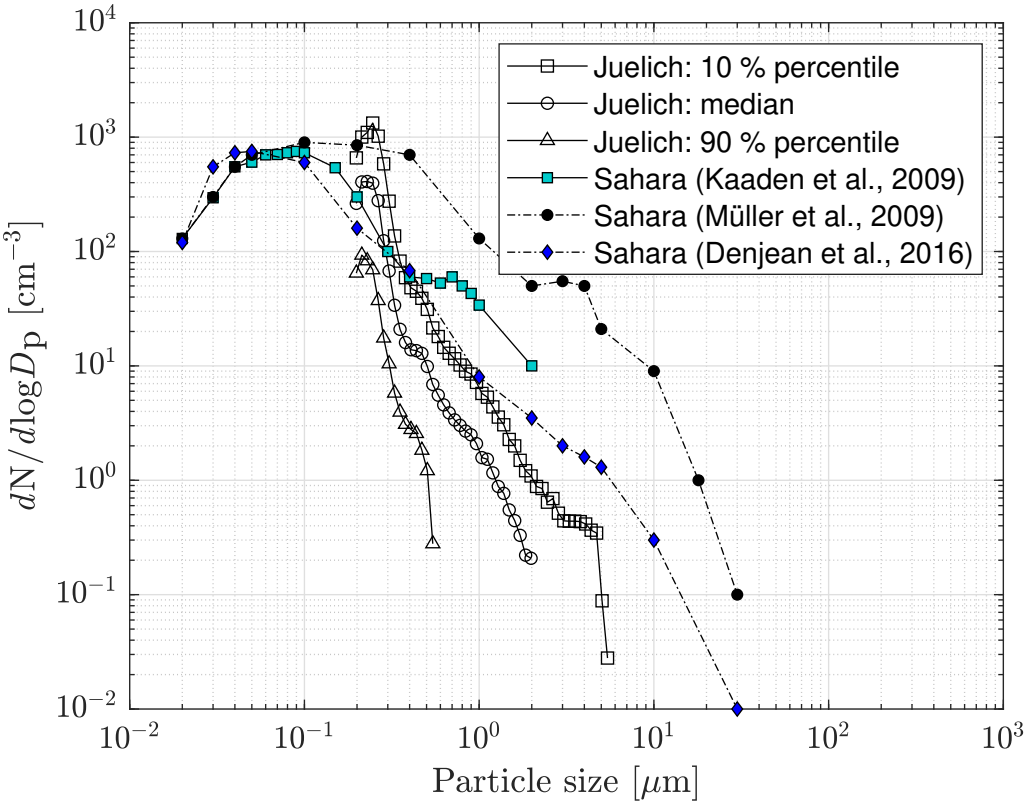

Figure 4.12: Particle number concentration as $dN/d\log D_p$ against the particle diameter for several days between March and August 2017 for the location Jülich, Germany, with a median total number of 65 particles/cm^3 for particle diameters between 0.19 and 17.6 µm. Also shown for the Jülich data are the low (90% percentile) and high (10% percentile) concentrations. Independently, Saharan particle distributions from Kaaden et al. (2009) (in situ ground-based measurement), Müller et al. (2009) (in situ ground-based measurement) and Denjean et al. (2016) (airborne measurements with flight levels up to 6 km) are shown in the graph for allowing a comparison between the site in Germany and in Africa (the measurement period is independent from Jülich).

Depending on the wavelength of the light and the particle diameter, the scattering effect for large particles may fall into geometric optics rather than Mie scattering (cf. Figure 4.10). Few, but large mineral dust particles may have a contributing effect for the CLCS. Particles with diameters >75 µm are referred to as giant mineral dust particles (van der Does et al. 2018) which are unlikely to have a contributing effect to

the CLCS as these rarely occur. For a further read on this topic, lognormal distribution graphs for particle number and size distributions at sites from Morocco, Spain and the Sahara desert can be found in numerous publications such as Kandler et al. (2009), Sorribas et al. (2011) and Wagner et al. (2012), respectively. An overview about different size ranges of particles measured at various locations in Africa, Asia and Spain as well as information on their shapes can be viewed, for example, in Knippertz & Stuut (2014) who gathered and summarised this information from various publications. Moreover, Knippertz & Stuut (2014) give the size ranges with the information whether the measurement was ground based, airborne, low-altitude airborne, high-altitude airborne etc., which is important with respect to the CLCS as only particle data measured near the ground is of relevance. In Morocco, the measured maximum particle diameters were 3 µm (high-altitude airborne), 30 µm (low-altitude airborne) and 200 µm (ground based). For the other measurements in Africa and Asia the maximum particle diameters were typically no more than 20 µm. It should be noted that for different size ranges often more than one particle counter needs to be used in order to cover the diameter ranges of interest. Knippertz & Stuut (2014) state that dust measurements often begin from diameters $\geq$0.1 µm because below this diameters the majority of airborne particles are no longer dust. Further, Knippertz & Stuut (2014) point out that the measurement of particles over large particle diameter ranges can be very complicated especially when carrying out airborne measurements. Hence, depending on the measurement technique, the difficulty of measuring larger particles differs, meaning, for example, that the particle collection efficiency of devices will differ from optical-scattering devices and therefore render a different result.

Biogenic aerosols

Insects, which are among the organic sources of biogenic aerosols, can also cause reflection or scattering when in the path of a laser beam. Similarly, lint can cause strong reflection or scattering. Regarding the CLCS, insects will not have a significant impact for the CLCS due to the low insect number density as described in more detail in the appendix.

Sea salt

According to Tomasi & Lupi (2017), the size of sea salt particles varies from about 0.05 to 10 µm, although Clarke et al. (2003) gives a lower limit of 0.01 µm. Clarke et al. (2003) show various graphs of the number concentration of sea salt from breaking waves for sea salt diameters between 0.01 and 10 µm.

When comparing the aerosol number and size distribution in Figure 4.12 with that of the sea salt, it is apparent that the particle concentration of sea salt particles is in the order of around factor 40 lower than that of mineral dust particles in the diameter range below $2{\cdot}10^{-1}$µm. Between $2{\cdot}10^{-1}$ µm and 10^{0} µm, the sea salt concentration is similar to that of the concentration shown for Jülich and between 10^{0} µm and

10^1 µm, the sea salt concentration is comparable to the dust particle concentration measured by Denjean et al. (2016). Therefore it can be concluded that for a CRS installed near the coast, sea salt is very likely to contribute to the scattering for the CLCS. However, as the main scattering type is Mie scattering, the scattering is strongly forward directed.

4.2.3 Complex refractive index

Complex refractive index of mineral dust

For Mie scattering the topic *complex refractive index* is very important when computing the scattering intensity from aerosol particles using Mie code. The complex refractive index of the aerosols must be known or assumed as it is a required input for the computation of Mie scattering functions (Mätzler 2002). The wavelength-dependent complex refractive index is composed of a real and an imaginary part and is described by $m=n+ik$ (Petzold 2015). The real part of the refraction index, n, denotes how well a particle reflects and thus scatters light. The imaginary part of the refraction index, k, expresses how well a particle absorbs light, where $k=0$ for non-absorbing particles and $k>0$ for absorbing particles (Petzold 2015). The complex refractive index m depends on the composition of the particle (Petzold 2015).

In a mix of different aerosols, multiple complex refractive indices would need to be applied. In this work, however, a single complex refractive index is assumed for all particles and the presence of soot is not considered. Generally, though, if a CSP system were located near urban developments, then soot formed from the incomplete combustion of fossil fuels may be present in the air, which may need to be considered. Soot, which is elemental carbon, is highly absorbing and thus has a high value of the imaginary part of the refractive index (Lelli 2014). Otto et al. (2007), Petzold et al. (2009), Wagner et al. (2012) and Knippertz & Stuut (2014) extensively studied complex refractive indices of particles originating from the Saharan desert. Otto et al. (2007) published a graph of the real and imaginary part of the complex refractive indices of mineral dust against the wavelength. As can be observed in that graph, the real part of the complex refractive index, n, is nearly constant up to a wavelength of around 1,000 nm and has a value of approximately $n = 1.6$. Petzold et al. (2009) reported the real part of the complex refractive index to be n =1.55 to 1.56 from a flight-based measurement campaign, which are similar values compared to the value reported by Otto et al. (2007). Moreover, according to the graph from Otto et al. (2007), between 1,000 and 2,000 nm, n drops to approximately $n = 1.3$. Further it can be observed that the imaginary part, k, varies strongly between 200 and 2,000 nm, whereby at 200 nm $k = 0.06$ and at 2,000 nm $k = 0.0045$. Knippertz & Stuut (2014) point out that the higher imaginary complex refractive index in the UV wavelength range is usually due to the presence of hematite, which, according to

Cornell & Schwertmann (2003), is a highly abundant iron oxide mineral that occurs not only in soils, but also in rocks.

As was pointed out above, for the location of the Saharan desert, various studies of the complex refractive index exist. At the location Falkenberg in Germany, Ebert et al. (2002) collected samples of particles with diameters between 0.1 to 25 µm and found the average real part, n, of complex refractive index of all the samples to be between 1.52 and 1.57 (or $1.50 - 1.66$ when size resolved) and was influenced by the number of present metal oxide/hydroxide particles. Furthermore, Ebert et al. (2002) found the average imaginary part, k, to be between 0.031 and 0.057 (or $0.008 - 0.192$ when size-resolved) whereby the large fluctuation occurred due to the varying amounts of soot and carbon/sulfate mixed particles in the samples. In another study at the rural location Kleiner Feldberg in Germany at an altitude of 825 m above sea level, Ebert et al. (2004) collected 12 dust samples with diameters between 0.1 and 25 µm over a period of about 10.5 months and analysed the complex refractive indices, among other things. The rural location is, at times, influenced either by a nearby urban region or by long-range particle transport from Eastern Germany and Eastern Europe (or both simultaneously) (Ebert et al. 2004). As the anthropogenic and natural sources of particles can be clearly distinguished by their morphology and chemical composition, Ebert et al. (2004) could present complex refractive indices both for rural and urban origin. Altogether 27.000 particles (from all samples) were analysed and categorised by Ebert et al. (2004) according to their morphology and chemical composition into the following groups: ammonium sulfates, calcium sulfates, sea salt, alumosilicates, silica, metal oxides/hydroxides, soot, biological particles, carbon/sulfate mixed particles as well as remaining carbon-rich particles. Urban sources of particles (i.e.polluted air masses) were identified due to their high number concentrations of soot, metal oxides and sulfates (Ebert et al. 2004). It was further found that polluted air from the urban region had a very high real part, n, of the complex refractive index varying between $1.60 - 1.73$ (the high values are mainly due to high amounts of metal oxide/hydroxide particles present in the air). The imaginary part, k, was found to vary between $0.034 - 0.086$ and its high values are mainly due to the presence of soot. Rural (non-polluted) air had a lower real part, n, of the complex refractive index varying between $1.54 - 1.61$, whereby the imaginary part, k, varied between $0.001 - 0.021$ (Ebert et al. 2004).

Complex refractive index of sea salt

Bi et al. (2018) state that for wavelengths below 3 µm, the real part, n, of the refractive index of dry sea salt mostly lies in the region from 1.4 to 1.5 whereas the imaginary part varies strongly. From a graph from Bi et al. (2018) it can be observed that, for example, at 0.2 µm the imaginary part $k \approx 10^{-4}$, at 0.3 µm the imaginary part $k \approx 10^{-6}$, at 0.4 µm the imaginary part $k \approx 10^{-8}$ and at 1 µm the imaginary part $k \approx 10^{-4}$ (Bi et al. 2018).

4.2.4 Normed Mie scattering intensities for various wavelengths

The following Figures 4.13 and 4.14 show normed Mie scattering intensities for s-polarised light wavelengths between $\lambda = 350\,\text{nm}$ and $\lambda = 1{,}000\,\text{nm}$ for the single particle sizes of 0.5 µm and 5 µm. The intensities (normed between 0-1) are shown for scattering angles from 0 to 180°, where 0° is equivalent to forward and 180° to backward scattering. A complex refractive index of $m = 1.56 + 0.008i$ was chosen for the computation. The calculations were carried out with the BHMIE code by Bohren & Huffman (1983, 2008) using an extended MATLAB® version of the code from Mätzler (2002).

As Figure 4.13 for particles of diameter 0.5 µm shows, only angles between around 0 and 40° lead to stronger scattering, especially for shorter wavelengths. The shortest wavelength chosen for the simulation was λ=350 nm. The strongest scattering is due to the wavelength λ=350 nm whereas for the wavelengths above around λ=700 nm the scattering intensity is fairly insignificant compared to the wavelength λ=350 nm. Sideways and backward scattering is comparatively low.

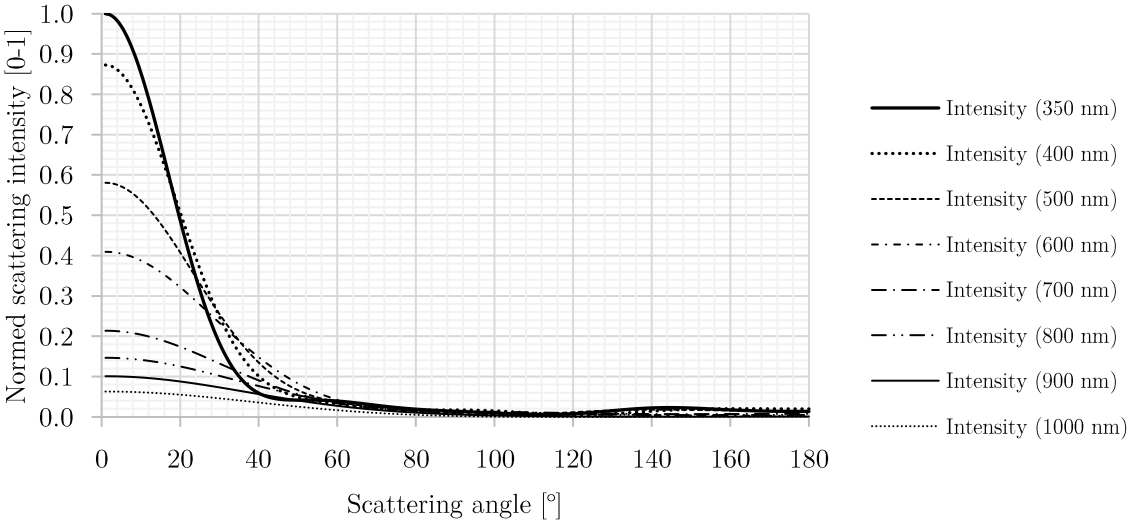

Figure 4.13: Normed Mie scattering intensities for various wavelengths for scattering angles between 0 and 180° for a single particle of diameter 0.5 µm.

As per Figure 4.14 for a particle size of 5 µm, scattering is almost entirely forward directed. However, it should be noted that as the scattering intensity shown in these graphs is normed, the sideways scattering intensity for single particle diameters cannot be compared to Figure 4.13 objectively.

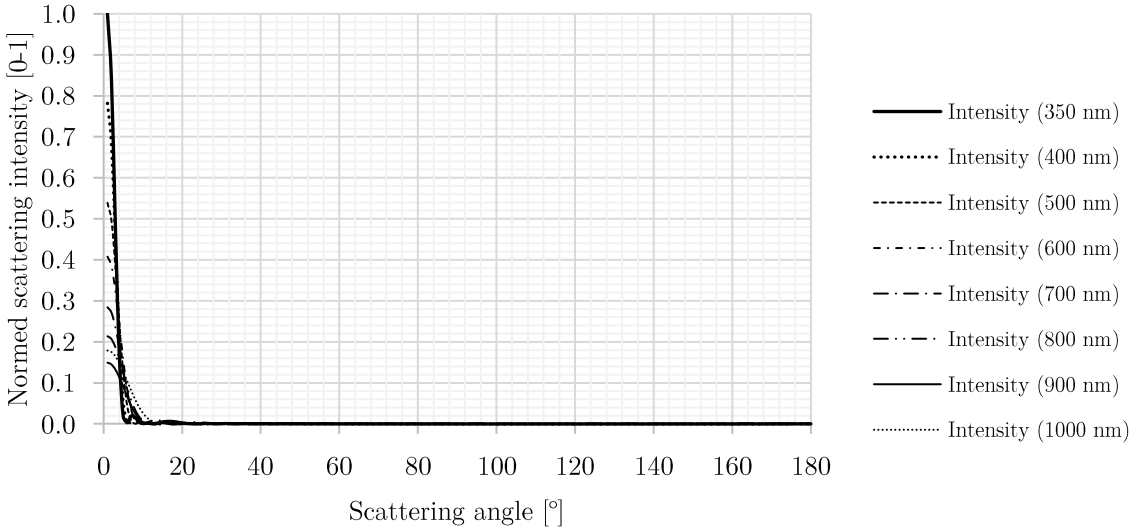

Figure 4.14: Normed Mie scattering intensities for various wavelengths for scattering angles between 0 and 180° for a single particle of diameter 5 µm.

To further assess at which laser wavelength the Mie scattering is most intense for the location of Jülich, Germany, a particle concentration and distribution from measurement data was used to calculate the normed scattering intensity for wavelengths between $\lambda = 350$ nm and $\lambda = 1{,}000$ nm shown in Figure 4.15. As expected, the total scattering intensity is strongest at the wavelength $\lambda = 350$ nm and weakest at $\lambda = 1{,}000$ nm. The scattering intensity is comparatively weak between the angles of about 40 and 180°. Between around 60 and 180° the scattering intensity is almost identical for all the wavelengths. Whether or not the scattering intensity of Mie scattering is of significant importance for the CLCS is discussed in chapter 6.

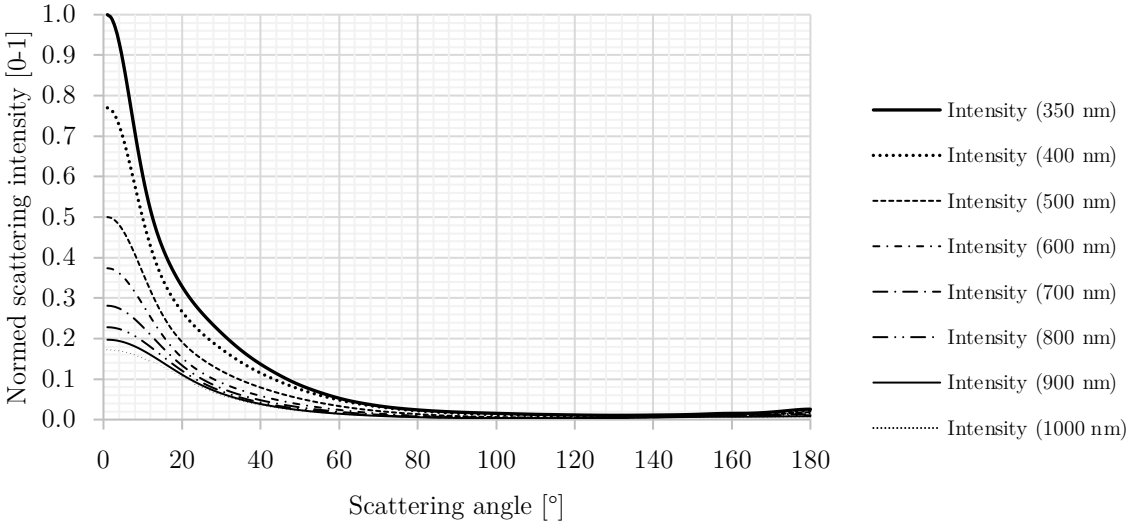

Figure 4.15: Normed Mie scattering intensities for various wavelengths for scattering angles between 0 and 180° for a selected particle concentration and size distribution for Jülich, Germany.

4.3 Camera technology

For machine vision applications, industrial cameras are broadly used worldwide, e.g. for reading bar codes or for quality inspections of products passing a camera on a conveyor belt. For scientific applications, however, so-called scientific cameras may serve the need of scientists better, e.g. in astrophotography. Scientific cameras are therefore designed with specific performance characteristics to suit various scientific applications and demands (Teledyne 2020), e.g. in low-lighting conditions. As both industrial and scientific cameras can be described with the same parameters, this section does not distinguish between them. For the CLCS, low scattering signals are expected and therefore the focus for the CLCS is on identifying suitable scientific cameras as well as highly specialised so-called image intensifier cameras. This section gives comprehensive information and descriptions on several topics including sensor types, noise, resolution, contrast and camera lenses, interfaces and image formats.

4.3.1 Basics of camera technology

Figure 4.16 shows an illustration of what a scientific camera, industrial camera or machine vision camera typically looks like. It consists of an image sensor, a lens mount (with thread), a housing and an interface (typically in the rear). Not shown in the illustration of the camera are the various types of existing interfaces (these are discussed in section 4.3.5).

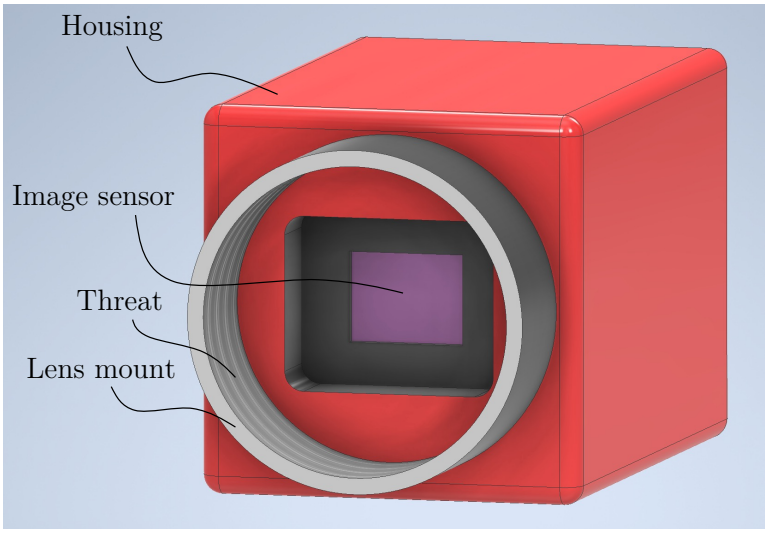

Figure 4.16: Illustration of a scientific camera, industrial camera or machine vision camera.

Figure 4.17 shows how an object is formed on an image sensor when taking a photograph with a digital camera. In this example, a house at distance R from the lens is being photographed and it is assumed that its real height h fills the height h_s

of the image sensor. If R is closer than in the example, then only a portion of the house will be visible on the image sensor. In the contrary, if the distance R is farther than in the given example, then the house will only fill a portion of the height of the image sensor. The denotions F' and F are the foci in front and behind the lens, respectively. Denotions A, B, O, C and D are start and end points of the lines.

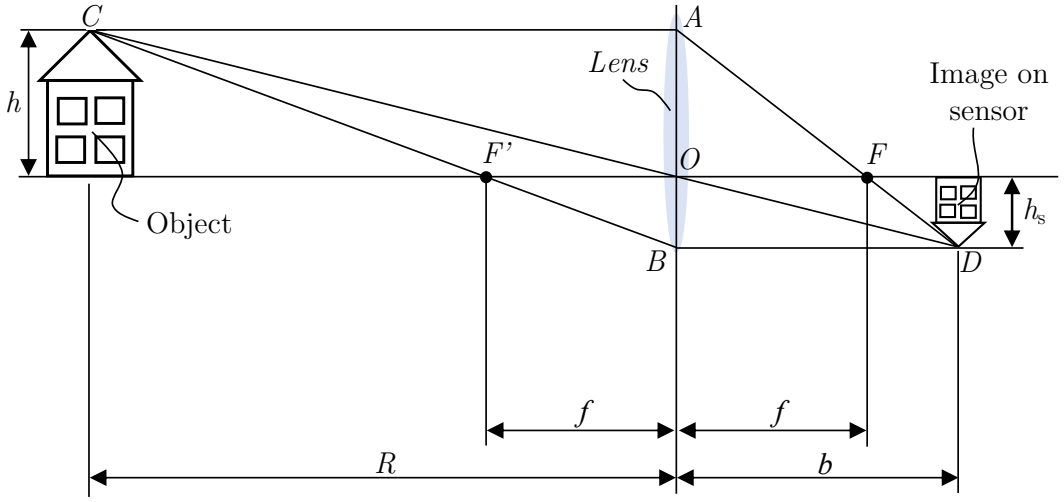

Figure 4.17: Illustration of the object and image dimensions for a thin lens with a certain focal length f (based on illustrations from Demant et al. (2011) and Hecht (2018)).

In the following, the image sensor technology is presented. Demant et al. (2011) describe that via a large number of light sensitive photodiodes, image sensors of digital cameras convert the voltage signal generated by the photons (light energy) into a digital number for further processing (e.g. image processing, displaying an image on a monitor, etc.). Made of semiconductors, image sensors produce electrons in the light-sensitive semiconductor crystals of a pixel during the integration phase (exposure time) of the image acquisition (Demant et al. 2011). During the integration phase, the produced electrons are accumulated in a so-called potential well (Stemmer Imaging 2018). The potential well can take up a limited number of electrons until it saturates. The amount of electrons a potential well can accumulate during the integration phase depends on the intensity of the impinging light, the exposure time and the pixel size.

There are two main types of sensors, namely CCD and complementary metal oxide semiconductor (CMOS) image sensors. There are different types of CCD sensors, which include the interline transfer, full frame and frame transfer CCD sensors (Stemmer Imaging 2018). CMOS sensors exist with on-chip and off-chip ADC conversion (Stemmer Imaging 2018). For scientific applications, the so-called scientific complementary metal oxide semiconductor (sCMOS) sensor was developed. Figure 4.18 shows an illustration of an interline transfer CCD sensor and a CMOS sensor.

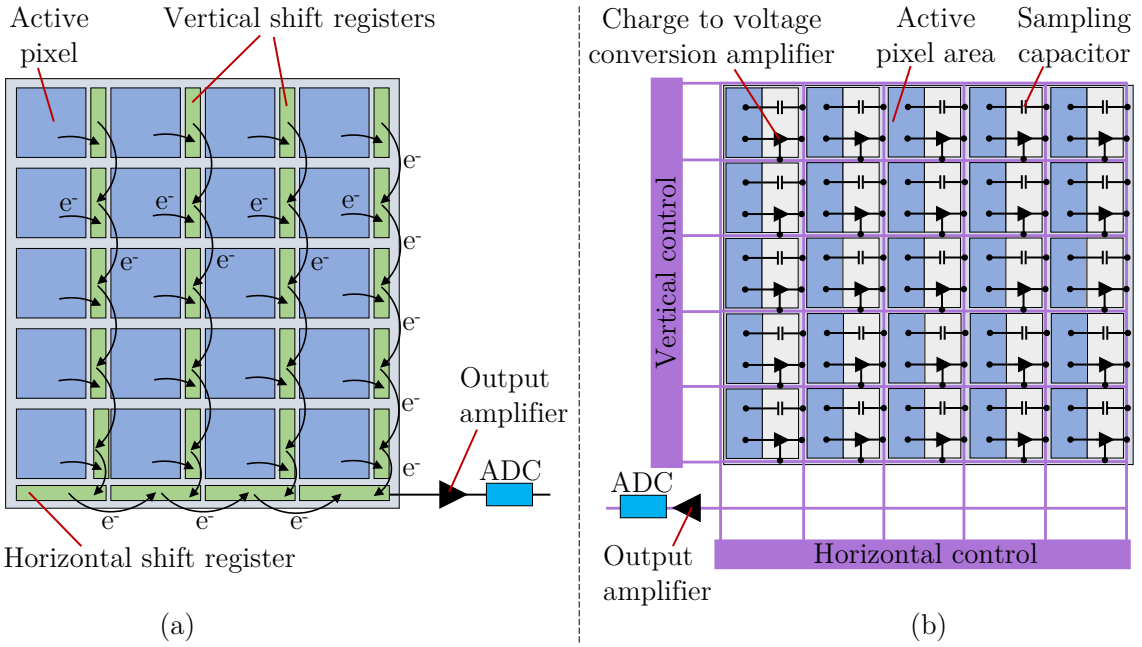

Figure 4.18: Illustration of (a) an interline transfer CCD sensor (based on illustration from Stemmer Imaging (2018)), and (b) a CMOS sensor (based on illustration mainly from Stemmer Imaging (2018) and partly from Demant et al. (2011)).

CCD sensor technology

Demant et al. (2011) describe the working principle of an interline transfer CCD sensor in such a way that the electrons produced in the individual pixels are moved into vertical shift registers after the integration phase is completed and are then moved into a horizontal shift register. For each column of pixels, there is one adjacent vertical shift register. Demant et al. (2011) also describe that the electrons are moved from the horizontal shift register into a readout amplifier which converts the electrons read out from a pixel into a voltage. Finally, the voltage is then converted into a digital signal in the so-called ADC converter (Demant et al. 2011).

CMOS sensor technology

CMOS sensors work differently to CCD sensors with respect to where the charge of a pixel is converted into a voltage. As shown in Figure 4.18 (b), next to each active pixel area there is an individual active amplifier and also a capacitor which converts the electrons into a voltage. Around the active pixel area (photodiode) there are three transistors which have several purposes such as resetting or activating a pixel as well as amplification and charge conversion (Edmund Optics 2011a).

Colour vs monochrome sensors

Monochrome sensors outperform colour sensors regarding image sharpness. For the

CLCS, sharp images are desired, therefore only monochrome sensors are considered and only greyscale imagery is discussed in the following topics.

Selection of an image sensor
Nowadays, CMOS sensors have a better performance in terms of sensitivity and dynamic range than CCD sensors (Adimec 2015) and are also widely used in science applications such as space photography. For certain applications, however, a CCD sensor may be a better choice than a CMOS sensor e.g. in low light conditions where lines need to be detected because CMOS sensors have a fixed pattern noise in the form of lines while CCD sensors do not have such a pattern. When choosing a camera with suitable sensor, there are many parameters to scrutinise before making a choice. As a rough overview, a comparison between CMOS and CCD sensors is presented by Fereyre & Powell (2016) and may be helpful in choosing the right sensor for the desired application.

Quantum efficiency
The quantum efficiency (QE) is the efficiency of a pixel (i.e. a semiconductor, mostly consisting of silicon) to convert a photon into an electron. The pixels of image sensors convert photons into electrons from a wide wavelength range, but as the sensitivity of the pixels varies depending on the wavelength of a photon, the quantum efficiency varies as a function of the wavelength. PCO (2018) give the equation for the QE, $\eta(\lambda)$, to be as follows.

$$\eta(\lambda) = (1 - R) \cdot \zeta \cdot \left(1 - e^{-\alpha \cdot d}\right) \qquad [-] \tag{4.5}$$

where R is the reflection of the surface of the pixel, ζ is the portion of the charge carriers (respectively the so-called electron-hole-pairs) that contribute to the photo current and did not recombine at the semiconductor surface, and $\left(1 - e^{-\alpha \cdot d}\right)$ is the portion of the photon flux absorbed by the semiconductor, whereby α is the absorption coefficient and d is the penetration depth. The quantum efficiency of sensors can be optimised by applying coatings onto the pixels which absorb specific wavelength ranges better than others (PCO 2018). The quantum efficiencies of sensors from scientific cameras can be as high as around 70%. Sensors are designed to be sensitive for certain spectral ranges, e.g. some sensors are especially suitable for the UV range (e.g. starting at 200 nm), other sensors have higher quantum efficiencies in the visible range and again other sensors are more sensitive in the IR range (typically up to around 1,100 nm). Specialised cameras especially for thermal imaging in the IR wavelength are also available.

Exposure time

The exposure time is the time span during which the pixels of the sensor absorb photons, convert the photons into charges and accumulate the charges (subsequently the charges are read out). The exposure times of modern scientific and industrial cameras can be as low as 1 µs and usually allow long exposure times up to around 10 to 60 s.

Shutter type

Shutters of modern industrial and scientific cameras are fully electrical, i.e. there is no mechanical shutter. There are two shutter types: rolling shutter and global shutter (PCO 2018). Rolling shutters operate in such a way that for each pixel or row or column, there is a different exposure start and end time, i.e. the exposure occurs sequentially (Stemmer Imaging 2018). When photographing fast moving objects with a rolling shutter, then the object shape will be distorted. Global shutters work in such a way that the exposure of the pixels and readout of the electrons is simultaneous (Stemmer Imaging 2018).

Figure 4.19 (a) shows the effect of fast-moving objects, in this example a lorry, when photographed with a global shutter and (b) shows the lorry photographed with a rolling shutter. The rolling shutter results in a distorted image. Hence, when photographing fast moving objects, a sensor with global shutter is more suitable. With respect to the CLCS, if a pulsed or continuous wave (cw) laser were to be photographed and if the exposure time of the camera were longer than the beam emission duration, then a camera with a rolling shutter is unsuitable.

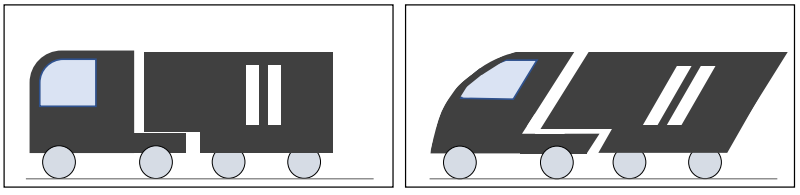

(a) (b)

Figure 4.19: Example of difference in capturing images with fast moving objects when using a sensor with (a) global shutter and (b) rolling shutter.

Noise

There are several types of sensor noise that are listed in data sheets from cameras which are briefly described in this section. To be able to compare cameras objectively, many manufacturers test their cameras according to the European Machine Vision Association EMVA 1288 standard, specifying also the values of various noise types.

As the CLCS shall operate during daylight conditions, the following type of non-constant noise is very important to consider: Photons from a light source underlie a statistical fluctuation (Poissonian) when they are collected by a photodetector, which means that the standard deviation of the detected number of photons μ_p after a given exposure time is $\sqrt{\mu_\mathrm{p}}$ (Jacubowiez et al. 1997), which is also commonly known as *shot noise*. The variance of the fluctuations is a Poisson distribution of the mean number of accumulated electrons ($\sigma_\mathrm{e}^2 = \mu_\mathrm{e,p}$). For the CLCS, shot noise will have an effect as the images of the laser beams shall be taken during the day in sunny and bright conditions. For a further read on the topic of noise, PCO (2018) and Hamamatsu Photonics (2019) provide detailed information.

In the appendix, several other types of noise are described.

Full-well capacity and saturation
The full-well capacity of a pixel is the maximum number of charge (electrons) it can hold without saturating. The greyscale value at full-well capacity is white. Larger pixels have a higher full-well capacity than small pixels. Sensors with pixel sizes of 4.65 µm have a full-well capacity of about 12,000 to 14,000 $\mathrm{e^-}$, pixels with 6.5 µm have a full-well capacity of about 48,000 $\mathrm{e^-}$, pixels with about 10 to 13 µm have a full-well capacity of about 90,000 to 120,000 $\mathrm{e^-}$ while pixels with 16 µm can have a full-well capacity of about 180,000 $\mathrm{e^-}$ (Teledyne 2021b, XIMEA 2021, Oxford Instruments 2020). When the full-well capacity of a pixel is reached, then the pixel is saturated (i.e. it cannot take up more charge).

Bit depth
The range of the greyscale values that an analogue-to-digital (A/D) converter can process is described with the parameter *bit depth* as a binary value, e.g. 2^{14} (equal to 16,384 discrete grey values) or 2^{16} (equal to 65,536 discrete grey values) (Hamamatsu Photonics 2021).

Dynamic range
The dynamic range is the ratio of maximum light signal (limited to the full-well capacity of a pixel) to the noise floor (i.e. minimum detectable) signal in an image (Hamamatsu Photonics 2021, Hilgart 2011). A sufficiently large dynamic range is an important parameter to consider if a large range of grey values in an image is required, for example, if the contrast between the object and the background in the image is small (for more information on contrast see section 4.3.3). The principle of the dynamic range of an image sensor is shown in Figure 4.20.

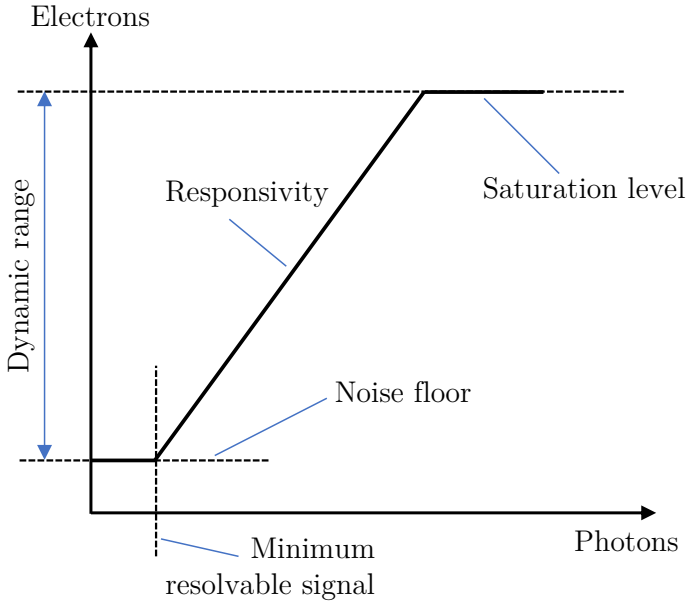

Figure 4.20: Principle of the dynamic range of an image sensor (based on illustration from Hilgart (2011)).

The dynamic range is given in the unit decibel (dB) as per equation 4.6 (PCO 2018):

$$\text{Dynamic Range} = 20 \cdot \log\left(\frac{\text{full-well capacity } [e^-]}{\text{readout noise } [e^-]}\right) \quad [\text{dB}] \tag{4.6}$$

Dynamic ranges in the order of around 60 to 70 dB are typical. Some sensors with large pixels can also reach dynamic ranges in the order of around 90 dB. The dynamic range is also expressed as presented in equation 4.7 showing how many charges can be taken up by a pixel as a multiplication factor of the noise floor:

$$\text{Dynamic Range} = \left(\frac{\text{full-well capacity } [e^-]}{\text{readout noise } [e^-]}\right) \quad [\text{-}] \tag{4.7}$$

Dynamic ranges in the order of around 1,000:1, 4,000:1, 13,000:1 and 30,000:1 are typical. Sensors with large pixels such as 11 µm may have even higher dynamic ranges in the order of around 60,000:1.

It should be noted that the dynamic range value will be smaller than the bit depth value due to the limitations regarding the minimum resolvable signal, as pointed out in equation 4.6.

Typical sensors and pixel sizes

There is a large selection of sensor types used for cameras. A selection of typical

image sensor types and dimensions is given in Table 4.4. Some sensor types are built with different pixel sizes which results in different sensor resolutions. Very small pixel sizes that exist are 1.2 µm wide, while very large pixel sizes have a width in the range of around 11 to 15 µm. Especially in low lighting conditions in science applications, sensors with very large pixel sizes can be useful.

Table 4.4: Selection of typical image sensor types and dimensions (Stemmer Imaging 2018).

Sensor type	Diagonal length [mm]	Width [mm]	Height [mm]
1/4"	4.60	3.65	2.74
1/2"	8.00	6.40	4.80
2/3"	11.00	8.80	6.60
1/1.2"	13.30	11.30	7.10
1"	15.80	12.70	9.50

Typical pixel sizes found on websites from vendors of scientific cameras (e.g. PCO AG, Oxford Instruments plc, etc.) include the following: 1.2 µm, 2.5 µm, 3.45 µm, 4.65 µm, 5.5 µm, 6.5 µm, 10 µm, 11 µm, 12 µm, 13 µm, 15 µm.

4.3.2 Image intensifier camera

An image intensifier camera is specifically designed for applications with very low light conditions and feature extremely short exposure times in the nanosecond or picosecond range. With image intensifier technology, the term exposure time is usually referred to as gating. An image intensifier is composed of three main components which are a photocathode, a microchannel plate (MCP) and a phosphor screen (PCO 2021). Additional components are an optical coupling lens system or fire optical taper (PCO 2021) as well as a camera with a global shutter. A drawing of a typical image intensifier camera is shown in Figure 4.21. The working principle of an image intensifier camera is as follows:
After passing a camera lens, photons move through the input window, for example made of quartz glass (Stanford 2021a), of the image intensifier camera towards the photocathode. The photocathode, which is only few micrometers thick, converts the impinging photons into photoelectrons by means of absorbing photons and emitting electrons (PCO 2021). From the photocathode, the photoelectrons move towards the MCP in a vacuum (PCO 2021). The function of an MCP is to act as a secondary electron multiplier. An MCP consists of a bundle of million of glass channels (tubes) whereby each channel acts as an individual multiplier for electrons (Hamamatsu Photonics 2020). When photoelectrons enter an MCP, a potential difference

across the MCP accelerates the photoelectrons. The accelerated photoelectrons hit the channel wall upon which secondary electrons are released which are also accelerated. These secondary electrons move on parabolic trajectories and, upon striking the opposite wall, release more secondary electrons (PCO 2021). After this multiplication of electrons inside each of the MCP's channels, a high number of secondary electrons is released that move towards a phosphor screen (Hamamatsu Photonics 2020). The phosphor screen receives the electrons and produces photons which then pass through an optical coupling lens system or fibre optical taper (PCO 2021) before striking on the sensor of a camera. The sensor must operate with a global shutter. The intensification of input light is in the order of up to around 10,000 times for single-stage intensification (Hamamatsu Photonics 2020)

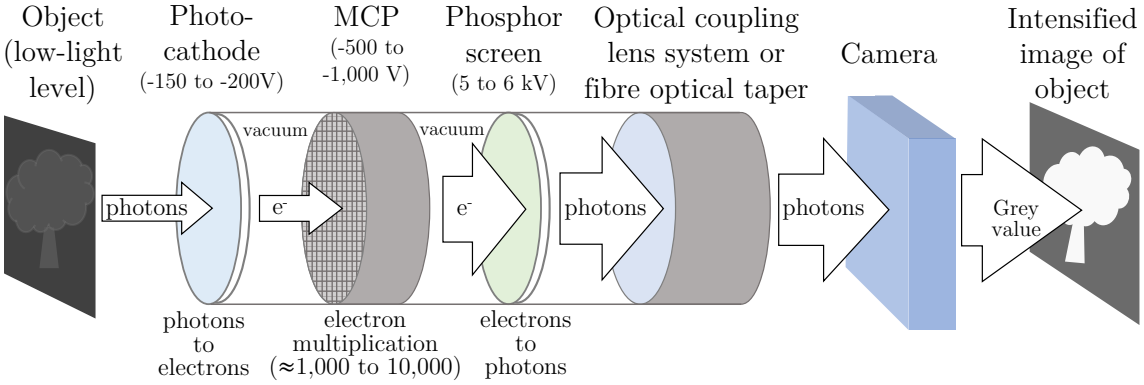

Figure 4.21: Working principle of an image intensifier camera with single-stage microchannel plate (MCP). Arrow sizes indicate the intensification of photoelectrons and photons which leads to an intensified grey value on the image sensor. Other designs of image intensifier camera may work with other voltages than those indicated here. The camera lens was omitted in the illustration.

Photocathode

The photocathode is located behind the entrance window of the intensifier camera and its purpose is to convert impinging photons into photoelectrons by means of collisional ionisation (Stanford 2021a). The distance between the photocathode and the adjacent MCP can be, for example, about 1 to 2 mm (Paschotta 2021a). There are various photocathodes to choose from depending on the wavelength of interest of the application, i.e. UV, visible or near IR such that an optimal photocathode with high quantum efficiency and spectral responsivity can be selected. The input window, which is in front of the photocathode, is made of materials such as quartz or Magnesium fluoride (MgF_2) (Stanford 2021a).

Typically, the lowest usable wavelength of a photocathode is around 200 nm in the UV range, while the highest wavelength is usually not beyond 1,100 nm in the IR

range. Common photocathodes for second generation image intensifiers are S25, S20 (UV), Solar Blind, S20, Hi-QE Red, Hi-QE UV, Hi-QE Blue and Hi-QE Green (Lambert Instruments 2021a). Common photocathodes for third generation image intensifiers are GaAsP (for the visible range 450 to 700 nm), GaAsP (enhanced red), GaAs (for the visible range and near IR), InGaAs (for the visible range and near IR) (PCO 2021, Lambert Instruments 2021a).

Microchannel plate

A microchannel plate (MCP) of an image intensifier camera is made of a circular plate with a bundle of glass tubes with a hexagonal array of tiny holes (Paschotta 2021a). During the process of amplifying electrons, a voltage of around 1 kV is applied to the electrodes and when the photocathode generates photoelectrons they are pulled towards the MCP by the MCPs voltage (Paschotta 2021a). The MCP must be enclosed in a high vacuum with a residual pressure of only 10^{-4} Pa (Paschotta 2021a). Usually the gain of an MCP is limited to about 10,000 to prevent ions from being accelerated in backward direction which can damage the photocathode (Paschotta 2021a). Higher gains are achieved by means of placing two or three MCPs adjacent to one another (i.e. double stage or triple stage MCPs). The optical resolution and also the image quality of a single stage MCP is better than that of double and triple stage MCPs (Stanford 2021b). An MCP built for image intensifier cameras generally is only available in the sizes of 18 mm and 25 mm in diameter. Regarding the design, it is a plate with a thickness of merely 0.5 mm and has several millions of channels of 6 µm width (Lambert Instruments 2021b). Paschotta (2021a) states, as example, a thickness of 1 mm. Apart from the advantage that low-level light is significantly amplified, MCPs also have the great advantage that they can be gated. Gating refers to switching on the MCP only for a very short time in order to achieve extremely short exposure times (Stanford 2021d) which can be as small as about 0.2 ns (depending on the component choice and design of the image intensifier camera). This allows fast processes to be captured (e.g. a light pulse) by the image intensifier camera (note that the image sensor must have a global shutter).

Phosphor screen, optics and image sensor

Behind the MCP a voltage of about 5 kV is applied to propel (i.e. accelerate) the electrons onto a metal-coated phosphor screen (Paschotta 2021a,b). The purpose of the phosphor screen is to convert the high number of electrons into photons which, after being emitted, impinge on an optical coupling lens system or fibre optical taper and subsequently the image sensor of a camera. There are several different types of phosphor screens of which the most common are P43 and P46 (Stanford 2021c), which each have different characteristics. When procuring an image intensifier camera, one must choose a suitable type of phosphor screen for the intended application. There are four main characteristics associated with phosphor screens: phosphor decay time, efficiency, spatial resolution and spectral emission range (Stanford 2021d). The phos-

phor decay time plays an important role with respect to the application's required frame rate. If the frame rate does not play an important role, a P43 screen may be a good choice because of its higher efficiency and higher spatial resolution due to smaller grain size. If fast frame rates are required, then a P46 phosphor screen can be used, but it has a lower efficiency and lower spatial resolution (Stanford 2021c, Proxitronic 2011). An overview on the characteristics of different phosphor screens is shown in Table A.2 in the appendix. Regarding the image sensor, it is absolutely essential for the image sensor to have a global shutter.

Performance degradation

Image intensifier cameras are delicate devices. A degradation of the devices performance during its lifetime cannot be avoided. One type of degradation is called ion feedback (Stanford Computer Optics 2013). If the vacuum becomes unstable and gas molecules build up, then positive ions can be formed from the gas molecules (Paschotta 2021b). Additionally, residual gas in the channels of the MCP can become ionised during the amplification process whereby the ions are accelerated (Stanford Computer Optics 2013). The negative effect from the ionisation is that the ions are accelerated by the voltage in backward direction towards the photocathode and hit it, leading to a degradation over time (Stanford Computer Optics 2013). The ion feedback can be reduced by means of an ion barrier film, which, however, reduces the quantum efficiency (Stanford Computer Optics 2013). The ionisation process inside the MCP is particularly strong when the image intensifier camera receives bright illumination from a light source (Paschotta 2021b) whereby the photographed image can burn into the photocathode and will thenceforth always be visible in any new image taken with the intensified camera. Therefore, ideally, the light source conditions must be well known before carrying out tests. Additionally, a combination of narrow optical bandpass filters and ultrashort gating times reduce the risk of overexposure during daylight conditions. To reduce the risk of ion feedback, MCPs are nowadays designed with shorter plate widths and by slightly tilting the channel array (Stanford Computer Optics 2013). To avoid damage, an image intensifier camera should only be operated if the user is fully aware of the operating conditions and is familiar with the hardware and software.

Signal-to-noise ratio

For applications with low-level light, standard scientific or industrial cameras reach their limits if the grey level in the image is near the threshold of detection. In this case, noise (e.g. read-out noise of the image sensor) may be dominant over the photographed details. The advantage of image intensifier cameras is their high signal-to-noise ratio after the amplification of the low-light signal well above to levels where image sensor noise no longer plays a role. Image intensifier cameras will outperform scientific and industrial cameras in conditions of extremely low light and especially in lighting events that occur e.g. in the nanosecond time range.

However, there is a special type of noise called ionic-noise created from ions in image intensifier cameras. Upon striking the walls inside the MCPs channels, ions produce more electrons which will move towards the phosphor screen and create what is known as ionic-noise in the image (Stanford Computer Optics 2013).

Image quality
Due to the way an image intensifier camera operates with respect to electrons travelling and multiplying in the MCPs channels and then hit the phosphor screen, there will be an image sharpness reduction because electrons impinge on the phosphor screen not only in straight parallel paths but also at angles when exiting the MCPs channels. This is best explained with the following example. Consider a fully dark environment with a very small light source. If this light source were photographed, for example, with a scientific camera whereby the light source would be visible on a single pixel, then with an image intensifier camera the light source would be visible on, for example, 25 pixels (i.e. one central pixel being brightest, 8 surrounding pixels being less bright and another 16 pixels surrounding the 8 pixels with again less brightness, like a Gaussian distribution).

4.3.3 Resolution, contrast and blurred edges in an image

Typically, for cameras and camera lenses, a resolution is specified in the unit pixels or megapixels. This is already helpful because with this information it can be avoided that an image sensor is combined with a camera lens that has a lower image resolving capability than the image sensor. Such a mismatch would result in the overall resolution of the camera system to be lower than the image sensor's resolution, which would be undesired. The resolution in the unit *pixel* for an image sensor and camera lens, however, only gives limited information about the actual potential quality of an image. More effectively, the so-called modular transfer function (MTF) charts can be used so that an optimal configuration of a camera and lens can be chosen (however, these charts are not always provided by the manufacturer). The MTF is of very high importance for measuring and specifying image quality (Edmund Optics 2011c). Details on MTF charts and related topics such as image sharpness and resolution are given in the appendix.

Before discussing the term *contrast*, the term *brightness* needs to be defined. The brightness is a measure of how bright (or dark) an image is. In a grey colour scale 8-bit image setting, the colour black of a pixel has the value 0 and white the value 256. The term contrast is a comparison of the brightest pixel to the darkest pixel in an image. For calculating the contrast of patterns, the Michelson equation can be used (Peli 1990, Edmund Optics 2014c). As per the Michelson equation, see equation

4.8, the contrast is calculated from the brightest luminance ($L_{\max}$) and the darkest luminance ($L_{\min}$) in an image:

$$\text{Contrast} = \frac{L_{\max} - L_{\min}}{L_{\max} + L_{\min}} \cdot 100\,\% \qquad [\%] \tag{4.8}$$

When considering that an eye-safe laser is used, the contrast in an image taken by a camera during daylight conditions can be imagined as per the following conceptual image depictions. In Figure 4.22 (a), no beam is visible in an image if no optical filter is used. In Figure 4.22 (b), an ideal conceptual image is shown whereby an optical filter is used and the beam is perfectly visible against the sky background. It should be noted that with image processing even a very small difference in brightness between the laser beam and the sky background should be sufficient for detecting the beam. Therefore, in lower contrast images as those shown in Figure 4.22 (c) and (d), the laser beam should still be visible. The conceptual images do not include noise or other effects that deteriorate the quality of the image.

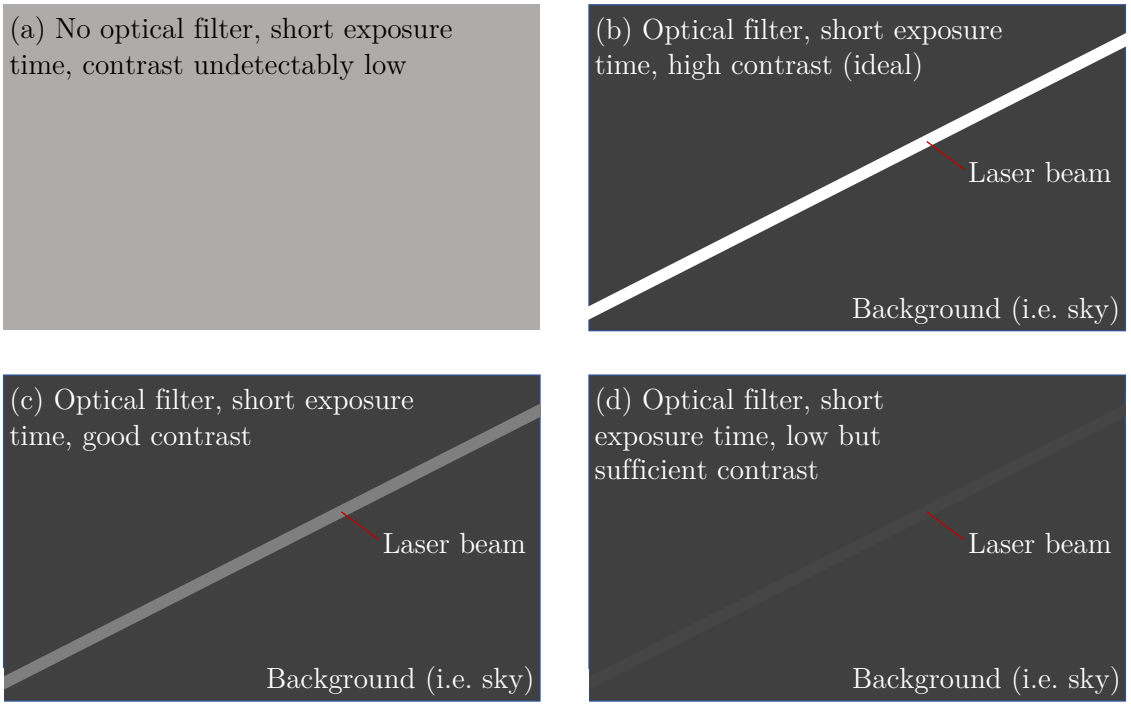

Figure 4.22: Conception of the quality of the visibility of a laser beam in a camera image depending on the contrast (the illustration is idealised and shown without noise).

4.3.4 Camera lenses

A camera lens is required for forming an image from an object (or scene) onto the image sensor of a camera. An example of a lens is shown in Figure 4.23. There are various types of lenses. In machine vision and for scientific and industrial cameras, it is typical to use lenses with a fixed focus lens. A fixed focus lens allows the adjustment of two parameters, namely the aperture ratio as well as the focus. With the ring for adjusting/selecting the aperture ratio (i.e. the f-stop), the amount of light passing through the lens can be regulated by means of adjusting the diameter of an opening. The opening becomes smaller with rising aperture ratio. The ring for adjusting the focus (or working) distance scale allows to set the sharpness of the lens depending on the distance of the object. In front of the lens there normally is a thread for mounting an optical filter. The so-called lens mount is located in the back of the lens. Camera lenses are made for various camera mounts such as C-mount, T-mount and F-mount (there are many more mount types).

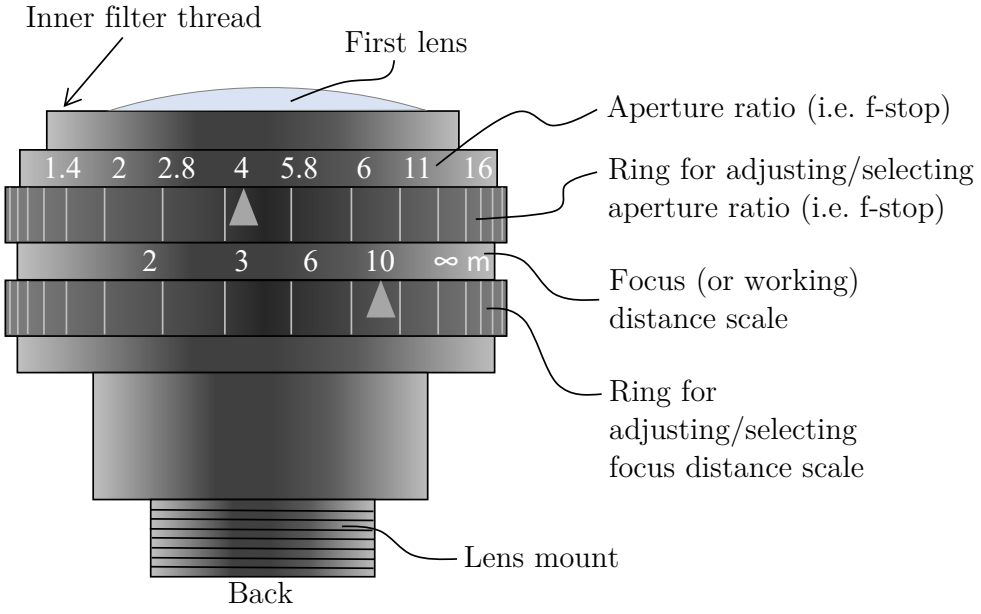

Figure 4.23: Components of a camera lens (based partly on illustration from Hecht (2018)).

In the following, the field of view (FOV) and AFOV are described. Figure 4.24 exemplarily shows a camera lens with the parameters R, AFOV and FOV.

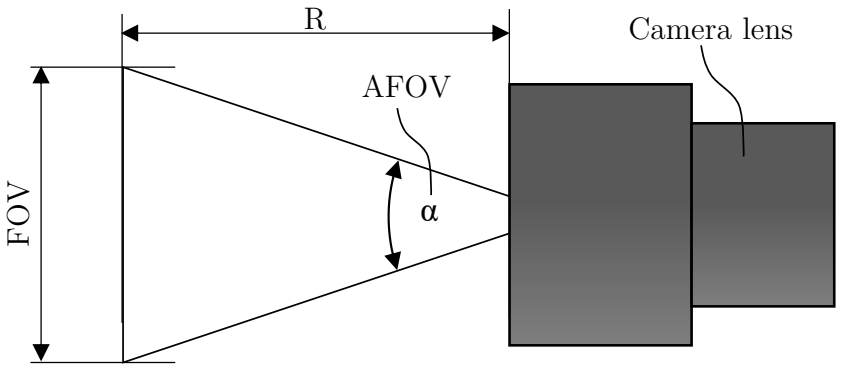

Figure 4.24: Illustration of the field of view (FOW) and angular field of view (AFOV) (based on illustration from Edmund Optics (2015)).

The angle that a camera system can observe, i.e. the AFOV, α, is calculated using equation 4.9 (Demant et al. 2011):

$$\alpha = 2 \cdot \tan^{-1}\left(\frac{w_\mathrm{s}}{2f}\right) \quad [^\circ] \tag{4.9}$$

where w_s is the width of the image sensor. The vertical AFOV is calculated by inserting the height of the image sensor, here denoted as h_s, instead of w_s. Lenses with a shorter focal length (e.g. $f = 18\,\mathrm{mm}$) have a wider AFOV. In the contrary, lenses with a longer focal length (e.g. $f = 105\,\mathrm{mm}$) have a narrower AFOV but they magnify the object. The AFOV is a very important criterion for the CLCS because if, for instance, the AFOV is very small then it is not possible to view the entire heliostat field while the camera is stationary. If, however, a lens with a longer focal length is desired and the AFOV is small, then it will be necessary to use a rotary drive to adjust the azimuthal direction (and perhaps also the elevation angle) of the camera system.

For an object at distance R, the object's height and width (i.e. the vertical or horizontal FOV) can be calculated via equation 4.10:

$$\mathrm{FOV} = 2 \cdot R \cdot \tan\left(\frac{\alpha}{2}\right) \quad [\mathrm{m}] \tag{4.10}$$

With respect to the suitability of camera lenses for certain wavelength ranges, camera lenses are widely available for the visible wavelength range. There are also several choices for camera lenses in the IR wavelength ranges. For the UV wavelength range, however, the choice of camera lenses is small. Another disadvantage of UV lenses is that the resolving ability is typically lower compared to camera lenses for the visible and IR wavelength ranges. While camera lenses in the visible wavelength

range can have resolving capabilities of e.g. 26 megapixels and above, UV lenses may have resolving performances of only up to around 2 megapixels for specific sensor sizes (potentially higher resolving UV may be available, but a high cost is to be expected).

Table A.4 in the appendix shows examples of the AFOV (α) for three selected image sensor types (1/2", 2/3" and 1") and three selected focal lengths (18 mm, 50 mm and 85 mm).

Table A.5 in the appendix shows examples of the width w and height h of the scenery for three different working distances (100 m, 500 m and 1,000 m) for three selected image sensor types (1/2", 2/3" and 1") and three selected focal lengths (18 mm, 50 mm and 85 mm).

Distortion

All camera lenses have a distortion. Distortion is always highest towards the edges of a lens, thus the distortion in an image is highest at the edges. Camera lenses with a short focal length (e.g. 20 mm) typically have a high distortion, while camera lenses with a higher focal length have lower distortions. This is due to the reason that lenses with short focal lengths capture light from a wide angle that requires a lens to have more curvature compared to lenses with higher focal lengths. Distortion in an image can be corrected with image post-processing. There are two types of distortion: *Pin cushion* distortion and *barrel* distortion which are shown in Figure 4.25 (a) and (b), respectively.

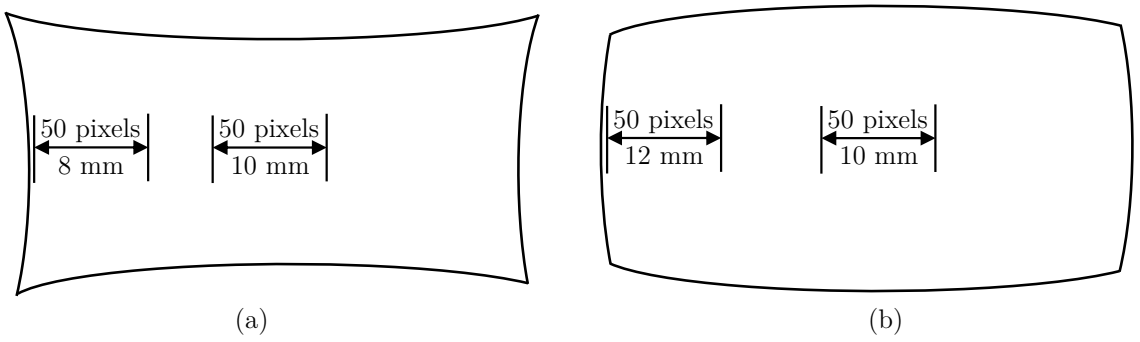

Figure 4.25: Distortion of type (a) pin cushion, and (b) barrel (based on illustration from Stemmer Imaging (2018)).

Compatibility

When choosing a camera lens for a camera it is important to ensure that it is suitable for the sensor type and that the mount is compatible (or that there is an adapter ring available). If a lens is designed to illuminate a 2/3" sensor but the chosen camera has a 1" sensor, then the edges of the image will be dark (this is called vignetting, i.e. when only a portion of the image sensor can be illuminated).

4.3.5 Camera interfaces

There are essentially two types of interfaces that are important to consider. The first is the data communication interface and the second is the trigger interface.

Data communication interfaces
For data communication, common interfaces are USB (USB 2.0, USB 3.0, USB 3.1), Gigabit Ethernet (GigE) and the Camera Link® among others, while older communication interfaces include FireWire® (IEEE1394) (PCO 2018). The communication interfaces greatly vary with regard to cable length and transmission speed of data. PCO (2018) present a list of communication interfaces, the cable types, cable length restrictions and data transmission bandwidths as shown in Table A.6 in the appendix.

The interfaces USB and GigE are usually standard on Windows computers. To connect a camera with a Camera Link® interface, it is necessary to use a so-called frame grabber card, which is a hardware device that needs to be installed in a computer system. Further advantages and disadvantages about the different interfaces are given in Demant et al. (2011).

Trigger interfaces and cable type
If a camera is equipped with a trigger interface, then it is commonly one of the following types: SubMiniature version A (SMA), SubMiniature version B (SMB) or Bayonet Neill-Concelman (BNC). SMA, SMB or BNC connectors are used in combination with coaxial cables. A trigger interface is needed when it is desired to trigger a camera exposure or to trigger individual functions of the camera using an external trigger source such as a pulse/delay generator. In addition, a trigger interface of a camera may also include trigger outputs such that the camera can potentially be used to trigger external devices, e.g. a laser. However, whether or not an external device can be triggered depends on the number of required trigger signals, the type of trigger signal and available triggering options (e.g. setting options for the trigger signal frequency). See further information on trigger cables in section 4.5.1.

4.3.6 Image formats

Several image file formats exist nowadays. Typical file formats such as JPEG, BMP and GIF contain compressed data with reduced image quality which can be noticed especially when zooming in on the image or, for example, when the compression is high (Tan 2006). Image formats can also be compressed but preserve all image data via so-called lossless compression where an algorithm replaces certain patterns with

an encoded formula (Tan 2006). For image processing where image details are very important, the *Tagged Image File Format* (file extensions being *.TIFF* or *.TIF*) is a good choice format as the image data can be stored uncompressed (Adobe 1992) (i.e. without loss of detail). TIFF file formats can also be processed with programming software such as OpenCV or MATLAB® which are both powerful tools for image data processing.

4.4 Optical filter technology

Edmund Optics (2012) describes that that the purpose of an optical filter is to selectively allow specified light wavelengths to pass through. Goldstein (1989) states that optical filters can be categorised into (1) absorbing filters made of glass and (2) multilayer thin-film interference filters. An absorptive filter consists of a glass substrate which allows specific wavelengths to transmit while it absorbs specific non-desired light wavelengths according to the absorption properties of the glass (Edmund Optics 2012). Absorptive filters are not sensitive to a non-orthogonal angle of incidence of light (Edmund Optics 2012). A multilayer thin-film interference filter is made of dielectric and/or metallic layers (Goldstein 1989) which are applied onto a transparent, optical glass substrate and reflect non-desired wavelengths (Baumeister 2004, Edmund Optics 2012). According to Baumeister (2004) the layers of interference filters are often made of non-absorbing dielectric materials. MacLeod (2010) writes that the thin-film structure of interference filters consists of alternating layers of high and low refractive index coatings that cause light to reflect.

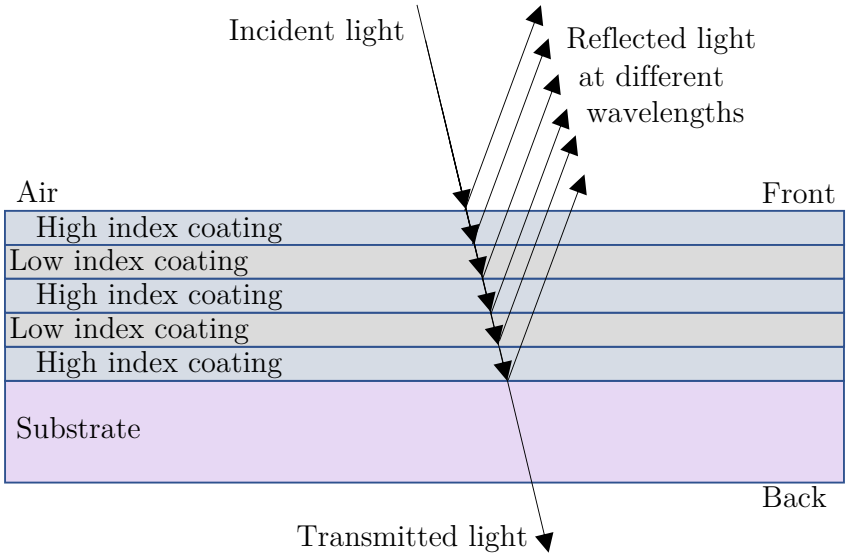

Figure 4.26: Conception of a thin-film structured interference filter (based on illustration from MacLeod (2010)).

Baumeister (2004) explains that interference filters are very well suited for scientific instrumentation due to the fact that this type of filter has well-defined transmission

and reflection characteristics and can be manufactured with steep transitions from reflection to transmission as well as narrow transmission bandwidths. The bandwidth can be described as the wavelength range of light that transmits through a filter (Edmund Optics 2012). More specifically, the bandwidth of a filter is given by the full width at half maximum (FWHM) which is the spectral bandwidth between the rising and falling edge of a bandpass filter where the transmission of light is still 50 % (Edmund Optics 2012).

According to Johansen et al. (2017), thin-film filters, especially ultra-narrow bandpass filters, are highly suitable and most often used for LiDAR applications as these allow only a very small bandwidth of light wavelengths around the LiDAR return signal to transmit (possible are bandwidths as small as 0.1 nm at a high transmission). The CLCS has a very similar requirement to LiDAR applications regarding optical filters. Therefore, it can be concluded that an ultra-narrow bandpass filter is the first choice for the CLCS in order to achieve the highest possible contrast in an image by reflecting or blocking undesired wavelengths of the diffuse solar irradiance outside a narrow bandwidth around the specific central wavelength (CWL) of a laser as shown in Figure 4.27 below.

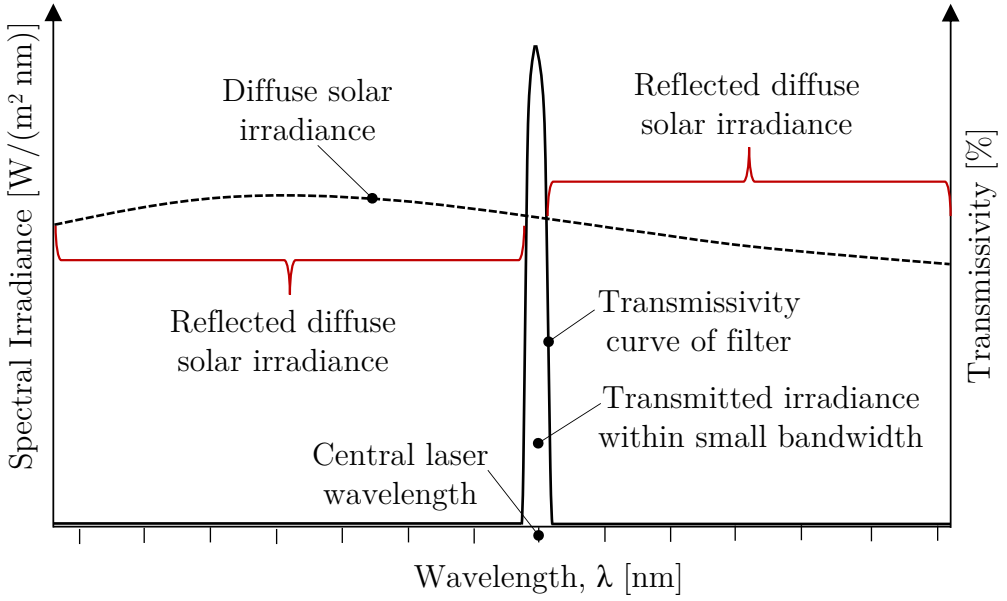

Figure 4.27: Conception of an ultra-narrow bandpass filter allowing only a small diffuse solar irradiance band to transmit (the curve of the diffuse solar irradiance is arbitrary and for the purpose of demonstration only).

There are also negative aspects about interference filters that must be considered. Choosing a bandpass filter with a very narrow spectral transmission bandwidth can lead to a disadvantage if the impinging (monochromatic) light enters the filter at a non-orthogonal angle. According to Edmund Optics (2012), the transmission characteristics of interference filters change when light impinges on the filter at non-

orthogonal angles such that the filter's CWL shifts towards the shorter wavelengths, which is referred to as blue shift. This means that depending on the bandwidth of a bandpass filter with a specified CWL, at a certain AOI, light from a monochromatic light source will no longer transmit through the filter. The angle shift can be calculated using the below equation 4.11 which can be found in literature, websites from optics manufacturers and publications, e.g. see Löfdahl et al. (2011):

$$\lambda_\theta = \lambda_0 \sqrt{1 - \left(\frac{n_0}{n_{\text{eff}}} \cdot \sin\theta\right)^2} \quad \text{[m]} \tag{4.11}$$

where λ_θ is the new centre transmission wavelength at the angle of incidence θ, λ_0 is the centre transmission wavelength at normal incidence angle, n_0 is the refractive index of the incident medium and n_{eff} is the refractive index of the optical filter. The refractive index of an optical filter either needs to be requested from the manufacturer or it is listed on the website of a manufacturer or retailer of optical filters.

How strong the blue shift effect is depends on the wavelength-dependent refractive index of the substrate material. According to equation 4.11, the higher the refractive index of the substrate is, the lower is the effect of the CWL shift for increasing angles of incidence (θ). Also it can be concluded that the longer the wavelength is, the higher is the effect of the CWL shift for increasing angles of incidence (θ). With respect to the CLCS, which uses a camera with camera lens to capture scattered photons of a laser beam, photons will impinge on the lens at various angles. This is also true for the background's diffuse solar irradiance which will impinge on the camera lens at various angles. The spectral transmission bandwidth of an optical filter needs to be wider than the laser's bandwidth around the CWL.

The effect of a blue shift is exemplarily shown in Figure 4.28 for AOI values of $\theta = 0°$, $\theta = 10°$ and $\theta = 20°$. With respect to the CLCS the effect may impact the length of a beam that can be seen by a camera lens if its focal length is very small (i.e. when the AFOV is very large). Also, if a filter's bandwidth is too narrow and if the AOI of the scattered beam is too steep, then the shifted centre transmission wavelength of the filter will block the scattered photons from the laser. Therefore, the filter's bandwidth must be carefully matched with the camera lens's AFOV. With respect to diffuse irradiance from the sky, various wavelengths around the central wavelength will pass through the filter as it is less dependent on the AOI.

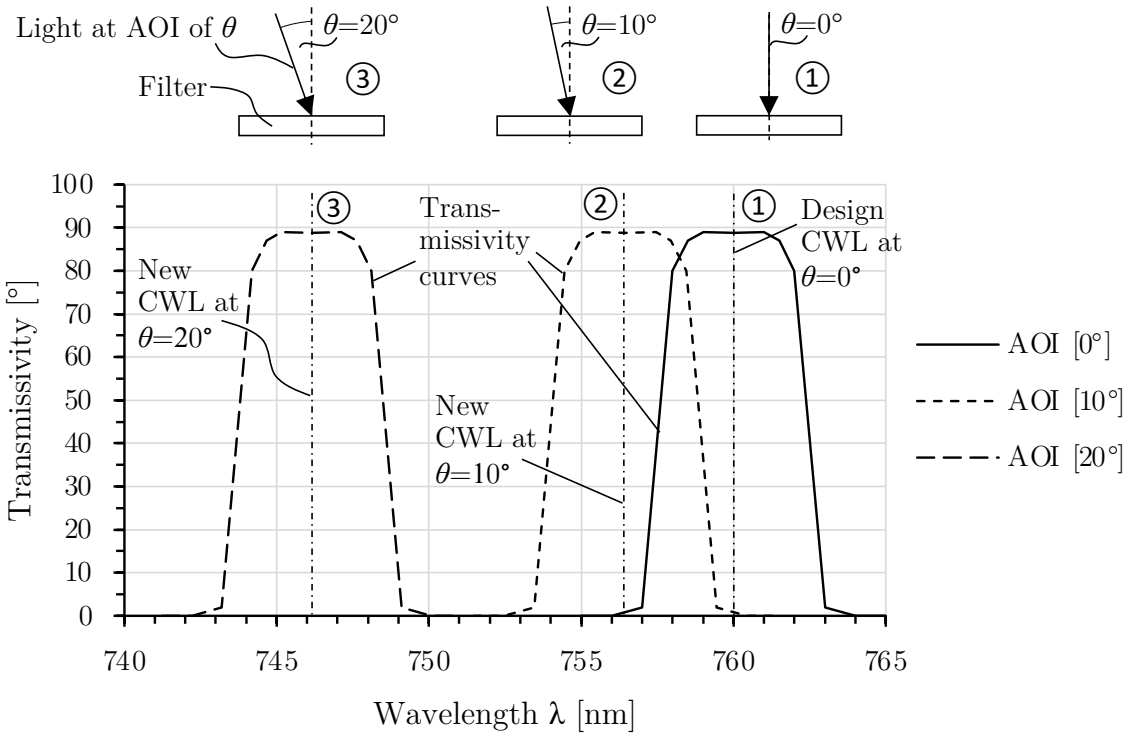

Figure 4.28: Example of a blue shift for three AOI for an optical filter with central wavelength at 760 nm.

OmegaOptical (2012) state that the typical effective refractive indices of typical coatings made of zinc sulfide and cryolite are between around 1.45 and 2.0. Based on this information, Figure 4.29 shows exemplarily three blue shift curves for an interference filter with CWL of 532 nm and AOI values between 0 and 30° for effective refractive indices of 1.5, 1.75 and 2.0. It should be noted that an optical filter will be able to transmit impinging light from angles within the AOI in the shape of cone, meaning that a camera will be able to capture double the AOI around the CWL.

For the CLCS, the AFOV of a camera is strongly limited by the optical filter's FWHM if an ultra-narrow bandpass filter is chosen. A FWHM below 1 nm must not be chosen as then the AFOV of the camera system is small and therefore impractical. If, on the other hand, the FWHM were much greater than necessary, then higher amounts of diffuse solar irradiance will pass through the optical filter, which increases the shot noise and reduces the contrast between the laser beam against the background. Therefore the FWHM must be carefully chosen and the acceptable AOI calculated such that it fits to the AFOV of the camera system (see Table A.4 with the AFOV for examples of sensors and focal lengths).

If, for example, a 1/2" sensor and f=18 mm lens were chosen for a bandpass filter with FWHM of 2 nm, then a vertically emitted laser beam would only be partly visible in the image as the vertical AFOV of the camera system would be 15.2° while the filter would only have an AOI of around ±5°. Considering that the filter's band-

width is given as FWHM, it means that light wavelengths beyond the 2 nm FWHM bandwidth still pass through, but at a lower transmission efficiency. However, it can be expected that for the given example of a camera, lens and filter combination, the beam would not be visible near the top and bottom edge in the image. It should also be noted that a mismatch in AFOV of the lens and AOI of the filter may still be acceptable for economical reasons. Such a reason can be, for example, if a price for a lens with small focal length were far cheaper than a lens with a larger focal length, but the quality differences between the lens were of less importance. In any case, a FWHM of no more than 2 nm should be considered as an approximate upper limit for the CLCS.

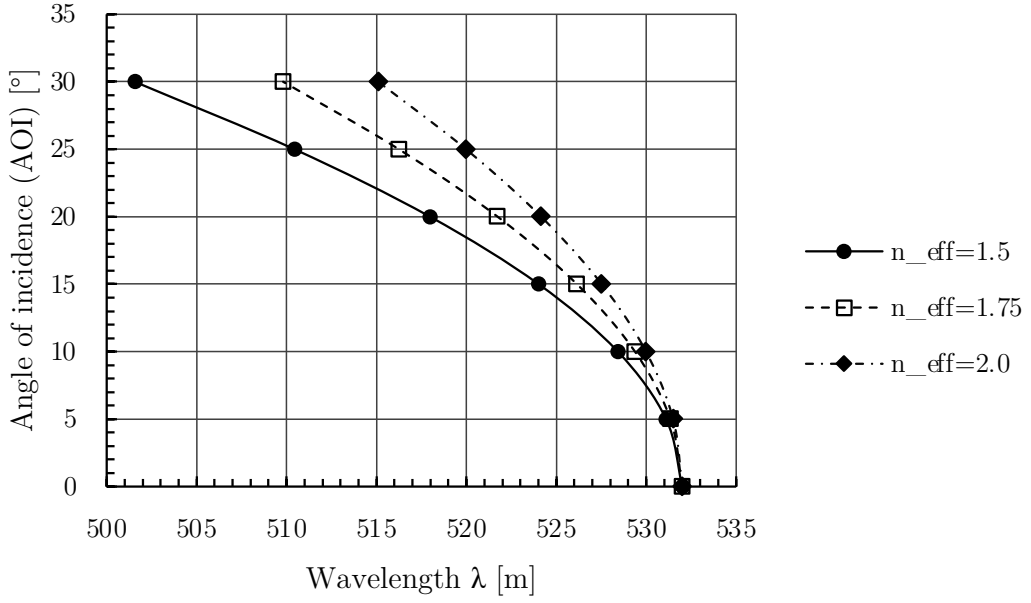

Figure 4.29: Example of blue shift curves for a filter with CWL of 532 nm and AOI values between 0 and 30° for effective refractive indices of 1.5, 1.75 and 2.0.

Basher & Matthews (1977) point out that the optical characteristics of dielectric layers are affected by temperature which results in a shift in the CWL. Interference filters have a blue shift with dropping temperature and a red shift with increasing temperature (Alluxa 2021). The angle shift is usually specified with a thermal coefficient given in the unit [pm/°C] (Alluxa 2021), where pm stands for picometre. The narrower the bandpass filter is, the stronger the temperature dependence takes effect. If the CLCS were designed to work both day and night, and if the temperature difference between midday to midnight were 30 °C, then it needs to be calculated whether the laser's scattered monochromatic light will still pass through the optical filter for the given temperature range at the site. If the change in temperature affects the filter's CWL too strongly, then the air around the camera system with attached optical filter needs to be temperature controlled. Alluxa (2021) specifies that for their hard-coated filters, the thermal coefficient is usually between 2–5 pm/°C. For

example, if the temperature difference between day and night were 30 °C and the thermal coefficient 5 pm/°C, then this would result in a CWL shift and shift of the entire transmittance curve of the filter by 0.15 nm. This implies that the optical filter's FWHM for the CLCS must be sufficiently larger than 0.15 nm.

Further one should note that at non-orthogonal AOI on interference filters, the transmission and reflection properties may also be affected if the impinging light is polarised (Erdogan 2011). OmegaOptical (2012) write that the transmittance through a filter is different for p-polarised light than s-polarised light and show an example illustration of the transmission characteristics of polarised light.

The amount of light energy at a specific wavelength passing though an optical filter is known as the transmittance (or also called transmission) given in the unit % or as a decimal (OmegaOptical 2012). The optical depth (OD) of a filter is another typical parameter that is used to describe the blocking performance of an optical filter and is calculated using equation 4.12 (Migdall et al. 1993, OmegaOptical 2012):

$$\mathrm{OD} = -\log_{10}(T) \quad [-] \tag{4.12}$$

where T is the transmission as decimal value between 0 and 1. Usually a spectral curve for a broader wavelength range with the transmittance and OD data is provided by manufacturers of optical filters which is important in order to assess the suitability of a filter for an application.

4.5 Laser technology

Commonly known light sources such as the sun and light bulbs emit light in all directions which is not in phase and varies in amplitude (Eichler & Eichler 2006). Such light sources also emit a broader spectral wavelength range and are known to be incoherent. A light source which emits light in a very narrow wavelength bandwidth is a laser, which is commonly said to be coherent. The term *laser* stands for *Light Amplification by Stimulated Emission of Radiation* (Schneeweiss et al. 2017, p. 6). According to Eichler & Eichler (2006), real lasers are not perfectly coherent, but instead behave in such a way that they are only partially coherent while the properties of laser beams also vary (i.e. the polarisation, power, frequency etc. are also not stable). Various types of lasers exist for various purposes or applications. Eichler & Eichler (2006) state that the possible choices for central laser wavelengths cover a wide spectral range from 10 nm up to 1 mm, which includes the ultraviolet, visual and infrared wavelength range.

Further, Eichler & Eichler (2006) describe that the light emitted by a laser has four main properties: The light has a (1) small spectral wavelength bandwidth, (2) high collimation which means that the divergence angle is small, and (3) high beam intensity or high beam energy. Moreover, with some laser types it is possible to (4) produce ultra short light pulses. Lasers are also known to be (near) monochromatic, i.e. the light is emitted at a single wavelength (or a relatively narrow wavelength bandwidth).

Working principle of a laser

Figure 4.30 shows the basic principle of how a laser works. Schneeweiss et al. (2017) state that a laser consists of three main components, namely a laser medium, the resonator (2 mirrors) as well as an energy source. Further Schneeweiss et al. (2017) describe that for light to be emitted by a laser, it is necessary to stimulate the atoms and molecules of a laser medium with an external energy source which is referred to as *pumping*. Depending on the type of laser, pumping is carried out optically using light or with electricity (Schneeweiss et al. 2017). The left resonator shown in Figure 4.30 has a reflectivity of 100 % while the partially transparent resonator reflects <100 % (a few percent less), thus allowing only a fraction of photons to exit the tube. Hence, the majority of photons is therefore reflected back and forth inside the tube (Schneeweiss et al. 2017).

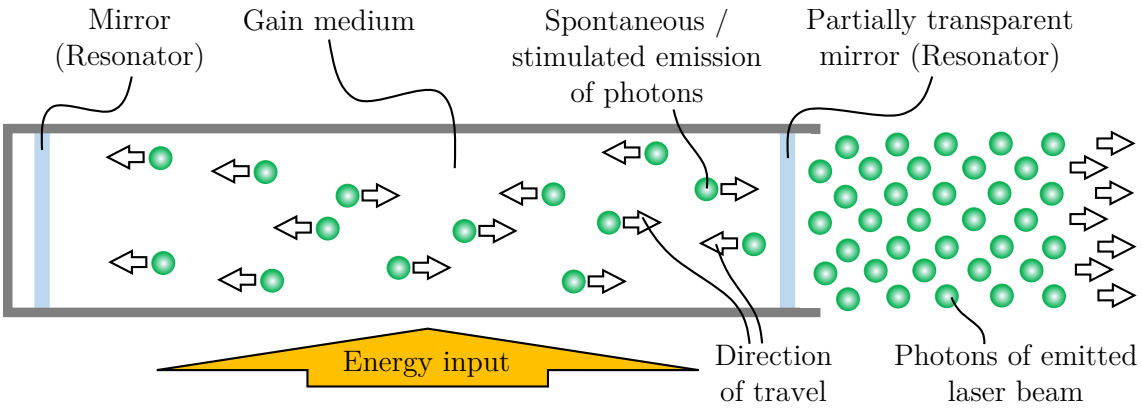

Figure 4.30: Working principle of a laser (based on description and partially on illustration from Schneeweiss et al. (2017))

Table A.7 in the appendix shows examples of typical types of gain media based on a solid, liquid, gas and semiconductor. A more comprehensive list of dyes for dye lasers can be found in a data sheet from Lumibird (2021), which shows typical dyes used for obtaining the various laser wavelengths.

Laser categories

Generally, one can distinguish between two categories of lasers: cw lasers and pulsed lasers, whereby it depends on the exposure time or pulse duration of the emitted

beam as to which category it is. In DGUV (2018) lasers are distinguished in four modes of operation as shown below (direct translation from German into English):

- Continuous wave (cw) laser (Mode of operation: “D”. Exposure time or pulse duration: $\geq 0.25\,\mathrm{s}$)
- Impulse laser (Mode of operation: “I”. Exposure time or pulse duration: $>1\,\mu\mathrm{s} - 0.25\,\mathrm{s}$)
- Q-switched pulse laser / Giant pulse laser (Mode of operation: “R”. Exposure time or pulse duration: $1\,\mathrm{ns} - 1\,\mu\mathrm{s}$)
- Mode-locked pulse laser (Mode of operation: “M”. Exposure time or pulse duration: $< 1\,\mathrm{ns}$)

The light emitted by a cw laser is given in units such as mW, W or kW. Regarding pulsed lasers, depending on the pulse duration, such a laser is categorised as impulse laser, Q-switched pulse laser / giant pulse laser or mode-locked pulse laser. The light emitted as a pulse is given in an energy unit such as µJ or mJ.

Lasers in outdoor applications
Lasers are also deployed in outdoor applications. Examples are: (1) Laser scanners used for scanning and mapping landscapes, industrial sites and building structures etc. in three dimensions, (2) lasers used for LiDAR applications such as atmospheric research, (3) Johansen et al. (2017) state that LiDAR is nowadays also used for object or obstacle detection in the automotive industry for vehicles such that the vehicles avoids potential dangers.

Categories of wavelength ranges
Depending on the laser wavelength, a laser falls into a certain wavelength range category. Table 4.5 shows the categories of wavelength range definitions from ultraviolet UV-C to far infrared IR-C.

Table 4.5: Wavelength ranges of optical radiation as shown in BAuA (2018a).

Wavelength range	Wavelength [nm]
Ultraviolet C (UV-C)	100 to 280
Ultraviolet B (UV-B)	280 to 315
Ultraviolet A (UV-A)	315 to 400
Visible range	380 to 780
Visible laser radiation	400 to 700
Infrared A (IR-A)	700 to 1,400
Infrared B (IR-B)	1,400 to 3,000
Infrared C (IR-C)	3,000 to 1,000,000

Preference of laser category
Continuous wave (cw) and pulsed lasers exist. To make an adequate choice for a specific laser category for the CLCS, it is necessary to assess how to achieve the highest contrast between the scattered photons from a laser beam and the photons from the diffuse solar irradiance of the sky.

As was established in section 4.4, an optical filter with a very narrow wavelength bandwidth for transmitting light must be used in order to block most of the diffuse solar irradiance that is not within a small wavelength bandwidth around the centre wavelength of the laser. With respect to increasing the contrast further, the most effective method is the reduction in diffuse solar irradiance that passes through the optical filter. This can only be accomplished by means of reducing the exposure time of the camera. The benefits of reducing the exposure time is presented in Table 4.6, which shows, with exemplary values which are within the expected range, various ratios of scattered photons from a laser beam and the diffuse solar irradiance for five different configurations A to E. For all five configurations it is assumed that the energy released during beam emission is identical such that an equal amount of scattered photons is generated. The table is discussed below.

In configuration A, a laser is assumed to emit a laser beam for a duration of Δt =10,000 ns (i.e. 10 µs). To capture the laser beam in an image, the exposure time of an arbitrary camera is set to Δt_{exp} =10,000 ns (i.e. 10 µs), which is equal to the laser beam emission time. Further it is assumed that – impinging on a single image sensor pixel – the number of photons from the scattered laser beam are $\mu_{\text{photons,L,p}}$ = 800 and the number of photons from the diffuse solar irradiance from the background are $\mu_{\text{photons,BGD,}\lambda\text{,p}}$ = 8,000. The contrast ratio $\mu_{\text{photons,L,p}}/\mu_{\text{photons,BGD,}\lambda\text{,p}}$ of this configuration is 1:10 (without considering noise).

Configurations B to E assume that a laser beam is emitted for a duration of just Δt =10 ns. In configuration B the cameras exposure time is set the same as for configuration A and therefore, configuration B renders the same result with respect to the contrast ratio as configuration A. Only for configurations C to E the contrast ratio significantly improves when setting the camera's exposure time to smaller values (the number of photons that pass through to the image sensor reduces). In configuration E, for example, the camera's exposure time is set to just 50 ns which reduces the photons from the diffuse solar irradiance by a factor of 200 down to just 40 photons and leads to such a high contrast ratio that the scattered laser beam photons are 20 times higher in number than the photons from the background irradiance. As configuration E leads to a high contrast ratio that is far higher than required, in a next adjustment the laser's pulse energy could be reduced to a value resulting in a lower contrast ratio while the laser beam is still easily identifiable in an image. Further it should be noted that there is a significant benefit when the beam emission

duration is far smaller than the exposure time of the camera because the effect of jitter, i.e. delay in the trigger timing of the individual laser and camera, will then play a lower role (in the worst case, a timing delay of one of the components could lead to the timing of the camera's exposure start to be unsynchronised with the laser beam emission timing). When the exposure time is greater than the emission duration of a laser beam, then the procedure should be to begin with the exposure time of the camera prior to an emitted laser beam entering the FOV and end once the laser beam is outside the FOV. This will avoid problems with jitter of the camera and laser.

It should be noted that one should not reduce the camera's exposure time to extremely low values such as 10 ns if a pulsed laser is used as then the photographed length of the beam in the image will be very short (just 6 metres) which is rather little for an adequate line detection. The length of a laser beam after having travelled for a duration of 50 ns is only just 15 metres but should be long enough for an adequate line detection.

Table 4.6: Difference in contrast ratio in images with laser beam when using a cw or pulsed laser for different camera exposure time and pulse widths.

Parameter	Laser				
	A	B	C	D	E
Δt_{pulse} [ns]	10,000	10	10	10	10
Δt_{exp} [ns]	10,000	10,000	1,000	100	50
$\mu_{\text{photons,L,p}}$ [-]	800	800	800	800	800
$\mu_{\text{photons,BGD,}\lambda\text{,p}}$ [-]	8,000	8,000	800	80	40
Ratio $\mu_{\text{photons,L,p}}/\mu_{\text{photons,BGD,}\lambda\text{,p}}$ [-]	1:10	1:10	1:1	10:1	20:1

Considering the argumentation regarding Table 4.6, a pulsed laser with preferably a short pulse duration in the small nanosecond range or below is favoured for the CLCS. Therefore either a *Q-switched pulsed laser / giant pulse laser* or a *mode-locked pulse laser* are best suited.

Commercial pulsed lasers

As per Figure 4.9, the conclusion was previously drawn that the laser wavelength for the CLCS must be at least 320 nm. Therefore, only wavelengths above 320 nm need to be considered for the CLCS. Moreover, from section 4.3.3 it can further be concluded that only pulsed lasers are suitable for the CLCS. For this reason, only pulsed lasers are considered in this work.
Table A.8 in the appendix exemplarily lists typical commercial lasers. Lasers are available for wavelengths from UV to IR depending on the gain medium. However,

the availability of wavelengths of cw and pulsed lasers is quite limited. For applications that require non-typical laser wavelengths, tunable lasers may be the first choice (e.g. dye lasers and optical parametric oscillator (OPO) lasers). The choice of a laser for the CLCS depends on the commercial availability of a laser at a specific wavelength, the suitability with respect to its specifications and the costs.

Suitability of laser types for the CLCS
For the CLCS, a laser should be chosen that is robust, has a stable CWL, has a small bandwidth around the CWL and a long lifetime. Therefore it is necessary to explore these characteristics for the typical gain media, i.e. solid-state lasers, dye lasers, gas lasers and semiconductor lasers.

Solid-state lasers
Solid-state lasers use solid gain media such as crystals or glasses (Paschotta 2021f). An example for a solid-state laser is a Nd:YAG laser which is the most commonly deployed laser type, using a laser diode for pumped lasers and for cw lasers (Schneeweiss et al. 2017). When using the Q-switch technique, an Nd:YAG laser can generate pulses with pulse widths of a few nanoseconds (Paschotta 2021f), which is suitable for the CLCS. As shown in Table A.8, many wavelengths are available with this type laser. Some of the wavelengths are produced via so-called frequency doubling or frequency tripling, e.g. from the base wavelength 1064 nm, the wavelength 532 nm is produced from frequency doubling and the wavelength 355 nm can be produced from frequency tripling.
In conclusion it can be said that a solid-state laser may potentially be suitable for the application in a CLCS.

Dye lasers
Dye lasers use solvents and dyes, which are often poisonous while some are also carcinogenic meaning that it is very important to avoid skin exposure and spilling (Paschotta 2021g). Furthermore, organic dyes degrade in a very short time of just tens or hundreds of hours (Abramczyk 2005) and therefore have a very limited lifetime that requires the exchange of the dye solution (Paschotta 2008). For many applications, dye lasers can nowadays be replaced by tunable solid-state lasers such as Ti:sapphire lasers but also fiber lasers which do not have the described disadvantages (Paschotta 2021g).
In conclusion it can be said that a dye laser is impractical for the CLCS as it would require too much maintenance.

Gas lasers
For many applications in modern times, semiconductor lasers (as well as to some extent solid-state lasers) have taken the place of gas lasers with the exception of a few applications such as in laser material processing where gas lasers are still

widely deployed (Paschotta 2021h). There are cw and pulsed gas lasers available, whereby some lasers can nowadays have pulse widths in the nanoseconds range (Paschotta 2021h). As there are various gases that can be used, gas lasers have various individual characteristics. Paschotta (2021h) describes that gas laser systems can have an operational lifetime of several thousand hours and that gases are robust while they are also simple to exchange. As disadvantage it is described that the lifetime could be limited by the erosion of electrodes and other factors. Table A.8 shows two examples of gas lasers, namely an N_2 laser an XeF-Excimer laser, which can be operated with pulse widths in the nanosecond range.
In conclusion it can be said that gas lasers may potentially be suitable for the application in a CLCS. However, as the available gas laser types have various and distinguishing properties, their individual suitability would need to be assessed in more detail, if a gas laser were to be preferred.

Semiconductor lasers
Semiconductor lasers are a special class of solid-state lasers which directly convert electrical energy into light and are constructed in a fairly compact and simple way (Eichler & Eichler 2006). Eichler & Eichler (2006) name disadvantages of semiconductor lasers such as the large beam divergence and the wide bandwidth of the emitted laser light compared to gas lasers and solid-state lasers. The majority of semiconductor lasers are laser diodes which exist for wavelengths in the near-infrared, red, blue, green and violet region (Paschotta 2021i, Eichler & Eichler 2006). Semiconductor lasers are used, for example, in laser pointers and in compact disk (CD) players (Paschotta 2021i). Paschotta (2021i) points out that most semiconductor lasers are cw lasers but also pumped semiconductor lasers exist. Semiconductor lasers are used for a wide range of applications such as metrology, optical data transmission, laser spectroscopy and laser material processing (Paschotta 2021i). A list with available semiconductor lasers is presented in Schneeweiss et al. (2017), whereby it becomes clear that the potential of semiconductor lasers for the CLCS is very limited with regards to cw power, pulsed laser energies and pulse widths.
In conclusion it can be said that semiconductor laser technology is unsuitable for the application in a CLCS.

Optical Parametric Oscillator (OPO)
An optical parametric oscillator (OPO) is defined as "coherent light sources based on parametric amplification within an optical resonator" and therefore is very similar to a laser "using a kind of laser resonator, but based on optical gain from parametric amplification (usually in a nonlinear crystal) rather than from stimulated emission of radiation" (Paschotta 2021j). Duarte (2016) states that the emitted coherent radiation from an OPO cannot be distinguished from the coherent radiation emitted from a laser. Its tunable wavelength range is very wide covering about 210 to 2,400 nm. One advantage of OPOs is that they can be tuned also to those wave-

lengths which other lasers do not cover (Paschotta 2021j). The interesting aspect for the CLCS is that an OPO can also be tuned to the Fraunhofer lines of interest at around λ=393.3682 nm and λ=396.8492 nm. As shown in Table A.8, pulses are emitted in the nanosecond range, which makes OPOs suitable for the CLCS from the perspective of the pulse width. (Paschotta 2021j) states that the pumping is carried out with a Q-switched laser for most OPOs. Whether an OPO is suitable for the CLCS depends not only on the specifications but also the costs. OPOs are commercially available and their main field of application is spectroscopy in the UV, near infrared (NIR) and mid infrared (MIR) wavelength ranges (Duarte 2016).

Linewidth

The linewidth of a laser describes the spectral width of a laser beam. The linewidth of a laser is usually given either in the unit m, Hz or reciprocal centimetre ($cm^{-}1$) (Duarte 2016). In the wavelength domain, equation 4.13, found in literature, can be used to calculate the approximate value of the linewidth $\Delta\lambda$ in the unit metres (m) via the laser's wavelength λ in the unit metres (m), frequency $\Delta\nu$ in the unit Hertz (Hz) and the speed of light c in the unit metres per second (m/s):

$$\Delta\lambda \approx \frac{\Delta\nu \cdot \lambda^2}{c} \qquad [\mathrm{m}] \tag{4.13}$$

For the CLCS, it is important that the linewidth (i.e. the bandwidth expressed in the unit metres) of a laser is ideally much smaller than the bandwidth of the optical filter (as discussed in section 4.4, the bandwidth of the optical filter should be between around 1 and 2 nm). If, for example, the linewidth of the laser were around 1 pm, then the effect of the optical filter's blue shift is less strong compared to if the linewidth were in the same magnitude as the filter's FWHM. Therefore it is important to analyse the approximate linewidths of the laser types presented in the previous section *Commercial lasers*.

According to examples from Eichler & Eichler (2006), the linewidth of Nd:YAG lasers in the unit frequency $\Delta\nu$ is around 120 GHz. In the unit of nanometres, this linewidth is around $\Delta\lambda$=0.05 nm at λ=355 nm, around $\Delta\lambda$=0.11 nm at λ=532 nm and around $\Delta\lambda$=0.45 nm at λ=1,064 nm. Nd:YAG lasers are therefore potentially suitable for the CLCS.

From datasheets of OPOs from company websites, it was found that linewidths for OPOs are in the order of around $1/\Delta x$=5 to 450 cm^{-1}. To give a few examples of linewidths at different wavelengths, $1/\Delta x$=5 cm^{-1} is equivalent to $\Delta\lambda$ =63 pm at λ=355 nm, $\Delta\lambda$ =141 pm at λ=532 nm and $\Delta\lambda$ =566 pm at λ=1,064 nm. For the CLCS an OPO could therefore be used if it has a linewidth in the order of around 5

to 50 cm^{-1} (i.e. up to around $\Delta\lambda$=0.5 nm) in the UV wavelength range and no more than around 5 cm^{-1} in the visible and IR wavelength ranges. OPOs are therefore potentially suitable for the CLCS.

Examples of linewidths for a ruby and a dye laser presented by Eichler & Eichler (2006) show that their linewidths in the unit of metres are even smaller than those of Nd:YAG lasers. However, Ruby lasers are nowadays rarely used (Schneeweiss et al. 2017). Dye lasers, as discussed before, are not suitable for the CLCS.

A gas laser of type Eximer laser can have linewidths of <1 pm with the deployment of wavelength-selective elements (Paschotta 2021c), which makes this type laser potentially suitable for the CLCS.

Characteristics of pulsed laser radiation

Schneeweiss et al. (2017) describe that to characterise pulse lasers radiation, two parameters are the most important, namely the pulse energy (Q) and the pulse width ($\Delta t_{\mathrm{pulse}}$). Moreover, it is described that via these two parameters it is possible to calculate the peak power (P_{peak}). From the pulse frequency f (i.e. the number of pulses emitted per second) it is further possible to calculate the mean power ($P_{\mathrm{m}} = Q{\cdot}f$) and the time between the pulses (Δt_f) (Schneeweiss et al. 2017). Figure 4.31 shows these characteristics.

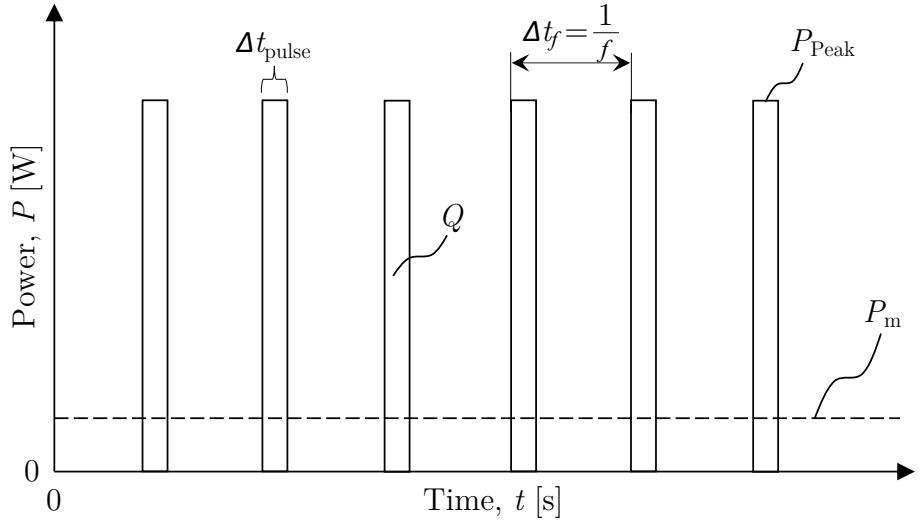

Figure 4.31: Characteristics of pulsed laser radiation (based on illustration from Schneeweiss et al. (2017)).

Polarisation

Laser beams are polarised whereby the polarisation is either (a) linear or (b) circular and elliptical (Paschotta 2021k). Figure 4.32 shows an example of a vertically polarised (also known as s-polarised) electromagnetic wave propagating in z-direction,

whereby the electrical field oscillates in the y-axis direction and the magnetic field oscillates in the x-axis direction.

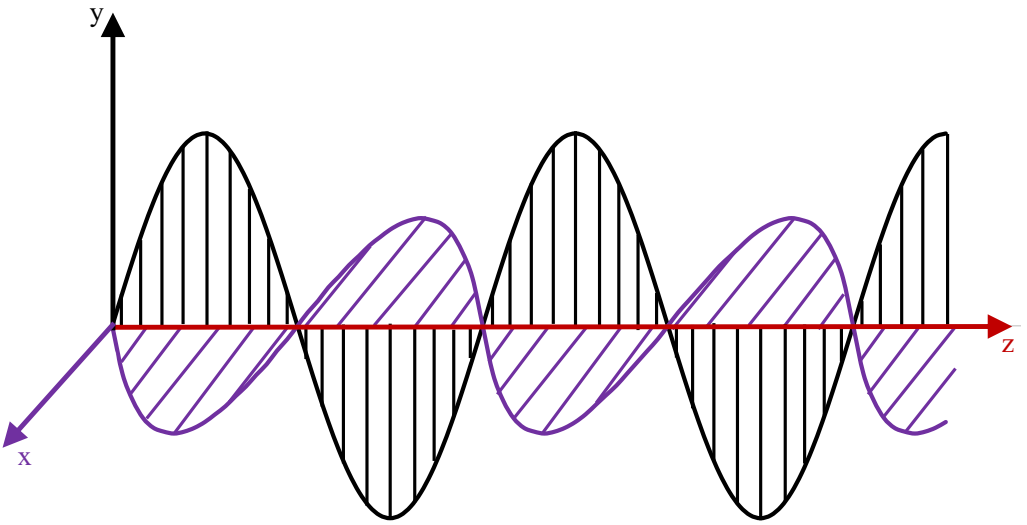

Figure 4.32: Electrical field oscillation (y-axis) and magnetic field oscillation (x-axis) of an electromagnetic wave propagating in z-direction (based on illustration from Paschotta (2021k)).

For operating the CLCS, it is important to know the polarisation state (i.e. s-polarised or p-polarised) of a laser beam as this has an effect regarding the scattering effectiveness at certain scattering angles. The beam polarisation of a laser beam can be varied with a waveplate.

Beam shapes

Typically, the beam shape of a laser has a Gaussian profile whereby the peak flux is in the centre of the beam which decreases with increasing beam diameter (Edmund Optics 2019). For some applications, however, it may be beneficial to use another beam shape. If beneficial with respect to laser safety for the CLCS, then a so-called *flat top* beam profile may be a suitable choice as it leads to a constant irradiance profile across the beam's cross-section (i.e. there is no central peak irradiance as is typical of a Gaussian beam profile). Another widely used term for describing a flat top beam profile is *top hat*. Figure 4.33 shows an image of the relative intensity (vertical axis) of a Gaussian, an ideal flat top and a real flat top beam profile. The beam radius from the centre as relative radial position is shown on the horizontal axis. With respect to peak power and compared to a Gaussian laser beam, the advantage of a flat top laser beam is that the peak power can be reduced while the mean power is identical (Edmund Optics 2019). Paschotta (2021l) describes that a real flat top beam profile still has smooth edges and that it is similar to the shape of a super-Gaussian profile. According to Edmund Optics (2019), refractive flat top beam shaper optics can be used to produce a flat top beam profile from a Gaussian beam profile, but other options are also available.

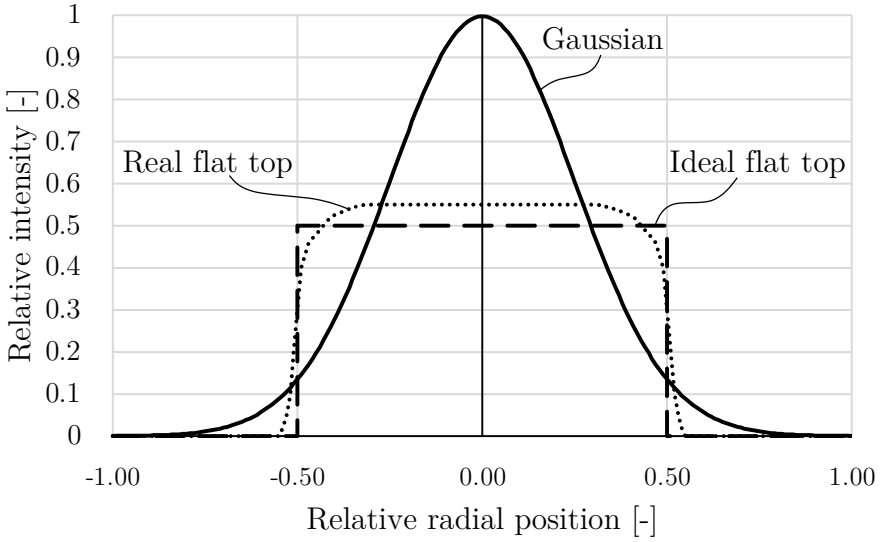

Figure 4.33: Beam profiles of type Gaussian, ideal flat top and real flat top (based on illustration from Edmund Optics (2019) and Paschotta (2021l)).

Laser safety

There are several laser classes which specify the danger level of a laser. These laser classes are: Class 1, Class 1C, Class 1M, Class 2, Class 2M, Class 3R, Class 3B and Class 4. The most dangerous laser class is class 4. Laser safety norms, rules and guidelines were reviewed by the author encompassing the DIN EN 60825-1, DGUV2018 (see DGUV (2018)), TROS (see BAuA (2018a), BAuA (2018b), BAuA (2018c), BAuA (2018d)), DIN EN 207, DIN EN 208 and DIN EN 12 254, but details are not described as part of this thesis due to the vast amount of details. Laser safety, especially for pulsed lasers, is a very complex topic which goes beyond the scope of this thesis. For more details on laser safety, the reader can refer to the above mentioned norms, rules and guidelines as well as literature such as the book from Schneeweiss et al. (2017). A few basic details, especially those regarding the design of the laser and the aspired laser class for the CLCS are given below.

One main aspect regarding the CLCS is that the diameter of the laser beam shall be expanded. The reason is that with respect to general laser safety, laser beam exposures can be made less harmful by increasing the beam diameter (Schneeweiss et al. 2017, p. 185). This method could make, for example, a class 3R laser become no more dangerous than a class 1M laser (see also example given by Schneeweiss et al. (2017)[p. 185]). This is exactly the method that should be used for the CLCS for laser safety reasons, i.e. using beam expansion optics to expand the beam diameter to a far larger diameter of, for example, around 200 mm.

As a basic specification it is desired that in a future CLCS application, the laser should fulfil the laser safety of class 1M. Class 1M lasers are similar to class 1 lasers with the difference that for outdoor applications there is the potential danger

that magnifying optical devices such as binoculars concentrate the beam, forming a more dangerous laser beam. Laser safety is of utmost importance. Whichever laser configuration is chosen, it must be ensured that one or multiple exposures of the human eye to laser radiation does not cause damage to the eye or skin. For additional safety, active and/or passive safety precautions or technical measures must or should be used. It will need to be assessed if potentially also a class 3R could be deployed safely. Further information on laser safety is given in the appendix.

4.5.1 Trigger interfaces

Lasers can be used for triggering external devices such as a camera or the laser itself can be triggered with an external device. An interface for a laser may have several BNC trigger connectors. A pulsed laser, for example, may be equipped with flashlamp (FL) sync and Pockels cell (PC) sync BNC trigger connectors for triggering other devices. To trigger a pulsed laser with an external device such as a pulse/delay generator, FL and PC BNC trigger connectors are possible trigger interfaces. The type of cable a BNC connector is compatible with is a coaxial cable.

Typically, the cable lengths are in the range of around 0.25 m to 10 m. For laboratory tests for testing the CLCS concept, trigger cable lengths of around 1.5 to 10 m will be sufficient. However, in order to prove that the CLCS components can be triggered synchronously and reliably even with cable lengths of several hundreds of metres, a test with such a long cable will become necessary. When using input or output triggers one must take precautions to prevent possible damage to the laser due to EM radiation reflections in the cables, especially when using long cables of around >10 m length, as cables act as large capacitors due to the comparatively large surface area of the metal wire. The use of 50 Ω termination resistors to attenuate the EM radiation reflections is an option, especially if the impedances of the laser and another connected device do not match because EM radiation reflections in a cable can cause a mismatch in triggering which is unfavourable when synchronising devices. Moreover, to further enhance the safety of the laser and other equipment, opto-isolation can be used to ensure that EM radiation reflections cannot cause a damage. Typically, devices have output impedances of 50 Ω.

4.5.2 3D tracking system for a laser

The laser used for a CLCS application in the future must be able to precisely aim at individual heliostat mirror facets. This can be realised with the use of two rotary piezo drives or one dual-axes piezo drive and a special mirror system. Piezo drives find application in various research and industry fields such as astronomy where an automatic tracking system is essential for precisely aiming telescopes in the night

sky. A highly precise piezo drive can have about 12 million steps per full revolution, which is more than sufficient for the CLCS application. However, also the rotational speed, path length, accuracy as well as the reproducibility need to be considered.

4.6 Image processing and line detection

In image processing there are techniques for image enhancement, for restoration and denoising as well as image segmentation.

Image enhancement
Image enhancement refers to the qualitative image enhancement that can be perceived by the human eye and includes simple processes such as brightness and contrast adjustment, the manipulation of image histograms (e.g. improving the visual quality of an image by redistributing grey values of pixels or, for example, setting the grey values of any pixels to zero (black) that have a grey value below a specified grey value threshold), neighbourhood operations (e.g. smoothing or sharpening with linear filters) and grey level slicing (highlighting a certain range of grey values with or without retaining the background), among other (Jayaraman et al. 2009). Errors in an image originate from disturbances such as faulty image signal transmission, among others (Jähne 2002).

Image restoration
Noise in an image is an error that occurs during the acquisition of an image and it refers to pixel values not taking the real intensity values from the photographed scenery (MathWorks® 2021a). The amount of noise present in an image during image acquisition depends on the amount of present light and the temperature of the sensor and other factors (Gonzalez & Woods 2018). The process of removing noise in a digital image using mathematical and probabilistic models is called image restoration (Gonzalez & Woods 2018). There are various types of noise that can occur in an image such as *salt and pepper noise*, *Gaussian noise* (Gonzalez & Woods 2018) and Poisson photon noise (Talbot et al. 2009). A noise related to electrical or electromechanical interference is called periodic noise which has the characteristic of a sinusoidal pattern in the image (Gonzalez & Woods 2018). A brief description of some of the relevant noise types for the CLCS is given below:

- Gaussian noise occurs in the electronics of the image sensor e.g. during an amplification process (Boyat & Joshi 2015) and is therefore an electronic circuit noise which has a Gaussian distribution (Gonzalez & Woods 2018).
- Poisson photon noise (i.e. photon shot noise) statistics are predominant in images (even at bright illumination), but often the less accurate additive Gaussian noise is assumed (Talbot et al. 2009).

- Salt and pepper noise: Dong et al. (2015) describe that this type of noise is a random occurrence of white and black pixels which, among other, occur due to faulty data transmission and ADC faults during image acquisition with a camera.

The type of noise in an image can be identified with the aid of a histogram. For the CLCS, the most relevant type of noise to consider is Poisson photon noise, i.e. shot noise from diffuse irradiance from the sky. More information on noise is given in the appendix.

Image segmentation
Image segmentation refers to the extraction of features in an image which includes techniques for detecting edges and lines in an image (Jayaraman et al. 2009). For detecting edges in an image, filters such as the Sobel operator, Laplace operator, Canny, Roberts operator and Prewitt operator can be used (Jayaraman et al. 2009, Demant et al. 2011). A broad variety of filter functions are available, for example, in MATLAB®, OpenCV and Python. With respect to the CLCS, applying an edge detection filter to detect lines (but not their orientation) or any other type of image filtering will require additional processing time which should be avoided. Image filtering can be avoided for the CLCS because there are two main algorithms available for detecting lines in an image which also give the orientation as output result without the need to use edge detection. These are the *Hough Transform* and the *Radon Transform*, which are, for example, both available as functions in MATLAB® as part of the Imaging Processing Toolbox™. Details about the Hough transform and the Radon transform are given in the appendix.

4.7 Heliostat field

Calibration of a heliostat field
A heliostat field consists of hundreds to more than a hundred thousand heliostats (Sattler et al. 2020). A heliostat usually has multiple flat or slightly concave mirror facets which are canted and focus light on the receiver atop of a tower. The distance between the heliostats and the tower can be several hundreds of metres. With time, the individual facets may need to be calibrated such that their canting orientation is optimal. Few heliostat calibration systems are able to measure the orientation of individual, misaligned mirror facets (see Sattler et al. (2020) for more details).

Reflection of a laser beam by the mirror of a heliostat
Mirror facets of heliostats are either flat or slightly concave. Additionally, a mirror has shape imperfections, which means that a mirror has slight local concave and/or convex curvatures called slope deviation (SD). Depending on the quality of

the heliostat, the flux density distribution can be quite distorted. In addition, deformations of the heliostat due to gravity and wind affect the flux quality of the flux density distribution (Pfahl et al. 2017). The SD can be measured with a measurement method called deflectometry, which gives as output the local SD but also the local focus deviations for the x,y-coordinates of a heliostat's mirror surface (CSPS 2015). The slope deviation is calculated from stripe patterns that are projected on a target and which are reflected by a heliostat towards a camera. The distortion of the stripe pattern allows the calculation of the SD. Nieffer et al. (2019) show an image of a stripe pattern reflected by a nearly rotationally symmetric concentrator (i.e. heliostat) and the resulting SD, which is given for the radial and the tangential direction for rotationally symmetric concentrators (Blume et al. 2020).

When a laser beam is reflected by a mirror surface, the reflected beam may become distorted due to the mirror shape imperfections and/or if a mirror already has a concave shape. For the CLCS, mirror curvature that is concave as well as a potential concentration by multiple facets need to be discussed as both can lead to a focus of the laser beam at a certain focal distance. As stated in Sattler & Göttsche (2023), "one important aspect regarding laser safety is to consider the potential danger of beam concentration if the beams are reflected by wavy mirror surfaces or by multiple facets". A reflection by multiple facets can occur, for example, where four (canted) facets meet. Figure 4.34 shows how a laser beam is concentrated if it impinges on two adjacent canted mirror facets (assumption: the mirror facets are perfectly flat, which, in reality, they are not either due to imperfections and/or if the facet itself is manufactured in curved form). Normally, also the beam divergence would need to be taken into account, which is not done here in order to show an extreme example. In the example given in Figure 4.34, the incoming laser beam is depicted by two red arrows marking the outer edge of a laser beam of diameter d_{L}. The beam is reflected by mirror facet 1 between the points A and S and by mirror facet 2 between the points B and S. Point F' marks the focal point of the outer edges of the reflected portions of the beam, while point S marks the focal point of the inner reflected portions of the beam. The increased laser beam concentration is an area in the shape of a rhombus between the points S, M, N and F'. The focal distance f' where the outer edges of the reflected portions of the laser beam meet can be calculated from equation 4.14 for a concave mirror given by Hering et al. (2004):

$$f' = r \cdot \left(1 - \frac{1}{2\cos\gamma}\right) \quad [\mathrm{m}] \tag{4.14}$$

where r is the curvature radius assuming that points A and B lie on a concave mirror and γ is both the angle of incidence as well as the angle of reflection. Small angles

of γ have no influence on the relationship of the radius of the curvature r and the focal distance f'.

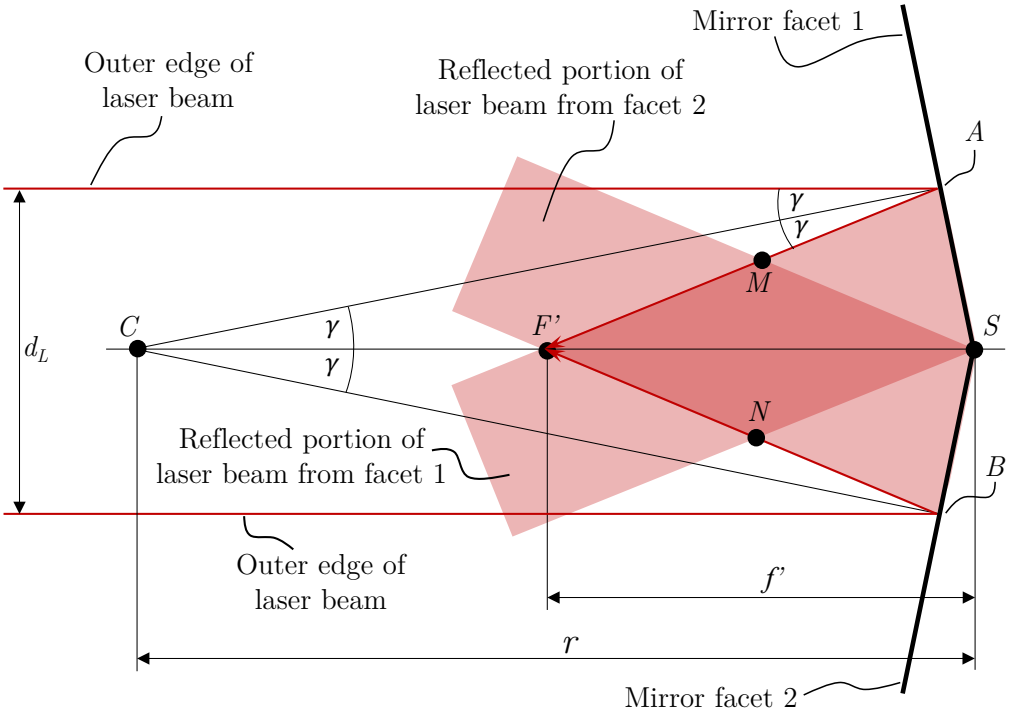

Figure 4.34: Concentration of reflected laser beam from multiple facets (based partly on illustration of the reflection of a paraxial ray parallel to the optical axis CS for a concave mirror from Hering et al. (2004)).

Table 4.7 shows for different radii r and three laser beam diameters d_L (0.1 m, 0.2 m and 0.3 m) the resulting values of the angles of γ as well as the focal distance f'. The given example, however, does not take into account the divergence of the laser beam. Regarding the mirror curvature of a single mirror facet due to slope imperfections, a similar effect of beam reflection and concentration as with the example of Figure 4.34 is to be expected.

Table 4.7: Calculation of focal distance f' for various concave mirror radii r and different laser beam diameters d_{L}.

r	d_{L} [m]	γ [mrad]	f'	r	d_{L} [m]	γ [mrad]	f'
100	0.1	0.5	50	1,000	0.1	0.05	500
100	0.2	1	50	1,000	0.2	0.1	500
100	0.3	1.5	50	1,000	0.3	0.15	500
300	0.1	0.17	150	1,500	0.1	0.032	750
300	0.2	0.33	150	1,500	0.2	0.067	750
300	0.3	0.5	150	1,500	0.3	0.1	750
500	0.1	0.1	250	2,000	0.1	0.025	1,000
500	0.2	0.2	250	2,000	0.2	0.05	1,000
500	0.3	0.3	250	2,000	0.3	0.075	1,000

The worst-case scenario, however, would be a beam concentration by a curved mirror where at F' the concentration of a laser beam would be extremely high.

In conclusion it can be said that there will be a beam concentration within the rhombus between the points S, M, N and F'. This means that this potential danger must be considered when specifying the laser design with regard to laser safety calculations. It should be noted that if parts of a mirror facet have a convex curvature then parts of the beam will widen and not concentrate.

5 Specification of the CLCS Components

In this section, all the relevant information from chapters 3 and 4 is used to make an objective decision on the optimal specification of the components of the CLCS.

5.1 General specification of a laser and camera system

Conclusion for section 3.1.3
The reflectance of typical mirror used in a solar field at a wavelength below around $\lambda = 320\,\text{nm}$ is insufficient. At $\lambda = 320\,\text{nm}$, the reflectance is still around 11 %. At $\lambda = 340\,\text{nm}$ and $\lambda = 350\,\text{nm}$, the reflectance is around 66 % and 77 %, respectively. The reflectance steeply rises to higher reflectance values at higher wavelengths.

Conclusion for section 4.1
From section 4.1 on the solar spectrum and atmosphere the following key data is relevant to the CLCS:

- The highest value of the DHI is about $0.3\,\text{W}/(\text{m}^2\text{nm})$ at around a wavelength of just over 400 nm.
- In the UV wavelength range, the Fraunhofer lines at $\lambda = 393.3682\,\text{nm}$ and $\lambda = 396.8492\,\text{nm}$, have DHI values as low as about $0.1\,\text{W}/(\text{m}^2\text{nm})$. At wavelengths between around 330 and 400 nm, the DHI is mostly very high with values in the range of about 0.15 and $0.25\,\text{W}/(\text{m}^2\text{nm})$.
- At wavelengths above around 700 nm, the DHI values are relatively low (between 0 and $0.12\,\text{W}/(\text{m}^2\text{nm})$, depending on the wavelength).
- Although in the O_2 absorption band at around 760.5 nm the DHI is only between 0.01 and $0.05\,\text{W}/(\text{m}^2\text{nm})$, this wavelength band is not suitable for the CLCS as high absorptance of the laser wavelength is to be expected due to the strong absorption characteristics.
- With respect to the CLCS, the absorption of UV laser wavelengths due to the O_3 molecule does not play a major role if the laser's wavelength is above around 325 nm.
- The scattering of light by air molecules is strongest in the UV wavelength range and significantly drops with rising wavelength. From this perspective, a laser in the UV wavelength range is suited best. When taking the product of the spectral mirror reflectance and the spectral scattering effectiveness into

account for choosing a wavelength which scatters most effectively with respect to the CLCS, then the best choice of laser wavelength is λ=350 nm, but other wavelengths between around 320 and λ=425 nm are also suitable (cf. Figure 4.9). The choice of an optimal laser wavelength must be accompanied by a thorough laser safety assessment by a qualified laser safety officer. Also, a suitable laser must be available at the preferred wavelength.

Conclusion for section 4.2

From section 4.2 on aerosols the following key findings relevant to the CLCS can be summarised:

- Mineral dust is the main type of aerosol that can contribute to the scattering for a CLCS application. Airborne sea salt also contributes to scattering, but it is present only in regions near the coast. Biogenic aerosols are likely to be insignificant for the CLCS.
- Larger solid mineral dust particles will be far better scatterers than small particles, but far fewer larger particles than small particles are suspended in the air.
- The scattering of light from aerosols is described by the Mie theory. The downside of Mie scattering is that scattering from aerosols is highly forward directed, i.e. sideways scattering and scattering in backward directions is far lower. The scattering intensities between around 40 and 180° is very low compared to smaller scattering angles.
- Scattering is highest in the UV wavelength range.

Conclusion for section 4.3

From section 4.3 on camera technology the following key findings relevant to the CLCS can be summarised:

- Cameras exist for various applications. Suitable scientific cameras may be able to detect scattered photons of a laser beam with respect to the CLCS application, but image intensifier camera technology will outperform scientific cameras if the scattering intensity of the laser beam is very weak and near the detection threshold of the sensor of a scientific camera. However, image intensifier cameras are more expensive than scientific cameras.
- The exposure time should be as low as possible to minimise the noise from the background irradiance from the sky, but no less than around 50 ns (if the exposure time were much shorter, then not only will the beam length visible in an image be very short, but also there can be problems with the synchronisation of the CLCS components due to jitter).
- Camera lenses that are suitable for the visible and IR wavelength range are available, but there are only few camera lenses available in the UV wavelength range.

- Regarding the camera lens mount, the compatibility with the camera mount must be checked.
- The camera needs to have a global shutter.
- As stated previously, the exposure time of the camera should begin before a laser beam enters the FOV and end when the laser beam is outside the FOV in order to avoid problems with jitter of the camera and laser.
- Note that for proving that the CLCS can, in principle, work, the camera system's resolution is not the most important criterium as the camera system can be optimised in a follow-on R&D project.

Conclusion for section 4.4
From section 4.4 on optical filters the following key findings relevant to the CLCS can be summarised:

- A wide choice of optical filters is available.
- It was determined that the best choice filter is an ultra-narrow bandpass filter and calculations showed that the ideal filter should have a FWHM between 1 and 2 nm. A FWHM below 1 nm must not be chosen as then the AFOV is too small. If the FWHM were much greater than 2 nm, then too much diffuse solar irradiance will pass through the filter, which increases the shot noise and brightness in the image unnecessarily.

Conclusion for section 4.5
From section 4.5 on laser basics the following key findings relevant to the CLCS can be summarised and concluded:

- Considering the argumentation regarding Table 4.6, a pulsed laser with preferably a short pulse duration in the small nanosecond range or below is favoured for the CLCS. Hence either a *Q-switched pulsed laser / giant pulse laser* or a *mode-locked pulse laser* are best suited.
- As was concluded in section 4.1, light wavelengths at around $\lambda = 350$ nm in the UV-A wavelength range have the best scattering characteristics for the CLCS, i.e. better than light wavelengths in the visible wavelength range (400 to 700 nm) or in the near-infrared wavelength range from 700 to 1400 nm. When choosing a laser wavelength in the UV-A wavelength range, then it must be a wavelength between $\lambda = 320$ nm and <400 nm (a lower wavelength is not advisable due to the rapidly falling reflectance values of a typical CSP mirror below around $\lambda = 320$ nm).
- Pulsed lasers exist for various CWLs. If a wavelength is desired for the CLCS that is not a standard wavelength, then it is possible to consider a pulsed OPO which allows flexible wavelength tuning.

Conclusion for section 4.7
Regarding the heliostat field, it is necessary to take the potential danger of beam focusing into account, which can occur due to the reflection of the beam by mirrors with surface imperfections (waviness), curved mirrors as well as edges where mirror facets meet. This means that this danger must be assessed for the CLCS layout and must be accompanied by a thorough laser safety assessment.

Outlook for a future CLCS application
The laser should, ideally, be a class 1M laser. Laser safety is of primary importance. The laser's diameter needs to be enlarged to increase laser safety (the optimal diameter for a future CLCS application must be calculated in a laser safety assessment). Also, for a future CLCS, additional active and/or passive safety precautions or technical measures must or should be used (depending on conclusion from a future laser safety assessment).

Summary of important criteria for the CLCS:
For the CLCS to work in daytime, it is essential that the influence from background irradiance in an image is reduced as much as possible in order to have sufficient contrast to detect a photographed beam in an image. Also it is of utmost importance that the laser must be eye-safe. To achieve this, it is (i) necessary to use an ultra-narrow bandpass filter which allows only a small wavelength bandwidth around the central laser wavelength to pass into the camera's lens (the FWHM should be around 1 to 2 nm), (ii) the most suitable type of camera is an image intensifier camera. Ideally, the camera's exposure time should be in the order of around $\geq$50 ns in order to minimise the noise from the background irradiance from the sky and also to avoid synchronisation issues between the components due to jitter, (iii) the laser must be a pulsed laser with a short pulse width in the low nanosecond range or below for realising the best contrast ratio in an image and also to ensure that the exposure time of the camera is greater than the pulse width such that synchronisation problems due to jitter (i.e. trigger delays) can be avoided (when specifying the CLCS it is important to check the jitter properties of the individual components), (iv) the laser must be designed eye-safe, (v) the scattering of light especially by air molecules must be strong, (vi) the solar light intensity at the laser's wavelength should be as small as possible or else be reduced in an image by setting short camera exposure times, (vii) the highest scattering effectiveness of a laser wavelength used for the CLCS is found via the product of the spectral mirror reflectance of the heliostat mirror and the spectral scattering effectiveness (cf. Figure 4.9) and (viii) there should be little absorption of the laser's wavelength by molecules present in the near-ground atmosphere. The CLCS shall be designed to perform a measurement rate per mirror facet of, ideally, around 10 Hz. Active and passive laser safety solutions may need to be deployed to guarantee safety for e.g. CRS maintenance personnel and air traffic. The dual-axis beam alignment system could be realised with piezo motors.

The camera may need to be rotated too, which could also be realised with piezo motors. The above criteria are taken from Sattler & Göttsche (2022) with slight modification.

5.2 Selection of the laser and camera system

In Table 5.1, a description of the chosen configuration of the CLCS components is presented.

Table 5.1: Selection of the CLCS components for upcoming tests.

Component	Description
Laser	The best choice wavelength for the CLCS with respect to the highest scattering effect when taking the reflectance of a heliostat mirror into account is λ=350 nm (cf. Figure 4.9). The best choice laser category is either a Q-switched pulsed laser or a mode-locked pulse laser. For the tests in project HeliBo, a SpitLight 300 Q-switched pulsed laser with a CWL at λ=355 nm was chosen in order to make use of a very high scattering effectiveness. A beam diameter of about 50 mm (after beam expansion) and maximum pulse energy of 8.5 mJ was selected. The pulse energy of 8.5 mJ was selected based on preliminary tests at the laboratory of project partner Radiant Dyes (see test described in section 6.2). For the upcoming tests at the Solar-Institut Jülich, the pulse energy could be reduced further though, allowing flexibility to test the CLCS also at pulse energies lower than 8.5 mJ. The diameter of 50 mm was chosen in project HeliBo because of cost constraints, although a diameter of 200 mm was preferred. Even though the diameter of about 50 mm was smaller than desired, it was suitable for the proof-of-concept tests in project HeliBo. This configuration and the chosen pulse energy was thought to be a good starting configuration as calculations showed that with a specialised scientific camera with interline CCD sensor for the UV wavelength range, it should be possible to capture the scattered light in images. By means of adjusting the Pockels cell delay time of the laser, it is possible to reduce the beam energy to lower energy pulse emissions such that the laser and camera configuration can therefore still be tested with weaker pulse energies in a controlled, shielded off environment.
Camera	Scientific cameras as well as image intensifier cameras specifically for the UV wavelength range are available. For most of the tests described in chapter 6, a monochrome scientific camera with the below key specifications was used: – Image sensor: Interline CCD. – Pixel resolution (horizontal×vertical): 1,392×1,040 (1.4 megapixels). – Pixel size: 4.65 µm × 4.65 µm. – Shutter: global (snapshot). – Minimum setting of exposure time/shutter time: 1 µs. – quantum efficiency: 34 % at λ=355 nm. – Binning modes: 1×1, 2×2 and 4×4. – Lens mount interface: C-mount

Lens	A UV camera lens with C-mount and a focal length of 25 mm was procured. The entrance lens aperture diameter was about 11 mm (measured). The maximum transmission at the wavelength λ=355 nm is 88 %. The resolving performance capability of this lens is 640×480 Pixels, i.e. about 0.3 megapixels (more details on the resolving performance capability of a lens is given in section 4.3.4).
Optical filter	As optical filter, an ultra-narrow bandpass filter with CWL transmission at λ=354.72 nm and FWHM of <1.2 nm was chosen. The maximum transmission at the wavelength λ=355 nm is 81.7 %. To allow flexibility with different camera lenses, a filter diameter of around 50 mm was selected in order to be flexible with various size lenses. Note: An adapter ring that was fitted to the optical filter limited the entrance aperture diameter of the filter to 46 mm.
Trigger device	For triggering the laser and camera, a pulse/delay generator was borrowed which allows on-demand manual triggering of single-pulse laser beam emissions and synchronised single image acquisitions. It has four individually configurable output BNC connectors. Therefore, for each output the timing of the pulse trigger, the pulse duration and the output voltage level can be configured individually such that a synchronisation with other devices is possible. The signal communication is discussed in more detail in section 6.1.
Cables	The following coaxial cables with BNC connectors were acquired: Two 10 m coaxial cables for triggering the laser as well as one 10 m and one 200 m coaxial cable for triggering the camera.

For the very last indoor laboratory test campaign (see section 6.5) and an outdoor test campaign at the end of project HeliBo (see section 6.6), an image intensifier camera was procured to assess, in detail, the suitability of image intensifier camera technology for the CLCS. The key specifications of the intensified CMOS camera are given below:

- Sensor type: CMOS.
- Minimum gate width: 40 ns.
- Intensifier stages: Single stage MCP with 18 mm diameter.
- UV sensitive photocathode.
- Phosphor screen: P43.
- Pixel resolution: 1,920×1,200 (2.3 megapixels).
- Pixel size: 5.86 µm ×5.86 µm.
- Lens mount interface: C-mount.

In addition, a second UV camera lens with a focal length of 78 mm was procured for the last tests.

6 Experiments and Simulation

In this chapter, laboratory experiments, simulation results as well as field experiments are in the focus and discussed. Tests were carried out with an InnoLas Spit-Light 300 Q-switched pulsed laser with a fitted telescope and optics as well as the components stated in section 5.2. Experimental results from a laboratory test are compared with results from the simulation model in section 6.2 (the equations of the model are given in chapter 3). Only the most relevant tests are discussed in detail in this chapter. Before describing the first laboratory tests, the topic of *signal communication* is discussed.

6.1 Signal communication

The synchronisation of the laser with the camera can be realised in several ways. In this work, the synchronisation was realised with a pulse/delay generator which has several output signal ports for triggering components. Pulse/delay generators typically use BNC connectors for sending or receiving signals. For triggering the laser in the experiments described in chapter 6, it was necessary to use two coaxial cables, i.e. one for triggering the flashlamp at a frequency of 10 Hz and the other for triggering a device called *Pockels cell*. In all experiments, only single-shot triggering was used such that single pulses are only emitted when required.

An oscilloscope was used for measuring the delay times of the cameras, the coaxial cables (lengths of 10 and 200 m) and the pulse/delay generator. All devices were triggered using a Transistor-Transistor Logic (TTL) signal at around 4 to 5 Volts.

The following Figure 6.1 shows the connections of the laser and camera with the pulse/delay generator.

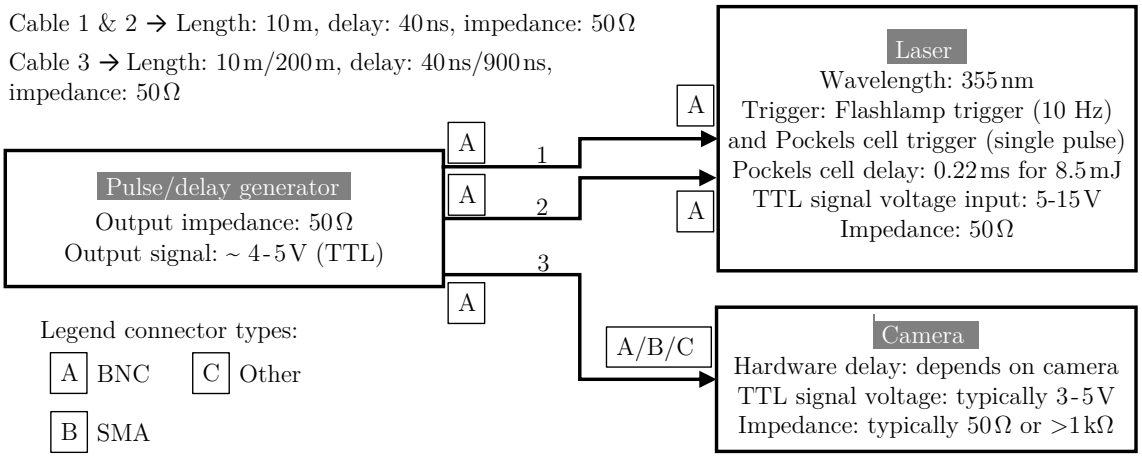

Figure 6.1: Signal diagram for the triggering of the laser and camera with a pulse/delay generator. The laser pulse energy can be decreased by increasing the Pockels cell trigger delay. The pulse energy of the original beam is 32.5 mJ at a Pockels cell delay of 220 µs (i.e 0.22 ms), but with a beam splitter, the pulse energy was reduced to about 8.5 mJ.

The synchronisation of the camera and laser is presented in another form in Figure 6.2 to show the times when the camera and laser receive their signal or signals. A visualisation of delay times is also given. Not shown are the cable delay times as well as the time needed for the scattered photons to travel to the camera. It should be noted that one must consider that a photon requires 3.3 ns to travel 1 m. Therefore, for travelling a distance of 1 km, a photon takes 3.3 µs. If the exposure time of the camera were 1 µs, the beam could easily be missed if not properly synchronised. Hence, it is necessary to pre-calculate the delay times depending on the location of a heliostat in a heliostat field and also the predicted direction of the reflected laser beam. The delay time in a coaxial cable is in the order of around 4 to 6 ns per metre, but this needs to be measured for a cable individually in order to determine the exact times. Figure 6.1 also shows the delay times that were measured for the 10 m and 200 m coaxial cables.

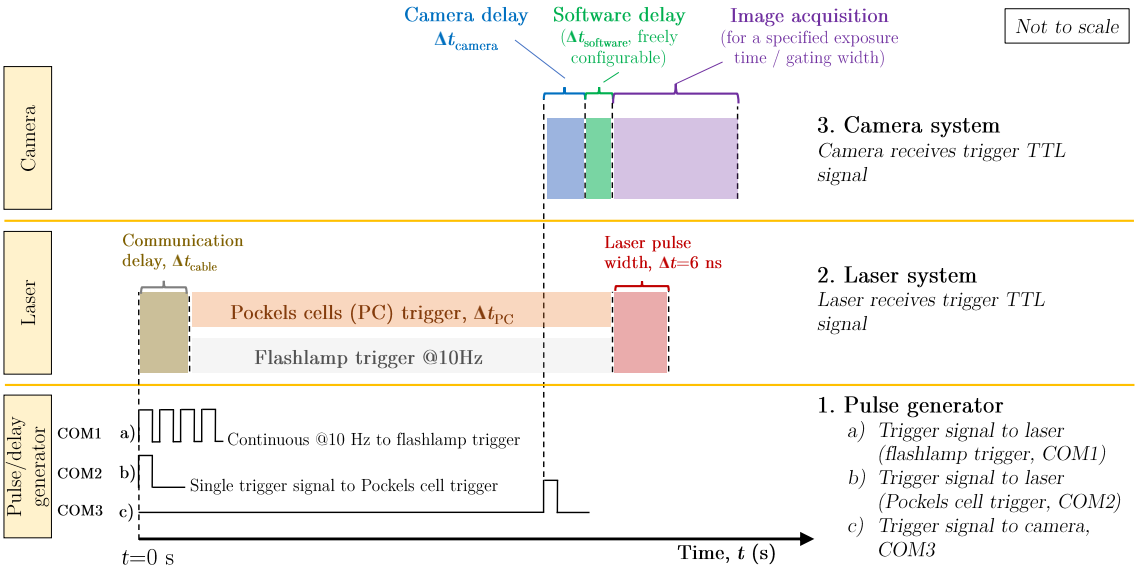

Figure 6.2: Trigger diagram for the synchronisation of the laser and camera with a pulse/delay generator via COM 1 to 3.

6.2 Experiments and validation of simulation model

In section 6.2, laboratory tests with a laser and camera (see section 6.2.1), a grey value analysis of images from the blue sky (without laser beam) (see section 6.2.2) and the validation of the CLCS simulation model (see section 6.2.3) are presented. A conclusion on the simulation results and a comparison with the experimental data is given in section 6.2.4.

Some of the contents and results presented in section 6.2 are already pre-published by Sattler & Göttsche (2022) and Sattler & Göttsche (2023) in a similar way (Reproduced from Sattler & Göttsche (2022) and Sattler & Göttsche (2023), with the permission of AIP Publishing). It should be noted that the results presented in sections 6.2.1 and 6.4 are more accurate than those presented by Sattler & Göttsche (2022) and Sattler & Göttsche (2023) because an optimised, more accurate image analysis method was applied after the publications had been submitted.

6.2.1 Laboratory tests with laser

The very first tests were carried out in the laboratory of a project partner. The setup of the laboratory test rig is shown in Figure 6.3 (a) and 6.3 (b). To expand the laser beam's diameter to effectively about 47 mm, a telescope was used, which consisted of expansion optics and a collimator lens. The path of the beam expansion was photographed with the equipment listed in section 5.2. Also, an image intensifier

camera was borrowed and briefly tested.

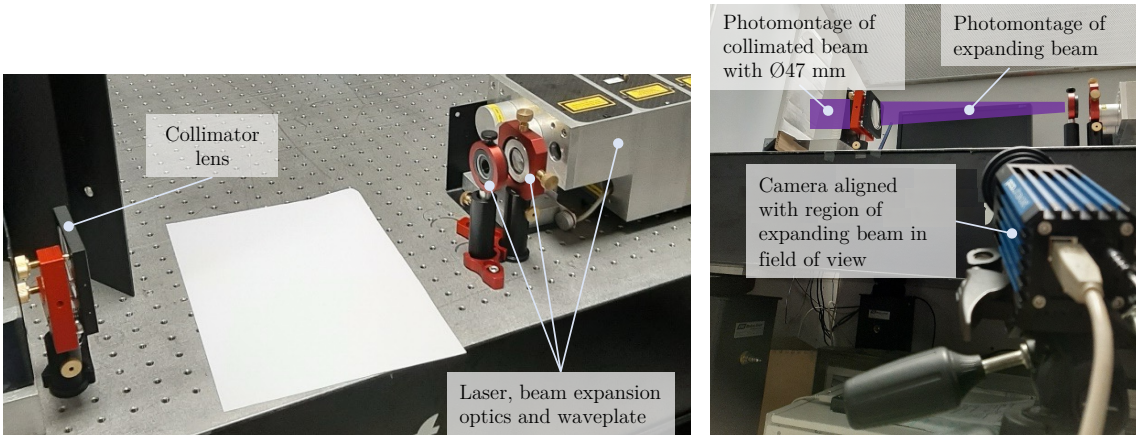

(a) (b)

Figure 6.3: Setup of first laboratory test. Reproduced from Sattler & Göttsche (2022), with the permission of AIP Publishing.

In the following, the tests with the monochrome scientific camera with interline CCD sensor are described. The test was carried out inside the laboratory with a camera distance of about 1.16 m from the fully expanded laser beam (the laboratory was small, therefore the distance could not be increased). The pulse energy of the laser was set to about 8.5 mJ. The camera was tested at two settings with resolutions of 348×260 pixel (4×4 binning mode) and 696 × 520 pixels (2×2 binning mode). Setting the camera to a binning mode at a lower resolution has the advantage that it improves the signal-to-noise ratio.

A strong signal from the scattered laser light was obtained at a resolution of 348×260 pixels as shown in Figure 6.4 (a). In the image, the laser beam's grey value had a maximum value of $\mu_{\mathrm{y,p}} = 320$ on the image sensor's pixels. A grey value of 0 is equivalent to black while a grey value of 16,384 is fully white (14 bit). However, the image of Figure 6.4 (a) still contains noise. The noise level was determined by calculating the mean grey value of a large section of the image without the laser beam. Then, in a next step, the mean grey value of the noise was deducted from the image of Figure 6.4 (a) to obtain Figure 6.4 (b). The mean grey value of the laser beam was then calculated from a large image section containing the laser beam. The mean grey value of the laser beam per pixel from Figure 6.4 (b) was determined to be $\mu_{\mathrm{y,p}} = 30.4$, which is a very low light signal, but the laser beam was still easily identified through image analysis.

When the camera was set to a resolution of 696 × 520 pixels (2 × 2 binning mode), the laser beam signal could also be identified in an image. It should be noted that in

the real-life application and from a greater distance (e.g. 200 m), the photographed laser beam will appear much narrower in width.

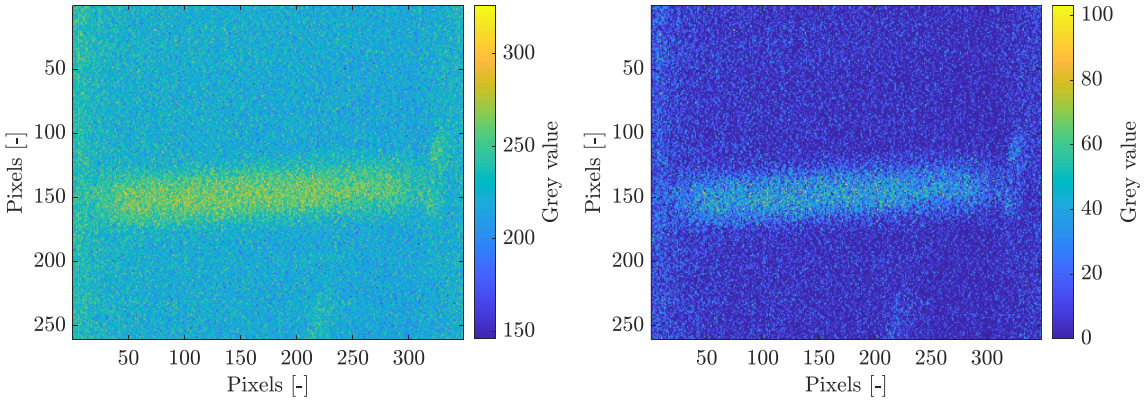

Figure 6.4: Images of laser beam. (a) Image of horizontal laser beam in scaled colours at a resolution of 348×260 pixels (with 4×4 binning) (left), (b) Post-processed image of laser beam (with 4×4 binning) after noise deduction (right). The left and bottom axes show the pixel number and the right vertical axis the grey value. Image (a) is reproduced from Sattler & Göttsche (2022), with the permission of AIP Publishing.

The borrowed image intensifier camera could only be tested briefly. The image showed a strong scattered beam signal. Image intensifier camera technology was found to generally be the more suitable camera option than a monochrome scientific camera because of the various, previously discussed advantages associated with this camera technology. However, the image data from the CCD camera was also good and useful for validating the simulation model.

6.2.2 Mean grey value of the blue sky

In the following, an analysis of the mean grey value of the blue sky is presented. Images of the sky were taken with the monochrome scientific camera, the f=25 mm lens and the ultra-narrow bandpass filter. The exposure time of the monochrome scientific camera was set to 1 µs.

The first images of a blue sky that were taken had a grey value between 100 and 180. The test was then repeated two more times on brighter days, which are described below.

Figure 6.5 (a) shows an image of the blue sky. The image also contains a mast and a tree. As the original image file (TIFF format) appears to be completely black because the greyscale values (GV) are very low, MATLAB® was used with the command *imagesc* for producing an image with scaled colours, such that the objects

and features become visible. Towards the edges of the image, the image becomes less bright due to the optical characteristics of the lens (high distortion towards the edges). Image (b) shows the histogram of the image. The diffuse irradiance from the sky has a Poisson distribution with GVs between around 400 and 500, while the mast and tree reflect far less light and are present in the image with GVs between around 200 and 350 (note that this image includes the dark noise in the image). Image (c) shows a histogram of just the blue sky marked with a dashed red line in image (a) showing a clear Poisson distribution. Finally, image (d) shows a histogram of the blue sky but with a deducted dark image. For image (d), the mean GV was 218. The standard deviation of the GV in image (d) is 26. A basic calculation of the mean shot noise can be carried out using the mean GV. Considering a quantum efficiency of the monochrome scientific camera of $\eta = 34\,\%$ at λ=355 nm and the camera's analogue to digital conversion (ADC) value, then within the area of the red dotted rectangle the mean number of photons that passed the optical filter and lens causes a grey value of $\mu_{y,p}$=513. The mean shot noise then calculates to $\sqrt{\mu_{y,p}}$=23. Furthermore, readout noise (7 to 9 e^- rms), DSNU=3 e^- and other noise types add to the noise in the image.

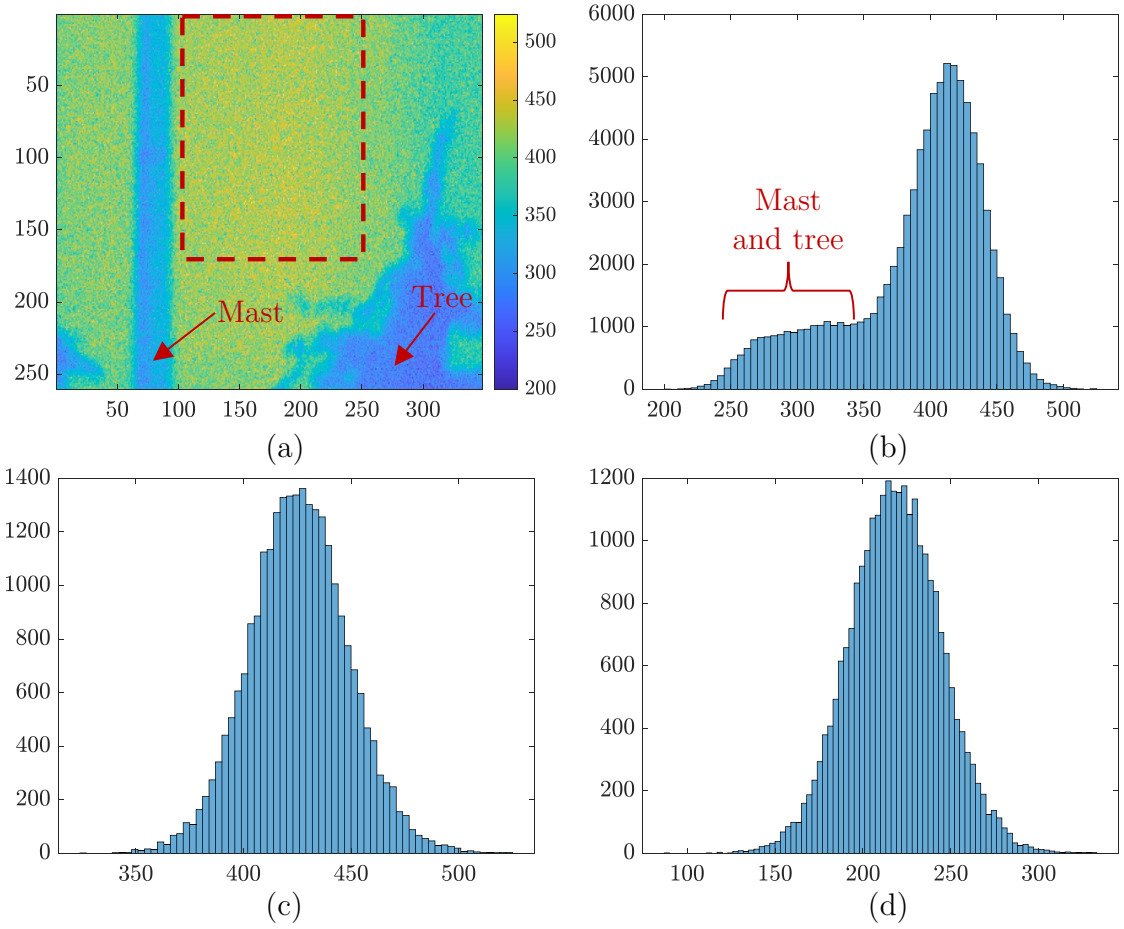

Figure 6.5: Grey value analysis in outdoor environment during a day with blue sky.

The image analysis was repeated for an even brighter image of the blue sky taken on a day in midsummer, shown in Figure 6.6 (a). The image was taken without objects in the AFOV of the camera. Image (b) shows the histogram of the entire image of the sky. The diffuse irradiance from the sky has a Poisson distribution with grey values between around 600 and 700. Image (c) shows a histogram of the blue sky marked with a dashed red line in image (a), omitting the darker edges in the image. Finally, image (d) shows a histogram of the blue sky but with a deducted dark image. For image (d), the mean GV is 413 and the standard deviation is 32. The mean number of photons that passed the optical filter and lens within the area of the red dashed rectangle resulted in a grey value of $\mu_{y,p}$=972. The mean shot noise then calculates to $\sqrt{\mu_{y,p}}$ =31.

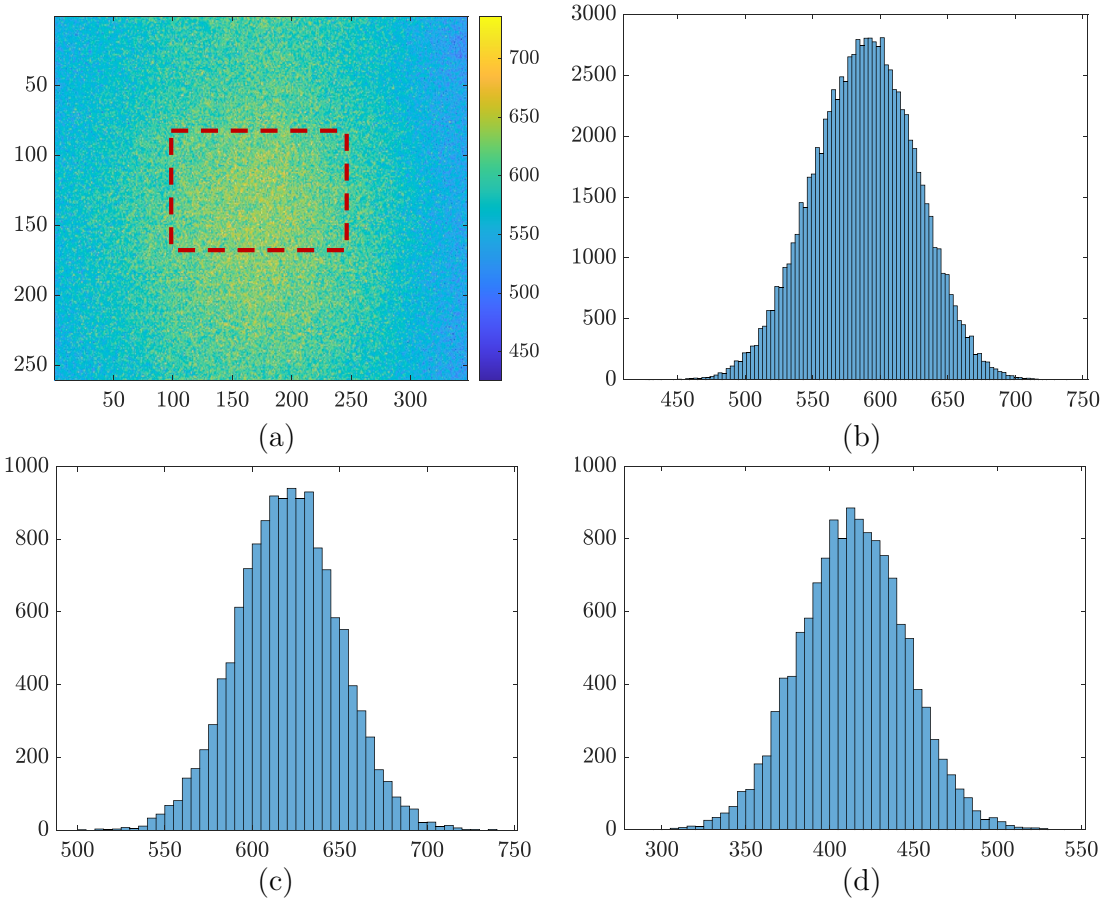

Figure 6.6: Grey value analysis in outdoor environment during a very bright day with blue sky in midsummer.

6.2.3 Validation of the simulation model

In the following, simulation results from Rayleigh and Mie calculations are presented for the monochrome scientific camera with interline CCD sensor. The simulations were carried out to validate (1) the experimentally obtained mean grey value of the laser beam from Figure 6.4 (b) (i.e. the image of the laser beam after noise deduction)

and (2) to validate the simulated grey value of a pixel of the sky (i.e. the diffuse irradiance).

Part of the input for the simulations were the beam diameter of 47 mm, the pulse energy of the laser of 8.5 mJ and a distance to the laser beam of about 1.16 m (same as in an experiment described in section 6.2). The following camera parameters were used as input in the model: The camera's exposure time was 1 µs, the camera's quantum efficiency at $\lambda = 355$ nm was 34 % and the transmissivity of the filter and lens at 355 nm were 81.6 % and 88 %, respectively. Among other parameters, the camera's overall system gain K was also an input parameter.

At the end of section 6.2.3 a comparison between the experimental results from section 6.2.1 and simulation results is made. Also, the result from the grey value analysis of the blue sky from section 6.2.2 is compared with the simulation result.

Parts of section 6.2.3 are already pre-published by Sattler & Göttsche (2022) in a similar way (Reproduced from Sattler & Göttsche (2022), with the permission of AIP Publishing). It should be noted, though, that the results presented in section 6.2.3 are more accurate than those presented by Sattler & Göttsche (2022) because an input parameter was further optimised after the publication had been submitted.

Simulations for Rayleigh scattering from molecules

The simulation of a pixel's mean grey value for a scattered laser beam due to Rayleigh scattering to validate the experimental data from Figure 6.4 (b) is presented below. Also, the calculation of a pixel's mean grey value for the diffuse irradiance from the blue sky background using the ASTM G173-03 reference spectrum was carried out. Both results are presented in Table 6.1. The first three lines, which are highlighted in grey colour, are the simulated values for the diffuse irradiance from the sky. Shown are the calculated mean number of photons ($\mu_{\text{photons,BGD},\lambda,\text{p}}$), mean number of electrons ($\mu_{\text{electrons,BGD},\lambda,\text{p}}$) and mean grey values ($\mu_{\text{y,p}}$) per pixel for the background irradiance from the sky. The simulation was carried out for three binning modes (1) 1×1 binning mode at a resolution of 1392×1040 pixels (1.3 MPixel), (2) 2×2 binning mode at a resolution of 696×520 pixels (0.36 MPixel) and (3) 4×4 binning mode at a resolution of 348×260 pixels (0.09 MPixels). The lower the resolution of the camera is set, the lower becomes the readout noise in the image due to the binning mode being active. Compared to the full sensor resolution of 1.3 MPixel, the resolution of 348×260 has a readout noise which is a factor of 16 smaller due to the binning mode of 4×4. In 4×4 binning mode (i.e. 16 pixels combined to be a single super size pixel), the grey value from the sky was calculated to be $\mu_{\text{y,p}} = 32.8$. At a resolution of 696×520 pixels (2×2 binning mode), the grey value from the sky is about four times weaker than in 4×4 binning mode ($\mu_{\text{y,p}} = 8.2$). At full camera

resolution (1.3 MPixel, i.e. at 1×1 binning mode), the grey value from the sky is weakest ($\mu_{\mathrm{y,p}} = 2.1$).

The simulation results of the mean grey value of a scattered laser beam are shown for the same three binning modes and camera resolutions in the last three lines of Table 6.1. In 4×4 binning mode, the laser beam will be visible best and the mean grey value of a pixel was calculated to be $\mu_{\mathrm{y,p}} = 27.7$. At a resolution of 696×520 pixels (2×2 binning mode), the grey value of the scattered beam is four times weaker in the image but it should still possible to detect it ($\mu_{\mathrm{y,p}} = 6.9$). At full camera resolution (1.3 MPixel, i.e. at 1×1 binning mode), the mean grey value of the scattered beam is only $\mu_{\mathrm{y,p}} = 1.7$. Also the mean number of photons ($\mu_{\mathrm{photons,L,p}}$) and mean number of electrons ($\mu_{\mathrm{electrons,L,p}}$) per pixel were calculated and are shown in Table 6.1.

Table 6.1: Calculated mean number of photons (μ_{photons}), electrons ($\mu_{\mathrm{electrons}}$) and mean grey value ($\mu_{\mathrm{y,p}}$) per pixel for the background irradiance (denoted with "BGD") and scattered laser beam (denoted with "L") due to Rayleigh scattering for three camera binning modes.

Parameter	Resolution 1,392 x 1,040 Binning 1x1	Resolution 696 x 520 Binning 2x2	Resolution 348 x 260 Binning 4x4
$\mu_{\mathrm{photons,BGD,\lambda,p}}$	4.8	19.3	77.3
$\mu_{\mathrm{electrons,BGD,\lambda,p}}$	1.6	6.6	26.3
$\mu_{\mathrm{y,p}}$ from background irradiance	2.1	8.2	**32.8**
$\mu_{\mathrm{photons,L,p}}$	4.1	16.3	66.1
$\mu_{\mathrm{electrons,L,p}}$	1.4	5.5	22.1
$\mu_{\mathrm{y,p}}$ from scattered laser beam	1.7	6.9	**27.7**

In a simulation study it was evaluated whether or not the mean grey value of a laser beam in an image will change with increasing distance between a laser beam and a camera. The outcome was that even though the scattering intensity impinging on a camera lens decreases with R^2, the grey value of a pixel will remain constant. In a simplification it was assumed that the laser beam's diameter does not change (in reality, though, a beam's diameter increases over the distance due to the diversion angle).

Simulations for Mie scattering from particles suspended in the air

The simulated grey value for a pixel that results from Mie scattering and is angle-dependent is discussed in this section. Two Mie scattering simulations are presented below. For the first simulation, the particle distribution that was chosen for the

simulation is the curve of "Juelich: median" of Figure 4.12 with 66 particles per cm^3. The Mie scattering calculation was carried out for an s-polarised laser beam using the beam parameters stated at the beginning of section 6.2.3 as input. When viewing the laser beam from smaller angles, e.g. 20°, then the Mie scattering intensity gives a more significant contribution of scattered light regarding the grey value of the beam in the image. Whether or not there is relevant contribution from Mie scattering depends strongly on the viewing angle onto the beam as Mie scattering is dominant in forward direction. The strong variation in Mie scattering intensity for angles between 0 and 180° represented as grey value on the image sensor of the monochrome scientific camera was calculated for 1×1, 2×2 and 4×4 binning and is shown in Figure 6.7. For 4×4 binning, at 20° viewing angle the grey value is about $\mu_{y,p}=11$, at 40° viewing angle the grey value is about $\mu_{y,p}=5$, at 60° viewing angle the grey value is about $\mu_{y,p}=2$ and at a viewing angle between 80 and 180° the grey value is $\mu_{y,p}\leq 1$. With rising viewing angle, Mie scattering becomes less and less significant for the CLCS. There was almost no difference in the result between s-polarisation and p-polarisation. Figure A.23 in the appendix shows the calculated angle-dependent Mie scattering intensity for the individual particle mean diameters for the mean particle distribution "Juelich: median" of Figure 4.12 multiplied by the laser beam volume within the AFOV of the camera. Additionally, a zoom for more details is shown in Figure A.24 in the appendix.

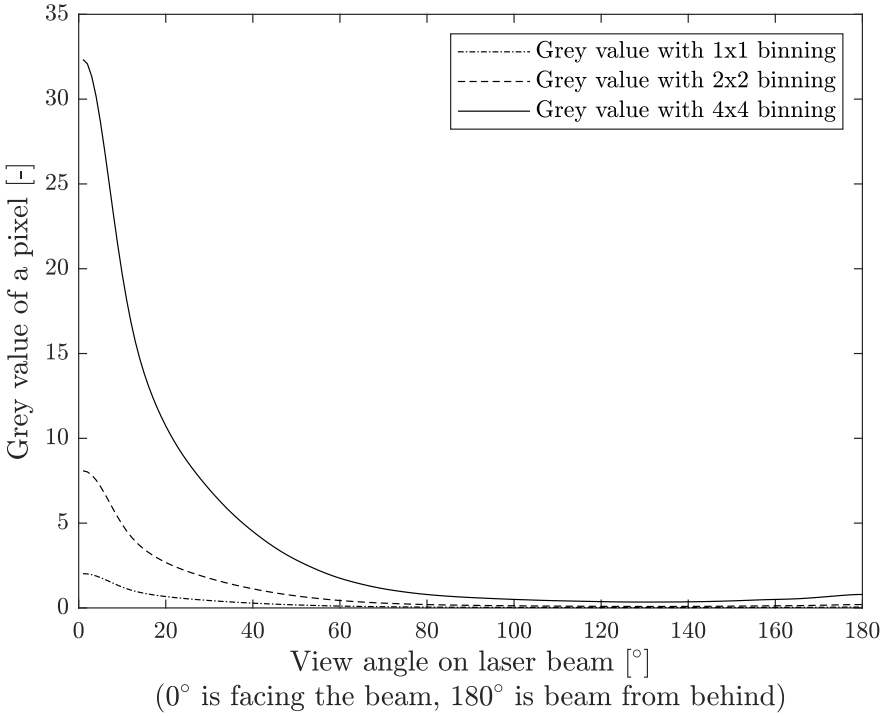

Figure 6.7: Calculated grey value produced from the Mie scattering of an s-polarised laser beam which would be captured with a camera system consisting of the monochrome scientific camera, f=25 mm camera lens and ultra-narrow bandpass filter with FWHM of <1.2 nm. The calculation was done for scattering angles (here called *View angle on laser beam*) from 0 to 180°. The particle data from the curve "Juelich: median" of Figure 4.12 was used as input.

A second simulation was carried out to determine the contribution from Mie scattering for a higher particle number and size distribution. Therefore, for this simulation, the particle distribution that was chosen is the curve of "Juelich: 10 % percentile" of Figure 4.12. This particles distribution contains 205 particles per cm^3. The simulation result is shown in Figure 6.8. For 4×4 binning, at 20° viewing angle the grey value is about $\mu_{y,p}$=40, at 40° viewing angle the grey value is $\mu_{y,p}$=17, at 60° viewing angle the grey value is about $\mu_{y,p}$=6 and at a viewing angle between 80 and 180° the grey value is $\mu_{y,p} \leq 5$. With higher numbers of particles suspended in the air, Mie scattering becomes more relevant for the CLCS for viewing angles below around 40 or 50°. Therefore, for higher particle concentrations such as the one that was used in this simulation, there can be a relevant contribution from Mie scattering at smaller scattering angles. More details about the Mie scattering simulations are shown in Figure A.25 and Figure A.26 in the appendix.

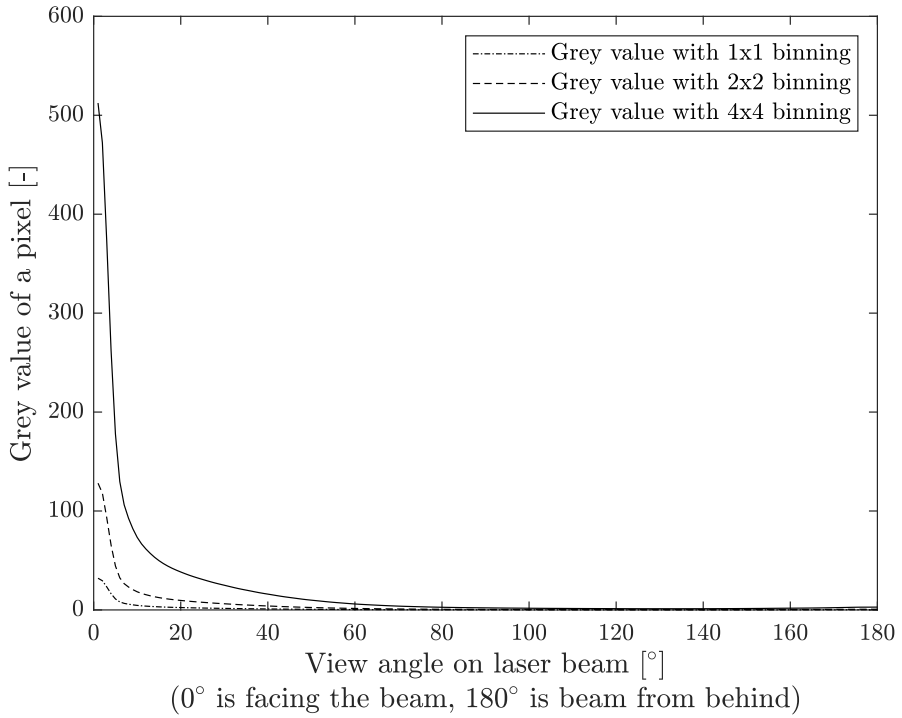

Figure 6.8: Calculated grey value produced from the Mie scattering of an s-polarised laser beam which would be captured with a camera system consisting of a monochrome scientific camera, f=25 mm camera lens and ultra-narrow bandpass filter with FWHM of <1.2 nm. The calculation was done for scattering angles (here called *View angle on laser beam*) from 0 to 180°. The particle data from the curve "Juelich: 10 % percentile" of Figure 4.12 was used as input.

Due to the strongly fluctuating particle concentrations suspended in the air it would be optimal if the CLCS can detect the beam at all times simply from scattered photons from molecular Rayleigh scattering only and thus be independent from particle number concentrations and particle sizes. In this case, if there are also scattered photons from Mie scattering this will increase the beam's brightness, but the scattering contribution from Mie scattering should not be essential for the functionality of the CLCS (Sattler & Göttsche 2022).

Simulations for Rayleigh scattering from very small particles

A calculation was carried out using equation 3.22 for a camera setting in 4×4 binning mode to determine whether or not Rayleigh scattering from very small particles is of significance for the CLCS. The calculation was carried out for a particle concentration of 6,000 particles per cm^3 (based on a value in Perim de Faria et al. (2018)) and a single particle of size of 30 nm. It was found that the contribution is a grey value of just $6.3 \cdot 10^{-10}$ and therefore irrelevant. As a next step, a Mie scattering simulation was carried out as a comparison. Figure A.27 in the appendix shows the simulation result for a particle concentration of 6,000 particles per cm^3

for a single particle of size of 30 nm for various binning modes of the monochrome scientific camera. The grey value of a pixel is below 0.0018 for 4×4 binning and even lower for the other binning modes.

In a second Mie scattering simulation, also 6,000 particles per cm^3 were assumed but the particle size was increased to 50 nm. Also here the simulated scattering contribution was irrelevant (the grey value was below about 0.04 for 4×4 and far lower for the other binning modes) as shown in Figure A.28 in the appendix.

The Mie simulations confirm that the scattering contribution even from comparatively many tiny particles is irrelevant.

6.2.4 Conclusion on data from simulations and experiments

Mean grey value from laser beam
In this section, a comparison of the mean grey value of the laser beam on a pixel determined from the experiment (described in the previous section 6.2.1) and the simulation (described in section 6.2.3) is made.

The experimentally determined grey value of a pixel from Figure 6.4 (b) is $\mu_{y,p} = 30.4$. The simulated grey value of a pixel from Rayleigh scattering from molecules was calculated to be $\mu_{y,p} = 27.7$. Regarding the laboratory experiment, the contribution in scattering from particles is likely to be very small due to the camera position in the laboratory which resulted in a high scattering angle of above 90°.

The particle distribution in the laboratory was not known as it could not be measured. When neglecting scattering from particles and only considering Rayleigh scattering from molecules, it can be concluded that the simulation model is highly accurate in calculating the mean grey value of a pixel for a scattered laser beam as the deviation is only around 8.9 %.

Mean grey value from diffuse irradiance from sky
The values in Table 6.1 for the calculated blue sky diffuse irradiance were compared to images from a blue sky during sunny conditions. As described in section 6.2.2, the mean grey value from the sky in the camera images varied between around 100 to about 413, which is far higher than the simulated grey value of $\mu_{y,p} = 32.8$ (using reference solar spectral irradiance data). As was confirmed with the camera manufacturer, when taking an image during daylight conditions, photons impinging on the sensor still produce electrons during sensor readout even though the exposure time is completed. For this reason, the image was brighter than anticipated. A scientific camera like the one that was used in the tests is therefore less suitable for

the CLCS in very bright light conditions. The described limitation, however, does not apply to image intensifier cameras. With image intensifier cameras no additional light can pass through the photocathode after the exposure duration is completed. Another great advantage of an image intensifier camera is that the exposure time can be set well below 1 µs which reduces the number of photons from the sky entering the lens. Due to these and other advantages, only image intensifiers are identified to be suitable for the CLCS.

6.3 Modifications of the laser system for further indoor laboratory tests

After the first tests confirmed that the laser beam can be photographed by cameras, modifications to the laser system were made. Figure 6.9 shows a schematic of the modifications. The following is a description of the laser telescope and fitted optics and is based on a non-published description provided by project partner Radiant Dyes Laser & Accessories GmbH from Wermelskirchen in Germany. The SpitLight 300 laser emits the wavelength λ=355 nm and small remains of the wavelengths λ=532 nm and λ=1,064 nm. The pulse energy of the original beam is 32.5 mJ at a Pockels cell delay of 220 µs. In the following it is described how with a special optics system (i) the undesired laser wavelengths are significantly attenuated and (ii) the output energy of the laser beam is reduced to 8.5 mJ (as was specified in project HeliBo after first laboratory tests): The laser beam first impinges on a harmonic separator (labelled #1, fixed at 45 ° angle) which has a high reflection (HR) of >99.5 % at λ=355 nm, a high transmission (HT) of >98 % at λ=532 nm and a HT of >99 % at λ=1,064 nm. Most of the rest of the wavelengths λ=532 nm and λ=1,064 nm are transmitted into a beam dump (labelled #1). The primary beam at λ=355 nm travels to a 30 % beam splitter where 70 % of the beam energy (i.e. photons) passes through and is dumped in a beam dump (labelled #2). The remaining 30 % of the beam energy (approximately 8.6 mJ) travel on and reach a second harmonic separator (labelled #2, fixed at 45 ° angle). With the use of a third harmonic separator (labelled #3, fixed at 45 ° angle), the laser beam again has the same direction as the original beam and now has an energy of 8.5 mJ. The beam then passes a waveplate, which is installed for changing the polarisation of the beam. After the waveplate, a lens with a focal distance of f=-60 mm expands the beams diameter to about 47 mm. A second lens, which has a focal distance of f=+500 mm collimates the beam. The divergence of the expanded, outgoing laser beam, was not measured.
Regarding laser safety, the occurrence of a hotspot within the laser beam can be very dangerous for the human eye. This problem is controlled with the 30 % beam splitter and the beam dump #2. The design foresees that a hotspot would destroy the coating of the beam splitter such that any subsequently emitted laser beams would either be absorbed by the burned coating or they would be transmitted into

a beam dump.

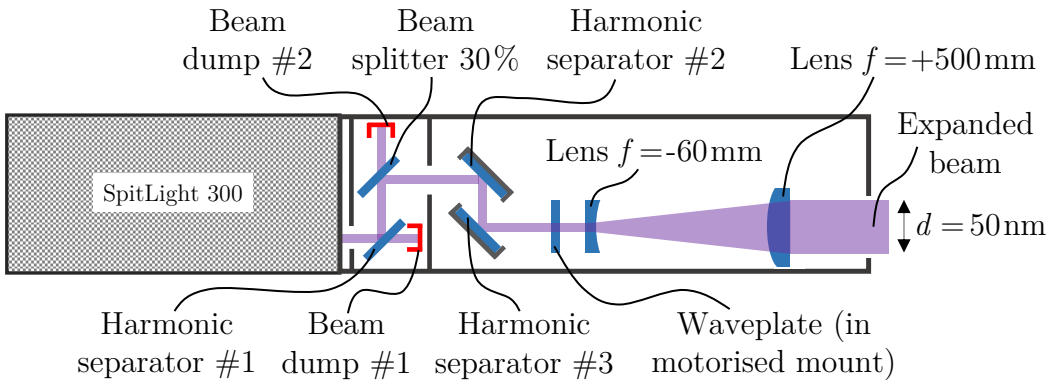

Figure 6.9: Technical drawing of the laser's telescope and its fitted optics based on design specifications from Solar-Institut Jülich. The harmonic separators have a HR at λ=355 nm, a HT at λ=532 nm and a HT at λ=1,064 nm. The drawing is based on a drawing that was provided by project partner Radiant Dyes Laser & Accessories GmbH from Wermelskirchen in Germany.

Figure 6.10 shows photos with details of the telescope attached to the SpitLight 300 laser.

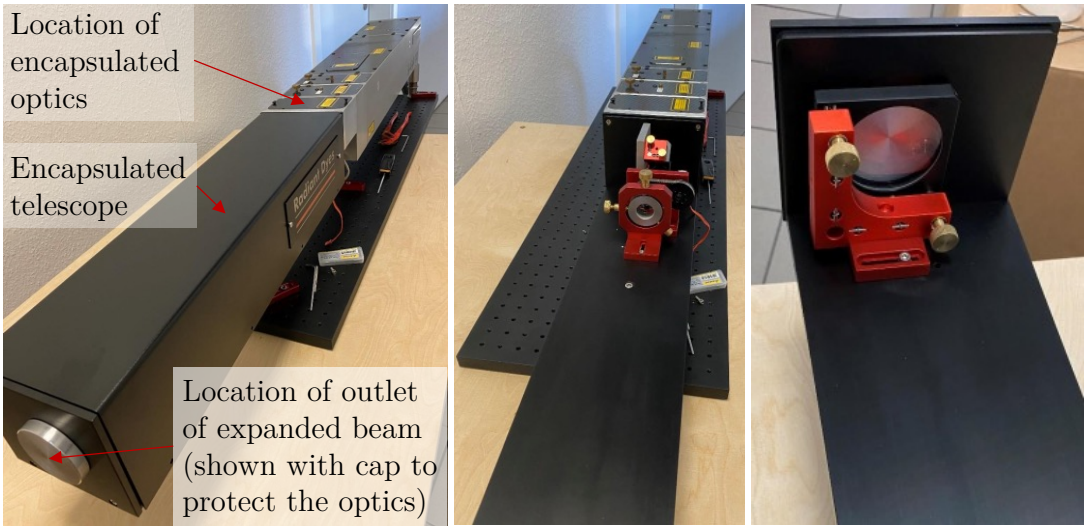

Figure 6.10: Three photos of the laser system showing (a) the beam outlet (closed with metal cap), (b) expansion optics and waveplate, and (c) collimation optics. The filter combination shown in Figure 6.9 is not shown in the photographs as they are encapsulated (the position is shown in image (a)). The photos were provided by project partner Radiant Dyes Laser & Accessories GmbH from Wermelskirchen in Germany.

A photo of the beam shape of the expanded beam is shown in Figure 6.11. The beam was emitted onto a white paper, whereby due to fluorescence the beam spot became visible to the human eye and an ordinary camera.

Figure 6.11: Beam shape of the laser system with a diameter of about 47 mm. The photo was provided by project partner Radiant Dyes Laser & Accessories GmbH from Wermelskirchen in Germany.

6.4 Investigation of a scattered laser beam's brightness

Parts of the content and results of section 6.4 are already pre-published by Sattler & Göttsche (2023) in a similar way and with modifications (Reproduced from Sattler & Göttsche (2023), with the permission of AIP Publishing).

The laser beam has a constant radiance (Sattler & Göttsche 2022, 2023). This means that a laser beam will appear constantly bright in an image over increasing distance, which is also what the calculation results from the general physical model of the CLCS predicted. A laboratory test at the Solar-Institut Jülich was conducted to assess if this can be verified with the laser system and the monochrome scientific camera. The monochrome scientific camera was set to a resolution of 348×260 Pixel and an exposure time of 1 µs. Images of the beam were taken from distances between about 0.9 and 10 m, whereby the horizontal laser beam was emitted onto an angled mirror such that its direction became vertical (the vertical beam was emitted into a beam dump). Images from the laser beam at different distances are presented in Figure 6.12. The images of Figure 6.12 imply that the grey value level of the laser beams is not greatly affected by changes in the distance.

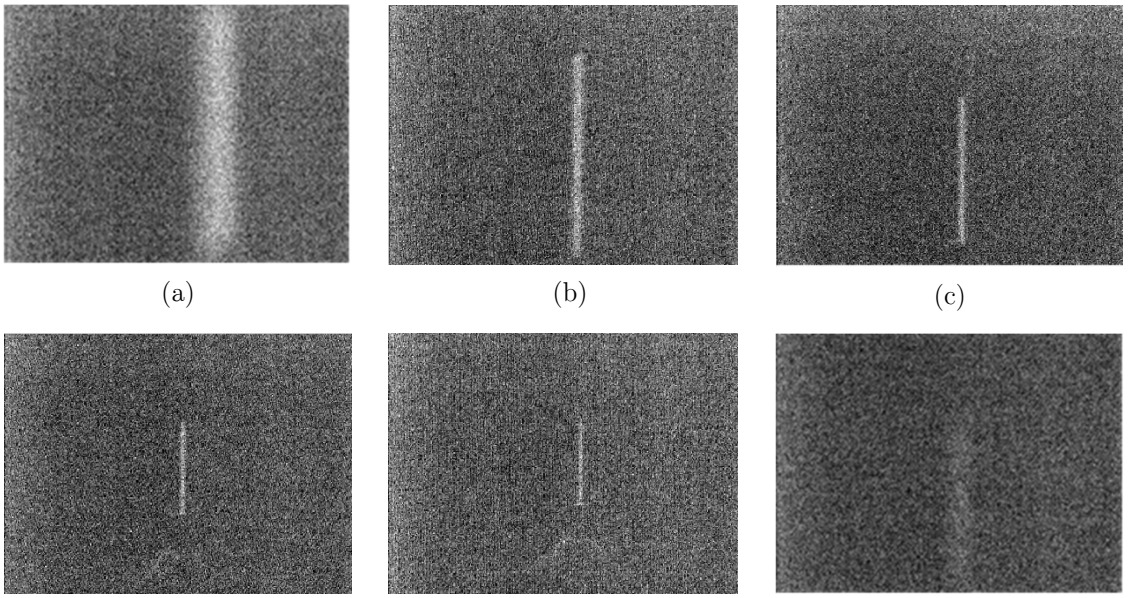

Figure 6.12: Images of laser beams emitted vertically, photographed with a scientific camera with interline CCD sensor in an indoor test. Distances between the camera and the laser beam of (a) 0.9 m, (b) 4.3 m, (c) 6 m, (d) 8.75 m, (e) 10.2 m, and (f) 6 m (bad focus). Reproduced from Sattler & Göttsche (2023), with the permission of AIP Publishing.

The images of the laser beams were then analysed in more detail to assess if, in practice, the grey value level of the beam changes with the distance. Table 6.2 shows the mean grey values of the laser beams in the images shown in Figure 6.12 (a) to (e) after the dark noise in the image was deducted. The analysis was carried out for the entire width and length of the laser beams. The overall tendency from the analysis was that the mean grey value levels reduce over the distance, which, of course, would have a negative impact regarding the CLCS. The reduction in the mean grey value was around 19 %. As in theory there should not be a reduction in the mean grey value along increasing distance, an attempt is made to explain this. It is likely that this has to do with the focal length setting of the lens, which may not have been suitably adjusted for the various distances (a suitable adjustment becomes more difficult especially when the beam becomes smaller in the image). Also, it becomes increasingly difficult to select the boundaries of a beam in the image analysis when the beam is only visible on a few pixels in width.

Another effect of an inadequate focal length setting for a lens with an ultra-narrow bandpass filter is described in the following. When using an ultra-narrow bandpass filter, there is, in particular, one important aspect to consider and that is the filter thickness and the material-dependent overall refractive index. The reason is that these cause an additional beam displacement due to refraction, which has an influence on the focus of the lens. In first laboratory tests, the lens's focus was set prior to fitting the filter. This led to strongly unfocused images from the laser beam with increasing distance. It was found that the focus of the camera lens needed to be significantly adjusted by turning the lens's mechanical focus ring by about 90° compared to when not using the optical filter. Figure 6.12 (f) shows an example of an unfocused image compared to the sharper focused image Figure 6.12 (c) at the same distance.

Table 6.2: Mean grey value of laser beam in images (a) to (e) after the deduction of the dark image noise.

Image	Mean grey value for full width of beam	Mean grey value reduction compared to (a) in [%]
(a)	24.7	100.0
(b)	23.4	94.6
(c)	21.6	87.3
(d)	20.0	81.2
(e)	22.0	88.9
		Reduction ca. 19 %

Table 6.2 also reveals that the mean grey value for the image shown in Figure 6.12 (a) is roughly 18.8 % lower than the mean grey value of the horizontal beam shown in Figure 6.4 (b) (the beams are at a similar distance away from the camera). The difference in the grey value can be explained from the reflectance of the used mirror at 355 nm being significantly lower than 100 % (for typical CSP mirror reflectance values see Figure 3.4 in section 3.1.3). The exact reflectance value of the used mirror, however, was not known as it was not required for the test described in this section.

6.5 Indoor laboratory tests with image intensifier camera

Parts of the content and results presented in section 6.5 are already pre-published by Sattler & Göttsche (2023) in a similar way.

As was written in section 6.2.4, only image intensifiers are properly suitable for the CLCS. For this reason, an image intensifier camera was procured for experiments. In the following, tests with the procured image intensifier camera in a fully dark laboratory are presented. In Figure 6.13 (a), the laser beam is strongly visible in the image and noise is completely insignificant. The beam was emitted vertically into a beam dump using a tilted mirror. As the reflectance at $\lambda = 355\,\text{nm}$ of the used mirror was unknown, the pulse energy of the beam is estimated to have been between around 5.0 mJ (assuming a mirror reflectance at of about 60 %) and 8.5 mJ (assuming a reflectance of 100 %). In Figure 6.13 (b), a zoom onto the same laser beam is shown. Clearly one can see that the image intensifier camera outperforms a scientific camera in terms of beam brightness and noise, delivering a very good contrast in the image. The triggering of the camera was also successfully tested with the 200 m coaxial cable.

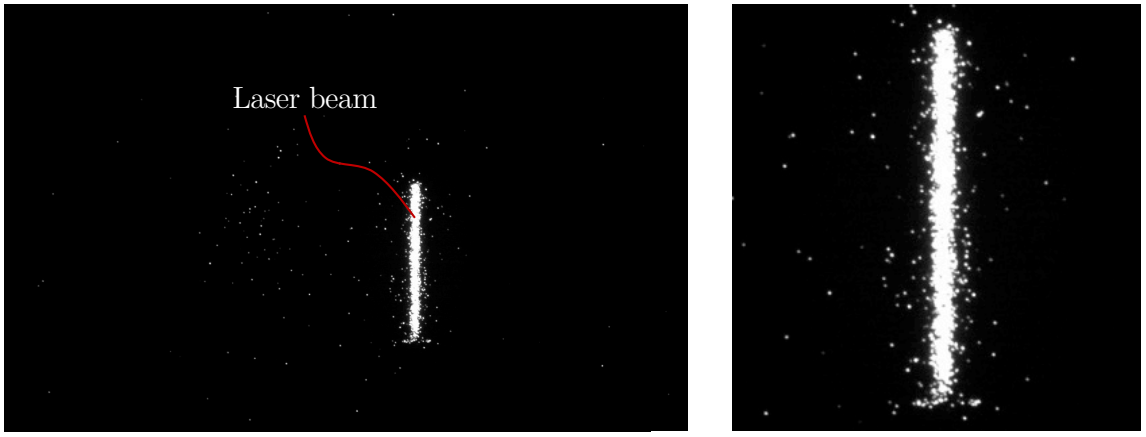

(a) (b)

Figure 6.13: Image of a laser beam emitted vertically, photographed with an image intensifier camera in an indoor test. (a) Photo of the laser beam with pulse energy between about 5.0 and 8.5 mJ in a dark laboratory, (b) Same laser beam shown in zoomed image.

As the laser beam is so clearly visible, the potential of the image intensifier camera to detect laser beams with pulse energies far lower than 8.5 mJ is high. Reducing the pulse energy as much as possible is highly desired for the CLCS in order to increase laser safety. Therefore, in a next step, it was investigated what the minimum impulse energy of the laser beam can be such that it can still be detected in an image in a dark laboratory environment. The pulse energy was reduced to about 0.5 mJ and the beam could also still be easily identified in the image as shown in Figure 6.14 (a). Figure 6.14 (b) shows a zoom onto the same laser beam. The true pulse energy after the reflection by the mirror may have been lower due to the likely reduced mirror reflectance at $\lambda = 355\,\mathrm{nm}$.

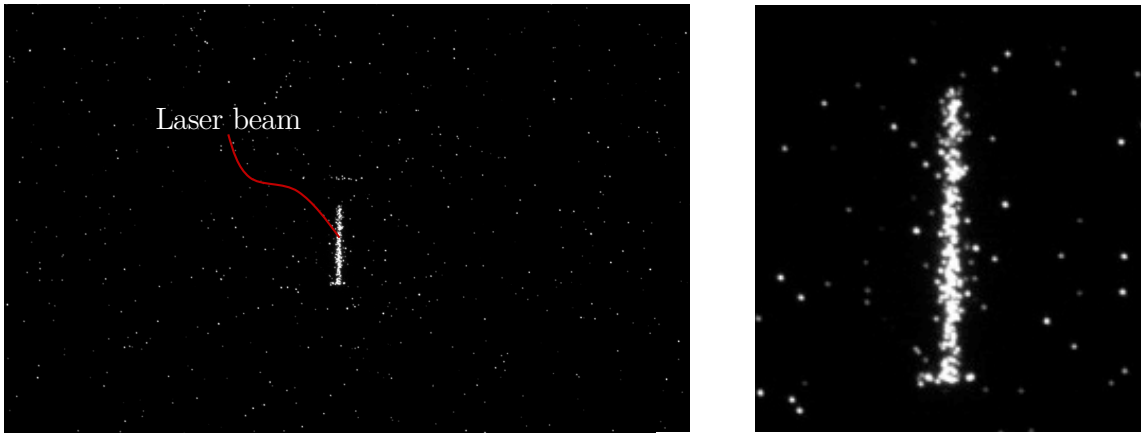

(a) (b)

Figure 6.14: Image of a laser beam emitted vertically, photographed with an image intensifier camera in an indoor test. (a) Photo of the laser beam with pulse energy of about 0.5 mJ in a dark laboratory. (b) Same laser beam shown in zoomed image.

The pulse energy was then further reduced to about 0.1 mJ as shown in Figure 6.15 (a). The beam can still be identified as a line. However, it should be noted that the conditions in the laboratory were ideal, i.e. there is no photon shot noise in the image. This will be different in outdoor conditions in daylight. In any case, having determined the capability of the image intensifier camera in the indoor environment was useful for upcoming outdoor tests. Figure 6.15 (b) shows a zoom onto the same laser beam. The true pulse energy after the reflection by the mirror may have been lower due to the likely reduced mirror reflectance at $\lambda = 355\,\mathrm{nm}$.

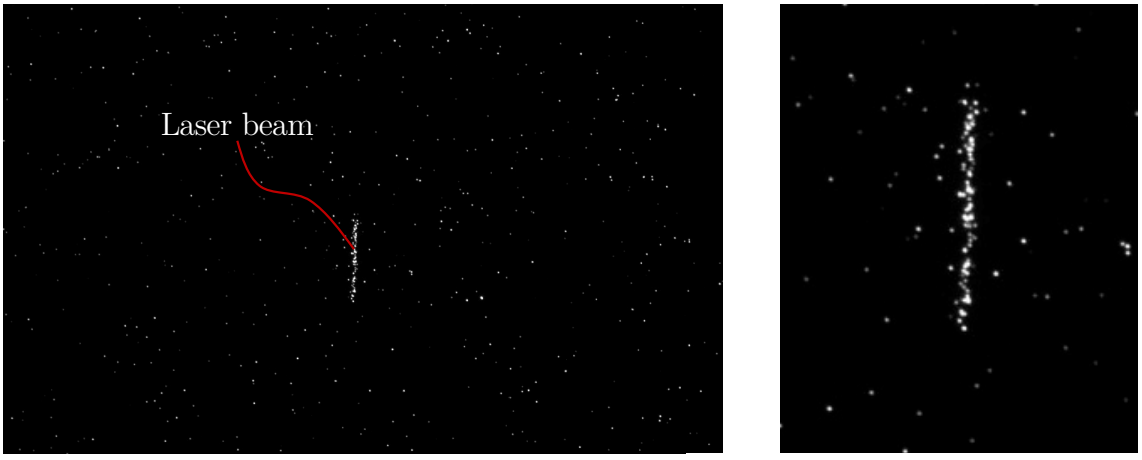

(a) (b)

Figure 6.15: Image of a laser beam emitted vertically, photographed with an image intensifier camera in an indoor test. (a) Photo of the laser beam with pulse energy of about 0.1 mJ in a dark laboratory. (b) Same laser beam shown in zoomed image (image (b) is reproduced from Sattler & Göttsche (2023), with the permission of AIP Publishing).

6.6 Outdoor test with image intensifier camera and image processing

In the following, the results of an outdoor test campaign as well as image processing with outdoor image data are presented. Parts of the description and results presented in section 6.6 are already pre-published by Sattler & Göttsche (2023) (Reproduced from Sattler & Göttsche (2023), with the permission of AIP Publishing).

For proving that the central laser and camera system can work in broad daylight an outdoor test became necessary. For the test to have significance, the desire was to emit the laser beam into the sky while taking an image of the laser beam from a longer distance. However, such a test campaign could not be realised at the Solar-Institut Jülich (SIJ) due to restrictions from the district council and air traffic control authorities because of laser safety, and therefore an alternative had to be found. A contact from the Karlsruhe Institute of Technology (KIT) offered the SIJ to connect the image intensifier camera to one of their lasers which was temporarily operational at the site of the German Meteorological Service (DWD) in Lindenberg, Germany, as part of the measurement campaign FESSTVaL (Field Experiment on Sub-mesoscale Spatio-Temporal Variability in Lindenberg). The laser from the KIT was from the same manufacturer as the laser used by the SIJ. The class 4 laser from the KIT had a beam diameter of 9 mm and emitted several wavelengths including the UV wavelength 355 nm. Although the laser beam diameter was far smaller than desired for the CLCS, the laser was found to be sufficiently suitable to demonstrate that

– in principle – the CLCS can work in broad daylight. The test was important for determining the minimum pulse energy that is needed while the beam is still visible in the photograph taken by the image intensifier camera during daylight conditions. For carrying out the tests, the image intensifier camera was placed up to 57 m away from the location of the laser, which was the furthest possible distance. The laser was located inside a container (the laser beam was emitted through an opening in the roof of the container).

The weather forecast predicted cloudy weather with spells of sunshine for the duration of the two-day test campaign. Although blue-sky conditions with strong sunshine was preferred, the predicted weather was sufficient for proving that the CLCS can work during daylight conditions (generally the summer of 2021 was very rainy in Germany so it was paramount to take the best available weather slot). The test setup required to connect the laser's flashlamp trigger output to a trigger input of the pulse/delay generator which, in turn, was used to trigger the image intensifier camera. Prior to the test campaign, the delay times of the image intensifier camera, the pulse/delay generator and coaxial cables of length 10 and 200 m had been measured with an oscilloscope as described before. In addition, the time needed for the scattered photons from the laser beams to arrive at the camera was calculated and included in the overall delay time set with the pulse/delay generator. Note: It was not possible to test the monochrome scientific camera as the requirement for carrying out tests was that the camera must be secured with an opto-isolator to prevent EM radiation reflections in the cables. Only the image intensifier camera could be tested as it is equipped with an opto-isolator on the used trigger input BNC connector.

Figure 6.16 (a) shows the container with the laser from the KIT and (b) the position of the container on the premises of the DWD. The container is not permanently installed at the site and is not shown on the satellite image. For this reason, the position is shown as orange rectangle. The blue dot is the position of the mobile phone of the author when the google maps screenshot was taken.

(a) (b)

Figure 6.16: Outdoor test site: (a) Photo of the container and the direction of the laser beam emission, (b) position of the laser on the site of the DWD. Map data for (b): Google, Imagery ©2021 GeoBasis-DE/BKG, Maxar Technologies, Map data ©2021 GeoBasis-DE/BKG (©2021).

Three campaigns with the camera were carried out over the course of two days, whereby the position of the setup was changed three times in order to photograph the laser beams from three different azimuth angles. The reason for this was to investigate the strength of the laser signal depending on different observation angles. The position of the laser as well as the three positions of the camera are shown in Figure 6.17. The maximum horizontal distance between the laser and the camera was about 57 m. Indicated by a blue dot, Figure 6.17 shows (a) the first camera position at about 52 m distance, (b) the second camera position at about 57 m distance, and (c) the third camera position at about 53 m horizontal distance from the location of the laser. Image (d) shows that the angle between positions (a) and (c) is about 56°. Images taken from position 1 will be presented on the following pages.

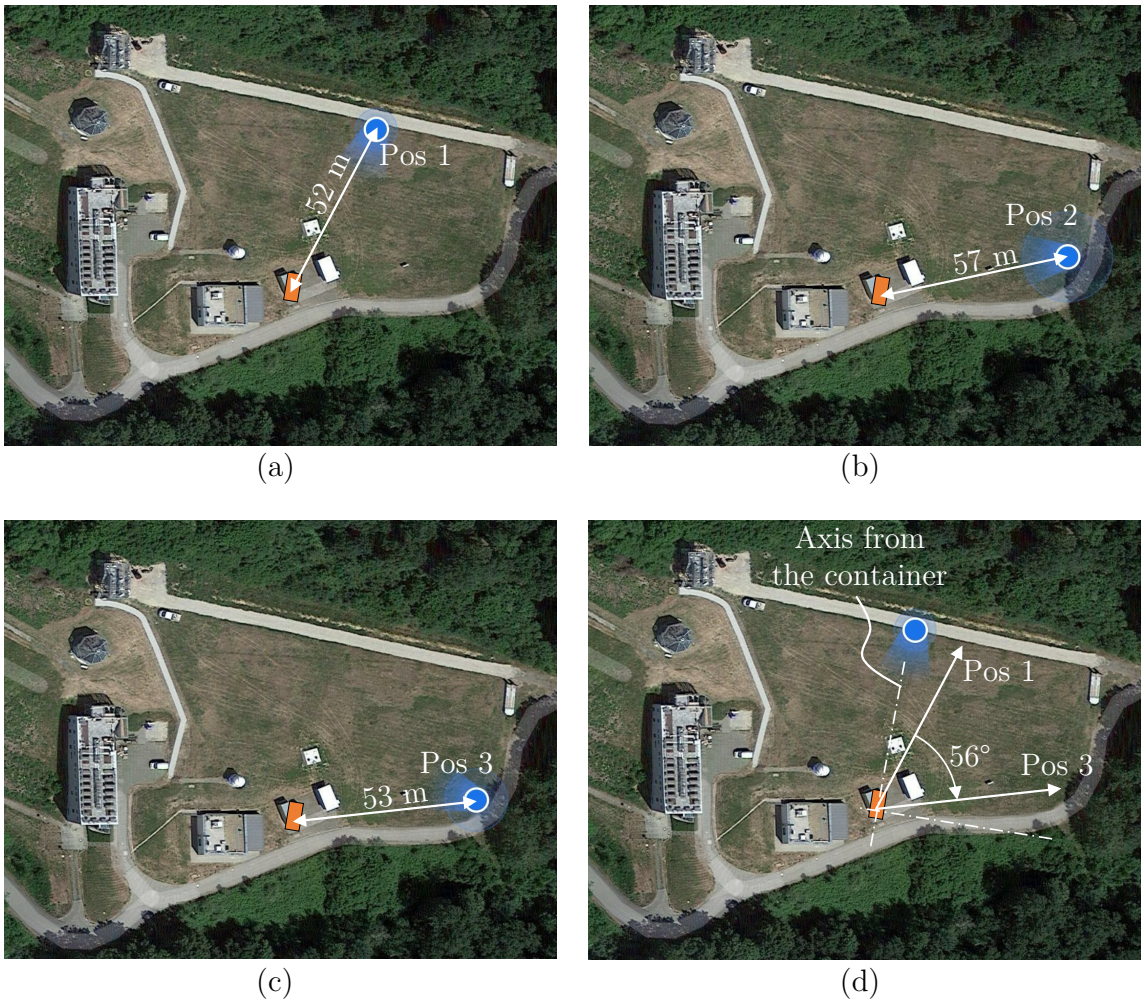

(a) (b) (c) (d)

Figure 6.17: Position of the laser and three positions of the image intensifier camera during the test campaign: (a) first camera position at about 52 m distance, (b) second camera position at about 57 m distance, and (c) third camera position at about 53 m horizontal distance from the location of the laser. Image (d) shows that the angle between positions (a) and (c) is about 56°. Map data: Google, Imagery ©2021 GeoBasis-DE/BKG, Maxar Technologies, Map data ©2021 GeoBasis-DE/BKG (©2021).

The camera was oriented towards the container and tilted upwards into the sky such that the actual distance between the laser beam and the camera was therefore about 50 and 80 m. The image intensifier camera shown in Figure 6.18 was placed near the ground. Regarding triggering the image intensifier camera, the 200 m coaxial cable was connected to the pulse/delay generator. The exposure time (gating) of the image intensifier camera was set to 100 ns. Two different camera lenses were tested, one with focal length $f = 25$ mm and the other with $f = 78$ mm. In front of the lens, an ultra-narrow bandpass filter with FWHM of <1.2 nm was attached. The laser beam pulse energy was about 5.5 mJ but it was also reduced to lower values for a few minutes on request of the author for taking photographs at other pulse energies. Most of the time the weather was cloudy and windy, but there were times when the sun came through with patches of blue sky. For the tests for camera positions 1 to 3 shown on the following pages, the camera was set into 8-bit mode which means that a fully white pixel has a greyscale value of 255 and a fully black pixel has a greyscale value of 0. The 8-bit mode was preferred over the 12-bit mode as according to the manufacturer the 8-bit mode setting results in less noise in an image.

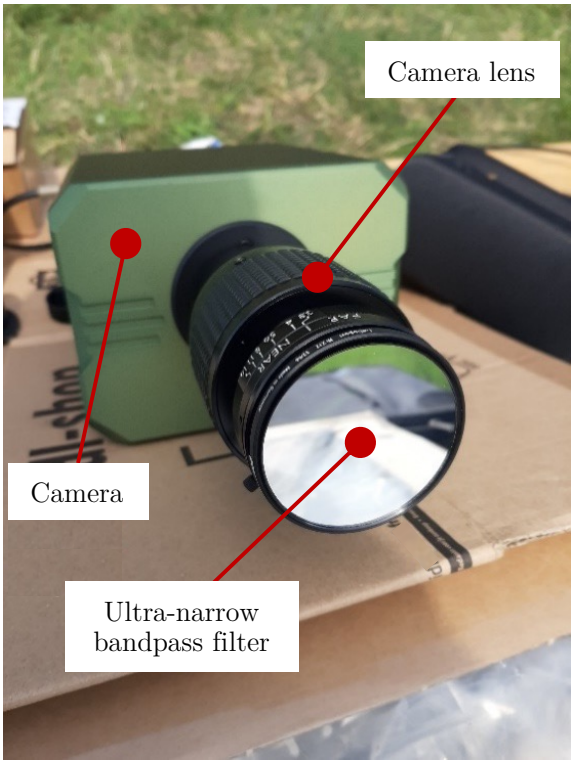

Figure 6.18: Image intensifier camera setup with camera lens ($f = 78$ mm) and ultra-narrow bandpass filter. Reproduced from Sattler & Göttsche (2023), with the permission of AIP Publishing (with a minor modification). Photograph: © Solar-Institut Jülich.

Images taken from position 1:
First the camera lens with focal length $f = 25$ mm was used. For this lens at a distance of 52 m, the photographed scenery had a width and height of about $h_v = 14$ m and

$h_h = 22.5\,\text{m}$, respectively. Figure 6.19 shows four images of a laser beam with pulse energy of about 5.5 mJ taken with the image intensifier camera with $f = 25\,\text{mm}$ camera lens and ultra-narrow bandpass filter. Image (a) is the original image without image processing, (b) the image after salt and pepper noise removal, (c) the image after a histogram manipulation method is applied where grey values <255 are set to 0 (fully black) (cf. section on *Image enhancement* in section 4.6), and (d) the image after a histogram manipulation method is applied as well as additional salt and pepper noise removal. The noise present in image (a) is primarily photon shot noise as with image intensifier cameras the other type noises do not play a significant role. One characteristic that is strongly noticed with the camera lens is that noise is greatest in the centre and reduces towards the edges of the image. The laser beam is cut off at the bottom and at the top of the image. The reason for that is the blue shift of the ultra-narrow bandpass filter at wider view angles. The vertical AFOV for the camera system without optical filter is about 16° (calculated using equation 4.9), but due to the used ultra-narrow bandpass filter, the AFOV is reduced to about 7.6°. This means that the f=25 mm camera lens is not perfectly matched with the used ultra-narrow bandpass filter, but this was already known and expected prior to the outdoor test. However, choosing an ultra-narrow bandpass filter with a wider FWHM leads to a wider AFOV, which increases the shot noise in the image unless the exposure time is proportionally reduced too.

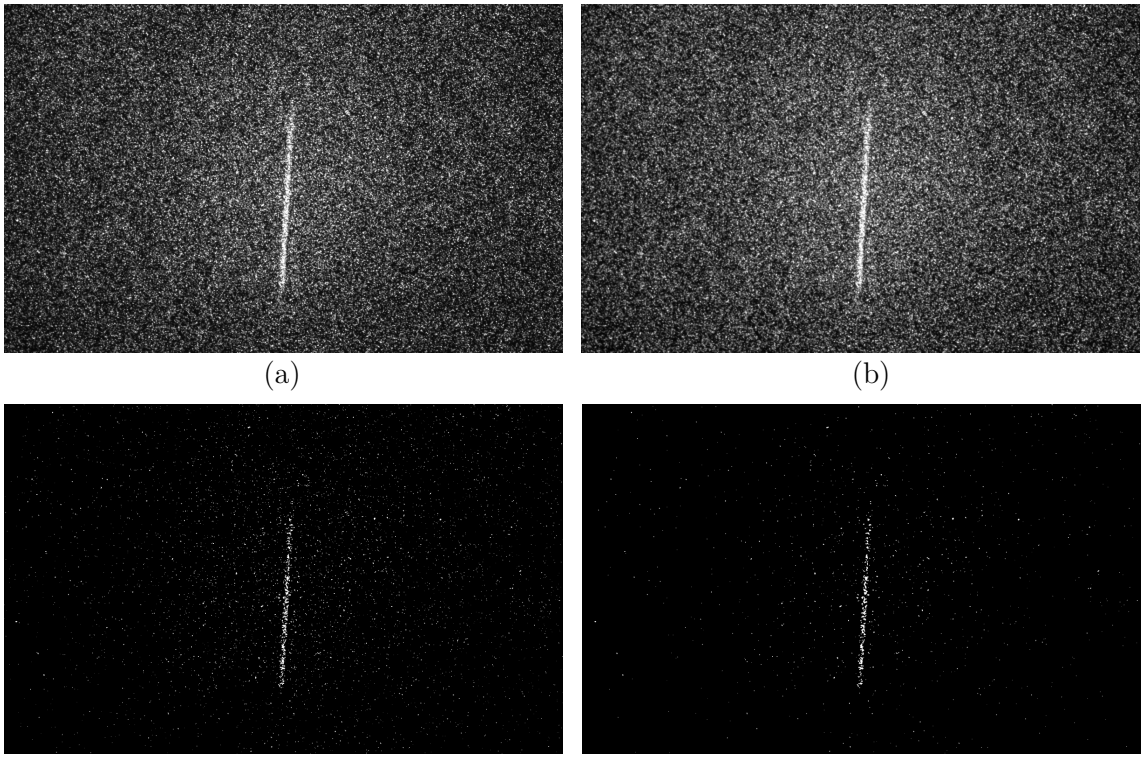

(a) (b)

(c) (d)

Figure 6.19: Images of a laser beam with pulse energy of about 5.5 mJ taken with the image intensifier camera with f=25 mm camera lens and ultra-narrow bandpass filter. (a) Image without image processing, (b) Image after salt and pepper noise removal, (c) Image after a histogram manipulation method is applied and (d) Image after a histogram manipulation method is applied as well as additional salt and pepper noise removal.

In a second round of tests, the camera lens was exchanged for the f=78 mm camera lens. With the f=78 mm camera lens at a distance of about 52 m, the photographed scenery has a width of w = 4.5 m and and height of h = 7.2 m, respectively (considerably less than the f=25 mm camera lens). Figure 6.20 shows four images of a laser beam with pulse energy of about 5.5 mJ taken with the image intensifier camera with f = 78 mm camera lens and ultra-narrow bandpass filter. Image (a) is the original image without image processing, (b) the image after salt and pepper noise removal, (c) the image after a histogram manipulation method is applied where grey values <255 are set to 0 (fully black) (cf. section on *Image enhancement* in section 4.6), and (d) the image after a histogram manipulation method is applied as well as additional salt and pepper noise removal. The laser beam is fully visible in the image as now the blue shift of the ultra-narrow bandpass filter is no longer a restriction.

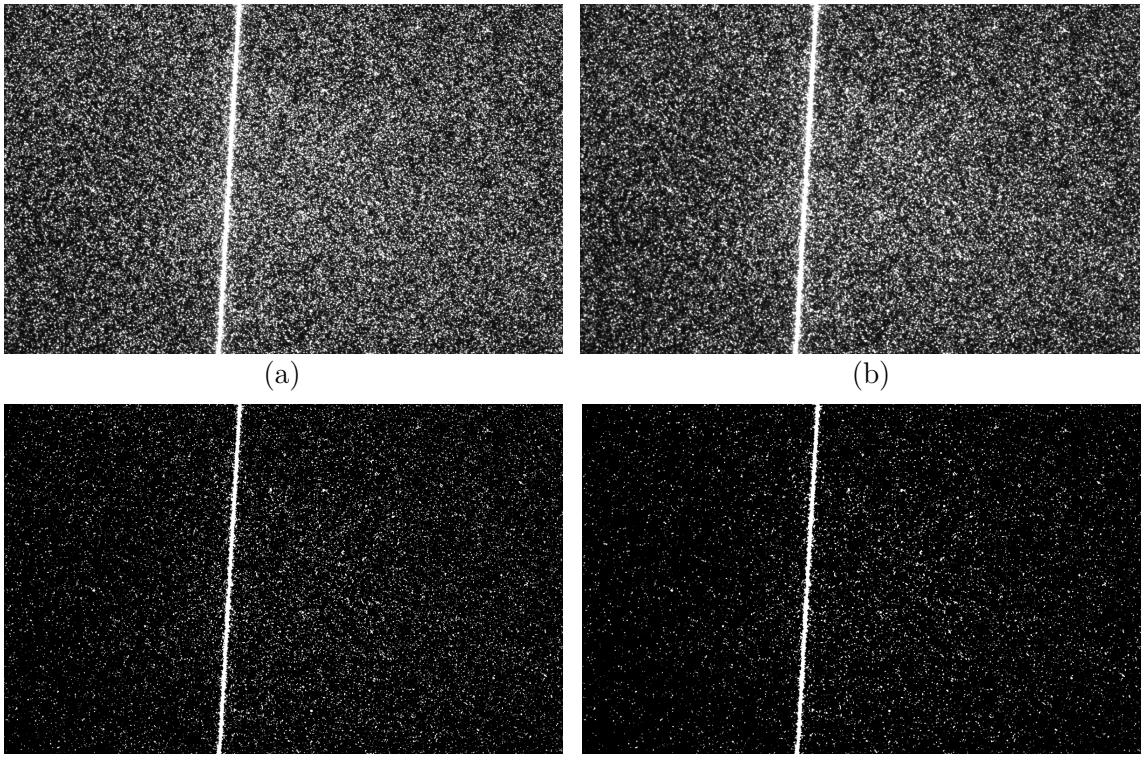

Figure 6.20: Images of a laser beam with pulse energy of about 5.5 mJ taken with the image intensifier camera with f=78 mm camera lens and ultra-narrow bandpass filter. (a) Image without image processing, (b) Image after salt and pepper noise removal, (c) Image after a histogram manipulation method is applied and (d) Image after the histogram manipulation method is applied as well as additional salt and pepper noise removal.

When the laser was set to about 1.3 mJ, the beam was still easily visible in the image as shown in Figure 6.21.

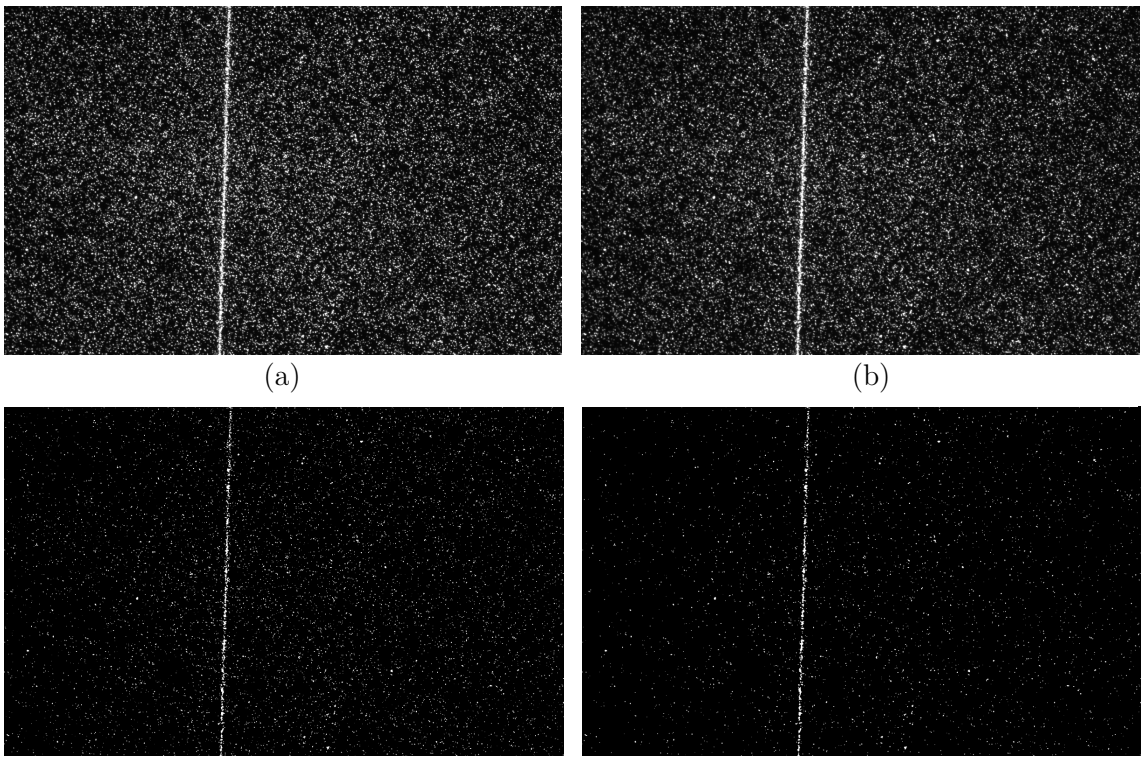

Figure 6.21: Images of a laser beam with pulse energy of about 1.3 mJ taken with the image intensifier camera with f=78 mm camera lens and ultra-narrow bandpass filter. (a) Image without image processing, (b) Image after salt and pepper noise removal, (c) Image after the histogram manipulation method is applied and (d) Image after a histogram manipulation method is applied as well as additional salt and pepper noise removal.

When the laser was set to an even lower pulse energy of about 0.5 mJ, the beam was barely visible in the image as shown in Figure 6.21.

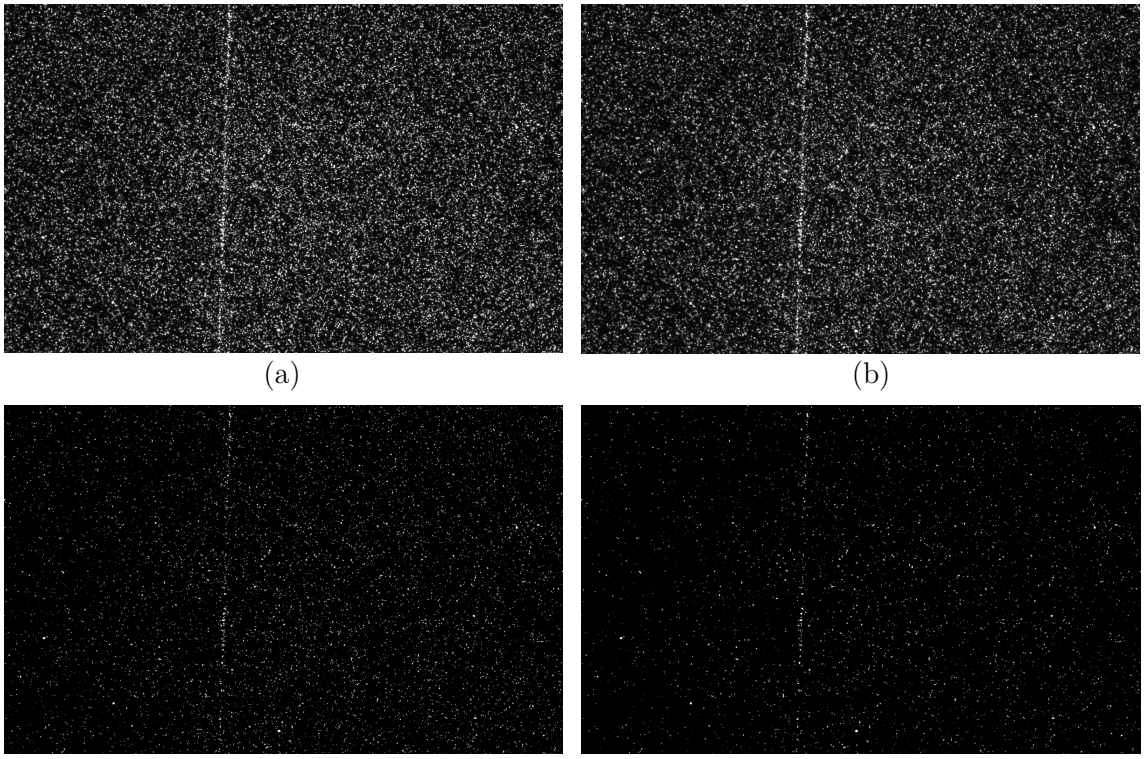

(a) (b) (c) (d)

Figure 6.22: Images of a laser beam with pulse energy of about 0.5 mJ taken with the image intensifier camera with f=78 mm camera lens and ultra-narrow bandpass filter. (a) Image without image processing, (b) Image after salt and pepper noise removal, (c) Image after the histogram manipulation method is applied and (d) Image after a histogram manipulation method is applied as well as additional salt and pepper noise removal.

Images of the laser beam were also taken from positions 2 and 3 at the DWD site. Generally, the beam could be captured from all positions. One important aspect to note here is that the view angle onto the beam was always such that the scattering angle of the beam towards the camera was greater than 90°. Hence, unless there were high particle concentrations suspended in the air, the contribution from Mie scattering may have been insignificant, i.e. Rayleigh scattering from molecules is likely to have been dominant.

Image processing for images from outdoor test

As presented in chapter 4, there are two prominent algorithms for detecting lines in an image that are widely applied, namely the Hough transform as well as the Radon transform. In this work, the Radon transform was chosen due to two reasons: it is suitable for (1) non-binary images (which means any range of greyscale values in images) and (2) images that contain a lot of noise. In this work, the output of the Radon transform was evaluated using a weighing function such that an angle of a wider line spreading across many pixels in width can be calculated at a high accuracy

(without the weighing function the accuracy would be lower as more potential lines would be detected). A line detected by the Radon transform is described by the two main parameters θ and x'. The parameter θ denotes the angle of the rotation about the centre of the image between 0 and 180° whereby the actual detected line runs along the angle $\theta_{\mathrm{i}} = \theta - 90°$. The parameter x' denotes the distance of the image centre to the detected line perpendicular to the rotated x-axis at angle θ_{i}. The weighing function for the parameter θ is given with equations 6.1 to 6.3 below. Equation 6.1 is used to find the peak or centre from the θ distribution:

$$R(\theta) = \max\{R(\theta,x')\} \tag{6.1}$$

where $R(\theta,x')$ is the Radon output matrix with the bin count values of θ and x', $R(\theta)$ is the vector with the maximum θ count values. Equation 6.2 is used to select a lower boundary bin count value near the peak so that a desired larger range of values of θ with high counts near the peak count value are also included in the weighing function:

$$R'(\theta) = wf \cdot \max\{R(\theta)\} \tag{6.2}$$

where $R'(\theta)$ is the boundary count value and wf is a factor between 0 and 1 (one can test various values between 0 and 1 for the weighing function and select a suitable value for wf). The weighing function is given with equation 6.3:

$$\theta_{\mathrm{weighed}} = \frac{\sum_{j=p}^{q} \theta_j \cdot (R_j(\theta) - R'(\theta))}{\sum_{j=p}^{q} (R_j(\theta) - R'(\theta))} \tag{6.3}$$

where $\theta_{\mathrm{weighed}}$ is the weighed value of θ and θ_j $\{\theta_j\colon p \leq j \leq q\ \}$ is the partial array containing the values of θ for which $R(\theta) - R'(\theta) > 0$. The same type weighing method is also applied for finding the weighed value of x'.

In the following, an example for the line detection in an image with a laser beam, pre-published by Sattler & Göttsche (2023), is shown (Reproduced from Sattler & Göttsche (2023), with the permission of AIP Publishing). Figure 6.23 (a) shows a photographed laser beam (the pulse energy was about 0.7 mJ) in an image from the outdoor test carried out at the site of the DWD. For the image processing, in a first step, a noise reduction filter for removing so-called salt and pepper noise

was applied. Figure 6.23 (b) shows that the Radon transform detected a peak at the rotation angle θ=175.4416° (the angle step for the rotation was 0.005° and the weighing function was used to increase the accuracy of the result) and Figure 6.23 (d) shows the detected distance x' of the line from the image centre. Figure 6.23 (c) shows a magenta line marking the detected line of the laser beam at the angle θ_i from the x-axis in the image (white coordinate system with x-axis and y-axis). The coordinate system of the Radon transform (x'-axis and y'-axis) is shown in yellow colour. The line crossing the x'-axis was detected at $x' = 82.9091$ pixels from the centre of the image. The presented descriptions on the Radon transform are based on knowledge acquired from the MATLAB® Image Processing Toolbox documentation (see MathWorks® (2021a) and MathWorks® (2021b)).

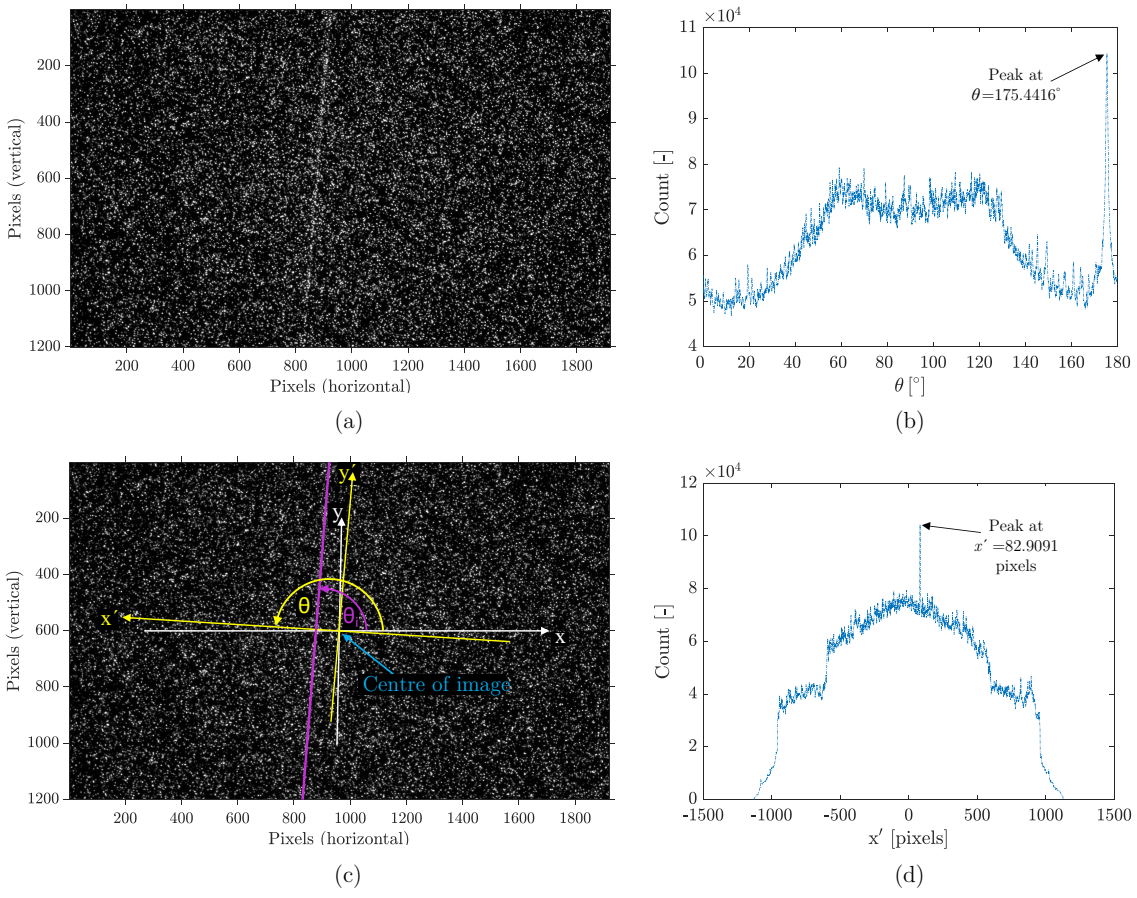

Figure 6.23: Photograph showing an image of a laser beam (the pulse energy was about 0.7 mJ) and the results of the Radon transform for detecting the angle θ and x'. Reproduced from Sattler & Göttsche (2023), with the permission of AIP Publishing.

A simulation study was carried out, which had the aim to assess the potential line detection accuracy for the CLCS (for the CLCS the aim is to realise the detection of a line with an accuracy of 0.1 mrad). For the study, a laser beam from an image taken at the DWD was extracted and rotated in an image of the sky containing

shot noise but not a beam. The laser beam shown in the image had a pulse energy of about 1 mJ. The result of the study was that the line detection accuracy (i.e. the measurement accuracy) was between about 0.05 and 0.9 mrad while the average was about 0.37 mrad (Sattler & Göttsche 2023). The angle step for the rotation was 0.005° (i.e. 0.0873 mrad and the weighing factor wf was 0.95). The details of this simulation study are shown in Table A.9 in the appendix. The study was also carried out by applying the previously described histogram manipulation filter method of setting those pixel values to 0 that are between 0 and 254 in greyscale value. This method showed no improvement with respect to the average line detection accuracy with the result also being 0.37 mrad. Hence, these results suggest that the use of noise removal algorithms may just slow down the image processing without a prospect to improve the result. The details of the second simulation study after histogram manipulation are shown in Table A.10 in the appendix.

Image noise from the diffuse solar irradiance has a strong influence on the accuracy of the beam detection and the more diffuse solar irradiance is present (i.e. brighter the sky), the more noise an image will contain (more noise reduces the line detection accuracy). When the test campaign was carried out, it was sunny but clouds were present most of the time (the weather conditions were varying strongly) and only for a short moment of time there was a blue sky background. One possibility to reduce noise in an image is to reduce the exposure time of the image intensifier camera (e.g. from 100 ns, which was used for the test campaign at the DWD site, down to, for example, 50 ns). Due to jitter (i.e. varying time delays) from the main CLCS components, a very short exposure time could, in the worst case, lead to components no longer being synchronised. In the test campaign, the camera settings were not yet optimised as prior to the test period there was not sufficient time for thorough tests. This means that there is still potential for reducing noise with optimised settings. (Sattler & Göttsche 2023)

The speed of the Radon transform calculations can be slow if very small angle steps are used (also, of course, it depends on the computer that is being used). To tackle this issue, a two-step analysis method could be applied where first coarse angle steps are applied to detect the approximate angle of the line, followed by small angle steps around a small angle of rotation where the line was first detected. (Sattler & Göttsche 2023)

7 Comparison of Calibration Methods

In this chapter, a simplified overview of the advantages and disadvantages of the calibration methods (i.e. calibration systems) of the classes A to D is given (see chapter 2 for the descriptions of the various calibration methods). Parts of this chapter are a short summary of a pre-published paper by Sattler et al. (2020). Serving as a quick reference, Figure 7.1 shows a compact overview of the calibration system illustrations that were already presented in chapter 2.

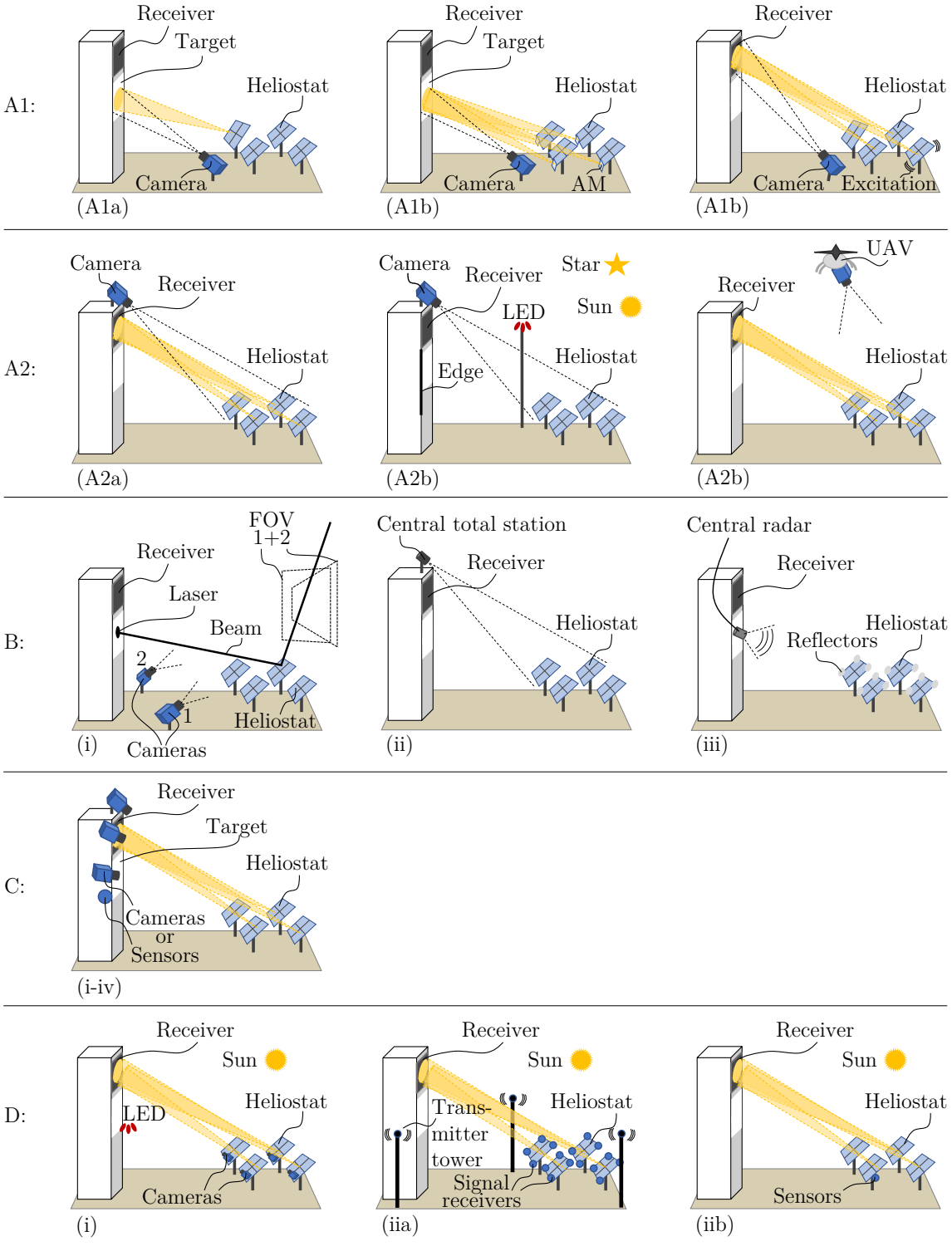

Figure 7.1: Compact overview of the calibration methods presented in chapter 2 (based on illustrations from Röger et al. (2018) and Sattler et al. (2020)).

7.1 Advantages and disadvantages of Class A to D calibration methods

Advantages and disadvantages of Class A calibration methods:
Class A1a: The class A1a is the state-of-the-art camera-target method which is widely deployed in CRS worldwide. This method allows a fine calibration of heliostats at an accuracy of about 0.1 mrad, but there are several disadvantages associated with this method. For a calibration, the heliostats must be moved out of the receiver focus onto a calibration target sequentially, which means that a calibration of a heliostat field consisting of tens of thousands of heliostats will take a considerable amount of time. A main problem is the calibration of heliostats that have a lower quality in precision because once they are calibrated and moved back into normal tracking mode, then its orientation can once again be inaccurate. (Sattler et al. 2020)

Class A1b: The methods of class A1b are heliostat excitation methods which use signal beams that allow the identification of individual heliostats. The advantage of these methods is that they allow the parallel calibration of heliostats as long as the individual heliostat signal beams can be distinguished from one another. The calibration accuracy can be very high (estimated at 0.2 mrad) allowing fine calibration. The disadvantage of using small auxiliary mirrors is that the contrast on the calibration target is low, which means that it is difficult to identify their sun spots. One disadvantage associated with mirror excitation can be an effective image broadening (depending on the amplitude). (Sattler et al. 2020)

Class A2a: The calibration methods of class A2a foresee the capturing of single or multiple photographs (photogrammetry) using a central camera on a mast/tower or a camera on an UAV. Advantages: An advantage of these calibration methods is that they work without needing to reflect sunlight and do not use a calibration target. Disadvantages: A disadvantage for methods with central cameras is that it is difficult to measure the orientation of a heliostat when it is oriented at an extreme angle. Regarding image processing, the detection of heliostats can be affected by reflections from the ground as well as small elevation angles of heliostats. Furthermore, distant heliostats may not be photographed with adequate lens zoom, which leads to a lower measurement accuracy. The image quality can also be affected by atmospheric attenuation and flickering. Most class A2a calibration methods have a measurement accuracy ranging from around 2 to 10 mrad. (Sattler et al. 2020)

Class A2b: The calibration methods of class A2b use a reflected image of an object, which can, for example, be an LED, the sun, the sun's brightness or a star. Advantages: When the object is photographed more than once such that it is visible in various mirror facet locations, then several normal vectors can be obtained and the

measurement accuracy increased. Most class A2b calibration methods have a higher measurement accuracy ranging from around 0.1 to <1.5 mrad. Disadvantages: As the reflection of an object in the mirror must always be seen by the camera, there may be measurement limitations for certain heliostat orientations. Also, if the object is a star or if an UAV is used, then closed-loop control is not possible. (Sattler et al. 2020)

Many of the class A2a and A2b methods are estimated to have measurement speeds in the order of around 1 s either when measuring groups of heliostats or individual heliostats sequentially. Very fast methods are those with a central camera on a tower or mast, which give an almost instantaneous result from image processing, while the heliostats can stay in tracking mode. The use of an UAV for the calibration of heliostats has a disadvantage if the tracking of the heliostat field must be paused for the duration of the flight. (Sattler et al. 2020)

Advantages and disadvantages of Class B calibration methods:
The calibration methods of class B have the lowest development status from all classes.

The detailed advantages and disadvantages of the CLCS are discussed as part of this thesis. The basic advantages of the CLCS are that it does not require any parts installed on heliostats, that it does not require the sun for calibration measurements (a calibration during the night is also possible) and that the main components are placed in central positions. Moreover, compared with the state-of-the-art camera-target method, the CLCS can potentially be operated at a far higher measurement speed of up to 300 times faster when the orientation of a heliostat is measured using only a single mirror facet (assuming a measurement rate of 10 Hz, i.e. 10 heliostats measured per second, and that the camera-target method takes 30 seconds for the calibration of a single heliostat). For achieving a higher measurement accuracy, the orientation of multiple mirror facets per heliostat can be measured from which an overall heliostat orientation can be computed. The disadvantages are that the CLCS is a sequential measurement method and that the topic laser safety needs a very thorough assessment. (Sattler et al. 2020)
More details on the advantages and disadvantages of the CLCS are presented in chapter 8.

The central laser scanner and central radar methods were both tested in a heliostat field but have not been investigated further. Their advantages are that the measurement device is at a central position and that these methods do not require the sun for calibration measurements. The disadvantages are that their measurement speeds in the current state of progress are relatively slow and only groups of heliostats can be measured at a time. For both methods to be practical it is necessary to install

reflectors on the heliostats. The accuracies of these methods are estimated to be around 2 mrad for the devices used in the tests (better accuracies can probably be obtained nowadays). (Sattler et al. 2020)

The calibration method using a total station is a concept which requires the installation of at least three prisms on each heliostat. The advantages of this concept method are that the measurement device is in a central position, it is relatively easy to install, and that this method does not require the sun for calibration measurements. Disadvantages are that the installation of the prisms is thought to be very time consuming and that the entrance angle into the prisms is limited. No estimation for the measurement speed was given. (Sattler et al. 2020)

Advantages and disadvantages of Class C calibration methods:
The class C calibration methods have cameras or sensors either around, in front or within the receiver. One method foresees the use a calibration target beneath the receiver consisting of cameras or sensors. Their general advantages are their estimated high measurement accuracy of $\leq$0.3 mrad and their high measurement speeds with OCS capability. (Sattler et al. 2020)

Several cameras or sensors around the receiver:
The advantages for these methods are that cameras are standard components which can be installed easily and the cameras have the entire heliostat field in their field of view such that all heliostats can be calibrated simultaneously. Furthermore, the heliostats do not need to be equipped with any hardware. Methods which use sensors around the receiver also have the advantage that sensors are standard components which should allow a fairly easy installation. But there are also disadvantages with some of the calibration methods. For some of the methods, a signalisation will be necessary such that heliostats can be distinguished from one another and the software development may be complex. Additional hardware such as piezo-electric actuators for realising a signalisation via vibration of a heliostat's mirror surface (beam excitation) increases investment costs. For some calibration methods it can be difficult to access the cameras or sensors atop of the tower for maintenance. For those calibration methods where cameras or sensors are subject to moderate to high solar irradiance flux density, it may be difficult to handle the cooling and also expensive camera systems may be required. (Sattler et al. 2020)

Several cameras embedded in the receiver:
The advantages are that if camera obscuras are installed in the receiver then no technical problems are to be expected and very detailed receiver flux density maps can be recorded. The disadvantages are that it may be difficult to accommodate (install) and access the cameras in the receiver, the camera design might be large

and also, due to the high solar irradiance flux density, the cooling may be complex and the camera system expensive. (Sattler et al. 2020)

Camera array on moving bar moved along the receiver:
The advantage of this method is that an entire heliostat field can be calibrated with one sweep along the surface of the receiver. The disadvantages may be the maintenance of the cameras (access), concentrated solar irradiance is blocked during a sweep and due to the high solar irradiance flux density the cooling may be complex and camera system expensive. Moreover, movements of the heliostats due to wind gusts may be a disadvantage as this could impact the measurement accuracy. (Sattler et al. 2020)

Camera array or sensor array as target:
One method foresees the use of an array of cameras or sensors as target. The advantage is that this calibration method may be both very fast and accurate. Indirect closed-loop tracking control can be realised. The disadvantages are the need to install small auxiliary mirrors on each heliostat, signalisation becomes necessary if sensors are used as target and the orientation of individual mirrors cannot be determined (only that of the auxiliary mirror). Moreover, the maintenance of the cameras or sensors may not be easy to carry out. (Sattler et al. 2020)

Advantages and disadvantages of Class D calibration methods:
Class D methods foresee that cameras or sensors are mounted to heliostats. There are several advantages associated with these methods which are as follows. Cameras or sensors are typically mass-produced, low-cost products which can easily be installed on heliostats. There are typically several options regarding reference objects for cameras (e.g. the sun) and the image processing is very fast such that these calibration methods allow a quasi-realtime orientation detection for each individual heliostat independently. It is generally possible to retrofit the heliostats of a heliostat field with cameras or sensors. With less than 1 second (estimated) the measurement speed is very fast. For most of these calibration methods the measurement accuracy is below 1 mrad. The disadvantages of class D methods with cameras are that the cameras may need recalibration once in a while, that dust settlement could require periodic cleaning, that it is not possible to measure the orientation of individual facets unless each facet is equipped with a camera, that the specific cost of calibration system depends on the size of the heliostat and the measurement accuracy depends on the resolution of the sensor as well as the quality of the image processing code. (Sattler et al. 2020)

Key data for selected calibration methods:
The key data for selected calibration methods for classes A to D is given in several tables in Sattler et al. (2020). In this publication, altogether 13 characteristics are covered in the categories *signal chain coverage*, *measurement process*, *possible applications* as well as *operational requirements and limits*.

7.2 Summary of the key characteristics of selected calibration systems

Each calibration method has advantages and disadvantages which have been described in this chapter and are found, in more detail and with more examples, in Sattler et al. (2020). A ranking of heliostat field calibration systems cannot be made as choosing a suitable calibration system for a CRS depends on various boundary conditions (e.g. number of heliostats, size of heliostats, heliostat tracking quality, technology preference of operator, type of receiver, etc.). For example, if a heliostat is designed and manufactured well and has a good tracking accuracy, then there may not be a need for a calibration system with OCS capability if a regular (fine) calibration once every few hours for each heliostat is sufficient.

When specifically comparing the CLCS with all the other existing calibration methods, there is one characteristic that none of the other methods have: the potential ability to indirectly measure the orientation of all mirror facets from a central position without needing the sun, receiver or any objects as reference and without interfering with the sun tracking of the heliostats. The CLCS can be operated in two ways: (1) A single measurement of just one mirror facet per heliostat allows a quicker measurement of the heliostat orientation, and (2) the orientation of multiple mirror facets can be measured in order to obtain more exact data of a heliostat's overall orientation (Sattler & Göttsche 2023). The latter multiple measurements could be affected by heliostat movement, for example in the event of wind gusts during measurements.

8 Conclusion and Outlook

8.1 Conclusion

The general feasibility of the CLCS method could be demonstrated in theory as well as in confined, shielded and secured tests. The most significant conclusions are summarised below:

It can be concluded that for an optimal operation of the CLCS, the laser wavelength needs to be in the short wavelength range (best UV-A) because, on the one hand, Rayleigh scattering from air molecules is more dominant and results in a stronger scattering signal over a wider scattering angle compared to Mie scattering. On the other hand, Rayleigh scattering from air molecules is constantly efficient unlike Mie scattering from particles, which not only fluctuates strongly depending on the current particle concentration and size distribution, but it is also strongly forward directed (cf. chapter 6). Mie scattering can contribute to the scattering of photons towards the camera, but it depends strongly on whether there is a high-dust event and on the scattering angle of the beam and the position of the camera. Own data evaluation using particle data for the location Jülich showed that the concentrations are highly fluctuating from low to high concentrations. For the location of Jülich (and probably Germany altogether), the contribution from Mie scattering is likely to not play too high a role for the CLCS most of the time. This will be different for locations such as the Sahara. In these regions, Mie scattering may have a relevant contributing factor in scattering photons towards the camera if the scattering angle is below around 80°. However, if the CLCS can rely mostly on Rayleigh scattering from molecules, then it is not necessary to know the particle data during the operation of the CLCS and this is how the laser configuration should be optimised. Therefore, if there are high numbers of particles in the air, then the beam may simply be visible better than at times with fewer particles. Lastly, simulation results showed that Rayleigh scattering from very small particles does not play a significant role for the CLCS.

As summarised in section 4.1, the scattering of light is strongest in the UV wavelength range and significantly drops with rising wavelength. From this perspective, a laser in the UV wavelength range is suited best. When taking the product of the spectral mirror reflectance and the spectral scattering effectiveness into account for choosing a wavelength which scatters most effectively with respect to the CLCS, then the best choice laser wavelength is λ=350 nm, but other wavelengths between around 320 and λ=425 nm are also suitable (cf. Figure 4.9). The choice of an optimal laser wavelength must be accompanied by a thorough laser safety assessment by a

qualified laser safety officer. Also, a suitable laser must be available at the preferred wavelength.

For the indoor tests in project HeliBo at the Solar-Institut Jülich (SIJ), a SpitLight 300 Q-switched pulsed laser with a CWL at λ=355 nm was chosen in order to make use of a very high scattering effectiveness in the UV-A wavelength range. A maximum pulse energy of 8.5 mJ, which could also be reduced for the tests, as well as a beam diameter of about 47 mm (after beam expansion) were chosen (the expanded beam diameter, however, was smaller than preferred). For the tests, single laser beam emissions were triggered manually using a pulse/delay generator.

As was shown in section 6.2.4, the simulation model accurately calculates the mean grey value of a laser beam (the deviation is only around 8.9%) using a scientific camera for the validation. The accuracy could, however, not be validated for the grey value from the diffuse irradiance from the sky due to constraints from the camera.

As shown in sections 6.5 and 6.6, image intensifier camera technology is suited best for the CLCS as they allow short exposure times which are necessary such that noise from the background irradiance from the blue sky is reduced as much as possible. Suitable exposure times in the range of $\geq$50 ns can be realised. As suitable optical filter technology, an ultra-narrow bandpass filter with FWHM of around 1 to 2 nm is the best choice for the CLCS. An image intensifier camera as well as a scientific camera were tested with two different camera lenses (one with a focal length of f=25 mm and the other with f=78 mm).

Outdoor tests were carried out a the site of the German Meteorological Service (DWD). Minimum pulse energies that allow the detection of the laser beam orientation in an image with high mean measurement accuracy ($<$ 0.4 mrad) in an outdoor environment were determined. The pulse energy for a future CLCS application will need to be approximately 0.5 to 1 mJ at the wavelength λ=355 nm such that the beam can still be identified in an image with a line detection algorithm at a sufficient accuracy. The laser must not emit any other wavelengths for reasons of laser safety.

More work regarding laser safety for an optimised laser system as well as an optimisation of the parameters to achieve a higher measurement accuracy are required. A follow-on R&D project in which a newly optimised laser system with a very large beam diameter and eye-safe (and skin-safe) design is built and tested is necessary and the involvement of a specialised company is required.

Comparison of the CLCS with other calibration methods

Regarding the measurement accuracy, most calibration systems require to measure about 5 to 10 times more accurately than the value of the overall tracking accuracy that is desired for a heliostat (Sattler et al. 2020). This is especially the case for calibration methods which only measure the orientation locally without considering the waviness of the mirrors or effects such as gravitational bending of the heliostat structure. For the CLCS to measure with a high accuracy, multiple spots of all mirror facets should be used in measurements in order to determine a weighed mean orientation of all mirror facets.

In the view of the author, every single calibration method that has been developed has one or more advantages, but also one or more disadvantages compared to other calibration methods. Whether one calibration method is preferred over another will also depend on preferences of individual operating companies of CRS with regard to advantages and disadvantages of individual calibration methods. Also, operating companies may prefer to use only calibration technology developed in their respective country. It should further be noted that the calibration methods proposed worldwide have different development statuses from being merely a concept up to trial deployment in real heliostat fields. Due to the complexity of measuring the orientation of thousands of heliostats multiple times during the day, there still has not yet been a breakthrough for a calibration method that has replaced the state-of-the-art camera-target method. For several reasons, including reasons that were stated previously, no representative ranking of calibration methods can be made.

Some of the proposed calibration methods stand out more than others due to unique features. The CLCS can be regarded as being one of these more unique calibration methods. One main, distinctive feature of the CLCS is that it shall be able to measure the orientation of mirror facets of heliostats from a central position via the reflection of laser beams from the mirror surfaces and the use of two cameras photographing the beams. This allows a detailed calculation of the overall orientation of the heliostat, which many other calibration methods are not capable of. In this work, in a simulation study, the potential measurement accuracy of the CLCS was evaluated to be between about 0.05 and 0.9 mrad (average around 0.37 mrad), which is sufficient for the application in a CRS. Another unique feature of the CLCS is that no other calibration methods using laser and camera technology in combination have been proposed. Moreover, the CLCS is one of few devised methods which are central and only require very few main components to function. This is a great advantage with respect to device maintenance compared to other methods such as those that require the installation of devices on each individual heliostat. However, the great disadvantage of the CLCS is that it requires the deployment of a laser system with beam expansion and automatic beam alignment system. Additionally, an extensive laser safety assessment is required, which is complex. Another disadvantage of the

CLCS is that it will only be able to measure the orientation of heliostats sequentially and at a limited frequency.

Compared with the state-of-the-art camera-target method, the CLCS has the advantage that it can potentially be operated at a far higher measurement speed. For the comparison, it is considered that the camera-target method takes 30 seconds for the calibration of an individual heliostat. If the CLCS is operated at a measurement frequency of 10 Hz (i.e. 10 mirror facets measured and calibrated per second), then the CLCS could potentially calibrate 300 times faster than the camera-target method. This would be the case if for each heliostat only a single mirror facet's orientation were measured. However, if the orientation of all mirror facets of a heliostat are needed to be measured for calculating the overall tracking accuracy of the heliostat, then the measurement speed reduces accordingly. Another advantage of the CLCS is that it can be operated during the night as, unlike the camera-target method, it is independent from the sun.

Publications
Three publications have been made, namely Sattler et al. (2020), which was presented as a summary in chapter 2 and chapter 7, as well as Sattler & Göttsche (2022) and Sattler & Göttsche (2023), from which relevant sections were taken and included in this PhD thesis in various chapters.

8.2 Outlook

In a step forward for realising a CLCS in an outdoor environment in the future, further work will be necessary. In the following sections, an outlook for the CLCS in a future application at a CRS and details on the main topics that require further work are given below.

8.2.1 Future configuration of the laser with modifications for a CLCS

Regarding the application of the CLCS in the future, the primary importance is laser safety, i.e. the laser must be eye safe. One possibility for improving laser safety is to increase the beam diameter. Using a large beam diameter such as e.g. 300 mm also has the advantage that with a single measurement, it is possible to measure the orientation of a large area of a mirror facet. However, here it must of course also still be considered that a laser beam diameter increases over the distance due to beam divergence, which means that for heliostats located near to the laser the beam diameter is smaller than for heliostats that are hundreds of metres away. One

potential solution to this issue is presented in section 8.2.8, while another potential solution is to design the laser such that the beam expansion, i.e. the beam outlet diameter, is variable (if technically feasible). Regarding a future measurement rate of the CLCS, a pulse frequency of around 10 Hz is desired and technically feasible regarding a fast two-axial tracking system, but whether or not this can be realised depends on the final specification of the laser system (including the pulse energy, the beam diameter (expanded by a telescope), safety optics, the beam shape and other parameters) as well as a thorough laser safety assessment. The beam shape options will need to be explored for the new laser design with expanded beam diameter because a flat-top beam could potentially be an advantage in terms of laser safety compared to having a Gaussian beam profile. If necessary, a beam shaper can be used to ensure that a flat-top beam is formed. The safety design of the new laser must also ensure that hot spots in the beam cannot form.

Whether or not active and/or passive safety systems may need to be deployed depends on the laser safety assessment for the chosen laser specification. The laser safety assessment must also include the safety for aircraft etc. which requires clearances from various authorities (including air traffic control). According to own estimations from laser safety calculations, it is very likely that a laser system used in a future CLCS application must be built and configured in such a way that it can officially be classified as a class 1M laser due to laser safety limitations. Although a class 3R laser classification would be better with respect to obtaining a stronger scattering signal from the laser beam because the beam detection accuracy should increase, it is less likely that this laser class can be realised due to reasons of laser safety (e.g. due to the potential danger of beam concentration from the heliostat mirror). Another complexity is that the original class of the laser is very likely to be class 4 and therefore very dangerous. The Solar-Institut Jülich needs to further investigate the topic laser safety in a follow-on R&D project and seeks to involve a company specialised on laser safety to carry out a thorough laser safety assessment using the valid norms and regulations etc. to assess whether or not it is safe to deploy a newly specified laser system for the application in a CLCS. Ideally, this company will build the entire laser system including all modifications and have the authority to classify a laser system. What also needs to be tested is a two-axial tracking system for the laser and – if needed – active and passive safety systems. The two-axial laser tracking system can be realised with high-accuracy, high-precision piezo drives. Regarding an active safety system, for example a radar system may need to be used to automatically detect aircraft and other flying objects in the sky. Further active systems may also need to be deployed. Regarding a passive safety measure, the beam outlet should be encapsulated leaving only a small opening which restricts the angular field of view in such a way that laser beams can only be emitted towards the ground within the heliostat field.

8.2.2 Optimisation of the choice of laser wavelength

If it is desired to test a central laser wavelength other than λ=355 nm for the CLCS in a follow-on R&D project, then the most promising candidate wavelength is λ=358.5 nm as at around this wavelength, the DHI is lower than at λ=355 nm (i.e. 0.14 and 0.22 W/(m^{2}nm), respectively). An ultra-narrow bandpass filter with FWHM of 1 nm is considered. For the configuration with λ=358.5 nm, it may be possible to reduce the number of photons passing though the filter by an estimated 32 % compared to the configuration for λ=355 nm, which would have a positive impact on the CLCS with respect to the reduction of shot noise in images.

Three further promising laser wavelengths, namely λ=337 nm as well as the two Fraunhofer lines at $\lambda = 393.3682$ nm and $\lambda = 396.8492$ nm are of interest. Although the two Fraunhofer lines have very low DHI values down to about 0.1 W/(m^{2}nm), one needs to consider that the DHI passes through the filter according to the ultra-narrow bandpass filter's FWHM and transmission properties, leading to background noise. It is expected that at these two Fraunhofer lines, the noise level will be similar compared to the other wavelengths. The results of the above discussion are given in Figure 8.1 which shows W_{DHI}, which is the product of the mirror reflectance, the scattering ratio (normalised to the wavelength $\lambda = 320$ nm) and the normalised DHI (represented by large black dots in 5 nm intervals). Equation 8.1 describes the calculation of W_{DHI}:

$$W_{\mathrm{DHI}}(\lambda) = \rho_{\mathrm{m}}(\lambda) \cdot SR(\lambda) \cdot \mathrm{DHI}_{\mathrm{normed}}(\lambda) \quad [\%] \tag{8.1}$$

Four promising wavelengths are labelled with the letter A to D. The wavelength λ=337 nm is labelled with the letter A, the wavelength λ=358.5 nm with letter B, the wavelength λ=393.3682 nm with letter C and the wavelength λ=396.8492 nm with letter D. Also shown in Figure 8.1 is W, which is the product of the mirror reflectance and the scattering ratio (normalised to the wavelength $\lambda = 320$ nm) from Figure 4.9 (represented by the dotted line).

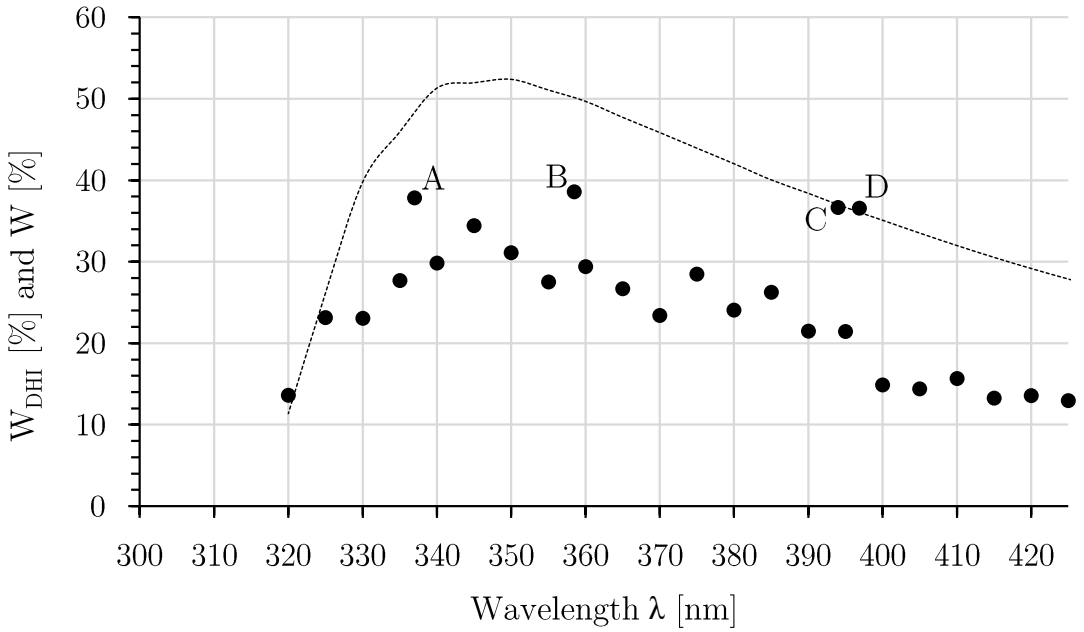

Figure 8.1: Graph showing W_{DHI}, which is the product of the mirror reflectance, the scattering ratio (normalised to the wavelength $\lambda = 320\,\mathrm{nm}$) and normalised DHI (represented by large black dots). Also shown is W, which is the product of the mirror reflectance and the scattering ratio (normalised to the wavelength $\lambda = 320\,\mathrm{nm}$) (represented by the dotted line) from Figure 4.9.

If it is desired to test the promising laser wavelengths (labelled A to D) in a follow-on R&D project, then, as light source, an OPO would need to be chosen as it is the only type light source (with the characteristics of a laser) that meets the demands of the CLCS and can be tuned to the desired wavelengths. However, suitable ultra-narrow bandpass filters must be available or, otherwise, be custom made. If a filter must be custom made, then its price will be higher compared to typical filters that are available as stock items, but this might be acceptable if the benefit of less noise increases the beam detection accuracy in an image.

8.2.3 Long-term test of an image intensifier camera

As stated before, the first choice type of camera for the CLCS is an image intensifier camera. The downside to these cameras is that they are relatively expensive and the camera's lifetime is limited (information on the lifetime, especially for the tested configuration with the ultra-narrow bandpass filter, is not available). A long-term test would need to be conducted to test the degradation (external support from a camera manufacturer may be needed to objectively assess any degradation). The author recommends to keep the exposure time (gating) as low as possible because low light conditions prolong the lifetime of the camera. In a study and if made available from camera vendors, the MTF charts of different image intensifier cameras should

be compared in order to evaluate which of the cameras may have the best potential for the CLCS. In a cost-quality evaluation it should be assessed if a comparatively low-cost image intensifier camera can produce images with sufficient quality for high-accuracy line detection. Also, test images of different image intensifier cameras should be requested and evaluated.

8.2.4 Accuracy of the CLCS

A study to optimise the accuracy of the CLCS needs to be conducted in a follow-on R&D project through a field test in a heliostat field and by varying more parameters of the image intensifier camera. Ideally, also other manufacturers' image intensifier cameras should also be tested to compare the quality and suitability of various cameras with different resolutions for the CLCS. The test should also include the evaluation of an ultra-narrow bandpass filter with a wider FWHM of e.g. 2 nm as well as other camera lenses. A wider FWHM would only be beneficial for lenses with a short focal length (e.g. f=25 mm) as a larger portion of the heliostat field would then be within the enlarged AFOV. However, the shot noise would be higher compared to an ultra-narrow bandpass filter with a narrower FWHM such as 1 nm. An example for why a lens with a short focal length (e.g. f=25 mm) could benefit from an optical filter with a larger FWHM can be observed from Figure 6.19, which has a reduced AFOV (the vertical beam is not visible along the entire height of the image due to the blue-shift effect). Regarding the f=25 mm lens used for photographing the laser beam shown in Figure 6.19, the vertical AFOV for the camera system without optical filter is about 16° (calculated using equation 4.9). However, due to the used ultra-narrow bandpass filter, the AFOV is reduced to about 7.6°. For a lens with a longer focal length (e.g. f=78 mm), if the AFOV is already small, then an increase in FWHM greater than about 1 nm would not be advisable if the beam is already fully visible in an image, as is the case, for example, in Figure 6.20.

8.2.5 Variable distance between laser beam and camera system

One disadvantage for the CLCS is that the distance between the laser and the heliostats but also the distance between the cameras and the heliostats is variable. As the laser beam expands over the increasing distance due to its divergence angle, the beam diameter will increase and the beam intensity will decrease. If the camera lens has a fixed focus then the grey values of a photographed laser beam in an image will reduce with increasing distance between the camera and the photographed beam. As proposed before, a potential solution is to design the laser system such that the beam expansion, i.e. the beam outlet diameter, can be variable (if technically feasible) such that even after a distance of some hundreds of metres the beam diameter will have the same diameter as a laser beam emitted on a heliostat that is close to the laser

source. If this design concept can be technically realised then the laser beam would appear in an image with a width that reduces with increasing distance between the laser source and a heliostat while the grey values of the laser beam in an image should remain constant (because, as per camera theory, the radiance remains constant).

The camera lens should be chosen such that the laser beam appears in a photograph across as few pixels in width as possible such that the grey values of the laser beam are as high as possible (adequate would probably be less than around 5 pixels). In order to assess the beam width in an image at different distances between the beam and the camera, a small study was carried out (it was assumed that the laser beam diameter remains constant). The camera and lens theory was applied to calculate the beam width as seen in the image of the image intensifier camera that was used for the experiments. The calculations were done (i) for selected camera lenses with different fixed focal lengths and (ii) when considering various distances between the camera system and the beam. The outcome of the study was that for very large beam diameters preferably camera lenses with short focal lengths of about 25 to 35 mm should be used because only with shorter focal lengths the beam is visible on few image pixels in width. For very short distance of below about 150 m it may even be better to use a focal length of less than 25 mm. A higher image distortion is to be expected though.

As stated before, the beam should be visible on as few pixels in width as possible in order to have the highest possible beam brightness in an image. However, it should be noted that especially with a camera lens with focal length of 25 mm, the used ultra-narrow bandpass filter reduced the field of view due to the blue shift. Taking the laser wavelength of $\lambda = 355$ nm as an example, photons at this wavelength will be reflected by the spectral filter if they impinge at angles greater than a certain incidence angle as the wavelength transmissivity through the optical filter is angle-dependent (see section 4.4). The effect of the blue shift can be reduced by choosing a spectral filter with a wider bandwidth, e.g. 2 nm (FWHM) which will therefore increase the field of view of the camera system for monochromatic light. However, the disadvantage will be that more diffuse solar irradiance reaches the sensor leading to more noise, which can only be countered by reducing the camera exposure time. This is therefore an optimisation problem. It should be noted that in the outdoor test campaign at the DWD site, the images taken with a lens with focal length of 78 mm had a better quality than a lens with focal length of 25 mm, but the downside is that the field of view was very small.

In a follow-on R&D project it should also be assessed whether a reasonably priced motorised UV lens with a variable focal length can be manufactured specifically for the CLCS.

8.2.6 Positioning of the camera system and field of view

The optimal positioning of the cameras in a real CLCS application is on stiff poles at a height slightly above the highest edge of the mirror facets of the heliostats. The elevation angle of the cameras should be 0° such that they look forward and not up into the sky as shown in Figure 8.2 (a). As the photographed reflected beam is still very close to the heliostat, it is very easy to predetermine the delay time of the scattered beam's photons until they reach the cameras based on the position of a heliostat in the field. Due to limitations in the AFOV of the camera system, it will most likely be necessary to rotate the camera system in the azimuth. For highly accurate azimuth positioning of the cameras, piezo drives with high a step resolution (e.g. 12,000,000 rotations per 360°) can be used. The cameras should be shielded off from direct sunlight, i.e. placed in a housing with an opening and cooled if necessary. An option to calibrate the orientation of the camera is to use UV-LED markers in the FOV of the cameras.

Another camera orientation method is to install the cameras such that the AFOV is just below the horizon as shown in Figure 8.2 (b), i.e. the sky is not in the field of view. This can reduce the background irradiance by at least around 20 % because the background of the beam will mostly be the heliostat mirrors which have a reflectance of around 79 % at the wavelength 355 nm. Also the ground will be visible between the heliostats and in these areas the beam will have a better contrast because the reflectivity of the soil at 355 nm is very low (see, for example, Bartholomeus (2006) for reflectivity data of soil). Less photon shot noise in an image with a laser beam will also lead to a better line detection accuracy. However, it depends on the heliostat field size how high the poles would need to be. As sufficiently stiff and suitable poles of e.g. 10 or 20 m height will be costly and because at these heights the cameras are not easily accessible for maintenance, this method may not be preferred though.

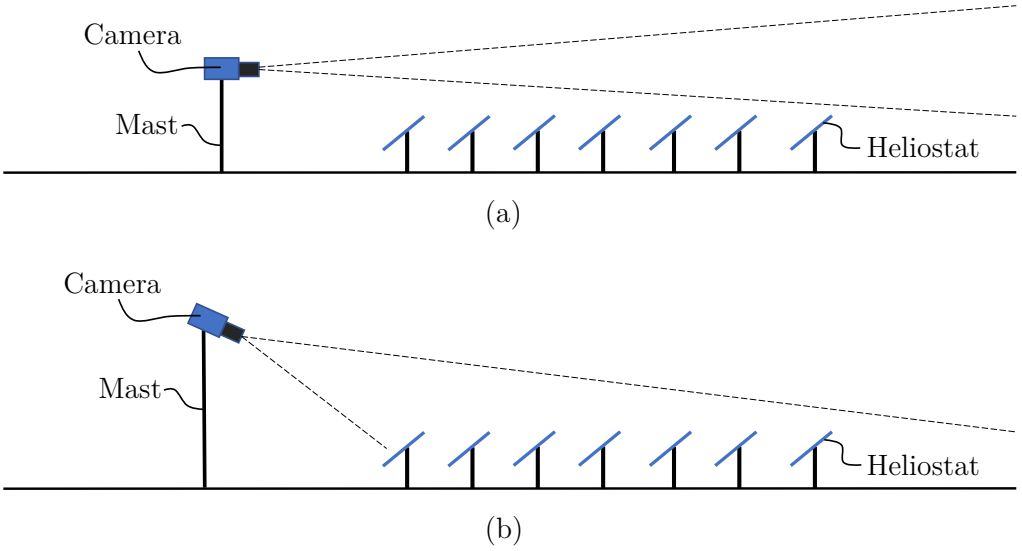

Figure 8.2: Two proposed orientation methods of a camera.

The delay time for the laser beam to reach a heliostat must be known, which is very easy to predetermine. Therefore, for each beam emission on a selected heliostat in the heliostat field, it will be necessary to have a computer system automatically select and set pre-calculated delay times that must be set for the cameras. This can be easily accomplished e.g. by means of taking the values from a simple look-up table or by means of a fast calculation.

8.2.7 Potential danger from reflecting laser beams off mirror facets

In section 4.7, a preliminary assessment of the risk of laser beam concentration when the beam is reflected by multiple canted facets was made. The beam concentration can occur where e.g. four (canted) facets meet or due to mirror surface imperfections with respect to concave slopes. A full assessment of this potential danger will need to be addressed in a follow-on R&D project.

8.2.8 Modular design concept for the CLCS

The author proposes a similar laser system design as shown in Figure 6.9 with further modifications. A modular design as shown in Figure 8.3 that allows multiple beams to exit the laser system from individual optical systems using a single laser source is one option to increase the measurement speed of the CLCS. In this case, each of the optics must have their own dual-axial tracking system such that the exiting enlarged beam can be aimed at any heliostat in the heliostat field. An easy-to-handle upscaling of the system and possibly even a simultaneous measurement of multiple

heliostats in the field or even multiple mirror facets of a single heliostat could be an interesting option if the cost is not too high. Moreover, one could foresee two or more different beam outlet diameters for the modular design. This allows accounting for the beam divergence and the resulting increasing beam diameter over the distance. This is important because the width of the beam as seen by the image sensor should best not vary with the distance as otherwise the beam will appear weaker in the image if the beam is spread across more pixels in width.

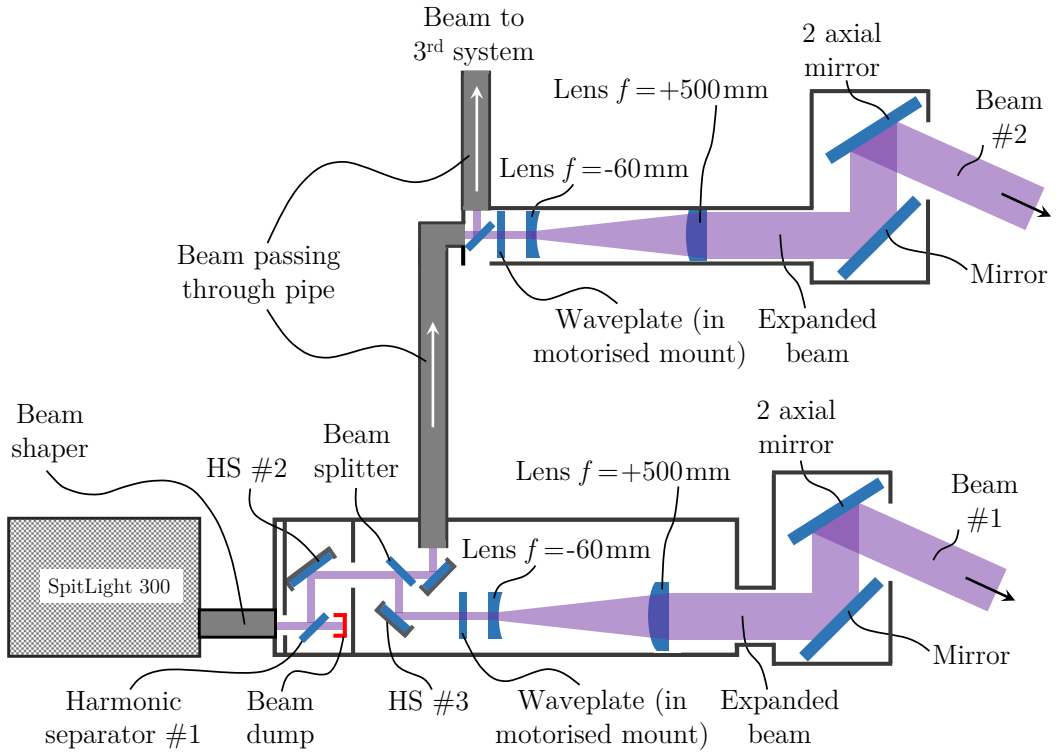

Figure 8.3: Proposition of a technical drawing of the laser with multi-beam optics. With beam splitters, multiple beams can be created.

8.2.9 Laser beam jitter or wandering

In outdoor applications an effect called beam jitter or beam wander can occur, for example, due to the refraction of the laser beam when it traverses through air layers of different densities. If this effect is large, then it can affect the accuracy of the CLCS. The extend of this effect could not be tested as part of this work. However, if the laser beam is emitted from a height of e.g. around 50 to 150 m and if the beam is photographed at a height near the ground, then possibly the effect of beam jitter is within an acceptable level.

8.2.10 Further applications using the CLCS

The CLCS can potentially also be used for other applications in the heliostat field while it is measuring the heliostat orientation. Should the entire heliostat's mirror facets' orientations be measured, then the curvature of the individual mirror facets can potentially also be determined (this would be an alternative method to deflectometry measurements).

The CLCS can potentially also be used for indirectly measuring the mirror reflectivity by means of evaluating the diffuse reflections of laser light off dust on the mirror facets. This could be done during the night to avoid noise from diffuse irradiance from the sky. During the night, the pulse energy can probably be further reduced because there are no shot noise photons from background diffuse irradiance.

Bibliography

Abramczyk, H. (2005), *Introduction to Laser Spectroscopy*. 1st ed. Elsevier Science. ISBN: 978-0-444-51662-6.

Adimec (2015). *CCD versus CMOS: blooming and smear performance*. Author: Alper, Gretchen. 2 April 2015. https://www.adimec.com/ccd-versus-cmos-blooming-and-smear-performance/. Last accessed: 3 July 2021.

Adobe (1992). *TIFF*, Revision 6.0. Final – June 3, 1992. Adobe Systems Inc. https://www.adobe.io/content/dam/udp/en/open/standards/tiff/TIFF6.pdf. Last accessed: 14 November 2021.

Alluxa (2021). *Temperature Dependence*. Alluxa, Inc. https://www.alluxa.com/optical-filter-specs/temperature-dependence/. Last accessed: 9 November 2021.

Andreae, M. O. & Rosenfeld, D. (2008). "Aerosol–cloud–precipitation interactions. Part 1. The nature and sources of cloud-active aerosols." In: *Earth-Science Reviews* 89(1-2), 13–41. https://doi.org/10.1016/j.earscirev.2008.03.001.

AQEG (2005). *Particulate Matter in the UK*. Defra, London. https://uk-air.defra.gov.uk/library/assets/documents/reports/aqeg/ch2.pdf, https://uk-air.defra.gov.uk/assets/documents/reports/aqeg/contents.pdf. Last accessed: 5 November 2021.

Bartholomeus, H. (2006). *Remote Sensing for Soil Science*. Lecture at Wageningen University. http://www.geo-informatie.nl/courses/grs20306/course/Schedule/Soil%20reflectance.pdf.

Basher, R. E. & Matthews, W. A. (1977). "Problems in the Use of Interference Filters for Spectrophotometric Determination of Total Ozone." In: *Journal of Applied Meteorology* 16(8), 795–802. https://doi.org/10.1175/1520-0450(1977)016%3C0795:PITUOI%3E2.0.CO;2.

BAuA (2018a). *TROS Laserstrahlung - Teil: Allgemeines, GMBl 2018 S. 962 [Nr. 50–53]*. Ausschuss für Betriebssicherheit - ABS-Geschäftsführung - BAuA. https://www.baua.de/DE/Angebote/Rechtstexte-und-Technische-Regeln/Regelwerk/TROS/TROS.html. Last accessed: 9 March 2021.

BAuA (2018b). *TROS Laserstrahlung - Teil 1: Beurteilung der Gefährdung durch Laserstrahlung, GMBl 2018 S. 982 [Nr. 50–53]*. Ausschuss für Betriebssicherheit - ABS-Geschäftsführung - BAuA. https://www.baua.de/DE/Angebote/Rechtstexte-und-Technische-Regeln/Regelwerk/TROS/TROS.html. Last accessed: 9 March 2021.

BAuA (2018c). *TROS Laserstrahlung - Teil 2: Messungen und Berechnungen von Expositionen gegenüber Laserstrahlung - GMBl 2018 S. 1000 [Nr. 50–53]*. Ausschuss für Betriebssicherheit - ABS-Geschäftsführung - BAuA. https://www.baua.de/DE/Angebote/Rechtstexte-und-Technische-Regeln/Regelwerk/TROS/TROS.html. Last accessed: 9 March 2021.

BAuA (2018d). *TROS Laserstrahlung - Teil 3: Maßnahmen zum Schutz vor Gefährdungen durch Laserstrahlung, GMBl 2018 S. 1030 [Nr. 50–53]*. Ausschuss für Betriebssicherheit - ABS-Geschäftsführung - BAuA. https://www.baua.de/DE/Angebote/Rechtstexte-und-Technische-Regeln/Regelwerk/TROS/TROS.html. Last accessed: 9 March 2021.

Baumeister, P. W. (2004), *Optical Coating Technology*, SPIE. https://doi.org/10.1117/3.548071.

Bern, G., Schöttl, P., Heimsath, A. & Nitz, P. (2016). "Novel imaging closed loop control strategy for heliostats." In: *SolarPACES 2016*, Abu Dhabi, UAE, 11 – 14 October, 2016.

Bi, L., Lin, W., Wang, Z., Tang, X., Zhang, X. & Yi, B. (2018). "Optical Modeling of Sea Salt Aerosols: The Effects of Nonsphericity and Inhomogeneity." In: *Journal of Geophysical Research: Atmospheres* 123(1), 543–558. https://doi.org/10.1002/2017JD027869.

Blume, K., Röger, M., Schlichting, T., Macke, A. & Pitz-Paal, R. (2020). "Dynamic photogrammetry applied to a real scale heliostat: Insights into the wind-induced behavior and effects on the optical performance." In: *Solar Energy* 212(1), 297–308. https://doi.org/10.1016/j.solener.2020.10.056.

Bodhaine, B. A., Wood, N. B., Dutton, E. G. & Slusser, J. R. (1999). "On Rayleigh Optical Depth Calculations." In: *Journal of Atmospheric and Oceanic Technology* 16(11), 1854–1861. https://doi.org/10.1175/1520-0426(1999)016%3C1854:ORODC%3E2.0.CO;2.

Bogumil, K., Orphal, J., Homann, T., Voigt, S., Spietz, P., Fleischmann, O., Vogel, A., Hartmann, M., Kromminga, H., Bovensmann, H., Frerick, J. & Bur-

rows, J. (2003). "Measurements of molecular absorption spectra with the SCIAMACHY pre-flight model: instrument characterization and reference data for atmospheric remote-sensing in the 230–2380 nm region." In: *Journal of Photochemistry and Photobiology A: Chemistry* 157(2-3), 167–184. https://doi.org/10.1016/S1010-6030(03)00062-5.

Bohren, C. F. (2007). *Atmospheric Optics.* In: *The Optics Encyclopedia*, 53–91. https://doi.org/10.1002/9783527600441.oe004.

Bohren, C. F. & Huffman, D. R. (1983, 2008), *Absorption and scattering of light by small particles*, Wiley-VCH, Weinheim. ISBN: 9780471293408.

Bovensmann, H., Burrows, J. P., Buchwitz, M., Frerick, J., Noël, S. & Rozanov, V. V. (1999). "SCIAMACHY: Mission Objectives and Measurement Modes." In: *Journal of Atmospheric Sciences* 56(2). https://doi.org/10.1175/1520-0469(1999)056%3C0127:SMOAMM%3E2.0.CO;2.

Boyat, A. K. & Joshi, B. K. (2015). "A Review Paper: Noise Models in Digital Image Processing." In: *Signal & Image Processing : An International Journal* 6(2), 63–75. https://doi.org/10.5121/sipij.2015.6206.

Bucholtz, A. (1995). "Rayleigh-scattering calculations for the terrestrial atmosphere." In: *Appl. Opt.* 34(15), 2765–2773. https://doi.org/10.1364/AO.34.002765.

Burisch, M., Olano, X., Sánchez, M., Olarra, A., Villasante, C., Olasolo, D., Monterreal, R., Enrique, R. & Fernández, J. (2018). "Scalable HeliOstat calibRation sysTem (SHORT) – calibrate a whole heliostat field in a single night." In: *AIP Conference Proceedings* 2033, 040009. https://doi.org/10.1063/1.5067045.

Chehade, W., Gorshelev, V., Serdyuchenko, A., Burrows, J. P. & Weber, M. (2013). "Revised temperature-dependent ozone absorption cross-section spectra (Bogumil et al.) measured with the SCIAMACHY satellite spectrometer." In: *Atmospheric Measurement Techniques* 6(11), 3055–3065. https://doi.org/10.5194/amt-6-3055-2013.

Clarke, A., Kapustin, V., Howell, S., Moore, K., Lienert, B., Masonis, S., Anderson, T. & Covert, D. (2003). "Sea-Salt Size Distributions from Breaking Waves: Implications for Marine Aerosol Production and Optical Extinction Measurements during SEAS*." In: *Journal of Atmospheric and Oceanic Technology* 20(10), 1362–1374. https://doi.org/10.1175/1520-0426(2003)020%3C1362:SSDFBW%3E2.0.CO;2.

Collins, M., Potter, D. & Burton, A. (2017). "Design and simulation of a sensor for heliostat field closed loop control." In: *AIP Conference Proceedings* 1850, 030009. https://doi.org/10.1063/1.4984352.

Convery, M. R. (2011). "Closed-loop control for power tower heliostats." In: *SolarPACES 2011*, Granada, Spain, 20 – 23 September, 2011.

Cornell, R. M. & Schwertmann, U. (2003), *The iron oxides: Structure, properties, reactions, occurences and uses / R.M. Cornell, U. Schwertmann*, 2nd ed. edn, Wiley-VCH, Weinheim and Cambridge.

Coseti (2006). http://www.coseti.org/9006-025.htm. Last accessed: 25 October 2021.

CSPS (2015). *Deflectometric Measurement System QDec*. CSP Services GmbH. https://www.cspservices.de/wp-content/uploads/CSPS-QDec.pdf. Last accessed: 19 July 2021.

Dabrowksi, J., Göttsche, J., Nettelroth, V. & Sauerborn, M. (2014), 'Verfahren zur Positionsbestimmung oder zur Antriebsregelung eines eine Spiegelfläche aufweisenden Heliostaten sowie System zur Positionsbestimmung oder zur Antriebsregelung des Heliostaten'. Pantent number: DE 10 2013 207 022 B3.

Dave, J. V. (1968). *Subroutines for Computing the Parameters of the Electromagnetic Radiation Scattered by a Sphere*. Report No. 320-3237, Palo Alto Scientific Center, IBM Corporation.

Dave, J. V. (1969). "Scattering of Electromagnetic Radiation by a Large, Absorbing Sphere." In: *IBM Journal of Research and Development* 13(3), 302–313. https://doi.org/10.1147/rd.133.0302.

Deirmendjian, D. (1969). *Electromagnetic Scattering on Spherical Polydispersions*. Santa Monica, CA: RAND Corporation, 1969. https://www.rand.org/pubs/reports/R0456.html. Also available in print form.

Demant, C., Streicher-Abel, B. & Springhoff, A. (2011), *Industrielle Bildverarbeitung: Wie optische Qualitätskontrolle wirklich funktioniert*, 3. aufl. edn, Springer-Verlag Berlin Heidelberg, Berlin, Heidelberg.

Denjean, C., Cassola, F., Mazzino, A., Triquet, S., Chevaillier, S., Grand, N., Bourrianne, T., Momboisse, G., Sellegri, K., Schwarzenbock, A., Freney, E., Mallet, M. & Formenti, P. (2016). "Size distribution and optical properties of mineral

dust aerosols transported in the western Mediterranean." In: *Atmospheric Chemistry and Physics* 16(2), 1081–1104. https://acp.copernicus.org/articles/16/1081/2016/.

DGUV (2018). *Auswahl und Benutzung von Laser-Schutzbrillen, Laser-Justierbrillen und Laser-Schutzabschirmungen*. Deutsche Gesetzliche Unfallversicherung. https://publikationen.dguv.de/regelwerk/publikationen-nach-fachbereich/energie-textil-elektro-medienerzeugnisse-etem/nichtionisierende-strahlung/249/auswahl-und-benutzung-von-laser-schutz-und-justierbrillen. Last accessed: 9 March 2021.

Dong, F., Chen, Y., Kong, D.-X. & Yang, B. (2015). "Salt and pepper noise removal based on an approximation of l0 norm." In: *Computers & Mathematics with Applications* 70(5), 789–804. https://doi.org/10.1016/j.camwa.2015.05.026.

Duarte, F. J., ed. (2016), *Tunable Laser Applications*, Optical science and engineering, third edition edn, CRC Press, Boca Raton. ISBN: 9781482261073.

Ebert, M., Weinbruch, S., Hoffmann, P. & Ortner, H. M. (2004). "The chemical composition and complex refractive index of rural and urban influenced aerosols determined by individual particle analysis." In: *Atmospheric Environment* 38(38), 6531–6545. https://doi.org/10.1016/j.atmosenv.2004.08.048.

Ebert, M., Weinbruch, S., Rausch, A., Gorzawski, G., Helas, G., Hoffmann, P. & Wex, H. (2002). "Complex refractive index of aerosols during LACE 98 as derived from the analysis of individual particles." In: *Journal of Geophysical Research* 107(D21), LAC 3-1-LAC 3-15. https://doi.org/10.1029/2000JD000195.

Edmund Optics (2011a). *Imaging Electronics 101: Understanding Camera Sensors for Machine Vision Applications*. Online article from the Imaging Resource Guide in the knowledge center on the website of Edmund Optics. Last updated: 3 November 2011. https://www.edmundoptics.eu/knowledge-center/application-notes/imaging/understanding-camera-sensors-for-machine-vision-applications/. Last accessed: 5 November 2021.

Edmund Optics (2011b). *Imaging Electronics 101: Camera Resolution for Improved Imaging System Performance*. Online article from the Imaging Resource Guide in the knowledge center on the website of Edmund Optics. Last updated: 3 November 2011. https://www.edmundoptics.com/knowledge-center/application-notes/imaging/camera-resolution-for-improved-imaging-system-performance/. Last accessed: 5 November 2021.

Edmund Optics (2011c). *Introduction to Modulation Transfer Function*. Online article from the Imaging Resource Guide in the knowledge center on the website of Edmund Optics. Last updated: 1 March 2011. https://www.edmundoptics.com/knowledge-center/application-notes/optics/introduction-to-modulation-transfer-function/. Last accessed: 25 October 2021.

Edmund Optics (2012). *Optical Filters*. Online article from the Imaging Resource Guide in the knowledge center on the website of Edmund Optics. Last updated: 29 February 2012. https://www.edmundoptics.eu/knowledge-center/application-notes/optics/optical-filters/. Last accessed: 6 November 2021.

Edmund Optics (2014a). *Resolution*. Online article from the Imaging Resource Guide in the knowledge center on the website of Edmund Optics. Last updated: 12 March 2014. https://www.edmundoptics.eu/knowledge-center/application-notes/imaging/resolution/. Last accessed: 25 October 2021.

Edmund Optics (2014b). *Object Space Resolution*. Online article from the Imaging Resource Guide in the knowledge center on the website of Edmund Optics. Last updated: 13 March 2014. https://www.edmundoptics.de/knowledge-center/application-notes/imaging/object-space-resolution/. Last accessed: 5 November 2021.

Edmund Optics (2014c). *Contrast*. Online article from the Imaging Resource Guide in the knowledge center on the website of Edmund Optics. Last updated: 13 March 2014. https://www.edmundoptics.eu/knowledge-center/application-notes/imaging/contrast/. Last accessed: 5 November 2021.

Edmund Optics (2014d). *The Modulation Transfer Function (MTF)*. Online article from the Imaging Resource Guide in the knowledge center on the website of Edmund Optics. Last updated: 13 March 2014. https://www.edmundoptics.com/knowledge-center/application-notes/imaging/modulation-transfer-function-mtf-and-mtf-curves/. Last accessed: 5 November 2021.

Edmund Optics (2015). *Understanding Focal Length and Field of View*. Online article from the Imaging Resource Guide in the knowledge center on the website of Edmund Optics. Last updated: 11 March 2015. https://www.edmundoptics.eu/knowledge-center/application-notes/imaging/understanding-focal-length-and-field-of-view/. Last accessed: 9 November 2021.

Edmund Optics (2019). *Why Use a Flat Top Laser Beam?*. Online article from the Imaging Resource Guide in the knowledge center on the website of Edmund Optics. Last updated: 31 December 2019. https://www.edmundoptics.eu/knowledge-center/application-notes/optics/why-use-a-flat-top-laser-beam/. Last accessed: 29 December 2021.

Eichler, J. & Eichler, H.-J. (2006), *Laser: Bauformen, Strahlführung, Anwendungen.* 6., aktualisierte Aufl. Berlin [u.a.]: Springer.

EMVA (2016). *EMVA 1288, Release 3.1: Standard for Characterization of Image Sensors and Cameras*. https://www.emva.org/standards-technology/emva-1288/emva-standard-1288-downloads/. Last accessed: 8 March 2021.

Erdogan, T. (2011). "Optical Filters – Polarization and Filters." Presentation. Semrock, A Unit of IDEX Corporation. 31 May 2011. https://www.semrock.com/Data/Sites/1/semrockpdfs/polarizationandfilters.pdf.

Fairman, P., Farrant, D. & Connor, P. (2019). "Closed loop optical tracking of heliostats." In: *AIP Conference Proceedings* 2126, 030021, https://doi.org/10.1063/1.5117533.

Fereyre, P. & Powell, G. (2016). *CMOS Image Sensors are entering a new age*. https://www.siue.edu/~sumbaug/e2v_CMOS_Image_Sensors_are_entering_a_new_age_V4.pdf. Last accessed: 2 July 2021.

Flesch, R., Belhomme, B., Ahlbrink, N. & Pitz-Paal, R. (2012). "Automatic Determination of Heliostat Orientation Using an Auxiliary Mirror". In: *SolarPACES 2012*, Marrakech, Morocco, 11 – 14 September, 2012.

Freeman, J., Keerthi, K. S. & Chandran, L. (2015). "Closed loop control system for a heliostat field." In: *International Conference on Technological Advancements in Power and Energy (TAP Energy)*, 272–277. https://doi.org/10.1109/TAPENERGY.2015.7229630.

Goldberg, N., Kroyzer, G., Hayut, R., Schwarzbach, J., Eitan, A. & Pekarsky, S. (2015). "Embedding a Visual Range Camera in a Solar Receiver." In: *Energy Procedia* 69, 1877–1884. https://doi.org/10.1016/j.egypro.2015.03.169.

Goldstein, F. (1989), "6 Optical Filters", *in* D. Malacara, ed., 'Geometrical and Instrumental Optics', Vol. 25 of *Methods in Experimental Physics*, Academic Press, pp. 273–301. https://doi.org/10.1016/S0076-695X(08)60214-8, https://www.sciencedirect.com/science/article/pii/S0076695X08602148.

Gonzalez, R. C. & Woods, R. E. (2018), *Digital image processing*. Fourth edition, global edition. New York, NY: Pearson. ISBN 978-1-292-22304-9.

Gordon, I., Rothman, L., Hargreaves, R., Hashemi, R., Karlovets, E., Skinner, F., Conway, E., Hill, C., Kochanov, R., Tan, Y., Wcisło, P., Finenko, A., Nelson, K., Bernath, P., Birk, M., Boudon, V., Campargue, A., Chance, K., Coustenis, A., Drouin, B., Flaud, J.-M., Gamache, R., Hodges, J., Jacquemart, D., Mlawer, E., Nikitin, A., Perevalov, V., Rotger, M., Tennyson, J., Toon, G., Tran, H., Tyuterev, V., Adkins, E., Baker, A., Barbe, A., Canè, E., Császár, A., Dudaryonok, A., Egorov, O., Fleisher, A., Fleurbaey, H., Foltynowicz, A., Furtenbacher, T., Harrison, J., Hartmann, J.-M., Horneman, V.-M., Huang, X., Karman, T., Karns, J., Kassi, S., Kleiner, I., Kofman, V., Kwabia-Tchana, F., Lavrentieva, N., Lee, T., Long, D., Lukashevskaya, A., Lyulin, O., Makhnev, V., Matt, W., Massie, S., Melosso, M., Mikhailenko, S., Mondelain, D., Müller, H., Naumenko, O., Perrin, A., Polyansky, O., Raddaoui, E., Raston, P., Reed, Z., Rey, M., Richard, C., Tóbiás, R., Sadiek, I., Schwenke, D., Starikova, E., Sung, K., Tamassia, F., Tashkun, S., Auwera, J. V., Vasilenko, I., Vigasin, A., Villanueva, G., Vispoel, B., Wagner, G., Yachmenev, A. & Yurchenko, S. (2021). "The HITRAN2020 molecular spectroscopic database." In: *Journal of Quantitative Spectroscopy and Radiative Transfer*, 107949. https://doi.org/10.1016/j.jqsrt.2021.107949.

Gorshelev, V., Serdyuchenko, A., Weber, M., Chehade, W. & Burrows, J. P. (2014). "High spectral resolution ozone absorption cross-sections – Part 1: Measurements, data analysis and comparison with previous measurements around 293 K." In: *Atmospheric Measurement Techniques* 7(2), 609–624. https://doi.org/10.5194/amt-7-609-2014.

Greenblatt, G. D., Orlando, J. J., Burkholder, J. B. & Ravishankara, A. R. (1990). "Absorption measurements of oxygen between 330 and 1140 nm." In: *Journal of Geophysical Research* 95(D11), 18577–18582. https://doi.org/10.1029/JD095iD11p18577.

Gross, W. (2016). *Closed loop tracking system using signal beam*. Patent number: US 9,523,759 B2.

Hamamatsu Photonics (2019). *Image sensors*. Handbook. https://www.hamamatsu.com/resources/pdf/ssd/e05_handbook_image_sensors.pdf. Last accessed: 3 July 2021.

Hamamatsu Photonics (2020). *Image Intensifiers*. https://www.hamamatsu.com/resources/pdf/etd/II_TII0007E.pdf. Last accessed: 24 June 2021.

Hamamatsu Photonics (2021). *Dynamic Range*. Author: Spring, Kenneth R. and Davidson, Michael W. https://hamamatsu.magnet.fsu.edu/articles/dynamicrange.html. Last accessed: 27 June 2021.

Hecht, E. (2018), *Optik*, De Gruyter Studium, 7. Auflage edn, Walter de Gruyter GmbH, Berlin and Boston. ISBN: 978-3-11-052665-3.

Hering, E., Martin, R. & Stohrer, M. (2004), *Physik für Ingenieure*, Engineering online library, 9. Aufl. edn, Springer, Berlin. Springer. ISBN: 3-540-21036-9.

Hilgart, A. (2011). *Noise in Image Sensors*. Presentation, Technische Universität Berlin. https://www.eecs.tu-berlin.de/fileadmin/fg144/Courses/10WS/pdci/talks/noise_sensors.pdf. Last accessed: 27 June 2021.

Hinds, W. C. (1999), *Aerosol technology: Properties, behavior, and measurement of airborne particles / William C. Hinds*, 2nd ed. edn, Wiley, New York and Chichester. ISBN: 0-471-19410-7.

Hoogerbrugge, R., Nguyen, P., Wesseling, J., Schaap, M., Wichink Kruit, R., Kamphuis, V., Manders, A. & Weijers, E. (2012). *Assessement of the level of sea salt in PM10 in the Netherlands: Yearly average and exceedance days*. Technical report. National Instititute for Public Health and the Environment.

HORIBA (2021). *Static Light Scattering (SLS) / Laser Diffraction Particle Size Distribution Analysis*. https://www.horiba.com/en_en/staticlight-scattering-sls-laser-diffraction-particle-size-distribution-analysis/. Last accessed: 28 February 2021.

IGACO (2016). Integrated Global Atmospheric Chemistry Observations (IGACO). http://igaco-o3.fmi.fi/ACSO/cross_sections.html. Last updated: 2 May 2016. Last accessed: 3 April 2021.

InnoLas (2021). InnoLas Laser GmbH. https://www.innolas-laser.com/. Last accessed: 24 December 2021.

IUP (2021). https://www.iup.uni-bremen.de/gruppen/molspec/databases/sciamachydata/index.html. Last accessed: 3 April 2021.

Jacubowiez, L., Roch, J.-F., Poizat, J.-P. & Grangier, P. (1997), "Teaching about photodetection noise sources in the laboratory", *in* C. H. F. Velzel, ed., 'Fifth International Topical Meeting on Education and Training in Optics', Vol. 3190,

International Society for Optics and Photonics, SPIE, pp. 166 – 178. https://doi.org/10.1117/12.294378.

Jähne, B. (2002), *Digital image processing*, Springer eBook Collection, 5th revised and extended edition edn, Springer, Berlin and Heidelberg.

Jayaraman, S., Esakkirajan, S. & Veerakumar, T. (2009), *Digital Image Processing*, New Delhi and Tata McGraw-Hill Education.

Jessen, W., Prahl, C., Röger, M. & Pitz-Paal, R. (2020). "Airborne photogrammetric heliostat pre-calibration". DLR, to be published.

Johansen, A., Czajkowski, A., Scobey, M., Egerton, P. & Fortenberry, R. (2017). *Thin-Film Interference Filters for LIDAR*, Alluxa White Paper Series, April 2017, Alluxa, Inc. https://www.alluxa.com/wp-content/uploads/2017/04/Alluxa-Thin-Film-Interference-Filters-for-LIDAR.pdf. Last accessed: 7 November 2021.

Kaaden, N., Massling, A., Schladitz, A., Müller, T., Kandler, K., Schütz, L., Weinzierl, B., Petzold, A., Tesche, M., Leinert, S., Deutscher, C., Ebert, M., Weinbruch, S. & Wiedensohler, A. (2009). "State of mixing, shape factor, number size distribution, and hygroscopic growth of the Saharan anthropogenic and mineral dust aerosol at Tinfou, Morocco." In: *Tellus B: Chemical and Physical Meteorology* 61:1, 51–63. https://doi.org/10.1111/j.1600-0889.2008.00388.x.

Kandler, K., Schütz, L., Deutscher, C., Ebert, M., Hofmann, H., Jäckel, S., Jaenicke, R., Knippertz, P., Lieke, K., Massling, A., Petzold, A., Schladitz, A., Weinzierl, B., Wiedensohler, A., Zorn, S. & Weinbruch, S. (2009). "Size distribution, mass concentration, chemical and mineralogical composition and derived optical parameters of the boundary layer aerosol at Tinfou, Morocco, during SAMUM 2006." In: *Tellus B: Chemical and Physical Meteorology* 61:1, 32–50. https://doi.org/10.1111/j.1600-0889.2008.00385.x.

Keller-Rudek, H., Moortgat, G. K., Sander, R. & Sörensen, R. (2013). "The MPI-Mainz UV/VIS Spectral Atlas of Gaseous Molecules of Atmospheric Interest." In: *Earth System Science Data* 5(2) 365–373. https://doi.org/10.5194/essd-5-365-2013.

Kerker, M. & Loebl, E. M. (1969), *The Scattering of Light and Other Electromagnetic Radiation: Physical Chemistry: A Series of Monographs*, Elsevier Science, Burlington. ISBN: 978-0-12-404550-7.

King, D. & Arvizu, D. (1981). "Heliostat characterization at the central receiver test facility." In: ASME. *J. Sol. Energy Eng.* 103(2), 82–88. https://doi.org/10.1115/1.3266229.

Knippertz, P. & Stuut, J.-B. W., eds (2014), *Mineral Dust: A key player in the earth system*, Springer Netherlands, Dordrecht and s.l. ISBN: 978-94-017-8977-6, https://doi.org/10.1007/978-94-017-8978-3.

Kurucz, R. (1992). "Synthetic infrared spectra." In: *Proceedings of the 154th Symposium of the International Astronomical Union (IAU)*; Tucson, Arizona. Kluwer, Academic. http://adsabs.harvard.edu/full/1994IAUS..154..523K.

Lambert Instruments (2016). *TRiCAM: Time-Resolved Intensified CMOS Camera*. https://www.lambertinstruments.com/s/TRiCAM_Specification_CMOS.pdf. Last accessed: 23 June 2021.

Lambert Instruments (2021a). *Photocathodes*. https://www.lambertinstruments.com/photocathodes. Last accessed: 24 June 2021.

Lambert Instruments (2021b). *Second Generation Image Intensifier*. https://www.lambertinstruments.com/technologies-1/2014/12/4/second-generation-image-intensifier. Last accessed: 24 June 2021.

Lambert Instruments (2021c). *Spatial Resolution of Image Intensifiers*. https://www.lambertinstruments.com/technologies-1/2014/12/4/spatial-resolution-of-image-intensifiers. Last accessed: 20 June 2021.

Lang, K. R. (2013), *Essential Astrophysics*, Springer, Berlin, Heidelberg. ISBN: 978-3-642-35963-7.

Lelli, L. (2014). *Aerosol and Clouds*. Lecture at Universität Bremen.

libRadtran (2020), 'Full resolution extraterrestrial spectrum'. http://www.libradtran.org/doku.php?id=download. Last modified: 23 December 2020. Last accessed: 19 April 2021.

Liou, K.-N. (2002), *An introduction to atmospheric radiation*, Vol. v. 84 of *International geophysics series*, 2nd ed. edn, Academic Press, Amsterdam and Boston. ISBN: 978-0124514515.

Liu, W., Zhang, Z., Li, S. & Tao, D. (2017). "Road Detection by Using a Generalized Hough Transform." In: *Remote Sensing* 9(6). https://doi.org/10.3390/rs9060590.

Lockwood, D. J. (2015). "Rayleigh and Mie Scattering." In: *Luo R. (eds) Encyclopedia of Color Science and Technology. Springer, Berlin, Heidelberg.* https://doi.org/10.1007/978-3-642-27851-8_218-1.

Löfdahl, M. G., Henriques, V. M. J. & Kiselman, D. (2011). "A tilted interference filter in a converging beam." In: *Astronomy & Astrophysics* 533, A82. https://doi.org/10.1051/0004-6361/201117305.

Long, D. A. (1977), *Raman Spectroscopy*, New York; St. Louis; San Francisco; [etc.]: McGraw-Hill. ISBN: 0070386757.

Lumibird (2021). Quantel laser by LUMIBIRD. https://www.quantel-laser.com/tl_files/client/docs_produits/Q-scan_Specs_042021.pdf. Last accessed: 30 December 2021.

Lundgren, K. (2006), *Numerical Simulation of the Spatial and Temporal Distribution of Sea Salt Particles on the Regional Scale.* Degree project in Meteorology, 20p, PhD thesis.

MacLeod, H. A. (2010), *Thin-Film Optical Filters*, CRC Press. https://doi.org/10.1201/9781420073034.

Maini, A. K. (2013), *Lasers and Optoelectronics*, John Wiley & Sons, Ltd, Chichester, United Kingdom. https://doi.org/10.1002/9781118688977.app1.

Marion, B. & Smith, B. (2017). "Photovoltaic system derived data for determining the solar resource and for modeling the performance of other photovoltaic systems." In: *Solar Energy* 147, 349–357. https://doi.org/10.1016/j.solener.2017.03.043.

MathWorks® (2021a). *Image Processing Toolbox™: User's Guide (R2021b).* Retrieved November 5, 2021 from https://de.mathworks.com/help/pdf_doc/images/images_ug.pdf.

MathWorks® (2021b). *Image Processing Toolbox™: Reference (R2021b).* Retrieved November 5, 2021 from https://de.mathworks.com/help/pdf_doc/images/images_ref.pdf.

Mätzler, C. (2002). *MATLAB* Functions for Mie Scattering and Absorption: Research Report No. 2002-08.

Mayer, B. & Kylling, A. (2005). "Technical note: The libRadtran software package for radiative transfer calculations - description and examples of use." In: *Atmospheric Chemistry and Physics* 5(7), 1855–1877. https://doi.org/10.5194/acp-5-1855-2005.

Mayer, Kylling, A., Emde, C., Hamann, U., Buras, R., Gasteiger, J. & Richter, B. (2017). *libRadtran user's guide. Edition for libRadtran version 2.0.2.* http://www.libradtran.org/doku.php. Last accessed: 9 March 2021.

MCIP-ATLAS (2021). http://satellite.mpic.de/spectral_atlas/cross_sections/Oxygen/O2.spc. Last accessed: 3 April 2021.

Meftah, M., Damé, L., Bolsée, D., Hauchecorne, A., Pereira, N., Sluse, D., Cessateur, G., Irbah, A., Bureau, J., Weber, M., Bramstedt, K., Hilbig, T., Thiéblemont, R., Marchand, M., Lefèvre, F., Sarkissian, A. & Bekki, S. (2018). "SOLAR-ISS: A new reference spectrum based on SOLAR/SOLSPEC observations." In: *A&A* 611(A1). https://doi.org/10.1051/0004-6361/201731316.

Merriam-Webster (2021a). "Extinction coefficient." *Merriam-Webster.com Dictionary*, Merriam-Webster, https://www.merriam-webster.com/dictionary/extinction%20coefficient. Accessed 6 Jan. 2021.

Merriam-Webster (2021b). "Scattering Coefficient." *Merriam-Webster.com Dictionary*, Merriam-Webster, https://www.merriam-webster.com/dictionary/scatteringcoefficient. Accessed 6 Jan. 2021.

Mie, G. (1908). "Beiträge zur Optik trüber Medien, speziell kolloidaler Metallösungen." In: *Annalen der Physik* 330(3), 377–445. https://doi.org/10.1002/andp.19083300302.

MiePlot (2018). *MiePlot: A computer program for scattering of light from a sphere using Mie theory & the Debye series.* http://www.philiplaven.com/mieplot.htm. Last accessed: 14 October 2021.

Migdall, A. L., Frenkel, A. & Kelleher, D. E. (1993). "Filter Transmittance Measurements in the Infrared." In: *Journal of research of the National Institute of Standards and Technology* 98(6), 691–697. https://doi.org/10.6028/jres.098.045.

Miles, R. B., Lempert, W. R. & Forkey, J. N. (2001). "Laser Rayleigh scattering." In: *Meas. Sci. Technol.* 12, R33–R51.

Mishchenko, M. I. (2009). "Gustav Mie and the fundamental concept of electromagnetic scattering by particles: A perspective." In: *Journal of Quantitative Spectroscopy and Radiative Transfer* 110(14-16), 1210–1222. https://doi.org/10.1016/j.jqsrt.2009.02.002.

Moosmüller, H. & Arnott, W. P. (2009). "Particle Optics in the Rayleigh Regime." In: *Journal of the Air & Waste Management Association* 59:9, 1028–1031. https://doi.org/10.3155/1047-3289.59.9.1028.

Müller, T., Schladitz, A., Massling, A., Kaaden, N., Kandler, K. & Wiedensohler, A. (2009). "Spectral absorption coefficients and imaginary parts of refractive indices of Saharan dust during SAMUM-1." In: *Tellus B: Chemical and Physical Meteorology* 61(1), 79–95. https://doi.org/10.1111/j.1600-0889.2008.00399.x.

Murillo-Bracamontes, E. A., Martinez-Rosas, M. E., Miranda-Velasco, M. M., Martinez-Reyes, H. L., Martinez-Sandoval, J. R. & Cervantes-de Avila, H. (2012). "Implementation of Hough transform for fruit image segmentation." In: *Procedia Engineering* 35, 230–239. https://doi.org/10.1016/j.proeng.2012.04.185.

Nieffer, D., Effertz, T., Macke, A., Röger, M., Weinrebe, G. & Ulmer, S. (2019). "Heliostat testing according to SolarPACES task III guideline." In: *AIP Conference Proceedings* 2126, 030039. https://doi.org/10.1063/1.5117551.

NREL (2021a). *Power Tower Projects.*. National Renewable Energy Laboratory (NREL). https://solarpaces.nrel.gov/by-technology/power-tower. Last accessed: 16 October 2021.

NREL (2021b). *Reference Air Mass 1.5 Spectra.*. National Renewable Energy Laboratory (NREL). https://www.nrel.gov/grid/solar-resource/spectra-am1.5.html. Last accessed: 13 October 2021.

OmegaOptical (2012). "Optical Interference Filters: For Life Sciences, Machine Vision, Astronomy, Aerospace." Omega Optical, LLC. Catalog 2012. www.omegafilters.com. Downloaded on 9 November from distributor OptoScience Inc. https://www.optoscience.com/maker/omega/pdf/Omega_Optical_2012_Catalog.pdf.

Otto, S., de Reus, M., Trautmann, T., Thomas, A., Wendisch, M. & Borrmann, S. (2007). "Atmospheric radiative effects of an in-situ measured Saharan dust

plume and the role of large particles." In: *Atmospheric Chemistry and Physics Discussions* 7(3), 7767–7817. https://doi.org/10.5194/acp-7-4887-2007.

Oxford Instruments (2020). *iXon Ultra*. https://andor.oxinst.com/assets/uploads/products/andor/documents/andor-ixon-ultra-emccd-specifications.pdf. Last accessed: 27 June 2021.

Paschotta, R. (2008), *Field Guide to Lasers*. SPIE Press, Bellingham, WA. ISBN: 9780819469618.

Paschotta, R. (2021a). Article on *Microchannel Plates* in the RP Photonics Encyclopedia. https://www.rp-photonics.com/microchannel_plates.html. Last accessed: 26 June 2021.

Paschotta, R. (2021b). Article on *Image Intensifiers and Image Converters* in the RP Photonics Encyclopedia. https://www.rp-photonics.com/image_intensifiers_and_image_converters.html. Last accessed: 26 June 2021.

Paschotta, R. (2021c). Article on *Excimer Lasers* in the RP Photonics Encyclopedia. https://www.rp-photonics.com/excimer_lasers.html. Last accessed: 25 December 2021.

Paschotta, R. (2021d). Article on *YAG Lasers* in the RP Photonics Encyclopedia. https://www.rp-photonics.com/yag_lasers.html. Last accessed: 25 December 2021.

Paschotta, R. (2021e). Article on *YAG Lasers* in the RP Photonics Encyclopedia. https://www.rp-photonics.com/yag_lasers.html. Last accessed: 25 December 2021.

Paschotta, R. (2021f). Article on *Solid-state Lasers* in the RP Photonics Encyclopedia. https://www.rp-photonics.com/solid_state_lasers.html. Last accessed: 20 November 2021.

Paschotta, R. (2021g). Article on *Dye Lasers* in the RP Photonics Encyclopedia. https://www.rp-photonics.com/dye_lasers.html. Last accessed: 20 November 2021.

Paschotta, R. (2021h). Article on *Gas Lasers* in the RP Photonics Encyclopedia. https://www.rp-photonics.com/gas_lasers.html. Last accessed: 20 November 2021.

Paschotta, R. (2021i). Article on *Semiconductor Lasers* in the RP Photonics Encyclopedia. https://www.rp-photonics.com/semiconductor_lasers.html. Last accessed: 20 November 2021.

Paschotta, R. (2021j). Article on *Optical Parametric Oscillators* in the RP Photonics Encyclopedia. https://www.rp-photonics.com/optical_parametric_oscillators.html. Last accessed: 29 December 2021.

Paschotta, R. (2021k). Article on *Polarization of Light* in the RP Photonics Encyclopedia. https://www.rp-photonics.com/polarization_of_light.html. Last accessed: 20 November 2021.

Paschotta, R. (2021l). Article on *Flat Top Beams* in the RP Photonics Encyclopedia. https://www.rp-photonics.com/flat_top_beams.html. Last accessed: 31 December 2021.

PCO (2018). *Everything you always wanted to know about sCMOS cameras: But were afraid to ask.* PCO AG. https://www.pco.de/fileadmin/fileadmin/user_upload/pco-product_sheets/PCO_scmos_ebook.pdf. Last accessed: 3 July 2021.

PCO (2021). *pco.dicam C1: Intensified sCMOS - whitepaper - v2.00.* PCO AG. https://www.pco.de/fileadmin/user_upload/pco-product_sheets/WP_PCODICAMTECHNOLOGY_V200.pdf. Last accessed: 24 June 2021.

Peli, E. (1990). "Contrast in complex images." In: *J. Opt. Soc. Am. A* 7(10), 2032–2040.

Penkała, M., Ogrodnik, P. & Rogula-Kozłowska, W. (2018). "Particulate Matter from the Road Surface Abrasion as a Problem of Non-Exhaust Emission Control.

Penndorf, R. (1957). "Tables of the Refractive Index for Standard Air and the Rayleigh Scattering Coefficient for the Spectral Region between 0.2 and 20.0 μ and Their Application to Atmospheric Optics." In: *Journal of the Optical Society of America* 47(2), 176–182. https://doi.org/10.1364/JOSA.47.000176.

Perim de Faria, J., Schmitt, S., Blomel, T., Bundke, U., Hohaus, T., Mentel, T., Zhao, D., Kiendler-Scharr, A., Petzold, A., Onasch, Timothy B. & Freedman, A. (2018). *Annual cycle, seasonality and vertical distribution of aerosol optical and chemical properties observed at a continental site in Western Europe.* Presentation at European Geosciences Union General Assembly. 8–13 April, Vienna, Austria.

Petty, G. W. (2006), *A first course in atmospheric radiation*, 2nd ed. edn, Sundog Pub, Madison, Wis.

Petzold, A. (2015). *Measurement Methods in Atmospheric Research: Aerosol Optical Properties and Measurement*. Forschungszentrum Jülich, IEK-8 Troposphere, Jülich, Germany. Lecture at University of Wuppertal.

Petzold, A., Rasp, K., Weinzierl, B., Esselborn, M., Hamburger, T., Dörnbrack, A., Kandler, K., Schuütz, L., Knippertz, P., Fiebig, M. & Virkkula, A. (2009). "Saharan dust absorption and refractive index from aircraft-based observations during SAMUM 2006." In: *Tellus B: Chemical and Physical Meteorology* 61(1), 118–130. https://doi.org/10.1111/j.1600-0889.2008.00383.x.

Pfahl, A., Buck, R. & Rehschuh, K. (2009). *Method for controlling the alignment of a heliostat with respect to a receiver, heliostat device and solar power plant*. US Patent Number: US 8,651,100 B2.

Pfahl, A., Coventry, J., Röger, M., Wolfertstetter, F., Vásquez-Arango, J. F., Gross, F., Arjomandi, M., Schwarzbözl, P., Geiger, M. & Liedke, P. (2017). "Progress in heliostat development." In: *Solar Energy* 152(1), 3–37. https://doi.org/10.1016/j.solener.2017.03.029.

PhotonicSolutions (2021). Photonic Solutions Ltd. https://www.photonicsolutions.co.uk/product-detail.php?prod=6401. Last accessed: 24 December 2021.

Pliutau, D. & Roslyakov, K. (2017). "Bytran - |- spectral calculations for portable devices using the HITRAN database." In: *Earth Sci Inform* 10, 395–404. https://doi.org/10.1007/s12145-017-0288-4.

Prahl, C., Göhring, F., Röger, M., Hilgert, C. & Ulmer, S. (2015). *Verfahren zur Vermessung von Heliostaten*. Patent DE 10 2015 217 086 B4. *Procedimiento para la medición de heliostatos*, Patent number: ES000002604554B2.

Prahl, C., Röger, M. & Kiewitt, W. (2009). "Advances in optical measurement techniques for solar concentrators". In: *SolarPACES 2009*, Berlin, Germany, 15 – 18 September, 2009.

Proxitronic (2011). *High Performance Image Intensifiers*. PROXITRONIC Detector Systems GmbH, Author: Ecker, P. https://www.proxivision.de/datasheets/image-intensifier-general-information.pdf. Last accessed: 23 June 2021.

QuantumComposers (2021). Quantum Composers Inc. https://www.quantumcomposers.com/. Last accessed: 24 December 2021.

Roedel, W. & Wagner, T. (2018), *Physik unserer Umwelt: Die Atmosphäre*, fifth edition edn, Springer Spektrum, Berlin, Heidelberg. ISBN: 978-3-662-54257-6.

Röger, M., Prahl, C., Jessen, W., Schwarzbözl, P., Sattler, J., Niederwestberg, S. & Göttsche, J. (2018). *Verfahren zur Vermessung und Kalibrierung von Heliostaten.* 21. Kölner Sonnenkolloquium. https://elib.dlr.de/122783/.

Röger, M., Prahl, C. & Ulmer, S. (2010). "Heliostat shape and orientation by edge detection." In: *J. Sol. Energy Eng.* 132(2), 21002. https://doi.org/10.1115/1.4001400.

Sattler, J. C. & Göttsche, J. (2022). "Progress in the Development of a Laser and Camera System for the Calibration of Heliostat Fields of Central Receiver Systems." In: *AIP Conference Proceedings* 2445, 070011. https://doi.org/10.1063/5.0086273.

Sattler, J. C. & Göttsche, J. (2023). "Progress in the Development of a Laser and Camera System for the Calibration of Heliostat Fields of Central Receiver Systems: Part 2." In: *AIP Conference Proceedings* 2815, 080012. https://doi.org/10.1063/5.0149568.

Sattler, J. C., Röger, M., Schwarzbözl, P., Buck, R., Macke, A., Raeder, C. & Göttsche, J. (2020). "Review of heliostat calibration and tracking control methods." In: *Solar Energy* 207, 110–132. https://doi.org/10.1016/j.solener.2020.06.030.

Sauerborn, M., Göttsche, J. & Hoffschmidt, B. (2013). *Machbarkeitsstudie zur Entwicklung einer radargestützten Positionsregelung von Heliostatenfeldern für Solarturmkraftwerke (HelioScan).* Schlussbericht, TIB Hannover.

Sauerborn, M., Klimek, J., Hoffschmidt, B., Sieger, S., Biegel, G., Essen, H., Göttsche, J. & Hilger, P. (2012). "Determination of heliostat mirror orientation by radar technology." In: *SolarPACES 2012*, Marrakech, Morocco, 11 – 14 September, 2012.

Schell, S. (2011). "Design and evaluation of esolar's heliostat fields." In: *Solar Energy* 85(4), 614–619. https://doi.org/10.1016/j.solener.2010.01.008.

Schneeweiss, C., Eichler, J. & Brose, M. (2017), *Leitfaden für Laserschutzbeauftragte: Ausbildung und Praxis / Claudia Schneeweiss, Jürgen Eichler, Martin Brose*, Springer Spektrum, Berlin, Germany. ISBN: 978-3-662-53523-3.

SENER (2018). *HE54 heliostat*. https://www.energy.sener/pdf-profile-project/he54-heliostat. Last accessed: 16 October 2021.

Serdyuchenko, A., Gorshelev, V., Weber, M., Chehade, W. & Burrows, J. P. (2014). "High spectral resolution ozone absorption cross-sections – Part 2: Temperature dependence." In: *Atmospheric Measurement Techniques* 7(2), 625–636. https://doi.org/10.5194/amt-7-625-2014.

Shapiro, A. I., Solanki, S. K., Krivova, N. A., Tagirov, R. V. & Schmutz, W. K. (2015). "The role of the Fraunhofer lines in solar brightness variability." In: *A&A* 581, A116. https://doi.org/10.1051/0004-6361/201526483.

Sorribas, M., de La Morena, B. A., Wehner, B., López, J. F., Prats, N., Mogo, S., Wiedensohler, A. & Cachorro, V. E. (2011). "On the sub-micron aerosol size distribution in a coastal-rural site at El Arenosillo Station (SW – Spain)." In: *Atmospheric Chemistry and Physics* 11(21), 11185–11206. https://acp.copernicus.org/articles/11/11185/2011/.

Stanford (2021a). *Image intensifier: Photocathode*. Stanford Computer Optics, Inc. https://stanfordcomputeroptics.com/technology/image-intensifier/photocathode.html. Last accessed: 25 October 2021.

Stanford (2021b). *Image intensifier: Multi-channel plate - MCP*. Stanford Computer Optics, Inc. https://stanfordcomputeroptics.com/technology/image-intensifier/multi-channel-plate.html. Last accessed: 25 October 2021.

Stanford (2021c). *Image intensifier: Phosphor screen*. Stanford Computer Optics, Inc. https://stanfordcomputeroptics.com/technology/image-intensifier/phosphor-screen.html. Last accessed: 25 October 2021.

Stanford (2021d). *Image intensifiers: How to make the right choice?*. Stanford Computer Optics, Inc. https://stanfordcomputeroptics.com/technology/image-intensifier/image-intensifiers-selection.html. Last accessed: 17 November 2021.

Stanford Computer Optics (2013). *Ion Feedback*. Technical note. https://stanfordcomputeroptics.com/download/ion-feedback.pdf. Last accessed: 26 June 2021.

Stemmer Imaging (2018). *The Imaging & Vision Handbook*. ISBN 978-3-9820109-1-5.

Strutt, J. W. (1871a). "LVIII. On the scattering of light by small particles." In: *The London, Edinburgh, and Dublin Philosophical Magazine and Journal of Science* 41(275), 447–454. https://doi.org/10.1080/14786447108640507.

Strutt, J. W. (1871b). "XXXVI. On the light from the sky, its polarization and colour." In: *The London, Edinburgh, and Dublin Philosophical Magazine and Journal of Science* 41(273), 274–279. https://doi.org/10.1080/14786447108640479.

Strutt, J. W. (1871c). "XV. On the light from the sky, its polarization and colour." In: *The London, Edinburgh, and Dublin Philosophical Magazine and Journal of Science* 41(271), 107–120. https://doi.org/10.1080/14786447108640452.

Sutter, F., Montecchi, M., von Dahlen, H., Fernández-García, A. & Röger, M. (2018). "The effect of incidence angle on the reflectance of solar mirrors." In: *Solar Energy Materials and Solar Cells* 176, 119–133. https://doi.org/10.1016/j.solmat.2017.11.029.

Swart, B. D. (2017). *A method for accurate measurement of heliostat mirror orientation*. Master's thesis, Stellenbosch University. sterg.sun.ac.za/wp-content/uploads/2010/.

Sympatec (2021). *Laser Diffraction*. https://www.sympatec.com/en/particle-measurement/glossary/laser-diffraction/. Last accessed: 28 February 2021.

Tagle-Salazar, P. D., Nigam, K. D. & Rivera-Solorio, C. I. (2020). "Parabolic trough solar collectors: A general overview of technology, industrial applications, energy market, modeling, and standards." In: *Green Processing and Synthesis* 9(1), 595–649. https://doi.org/10.1515/gps-2020-0059.

Talbot, H., Phelippeau, H., Akil, M. & Bara, S. (2009). "Efficient Poisson denoising for photography." In: *16th IEEE International Conference on Image Processing (ICIP)*, 3881–3884. https://doi.org/10.1109/ICIP.2009.5414042.

Tan, L. (2006). "Image file formats." In: *Biomedical imaging and intervention journal* 2(1), e6. https://doi.org/10.2349/biij.2.1.e6.

Teledyne (2020). *What is Scientific Imaging Quality*. Author: Keal, Louis.https://www.photometrics.com/wp-content/uploads/2021/01/

Scientific-Image-Quality-A3-19-11-2020.pdf. Last accessed: 4 July 2021.

Teledyne (2021b). *Full Well Capacity and Pixel Saturation. Educational Notes*. Teledyne Princeton Instruments. https://www.princetoninstruments.com/learn/camera-fundamentals/full-well-capacity-pixel-saturation. Last accessed: 27 June 2021.

Temme, N. M. (1987). "The Radon Transform: First Steps." https://www.researchgate.net/publication/241882515_The_radon_transform_first_steps/references.

Thakur, K. V., Damodare, O. H. & Sapkal, A. M. (2016). "Poisson Noise Reducing Bilateral Filter." In: *Procedia Computer Science* 79, 861–865. https://doi.org/10.1016/j.procs.2016.03.087.

Toft, P. A. (1996). *The Radon Transform - Theory and Implementation*. Technical University of Denmark. https://backend.orbit.dtu.dk/ws/portalfiles/portal/5529668/Binder1.pdf. Last accessed: 12 July 2021.

Tomasi, C. & Lupi, A. (2017), *Primary and Secondary Sources of Atmospheric Aerosol*, chapter 1, pp. 1–86. John Wiley & Sons, Ltd. In: *Atmospheric Aerosols*. https://onlinelibrary.wiley.com/doi/abs/10.1002/9783527336449.ch1.

Träger, F. (2007), *Springer Handbook of Lasers and Optics*, Springer, New York. ISBN: 978-0-387-30420-5.

Trickl, T. (2018). Personal communication.

Trieb, F. (2018). *Interference of Flying Insects and Wind Parks: Study Report*. Deutsches Zentrum für Luft- und Raumfahrt. https://www.dlr.de/tt/Portaldata/41/Resources/dokumente/st/FliWip-Final-Report.pdf. Last accessed: 11 August 2021.

Trochkine, D., Iwasaka, Y., Matsuki, A., Yamada, M., Kim, Y.-S., Nagatani, T., Zhang, D., Shi, G.-Y. & Shen, Z. (2003). "Mineral aerosol particles collected in Dunhuang, China, and their comparison with chemically modified particles collected over Japan." In: *Journal of Geophysical Research* 108(D23), 1620. https://doi.org/10.1029/2002JD003268.

TSI (2012). *AEROSOL STATISTICS LOGNORMAL DISTRIBUTIONS AND dN/dlogDp*. Application Note PR-001. TSI Incorporated. https:

//tsi.com/getmedia/1621329b-f410-4dce-992b-e21e1584481a/PR-001-RevA_Aerosol-Statistics-AppNote?ext=.pdf. Last accessed: 25 October 2021.

TSI (2018). *Urban Air Quality Monitoring: Number- and mass-based solutions from TSI.* TSI Incorporated. Application note ENV-002 (US), (8/21/2018) REV A. https://tsi.com/getmedia/4462d747-26ba-40a4-9609-b7ccd2bdd22e/Application-Note-ENV-002-(US)-Rev-A_Web?ext=.pdf. Last accessed: 5 November 2021.

Tsunogai, S. (1975). "Sea salt particles transported to the land." In: *Tellus* 27(1), 51–58. https://doi.org/10.3402/tellusa.v27i1.9883.

Tucsen (2021). *Dhyana 400BSI V2: BSI Scientific CMOS Camera.* http://www.tucsen.com/Public/upload/download/pdf/Dhyana%20400BSI-EN.pdf. Last accessed: 4 July 2021.

Tyndall, J. (1869). "IV. On the blue colour of the sky, the polarization of skylight, and on the polarization of light by cloudy matter generally." In: *Proceedings of the Royal Society of London* 17, 223–233. https://doi.org/10.1098/rspl.1868.0033.

van de Hulst, H. C. (1957, 2012), *Light Scattering by Small Particles*, Dover Books on Physics, Dover Publications, Newburyport. ISBN: 9780486642284.

van der Does, M., Knippertz, P., Zschenderlein, P., Giles Harrison, R. & Stuut, J.-B. W. (2018). "The mysterious long-range transport of giant mineral dust particles." In: *Science advances* 4(12). https://doi.org/10.1126/sciadv.aau2768.

Wagner, R., Ajtai, T., Kandler, K., Lieke, K., Linke, C., Müller, T., Schnaiter, M. & Vragel, M. (2012). "Complex refractive indices of Saharan dust samples at visible and near UV wavelengths: a laboratory study." In: *Atmospheric Chemistry and Physics* 12(5), 2491–2512. https://acp.copernicus.org/articles/12/2491/2012/.

Weidel, H. (2008). *Die Verteilung des Aeroplanktons über Schleswig-Holstein.* Dissertation, Christian-Albrechts-Universität Kiel, 2008, https://d-nb.info/1019553197/34. Last accessed: 11 August 2021.

Wilson, W. E. & Reist, P. C. (1994). "A PC-based Mie scattering program for theoretical investigations of the optical properties of atmospheric aerosols as a function

of composition and relative humidity." In: *Atmospheric Environment* 28(5), 803–809. https://doi.org/10.1016/1352-2310(94)90239-9.

Wiscombe, W. J. (1979). *Mie Scattering Calculations: Advances in Technique and Fast, Vector-Speed Computer Codes*. Technical note. National Center for Atmospheric Research.

Wiscombe, W. J. (1980). "Improved Mie scattering algorithms." In: *Applied optics* 19(9), 1505–1509.

XIMEA (2021). *Scientific sCMOS front and back illuminated*. https://www.ximea.com/en/products/xilab-application-specific-custom-oem/scientific-scmos-cameras-with-front-back-illumination. Last updated: 25 October 2021. Last accessed: 4 July 2021.

Yogev, A. & Krupkin, V. (1999). *Control of a heliostat field in a solar energy plant*. US Patent Number: 5,862,799. Patent issue date: 26 January 1999.

Young, A. T. (1982). "Rayleigh scattering." In: *Physics Today* 35(1), 42–48. https://physicstoday.scitation.org/doi/10.1063/1.2890003.

A Appendix

Continuation from section 3.1.4 on the topic: *Mie scattering.*

The previously mentioned scattering amplitudes $S_1(\theta)$ and $S_2(\theta)$ are described by equations A.1 and A.2 (Kerker & Loebl 1969, p. 62).

$$S_1(\theta) = \sum_{n=1}^{\infty} \frac{2n+1}{n(n+1)} \left[a_n \pi_n(\cos\theta) + b_n \tau_n(\cos\theta) \right] \tag{A.1}$$

$$S_2(\theta) = \sum_{n=1}^{\infty} \frac{2n+1}{n(n+1)} \left[a_n \tau_n(\cos\theta) + b_n \pi_n(\cos\theta) \right] \tag{A.2}$$

In equations A.1 and A.2 the equations of the Legendre functions are $\pi_n(\cos\theta) = \frac{1}{\sin\theta} P_n^{(1)}(\cos\theta)$ and $\tau_n(\cos\theta) = \frac{d}{d\theta} P_n^{(1)}(\cos\theta)$ (Kerker & Loebl 1969, p. 62) and the variables a_n and b_n are the so-called scattering coefficients. Mätzler (2002) states that "The functions $\pi\cos(\theta)$ *and* $\tau\cos(\theta)$ describe the angular scattering patterns of the spherical harmonics used to describe S_1 and S_2 and follow from the recurrence relations" (p. 8) given by equations A.3 and A.4 for $0 \leq \theta \leq \pi$. The expression $P_n^{(1)}$ is the Legendre polynomial of order n and first degree.

In the BHMIE algorithm from Bohren & Huffman (1983, 2008)[p. 477], n is limited by the equation $n_{\max} = x + 4x^{1/3} + 2$ because values well beyond $n_{\max}$ might lead to scattering coefficients to be computed inaccurately.

$$\pi_n = \frac{2n-1}{n-1} \cos\theta \cdot \pi_{n-1} - \frac{n}{n-1} \pi_{n-2} \tag{A.3}$$

$$\tau_n = n\cos\theta \cdot \pi_n - (n+1)\pi_{n-1} \tag{A.4}$$

The following are the values for π and τ for $n = 0$ to 2 (Deirmendjian 1969, p. 15).

$$\pi_0 = 0 \qquad \tau_0 = 0$$
$$\pi_1 = 1 \qquad \tau_1 = \cos\,\theta$$
$$\pi_2 = 3\cos\,\theta \qquad \tau_2 = 3 \cdot \cos 2\theta$$
$$\pi_3 = \tfrac{5}{2}\cos\,\theta - \tfrac{3}{2} \qquad \tau_3 = 3\cos\,\theta$$

Figure A.1 shows the values of the functions π and τ against the scattering angle θ, respectively, and are also shown in (van de Hulst 1957, 2012, p. 125). The same data of the functions π and τ can also be presented as polar plots as shown in Figure A.2 and Figure A.3 (in these plots the values of π and τ, that are normally shown on the radial axes, were omitted).

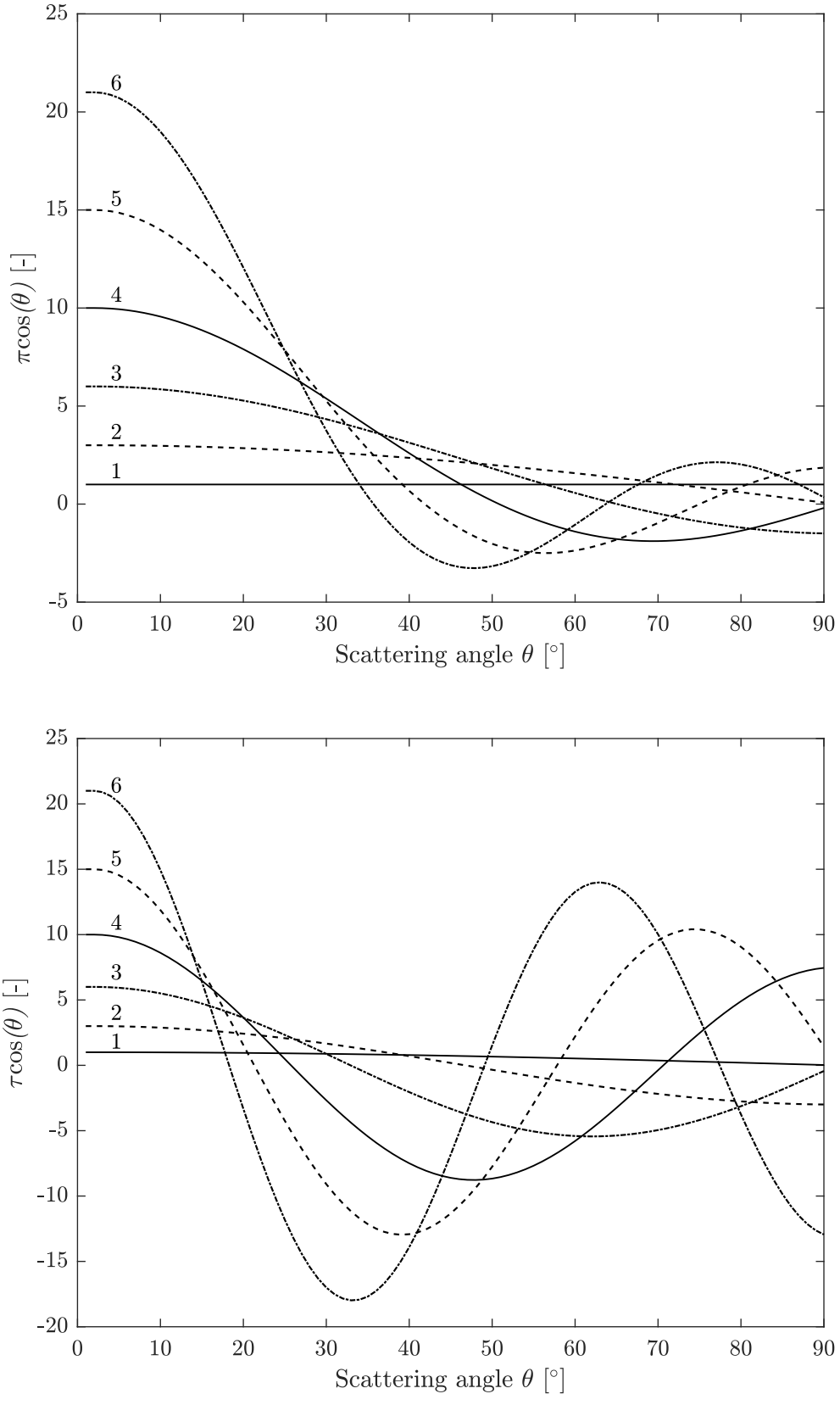

Figure A.1: Values for the functions π (top) and τ (bottom) against the scattering angle θ (created using data from Mie MATLAB® code from Mätzler (2002)).

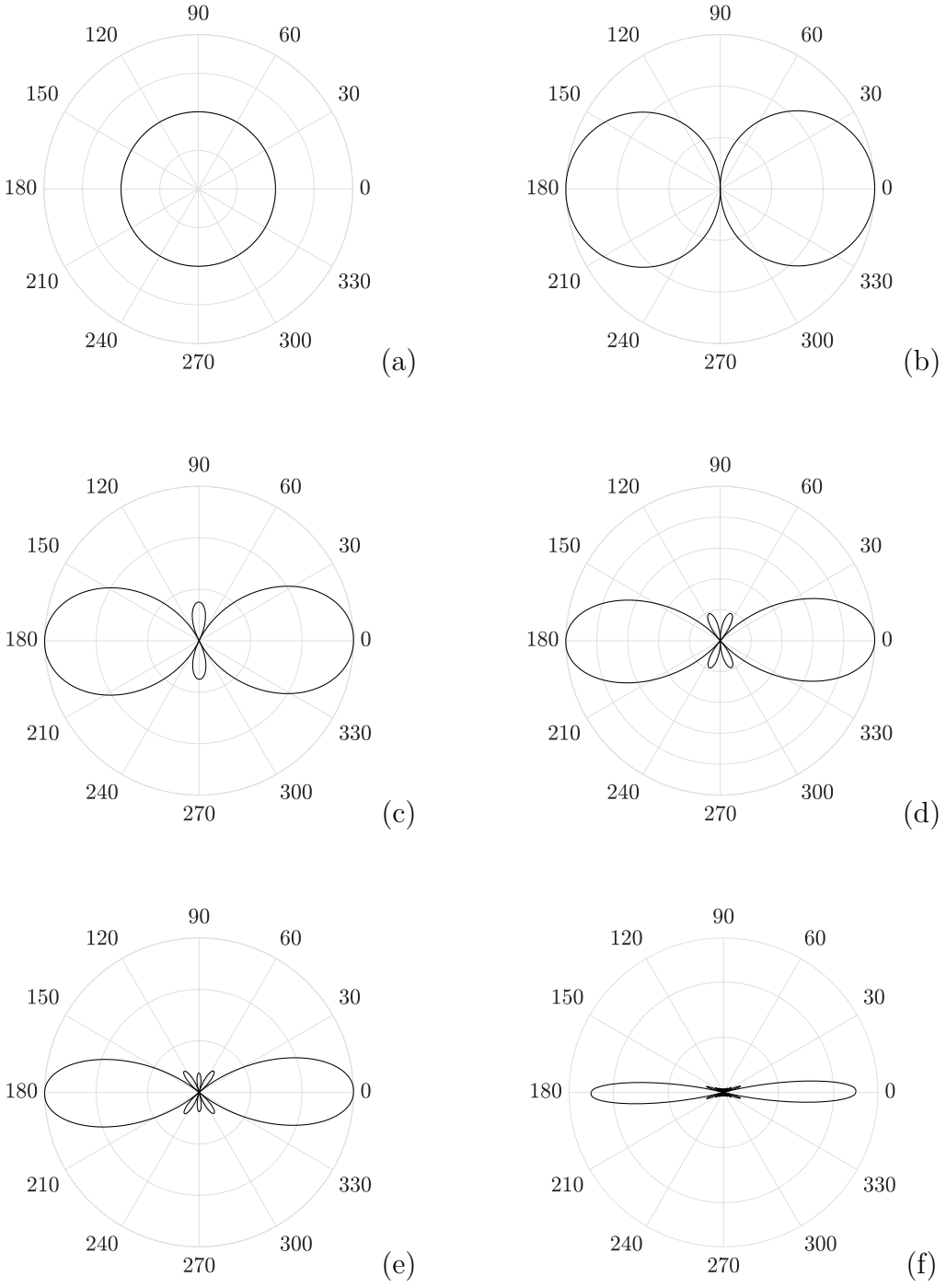

Figure A.2: Function π describing the angular scattering patterns of the spherical harmonics (created using data from Mie MATLAB® code from Mätzler (2002)).

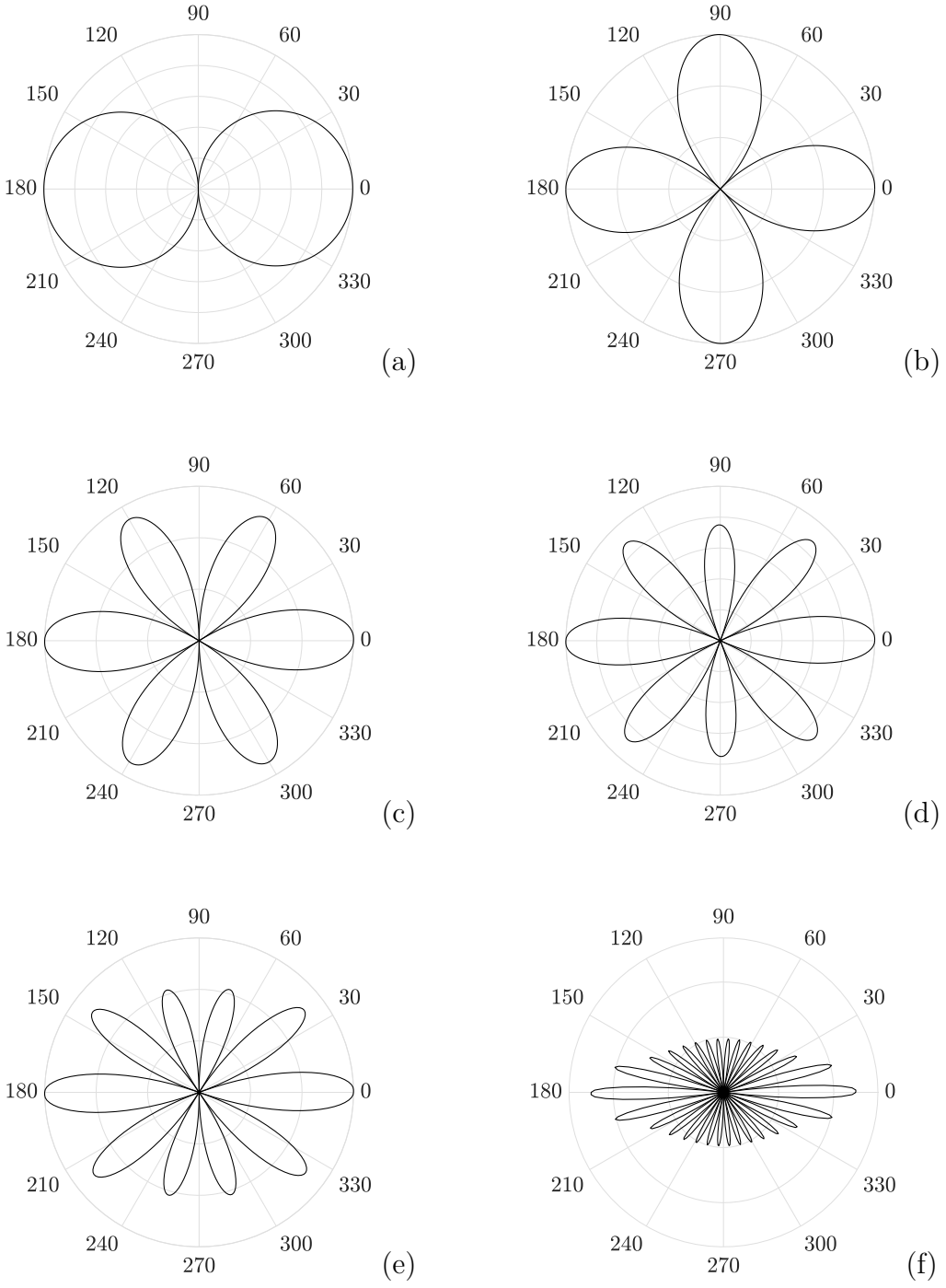

Figure A.3: Function τ describing the angular scattering patterns of the spherical harmonics (created using data from Mie MATLAB® code from Mätzler (2002)).

The scattering coefficients a_n and b_n are needed for computing the amplitudes of the scattered fields (Mätzler 2002). With equations A.5 and A.6 the scattering coefficients a_n and b_n can be calculated (Bohren & Huffman 1983, 2008, p. 100):

$$a_n = \frac{\mu m^2 j_n(mx)[x j_n(x)]' - \mu_1 j_n(x)[mx j_n(mx)]'}{\mu m^2 j_n(mx)[x h_n^1(x)]' - \mu_1 h_n^1(x)[mx j_n(mx)]'} \tag{A.5}$$

$$b_n = \frac{\mu_1 j_n(mx)[x j_n(x)]' - \mu j_n(x)[mx j_n(mx)]'}{\mu_1 j_n(mx)[x h_n^1(x)]' - \mu h_n^1(x)[mx j_n(mx)]'} \tag{A.6}$$

where the parameter μ_1 is the magnetic permeability of the sphere, μ is the magnetic permeability of the ambient medium, m is the relative refractive index (ratio of complex refractive index of particle and the surrounding medium, respectively), x is the so-called size parameter and the functions $j_n(x)$ and $h_n^1(x)$ are spherical Bessel functions of the order n (with n = 1,2,...) (Mätzler 2002, p. 2). In other literature the functions are written $j_n(z)$ and $h_n^1(z)$. The scattering coefficients a_n and b_n are independent of the scattering angle. When considering non-absorbing spherical particles, then the values of the scattering coefficients a_n and b_n are always within the conditions $|a_n - \frac{1}{2}|^2 = \frac{1}{4}$ and $|b_n - \frac{1}{2}|^2 = \frac{1}{4}$ and therefore are plotted within a radius of 0.5 on the real axis and the plot will look like a spiral (Deirmendjian 1969, p. 24). For spherical particles with absorbing characteristics (i.e. the complex refractive index will have an imaginary part), the plot will look different to an ordered spiral.

For more details on the scattering coefficients see, for example, Bohren & Huffman (1983, 2008), Deirmendjian (1969) and Mätzler (2002) (the latter two also describe the equations in computational forms). Moreover, in the work of Deirmendjian (1969), the scattering coefficients are shown and discussed.

Plots of phase functions and polar plots of phase functions are shown in Figure A.4 and Figure A.5.

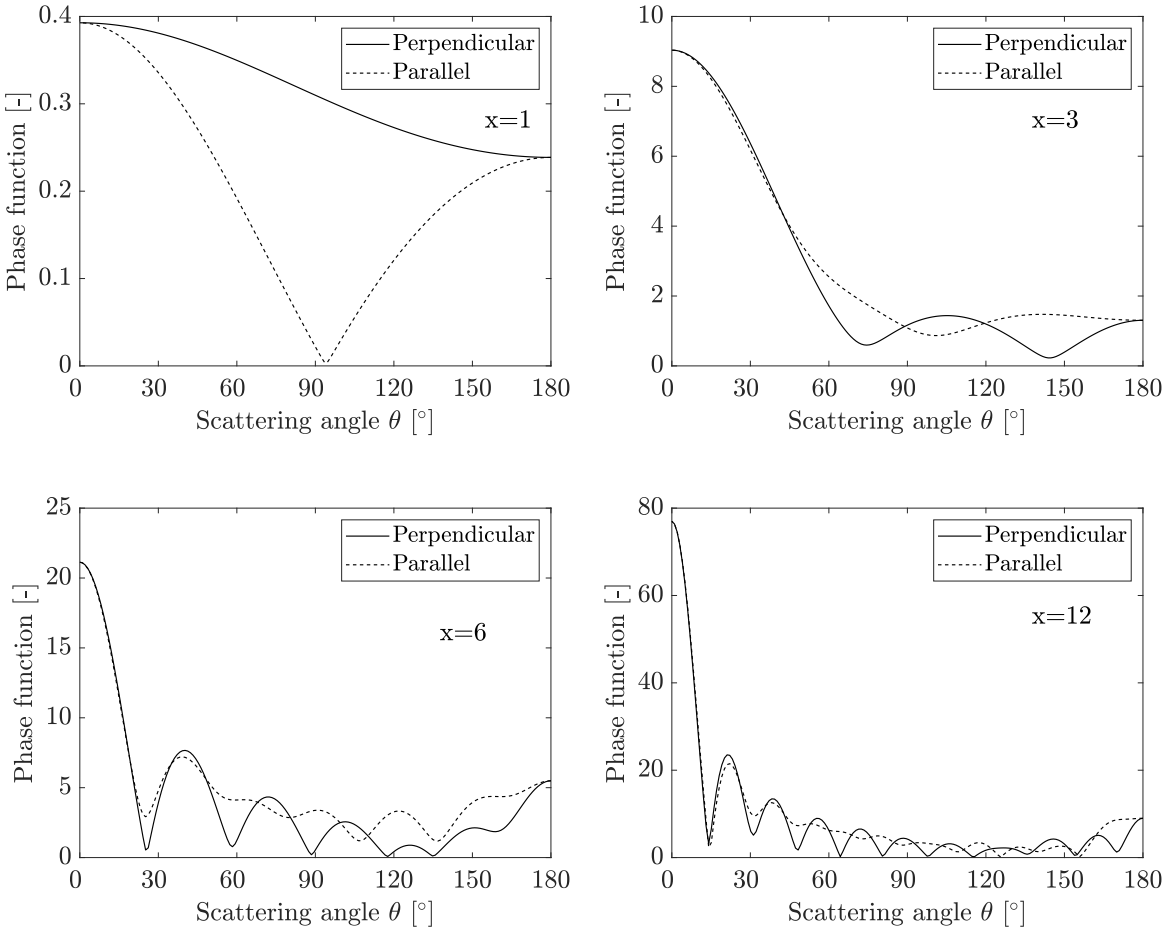

Figure A.4: Plots of phase functions for various size parameters x. The data for the plots was extracted from calculations with the MATLAB® version of the BHMIE computer code by Mätzler (2002).

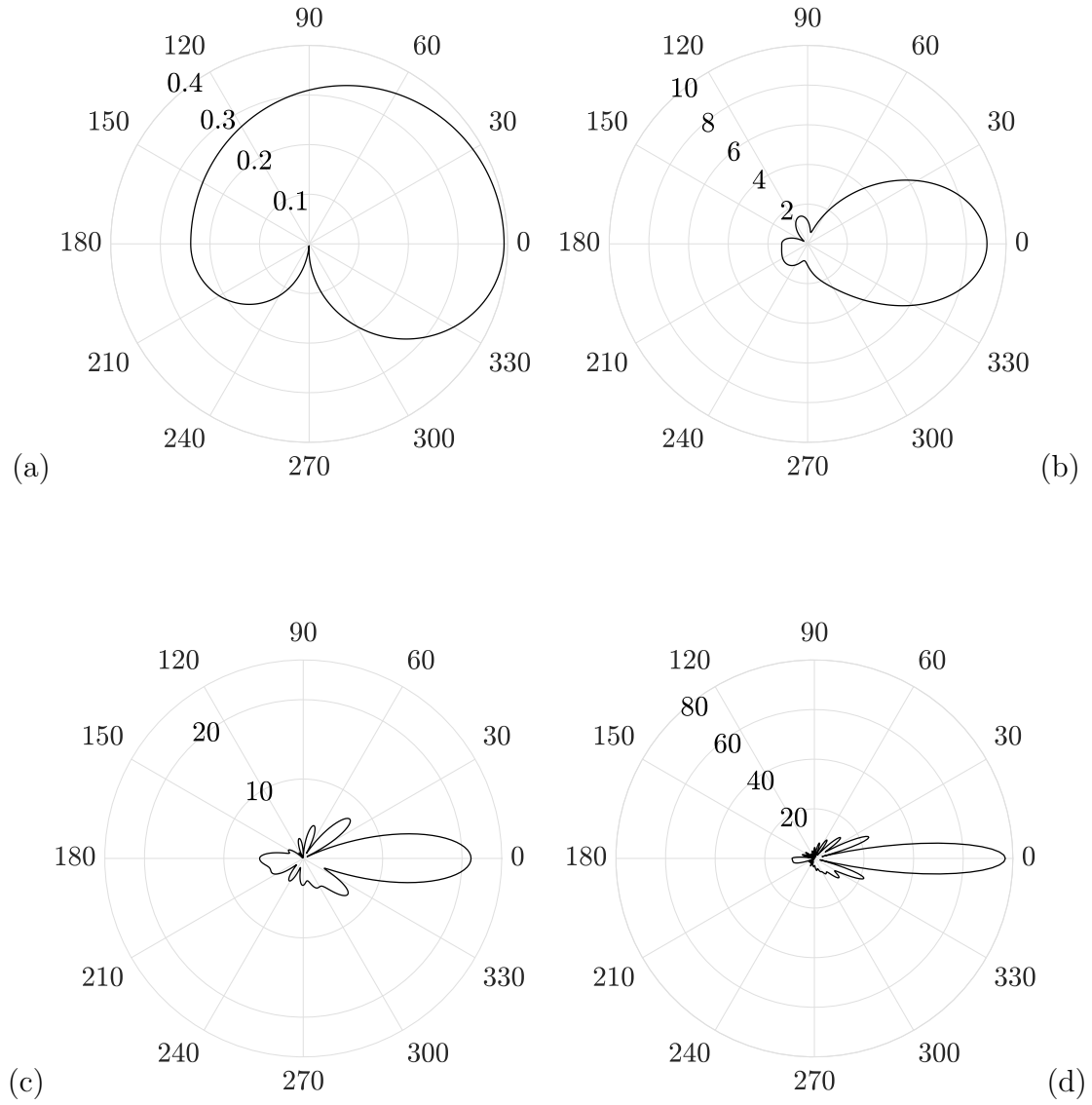

Figure A.5: Polar plots of phase functions for various size parameters x. a) $x = 1$, b) $x = 3$, c) $x = 6$ and d) $x = 12$.

Continuation of excursus from section 4.1 on the topic: *Exploration of low DHI in the O_2 absorption A-band.*

The below Figure A.6 (top) shows in detail that the SSI in the IR wavelength range fluctuates strongly, but there are far fewer fluctuations than in the UV range. Previously it was stated that there is a minimum in the DHI around the wavelength 760.5 nm. In Figure A.6 (bottom), which shows in detail the SSI for the wavelengths 759 to 769 nm, no minimum is visible. This is because the attenuation of the light around this wavelength band is of terrestrial nature. As in the IR spectral range absorption minima occur due to gases in Earth's atmosphere, it is necessary to investigate how strong the absorption effect would be for the CLCS for which only a

laser beam path distance of around 1 to 1.5 km needs to be considered. The transmission of monochromatic light for a specified molecule concentration (e.g. for O_2) at a specific altitude can be calculated via equation 4.1. The wavelength-dependent absorption cross-sections of O_2 can be obtained from various sources such as Greenblatt et al. (1990) and Bogumil et al. (2003).

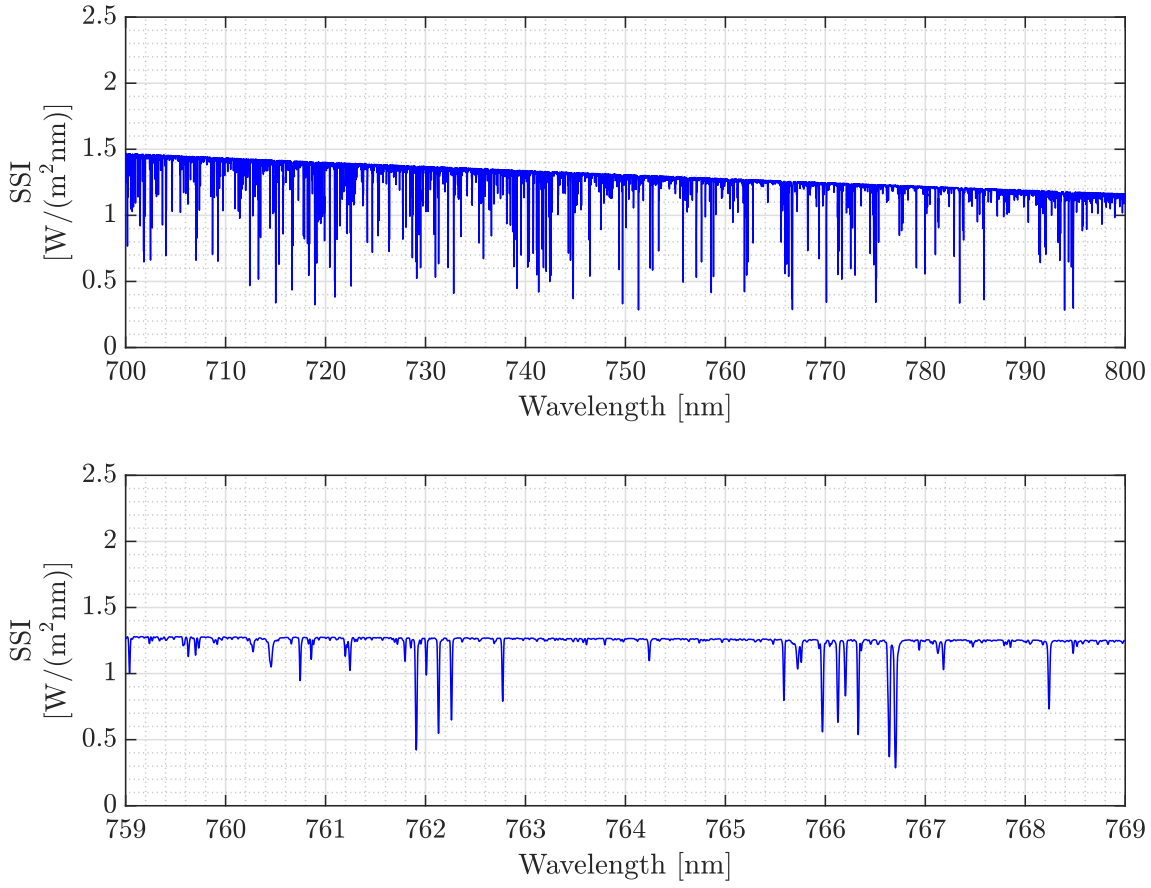

Figure A.6: High resolution SSI for the IR range from 700 to 800 nm (top), and from 759 to 769 nm (bottom). Data based on Kurucz (1992), obtained from libRadtran (2020).

Figure A.7 (top) shows absorption cross-sections of O_2 at a temperature of 293 K for the wavelengths 759 to 769 nm (measurement data with a spectral resolution of 0.47 nm (FWHM)) using data from the SCIAMACHI satellite spectrometer from Bogumil et al. (2003). Absorption cross-section data can be obtained from MCIP-ATLAS (2021) with details described by Keller-Rudek et al. (2013). In the work of the present thesis, the data used was "O2_Bogumil(2003)_293K_650-799.6nm.txt". Another source for absorption cross-section data is IUP (2021). Figure A.7 (bottom) shows how much of the wavelengths between 759 and 769 nm is absorbed by O_2 molecules for a transmission through 1 km of near-ground atmosphere as per the requirements of the CLCS. An O_2 volume concentration of 20,9 % was used for the calculations which is equivalent to about $5.3 \cdot 10^{18}$ O_2 molecules/cm^3.

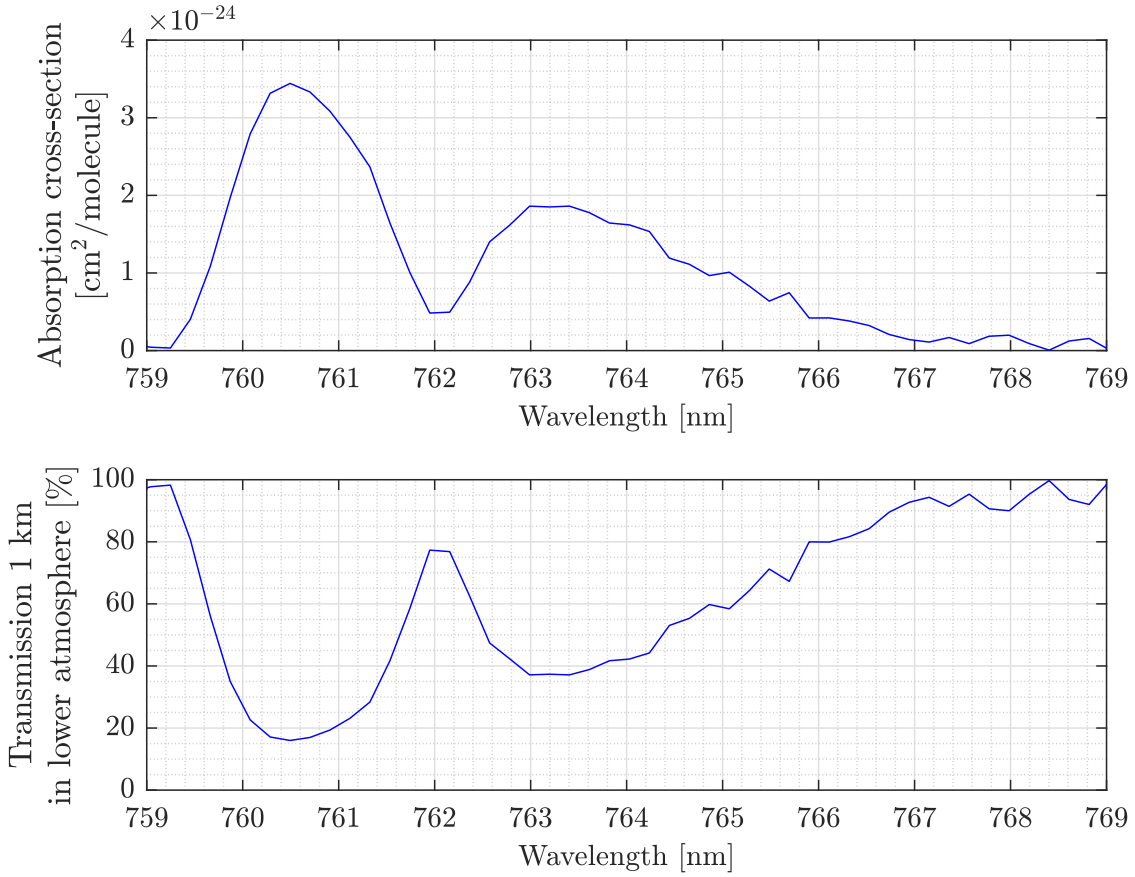

Figure A.7: Absorption cross-sections (top) and transmission of light through 1 km of near-ground atmosphere (bottom) of O_2 in the A-band with minima at around 760.5 nm and 763 nm. Absorption cross-section data from Bogumil et al. (2003).

Using the absorption cross-section measurement data has its limits in the resolution. The molecular absorption spectra in the IR wavelengths contain thousands of absorption lines (Mayer & Kylling 2005, Mayer et al. 2017) due to atmospheric gases such as O_2. In order to analyse these in more detail, the so-called *line-by-line method* can be used. Software applications such as MODTRAN®, libRadTran (library for radiative transfer) or bytran can be used to carry out highly resolved spectral calculations using the *line-by-line method*. An alternative to the line-by-line method is a so-called *band parametrisation* (Mayer & Kylling 2005, Mayer et al. 2017). All three software applications use the HITRAN database (high-resolution transmission molecular absorption database) as a data source for the line-by-line calculations (see Gordon et al. (2021) for more details).

The application bytran, which is described in detail in Pliutau & Roslyakov (2017), was used in the work of the present thesis to calculate the line-by-line data for the O_2 absorption A-band around the wavelength 760.5 nm. The result is shown in

Figure A.8 for the wavelengths 759 to 769 nm for a transmission of light through 1 km of ground altitude atmosphere for the same O_2 concentration as was used for Figure A.7. The graph at the top, created with the line-by-line method, reveals that in more than a dozen very narrow wavelength bands, there is a full absorption of light (i.e. 0 % transmission of light). The graph at the bottom shows the smoothed transmission data. Compared to Figure A.7, bytran calculated the transmission to be around 5 % lower at around 760.5 nm. For the CLCS, it would be necessary to select a laser wavelength in the O_2 absorption A-band where the transmission is very high (the linewidth of the laser would need to be sufficiently narrow). Nonetheless, when referring to Figure 4.9, the power or energy of a laser with a wavelength in the O_2 absorption A-band would have to be 19× stronger in order to produce the same scattering effect as a laser with a wavelength of 350 nm.

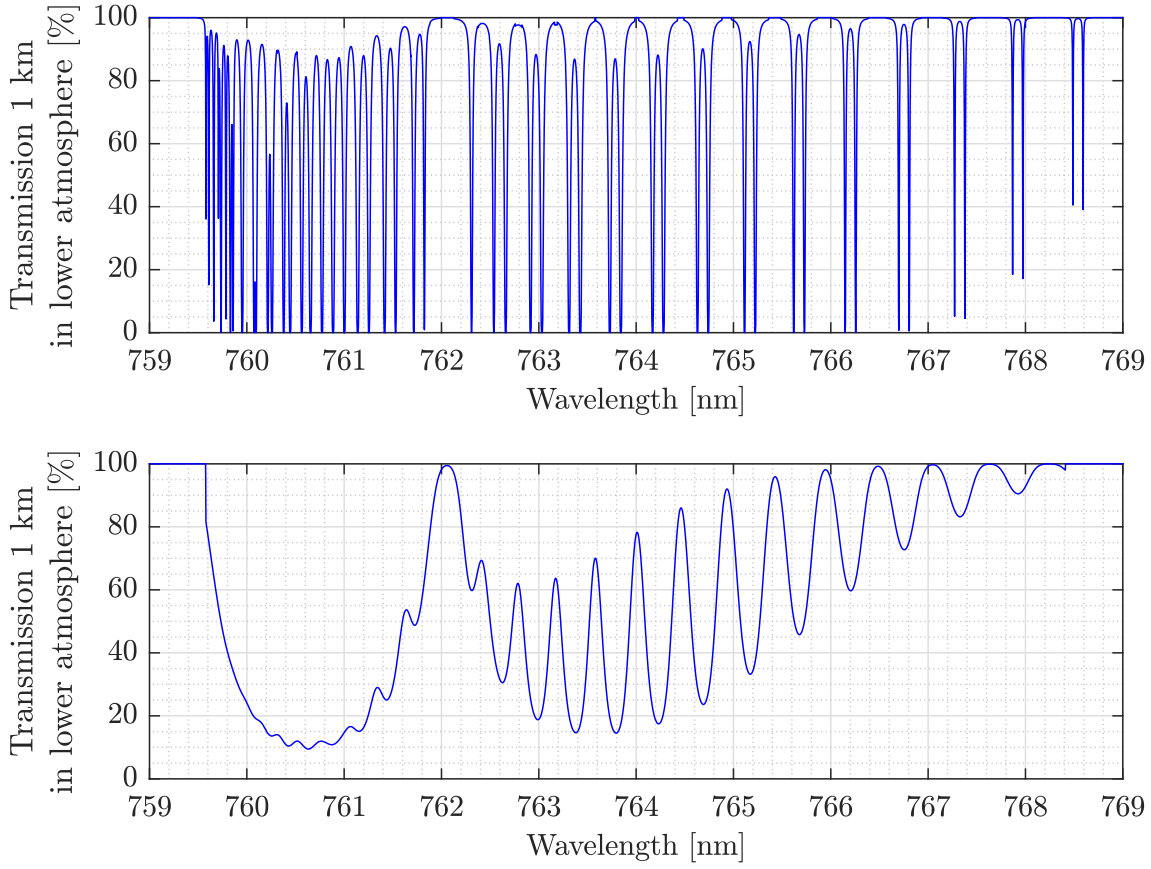

Figure A.8: Transmission of light in the O_2 A-band through 1 km at ground altitude with minima at around 760.5 nm and 763 nm. Transmission data created with the bytran software application. Top graph shows high-resolution data using the line-by-line method. Bottom graph shows the smoothed transmission data.

Continuation from section 4.2.2 on the topic: *Mineral dust.*

Figure A.9 shows daily median particle density data for particle diameters above 0.19 µm for the location Jülich between (a) April 2011 and April 2018 and (b) May 2018 and September 2018 for selected days with sunny weather conditions.

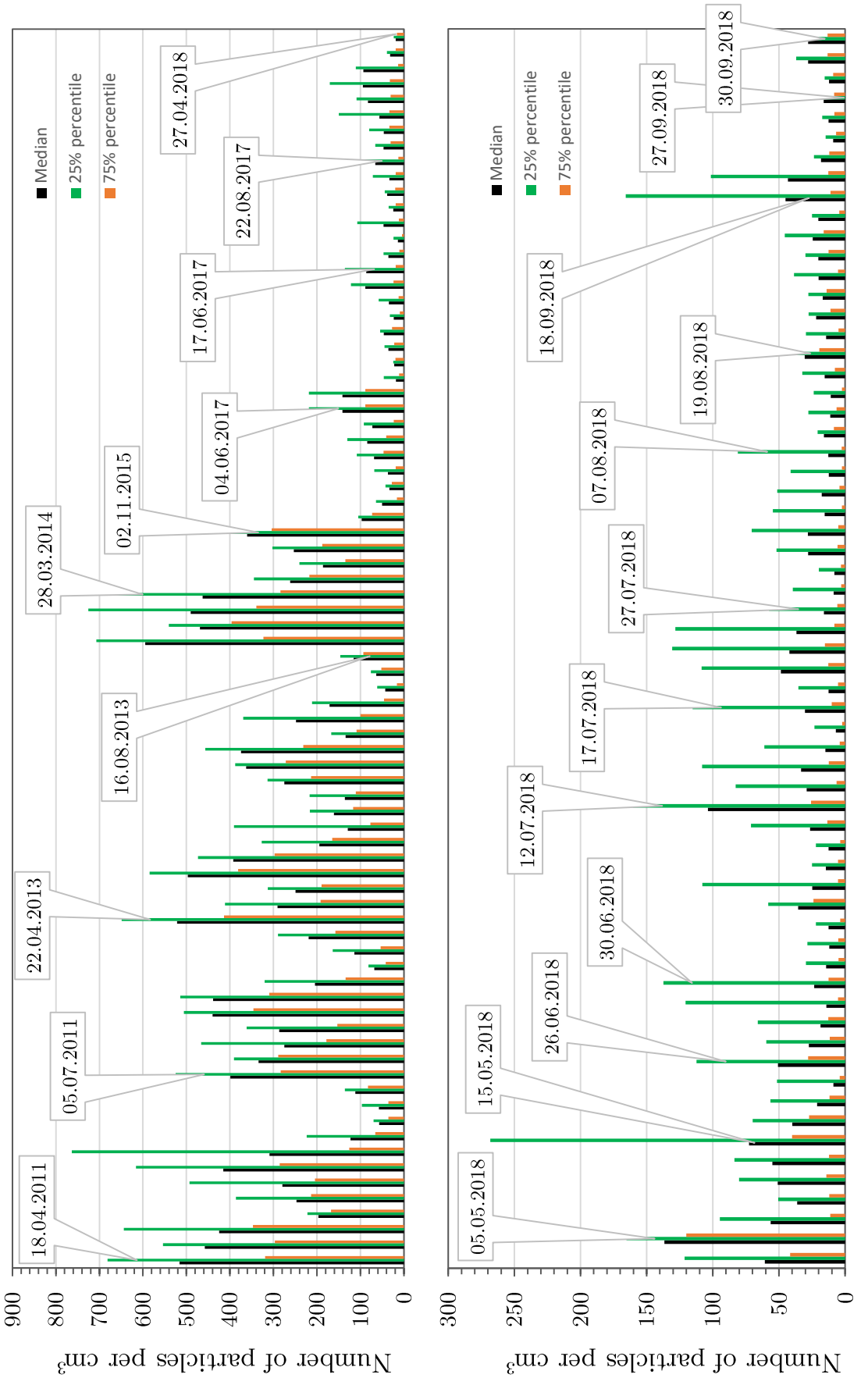

Figure A.9: Daily median particle density data for particle diameters above 0.19 µm for the location Jülich between (a) April 2011 and April 2018 and (b) May 2018 and September 2018 for selected days with sunny weather conditions.

Continuation from section 4.2.2 on the topic: *Grouping of particles into bins with defined size ranges by Particle counters.*

Table A.1: Grouped particle data showing the size ranges (bins), particle count, portion and cumulative portion (data was chosen randomly, table based on Hinds (1999)).

Size range [µm]	Count [-]	Portion [%]	Cumulative Portion [%]
0.18-0.3	113	18.0	17.97
0.3-0.8	174	27.7	45.63
0.8-1.0	155	24.6	70.27
1.0-1.5	85	13.5	83.78
1.5-2.0	42	6.7	90.46
2.0-4.0	23	3.7	94.12
4.0-7.5	16	2.5	96.66
7.5-9.5	11	1.7	98.41
9.5-11.0	8	1.3	99.68
11.0-13.5	2	0.3	100.00
13.5-18.0	0	0.0	100.00
Total	629		

Continuation from section 4.2.2 on the topic: *Biogenic aerosols.*
Depending on the type and origin of plant-based biogenic aerosol, the sizes vary from 0.1 µm to at least 250 µm and can come in various shapes (Tomasi & Lupi 2017).
In a laboratory test at the Solar-Institut Jülich by the author of the present thesis, a test with a class 2 Nd:Yag laser (wavelength of 532 nm, green colour) was carried out. Images were taken in a dark environment with a camera set to exposure times of several dozen of seconds and a strong beam signal was captured as shown in Figure A.10 a). In some images, lint (or some similar material) suspended in the air and visible to the eye strongly scattered light and appeared as a bright spherical spot in the images as shown in Figure A.10 b). Although, of course, lint is not a biogenic material, it shall serve the purpose of demonstrating the scattering effect of very large aerosols.

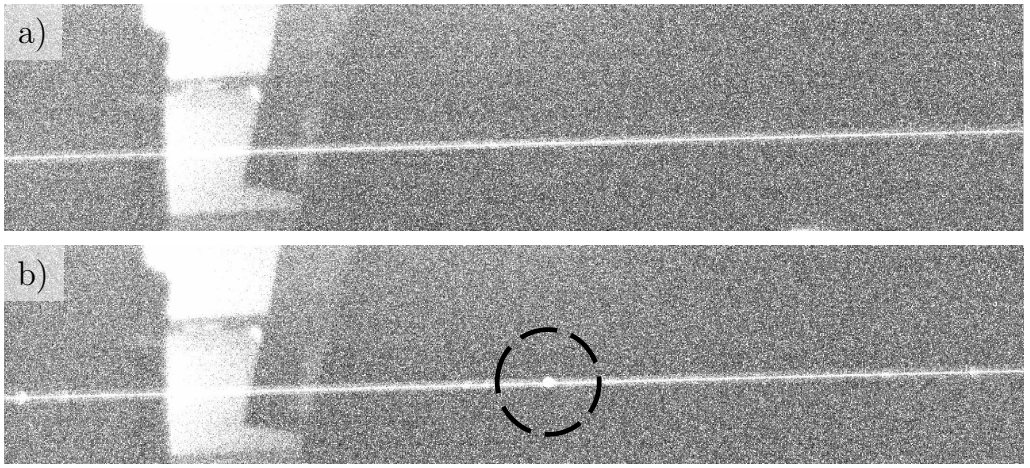

Figure A.10: Photographs showing a) a laser beam without lint (or similar material) in the path of the beam, (b) lint (or similar material) suspended in air strongly scattering a laser beam (marked with black circle).

Regarding the CLCS, macroscopic objects that are in the path of a laser beam will scatter or reflect stronger than microscopic objects. Therefore, in the following it is explored whether or not insects can play a significant role for the CLCS with respect to reflecting laser light towards a camera.
Trieb (2018) presents calculations on the amount of insects that decease from being hit by rotor blades from wind farms in Germany. Also shown is data from Weidel (2008) who studied typical flight altitudes of airborne insects and the corresponding insect density per km^3 for a location in the north of Germany. Weidel (2008) investigated the types and amounts of different insects that fly at different altitudes using an aeroplane and two attached insect catching devices. The key findings of Weidel (2008) are summarised below. More than 100 flights were conducted at flight altitudes between 90 and 1,830 m and the different insects and their numbers found at the various altitudes were then counted. Considering the total flight hours, altogether 817 insects were caught. To catch the insects, an air volume of 132,900 m^3 was passed through the insect catching devices. This means that for an air volume of 1 m^3, the insect density is only $6 \cdot 10^{-3}$ m^3 (i.e. $6 \cdot 10^{-9}$ cm^3). The highest insect density was found at altitudes between 0 and 400 m.
Regarding the CLCS, the laser beam will be photographed at near-ground altitude. Therefore, only the insect density at a low altitude of e.g. <100 m is relevant. However, due to the low insect number density it can be concluded, that insects will not have a significant impact for the CLCS.

Continuation from section 4.3.1 on the topic: Noise.

First introduced in equation 3.38, *dark noise* $\mu_{\text{y.dark,p}}$ is the mean dark signal in the absence of light due to thermal processes in every pixel. Affected by heat, the dark noise increases with rising sensor temperature. The dark noise also increases with longer exposure times (Edmund Optics 2011b, Stemmer Imaging 2018). The dark noise level can be reduced by cooling the camera. *Readout noise* arises in the process when the pixels are read out, i.e. when the electrons held by the pixels are converted into a voltage (Stemmer Imaging 2018). Additionally, readout noise arises for CCD sensors when after an image acquisition electrons are transferred through the shift registers (Stemmer Imaging 2018). CMOS sensors typically have lower readout noise levels than CCD sensors (Stemmer Imaging 2018). Quantisation noise occurs during the analogue-to-digital conversion, i.e. in the process of converting the voltage into a digital value (grey value for monochrome sensors) (Stemmer Imaging 2018). The term *temporal noise* is a single term used to describe the above noise types (Stemmer Imaging 2018).
The noise types dark signal non-uniformity (DSNU) as well as pixel response non-uniformity (PRNU) are fixed pattern noises and can be corrected either via image post-processing or it is already corrected by the camera directly in a built-in correction feature (Stemmer Imaging 2018). DSNU is a constant grey value offset between the pixels in a dark environment which can be corrected (Stemmer Imaging 2018). PRNU describes the differences in the grey values of the pixels across the sensor when the sensor is illuminated with a homogeneous light source (Hilgart 2011) and it practically cannot be eliminated (Stemmer Imaging 2018). Figure A.11 shows exemplarily drawn images of DSNU and PRNU before and after correction (note that in real corrected images the noise would be more random). Tucsen (2021) show examples of images for a camera with scientific CMOS sensor for which the DSNU as well as PRNU were corrected by calibration as follows. For an image with stripes due to DSNU, the value of the DSNU was corrected from 0.3 e^- down to 0.2 e^- which had a large, positive effect on the image quality. Also the PRNU was corrected and reduced from 1.6 % down to 0.3 %, giving a major improvement to the image quality. The stripes effect of DSNU are common with CMOS sensors.

The following noise levels are examples for scientific CMOS sensors (approximate values): Readout noise between 1.1 and 2.5 e^- rms , DSNU <1 e^- rms and PRNU <1.2%. The dark current can be very different from camera to camera.
The following noise levels are examples for scientific interline CCD sensors (approximate values): Readout noise 7 e^- rms, DSNU 3 e^- rms and PRNU <1 %.

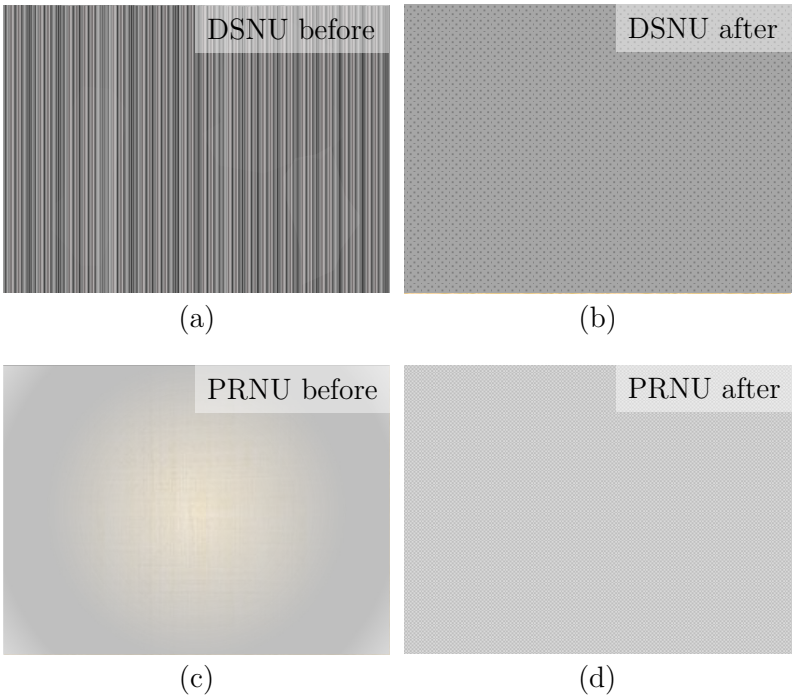

Figure A.11: Examples of DSNU and PRNU in images before and after correction (based on real images from Tucsen (2021)).

Continuation from section 4.3.2 on the topic: Phosphor screen

Table A.2: Characteristics of phosphor screens (Data from Proxitronic (2011) and Lambert Instruments (2016)).

Type	Composition	Light emission	Efficiency	Decay time	
		Maximum		Decay of light intensity	
		typically at		from 90% to 10% in	from 10% to 1% in
P43	Gd_2O_2S:Tb	545 nm	20 photons/e-/kV	1 to 1.5 ms	1.6 to 3 ms
P46	$Y_3Al_5O_{12}$:Ce	530 nm	6 photons/e-/kV	300 to 500 ns	2 to 90 µs
P47	Y_2SiO_5:Ce,Tb	400 nm	N/A	100 ns	2.9 µs

Continuation from section 4.3.3 on the topic: *MTF charts.*

In an MTF chart, a spacial resolution is specified as a frequency in the unit line pairs per mm (lp/mm) for a specified contrast. The measurement of the limiting spacial resolution in an image measured in line pairs per mm is carried out with a special target, of which different type targets exist. One example of a resolution target, developed by LaserSoft Imaging in 1951, consists of black and white stripes of different sizes (Lambert Instruments 2021c). To measure the limiting spatial resolution, an image of the target is analysed and it is assessed how many line pairs can be distinguished per millimetre, hence the unit lp/mm. The limiting spatial resolution is also referred to as Nyquist limit (Edmund Optics 2014a). As an example, if one line is 10 µm wide, then a line pair will have a width of 20 µm resulting in 50 line pairs that can be distinguished per millimetre. With respect to the pixel size, a pixel would need to be exactly 10 µm wide in order to fully resolve 50 lp/mm from the given example. If a pixel were 20 µm wide, then the resolution would be limited to only 25 lp/mm (example based on Lambert Instruments (2021c)). The Nyquist limit (i.e. the spacial resolution) hence reduces with increasing pixel size (Lambert Instruments 2021c, Edmund Optics 2014a). Therefore, the components of an image intensifier camera must be carefully matched. Additionally, a suitable camera lens must be chosen which can resolve objects sufficiently high.

The resolution targets are used both for assessing image sensor resolution limits as well as the resolution limits of lenses. The following example, based on PCO (2018), is a description of the resolution assessment for an image sensor. Figure A.12 (a) shows black and white (B&W) line pairs and how they appear on pixels (represented by green squares) that have a width equal to the width of a line pair. Below the pixels is a representation of the resulting GV of that pixels. Due to the large pixel size compared to the line width, the pixels will never appear fully black, but will appear as a GV between black and white. Only the pixel on the right will be fully white. Figure A.12 (b) shows the same configuration as in (a) except that the line pairs are slightly shifted such that the edges of two adjacent pixels are at the centre of a black line. The resulting GV is different compared to (a) as now the outermost pixels have a brighter GV than the pixels in the centre. A better resolution has configuration (c) as here the camera resolution is four times higher and the pixel width and height are only half as large compared to (a) and (b) such that now the pixel width is half as wide as a line pair, i.e. one pixel is as wide as a black or as a white line. When pixels overlap with either a black or a white line, the result will be fully black or fully white pixels. When, compared to configuration (c), the line pairs are slightly shifted to the left as shown in configuration (d), only the outermost pixels are fully white and all other pixels have a GV between black and white. Configuration (e) shows an even better image quality with a four times higher pixel resolution and a four times smaller pixel width and height compared to configurations (c) and (d).

A black or a white line is now resolved by eight pixels as shown in (e). When the line pairs are shifted half a pixel width to the side, the black and white lines will appear on single pixel columns but will have adjacent columns with grey colour. Image sharpness therefore depends strongly on the camera resolution and the pixel size. (cf. PCO 2018)

Describing image sharpness with the term contrast, Stemmer Imaging (2018) points out that large line pairs with wide spacing will appear in an image with a relatively good contrast, while, on the contrary, finely spaced line pairs will have a low contrast (for more details on the term *contrast* see the description given for equation 4.8). To ensure the best possible image sharpness for a chosen image sensor, it is vital – as noted before – that a suitable high quality camera lens is chosen that can resolve and match the resolution of the image sensor. As an optically perfect lens does not exist, the effect of blurred edges will always occur due to diffraction and other optical errors, space between object details (Edmund Optics 2014c) and also due to the resolving performance of the lens.

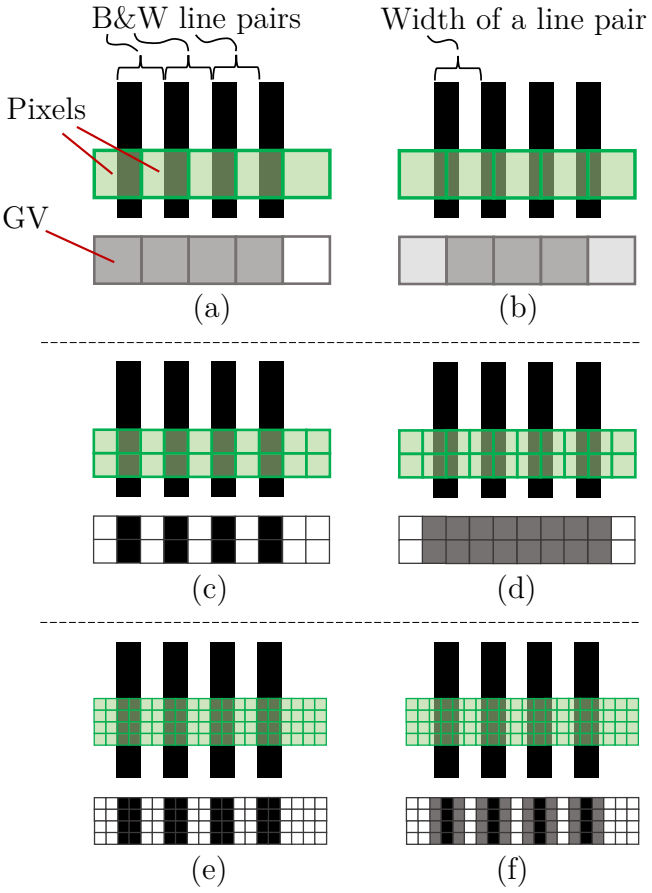

Figure A.12: Images (a) & (b) showing resulting grey values (GV) for pixels (green squares) with the width of a line pair. Images (c) & (d) showing resulting grey values (GV) for pixels (green squares) with the width of half a line pair and images (e) & (f) showing resulting grey values (GV) for pixels (green squares) with the width of quarter of a line pair. Images (c) and (e) show the best case for which the black and white is preserved, while images (d) and (f) show the worst case with a formation of grey tones, i.e. a reduced contrast in the image with blurred lines. Based on illustration from PCO (2018).

The MTF chart shows the contrast (in %) against the resolution (in lp/mm) for the optical components (e.g. a lens or a sensor). With an MTF chart, the parameters contrast (respectively modulation) and resolution allow the assessment of the total performance of an image sensor (Edmund Optics 2011c). The higher the contrast, the lower will be the resolution (for more details on the term *contrast* see the description given for equation 4.8). Figure A.13 shows two examples of MTF curves in a chart for a camera lens. In the given example, curve "Example 1" represents a lens with a better resolving quality than a lens with a curve such as "Example 2". MTF curves are measured for camera lenses as well as image sensors individually, but also as a combined MTF curve for a system composed of a camera lens and image sensor. MTF curves also exist for communication cables and frame grabber cards. In the

case of a camera system, the MTF curve of the lens is multiplied with the MTF curve of the sensor (Edmund Optics 2011b) in order to obtain a total MTF curve. For a more accurate result, the MTF curves of the communication cable and the frame grabber card should also be included in the total MTF curve. Regarding the CLCS, a laser beam in a photograph can have a lower contrast as long as the noise level is at an acceptable level and the bit-depth is sufficiently high. A relatively sharp image at a reasonable resolution is in any case important for the CLCS because the line detection accuracy depends on both.

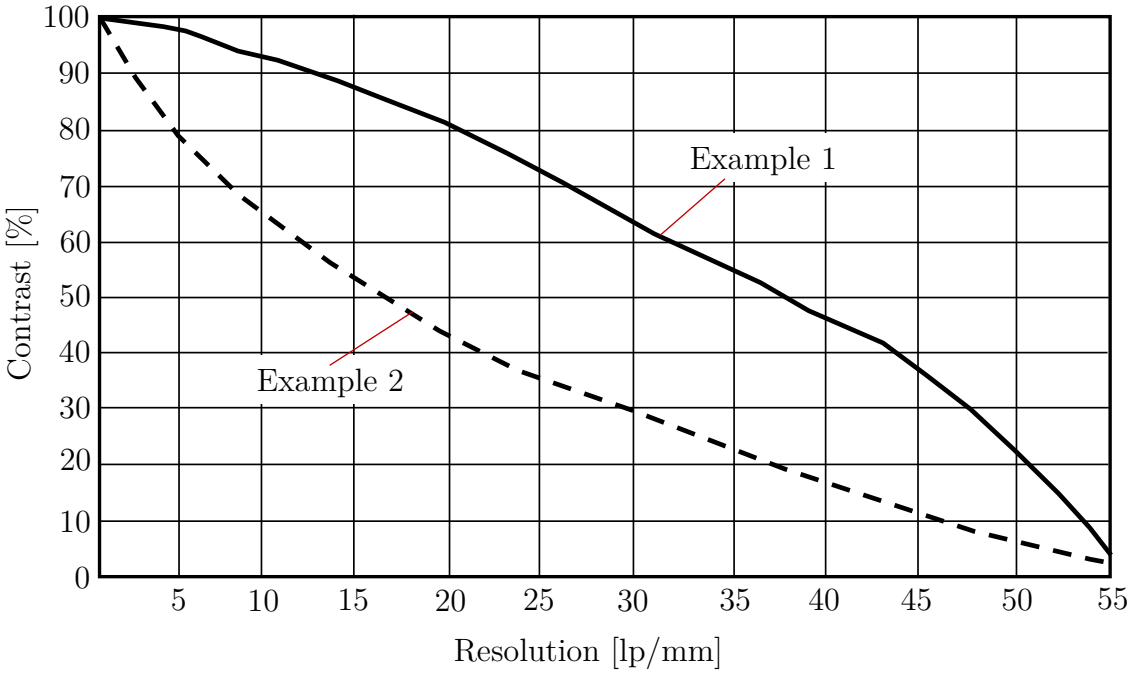

Figure A.13: Example of an MTF curve (based on illustration from Edmund Optics (2011b) and Edmund Optics (2011c)).

There are several types of MTF charts for camera lenses. One type is the same as described above (i.e. contrast in % vs frequency in lp/mm). Another very common type MTF chart is to show contrast vs field, i.e. the vertical axis shows the contrast and the x-axis the distance from the centre of the lens to the right edge of the lens. The MTF curves for camera lenses allow to assess the way optical aberrations affect the lens performance at a specified working distance, f-stop, sensor size as well as wavelength range (Edmund Optics 2014d).

Some manufacturers of camera lenses give the spacial resolution in lp/mm alongside the resolution in megapixels. For image intensifier cameras, in general, only the spacial resolution in lp/mm at a specific contrast is given, e.g. $> 41\,\text{lp/mm}$ @4 % MTF, with @4 % MTF referring to @4 % contrast. An MTF chart is usually not provided, but can be requested directly from a company that sells image intensifier cameras. The unit of lp/mm, however, is more difficult to apply, therefore it may

be more useful to convert it to the more practical unit of µm. The equations for the conversion are given below.

The sensor resolution, ξ_{Sensor}, which is also referred to as the system's image space resolution, $\xi_{\text{Image Space}}$, is calculated with equation A.7. The result is the number of line pairs that the sensor can resolve per mm when assuming that the line width (either of a black or a white line) is identical to the width (or height) of one pixel. Therefore, effectively, the highest resolvable frequency, i.e. the Nyquist limit, is two pixels (e.g. one pixel having a white colour and the other pixel a black colour). The bigger the pixel size of a sensor is, the lower is the Nyquist limit (Edmund Optics 2014a).

$$\xi_{\text{Sensor}} = \xi_{\text{Image Space}} = \left(\frac{1}{2 \cdot \text{s}}\right) \cdot \left(\frac{1{,}000\,\mu\text{m}}{1\,\text{mm}}\right) \quad [\text{lp/mm}] \tag{A.7}$$

where s is the pixel size in the unit of µm (i.e. the vertical or horizontal length or width of a pixel as given in equations 3.27 or 3.28). Using equation A.7, the Nyquist limit can be calculated for the pixel dimensions of any sensor, i.e. the maximum number of line pairs that can be resolved by a sensor with a specific pixel dimension. Table A.3 shows, exemplarily, Nyquist limits for selected pixel dimensions.

Table A.3: Examples of Nyquist limits for selected pixel dimensions.

Pixel size [m]	16	13	11	6.5	3.45
Nyquist limit [lp/mm]	31.25	38.46	45.45	76.9	144.9

According to Edmund Optics (2014b) and Edmund Optics (2011c), the so-called object space $\xi_{\text{Object space}}$ is calculated to determine the absolute minimum resolvable feature of an object in the typical unit of µm. First, the ratio of the sensor size to the FOV is calculated (note that here the FOV is equivalent to the parameters h or w in Figure 3.8 and should not to be confused with the angular field of view, α, from equation 4.9. This ratio is called primary magnification (PMAG) as given by equation A.8. Regarding both the FOV and the sensor size, either their horizontal or vertical lengths are taken.

$$\text{PMAG} = \frac{\text{Sensor size}}{\text{FOV}} \quad [\text{mm/mm}] \tag{A.8}$$

Next, the object space resolution in the unit lp/mm, $\xi_{\text{Object Space (lp/mm)}}$, is calculated from the image space resolution and PMAG using equation A.9.

$$\xi_{\text{Object Space (lp/mm)}} = \xi_{\text{Image Space}} \cdot \text{PMAG} \quad [\text{lp/mm}] \tag{A.9}$$

To convert the unit lp/mm into µm (or to be more exact µm/lp, but lp is omitted) for the object space $\xi_{\text{Object Space}}$, equation A.10 is used.

$$\xi_{\text{Object Space (µm)}} = \frac{1{,}000\frac{\text{µm}}{\text{mm}}}{2 \cdot \xi_{\text{Object Space (lp/mm)}}} \quad [\text{µm}] \tag{A.10}$$

The above equations may be useful when comparing image intensifier cameras.

Continuation from section 4.3.4 on the topics: *(i) AFOV (α) for selected image sensor types and focal lengths (see table A.4) and (ii) height and width of scenery for different working distances and selected image sensor types (see table A.5).*

Table A.4: Examples of the AFOV (α) for three different working distances for three selected image sensor types and three selected focal lengths.

Sensor type	Focal length [mm]	Sensor width [mm]	AFOV (α) horizontally [°]	Sensor height [mm]	AFOV (α) vertically [°]
1/2"	18	6.4	20.2	4.8	15.2
1/2"	50	6.4	7.3	4.8	5.5
1/2"	85	6.4	4.3	4.8	3.2
2/3"	18	8.8	27.5	6.6	20.8
2/3"	50	8.8	10.1	6.6	7.6
2/3"	85	8.8	5.9	6.6	4.4
1"	18	12.7	38.9	9.5	29.6
1"	50	12.7	14.5	9.5	10.9
1"	85	12.7	8.5	9.5	6.4

Table A.5: Examples of the width w and height h of the scenery for three different working distances for three selected image sensor types and three selected focal lengths.

Sensor type	Focal length [mm]	Object width* [m]	Object height* [m]	Object width** [m]	Object height** [m]	Object width*** [m]	Object height*** [m]
1/2"	18	35.6	26.7	177.8	133.3	355.6	266.7
1/2"	50	12.8	9.6	64.0	48.0	128.0	96.0
1/2"	85	7.5	5.7	37.7	28.2	75.9	56.5
2/3"	18	48.9	36.7	244.4	183.3	488.9	366.7
2/3"	50	17.6	13.2	88.0	66.0	176.0	132.0
2/3"	85	10.4	7.8	51.8	38.8	103.5	77.7
1"	18	70.6	52.8	352.8	263.9	705.6	527.8
1"	50	25.4	19.0	127.0	95.0	254.0	190.0
1"	85	14.9	11.2	74.7	55.9	149.4	111.8

*Working distance 100 m, **Working distance 500 m, ***Working distance 1,000 m

Continuation from section 4.3.5 on the topic: *Data communication interfaces.*

Table A.6: List of communication interfaces, cable types, cable length restrictions and data transmission bandwidths (cf. PCO 2018).

Communication interface	Cable type	Max. cable length [m]	Bandwidth [MB/s]
Firewire®	Twister Pair / Fiber	4.5 / 100	125
USB 2.0	Twisted Pair	5	50
USB 3.1 Gen 1	Twisted Pair	3	450
USB 3.1 Gen 2	Twisted Pair	2	1,100
USB 3.2	Twisted Pair	2	2,200
GigE	Twister Pair / Fiber	100 / 10,000	118
10 GigE	Twister Pair / Fiber	100 / 10,000	1,183
CoaXPress	Coax Cable	212 / 68	116 / 580 (single link)
Camera Link® HS	Fiber	10,000	1183 (single link)
Thunderbolt	Twisted Pair	3	515 (PCIe Gen 2 x2)

Continuation from section 4.5 on the topic: *Examples of typical gain media of lasers*

Table A.7: Examples of typical gain media of lasers (Eichler & Eichler 2006)

Gain medium based on a			
solid (e.g. crystal or glass)	liquid (typically dye)	gas	semiconductor
Nd:YAG (neodymium-doped yttrium aluminum garnet	stilbene	Eximer (e.g. ArF (argon fluoride), KrF (krypton fluoride))	GaN (gallium nitride)
Cr: Al_2O_3 (ruby)	coumarin	N_2 (Nitrogen)	ZnSe, GaAlAs (zinc selenide)
Cr: $BeAl_2O_4$ (alexandrite)	rhodamine	He-Cd (helium cadmium)	GaAs, InGaAsP (gallium arsenide)
Nd:Glass (neodymium glass)	oxazine	CO_2 (carbon dioxide)	PbCdS, PbSSe, PbSnTe (lead salt)
Ti: Al_2O_3 (titan sapphire)			

Continuation from section 4.5 on the topic: *Examples of available commercial laser products.*

Table A.8: Examples of available commercial laser products (data from various sources: Paschotta (2021c), Paschotta (2021d), Paschotta (2021e), InnoLas (2021), QuantumComposers (2021), PhotonicSolutions (2021), Lumibird (2021) and Schneeweiss et al. (2017)).

Name of pulsed laser	Wavelength [nm]	Type of laser	Pulse energy	Frequency	Pulse width
N_2 laser	337	Gas laser	0.25…225 J, mJ	80…300 Hz	few ns
XeF-Eximer laser	351	Gas laser	200 to 300 mJ	≤100 Hz	few ns
Nd laser (freq. tripled)	1064/532/ 355/266 (other emission lines are: 946/1,123/ 1,319/1,338/ 1,415/1,444/ 1,540/1,570)	Solid-state laser	Various pulse energies in the range of J, mJ and J	kHz if pulse energy in J range, around 10 to 1,000 Hz if pulse energy in mJ range	s, few ns
Dye laser	200 … 4,500	Dye laser	Various pulse energies, e.g. 3…210 mJ	10…100 Hz	few ns
Optical Parametric Oscillator (OPO)	~210 … 2,400	Light source (similar to a laser)	e.g. 0… 9.4 mJ	1 to 20 Hz	few ns
Ruby laser	694	Solid-state laser	High pulse energies possible, e.g. 400 J		ms, ns, ps
Alexandrite laser	700 … 800	Solid-state laser	e.g. 1 J		few s

Continuation from section 4.5 on the topic: *Laser safety.*

As a brief insight into the topic of laser safety, the so-called maximum permissible exposure (MPE) is introduced. The "maximum permissible exposure (MPE) is the highest power or energy density of the light source measured in W/cm^2 or J/cm^2, respectively, that is considered safe and has negligible probability of causing any damage to the eyes. MPE is usually taken as 10 % of the power or energy density that has 50 % probability of causing damage under worst-case conditions" (Maini 2013).

Disclaimer: All information regarding laser safety, laser design and laser data etc. used in this thesis must not be used as a guideline for your own work. No liability is assumed in any way for the content of this work.

Continuation from section 4.6 on the topic: *Image restoration.*

Figure A.14 shows (a) a uniform grey image, (b) Poisson noise added to the uniform grey image, and (c) a histogram of the Poisson distribution. The probability density function (PDF) of the Poisson distribution is defined as shown in equation A.11 (Thakur et al. 2016).

$$P(k) = \frac{e^{-\lambda}\lambda k}{k!} \tag{A.11}$$

where λ is the mean value, k is the number of occurrences and $k!$ is the factorial of k.

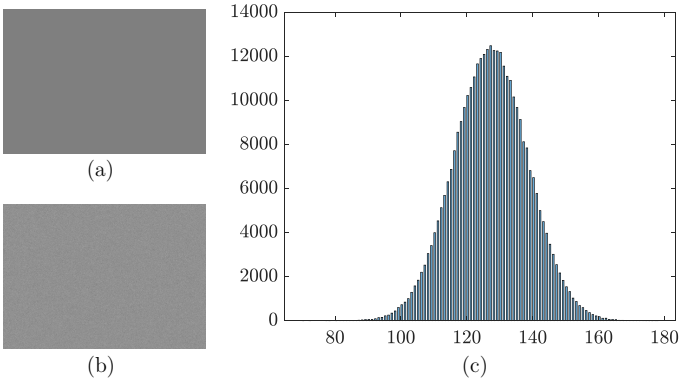

Figure A.14: (a) Uniform grey image, (b) Poisson noise added to the uniform grey image, and (c) a histogram of the Poisson distribution.

Continuation from section 4.6 on the topic: *Hough transform and Radon transform.*

Hough transform

To detect a line or multiple lines in an image, this cannot be done with the standard equation of a line because it cannot resolve the slope of a vertical line. The equation of a straight line is $y = mx + c$, where m is the slope and c is the value of y at the interception of the line with the y-axis. Regarding the equation of a straight line, if a line is vertical then $m = \infty$, which cannot be resolved. In order to detect a line in an image, a parametric representation of a line is used as a working approach which is formulated with equation A.12 using the polar coordinate system (MathWorks® 2021a):

$$\rho = x \cdot \cos(\theta) + y \cdot \sin(\theta) \qquad [-] \tag{A.12}$$

where, as exemplarily shown in Figure A.15 (a), x and y are the coordinates of a pixel in an image, ρ is the distance of the line in the image to the origin and θ is the angle between the x-axis and a dashed support line that is perpendicular to the line in the image (MathWorks® 2021a). For example, MathWorks® (2021a) writes that the angle θ can take values between $-90° \leqslant \theta < 90°$. As in an image the coordinate (0,0) is always in the top left corner, the vertical y-axis is drawn downwards. For each white pixel, the angle θ of the dashed support line is rotated altogether (almost) 180° in pre-defined angular steps (e.g. 1°) and 180 values of ρ are calculated. A line consisting of white pixels would be identified as a line if for each pixel the distance ρ and θ is (nearly) identical as is shown in Figure A.15 (b) and (c). For a further read on the Hough transform see, for example, MathWorks® (2021b), Liu et al. (2017) and Murillo-Bracamontes et al. (2012). For carrying out a Hough transform on an image with a line or multiple lines, it is necessary to use a binary black and white image whereby the line(s) must take the pixel colour white and everything else the pixel colour black. If colour or greyscale images are used, then these must be converted into a binary black and white image.

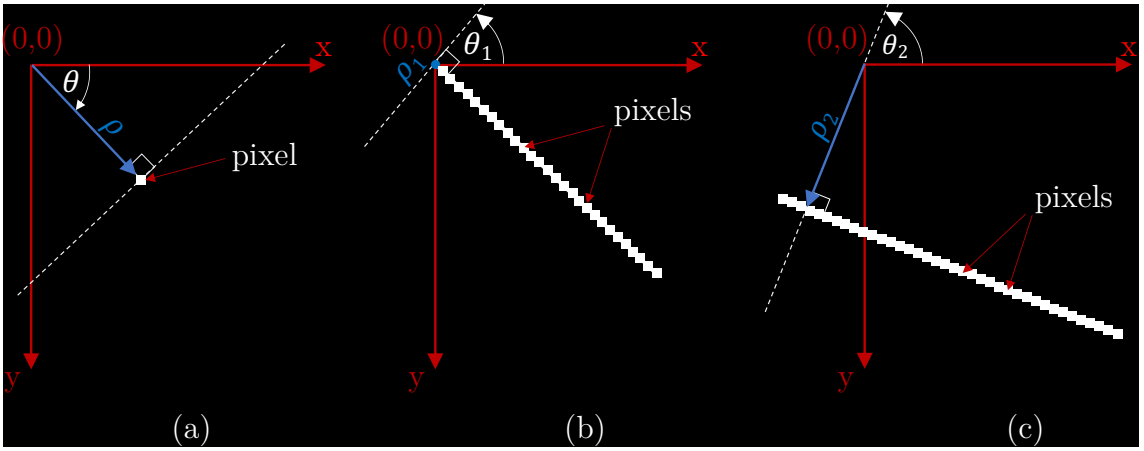

Figure A.15: Working principle of the Hough transform for a (a) single white pixel, (b) a line consisting of white pixels and (c) another example of a line consisting of white pixels.

As previously stated, for each white pixel, the support line through the analysed pixel is rotated altogether (almost) 180° in pre-defined angular steps (e.g. 1°) and values of ρ are calculated. Figure A.16 shows the two images (a) and (b) which each contain two pixels that represent a straight line in an image of 50×50 pixels in size. When for each of the pixels the respective values of ρ are calculated for the angles from $-90° \leqslant \theta < 90°$, then it results in a sinusoidal line in a graph of distance ρ versus the angle θ in the so-called *Hough space*. In the case of two pixels in a single image there will be two sinusoidal lines. The point where the two lines intercept represents the closest pixel of a line to the origin (0,0) and its corresponding line at a slope with an angle of θ. If a line were to consist of 100 pixels, then altogether there will be 100 lines which each intercept at one point.

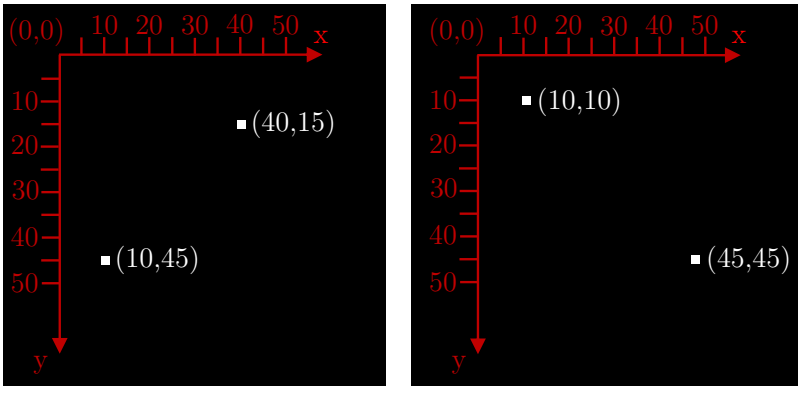

Figure A.16: Two lines represented by two pixels in images (a) and (b).

The Hough space for the two images shown in Figure A.16 is shown in Figure A.17. The two black lines in Figure A.17 (a) represent the Hough space for the two pixels of Figure A.16 (a) where the continuous line represents pixel (10,45) and the dashed

line represents pixel (40,15). The black lines in Figure A.17 (b) represent the Hough space for the two pixels of Figure A.16 (b) where the continuous line represents pixel (10,10) and the dashed line represents pixel (45,45).

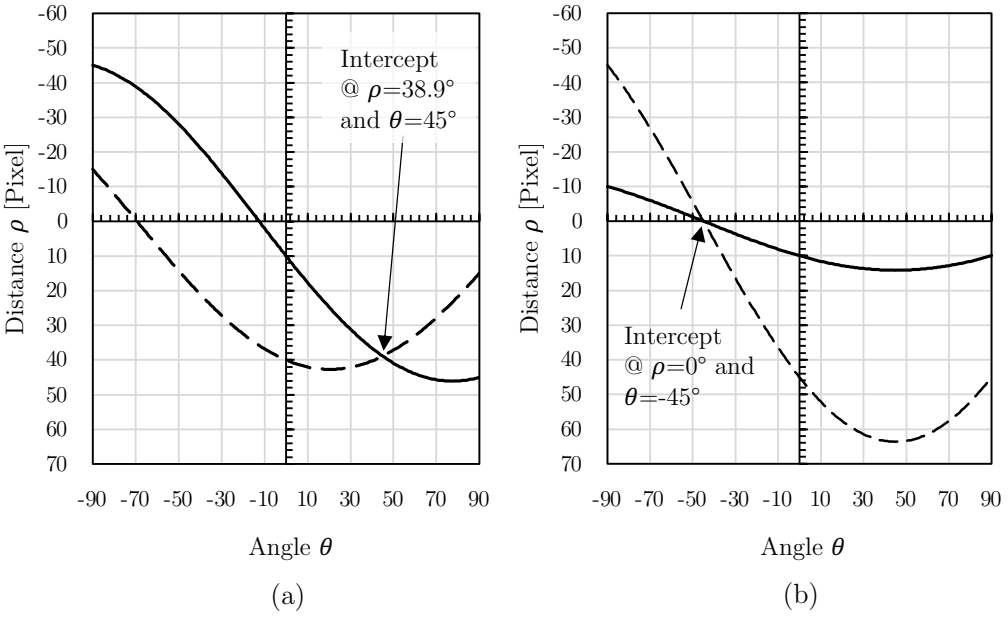

Figure A.17: Hough space for the two images shown in Figure A.16.

In the above example only two pixels were used. If instead a single line were to exist in an image, then many more sinusoidal lines in the Hough space will intercept at one coordinate (this can be regarded as a peak) while there are no interceptions elsewhere in the Hough space. This means that a straight line, expressed by the two parameters ρ and θ, has been identified at this peak. If multiple lines exist then several peaks exist.

Radon transform

The Radon transform can be used for detecting straight lines in greyscale images (Liu et al. 2017). In image processing, the Radon transform works in such a way that the greyscale values of the pixels across the entire sensor are projected along a radial line path oriented at a specific angle θ into virtual bins (MathWorks® 2021b). This is repeated for a range from $0° \leqslant \theta \leqslant 180°$ in pre-defined rotation steps, e.g. 1°. Inside the bins, the intensities of the greyscale values are accumulated for each rotation angle (MathWorks® 2021b). The software MATLAB®, for example, virtually divides each pixel into four subpixels for a greater accuracy. Figure A.18 (a) shows, exemplarily, an image sensor with a 4×5 pixel matrix which has four pixels in grey tone and the rest in white tone. Virtual multiple parallel projections pass via all the pixels and count the accumulated grey values in virtual bins. In the bins an intensity map is created for each rotation angle θ. For reasons of clarity, only a few projection lines are shown which, here, do not cover the entire sensor.

After the projections of all angles are accumulated in the bins, a graph is produced showing $x(\rho,\theta)$ versus θ which looks almost identical to the ρ versus θ graph of the Hough transform, but will be more accurate at the loss of speed.

Temme (1987) describes in detail the equation of the Radon transform. In a similar representation as given by Temme (1987), the equation of the Radon transform is shown below according to MathWorks® (2021a) (the coordinate system can be compared with the one shown in Figure A.18 (b)):

$$R_\theta\left(x'\right) = \int_{-\infty}^{\infty} f\left(x\cos\theta - y\sin\theta, x\sin\theta + y\cos\theta\right) dy' \tag{A.13}$$

MathWorks® (2021a) states that the Radon transform of $f(x,y)$ is the line integral of f parallel to the y'-axis. The Radon transform $R_\theta\left(x'\right)$ holds the projections of the pixels as intensity in the bins, as shown, exemplarily, in Figure A.18 (b). Examples of the Radon transform being applied in real-life applications in medicine are described by Gonzalez & Woods (2018).

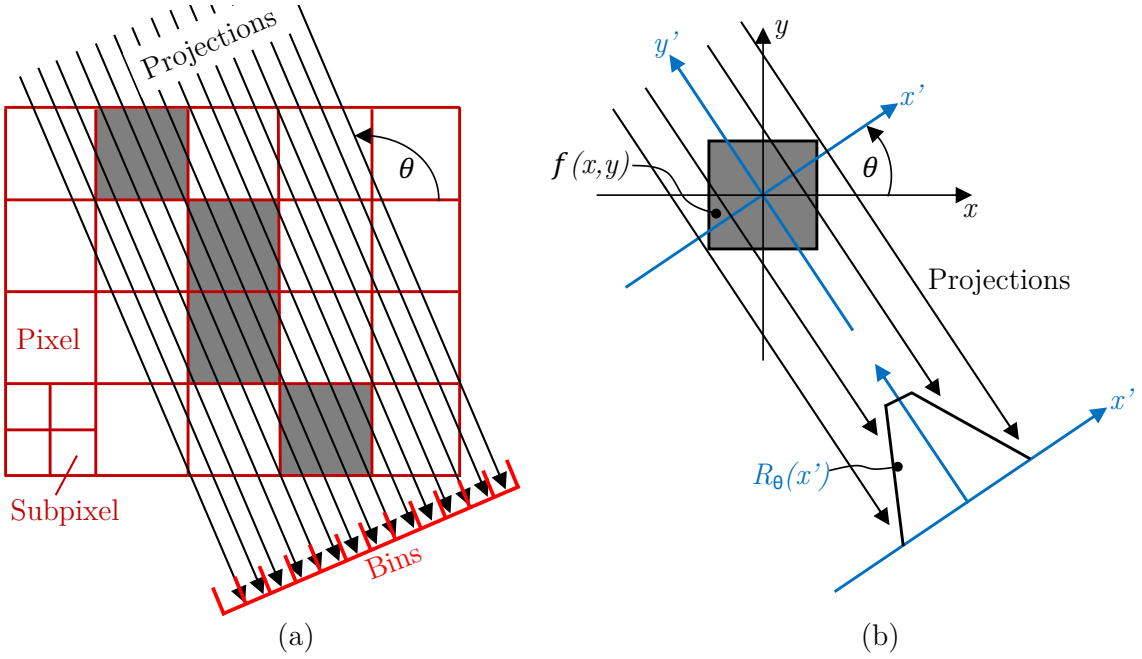

Figure A.18: Working principle of the Radon transform (based on illustrations from MathWorks® (2021a) and MathWorks® (2021b)).

The way the Radon transform works can best be understood with the example of Figure A.19, which shows the projections of exemplary black and white pixels into the bins at the three rotation angles $\theta = 0°$, $\theta = 90°$ and $\theta = 42°$. Two vertical lines can be clearly identified at $\theta = 0°$ because of two bins with high columns. At $\theta = 90°$,

one line can be clearly identified due to one high column. At the angle of $\theta = 142°$ no line can be identified as there is no high column (there is just noise). An advantage of the Radon transform is that lines can also be extracted from an image which has a lot of noise, while other line detection algorithms would fail (Toft 1996).

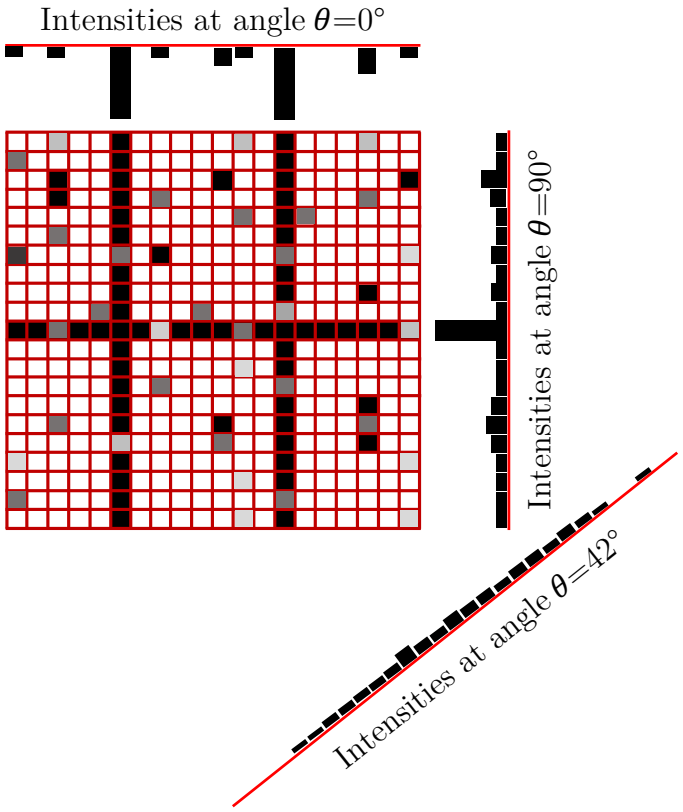

Figure A.19: Working principle of the Radon transform for an entire image with intensities in the bins shown at three exemplary rotation angles.

To demonstrate how to interpret the Radon transform in a black and white image, a Radon transform was carried out for three white lines with the Radon transform coordinates at (a), (b) and (c) shown in Figure A.20. The corresponding black and white image is shown in the top right corner. Figure A.21 illustrates how to interpret the Radon transform coordinates for lines a) and b) starting from the centre of the image (0,0). The line at coordinate b) is the red line perpendicular to the support line at $x' = 300$ pixels at an angle of $\theta = 90°$. The line at coordinate a) is the red line perpendicular to the support line at $x' = -120$ pixels at an angle of $\theta = 34°$.

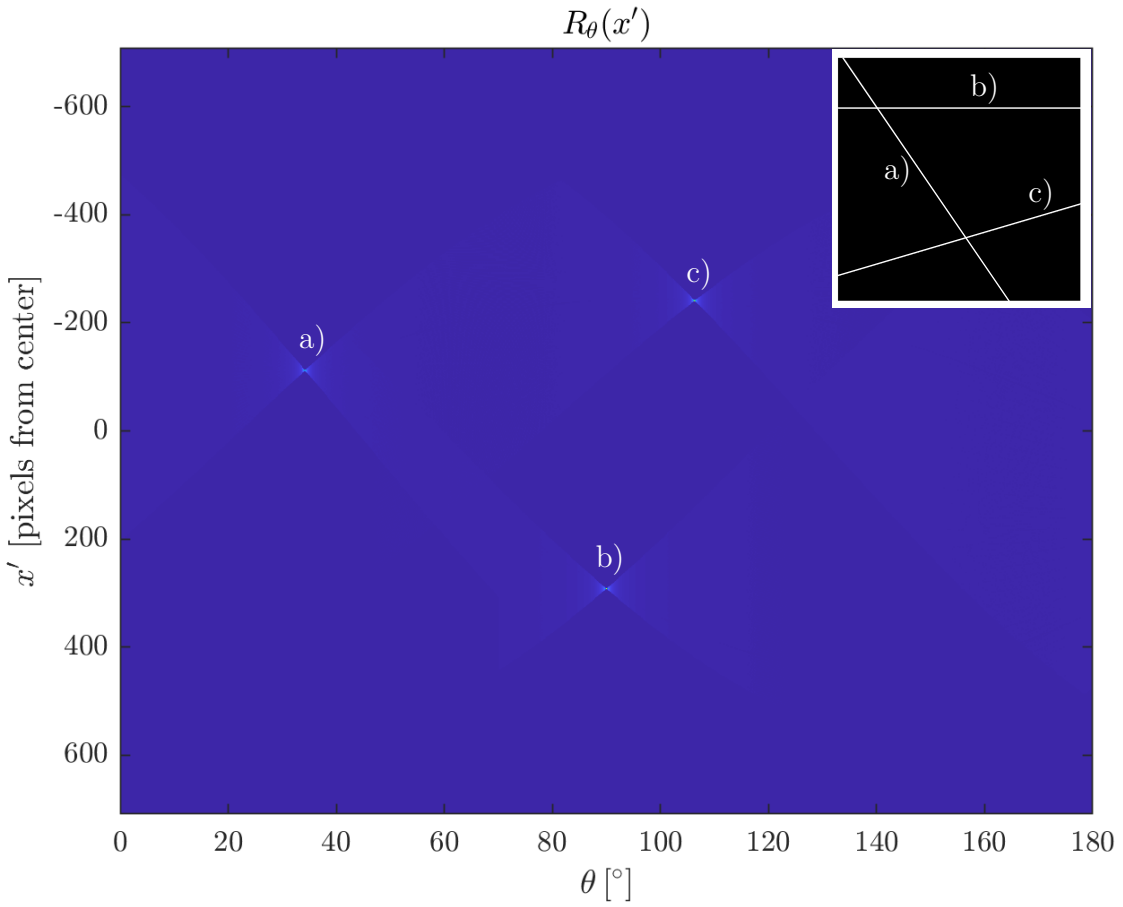

Figure A.20: Radon transform performed on three lines. Image created with MATLAB®.

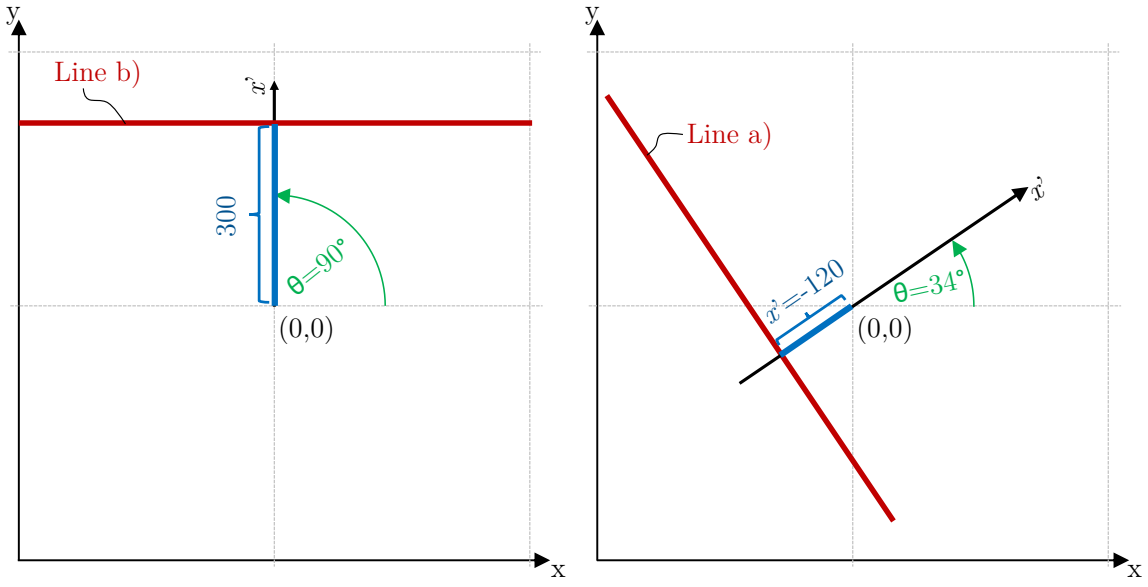

Figure A.21: Multiple lines of different thickness detected by the Radon transform.

In the following, an example is shown for how lines are detected and processed in MATLAB®. Figure A.22 (a) shows an image with 7 lines which are numbered. Figure A.22 (b) shows the Radon transform and where the 7 white lines are found in the Radon transform graph. Figure A.22 (c) and (d) show the values of θ and x' of the detected 7 lines.

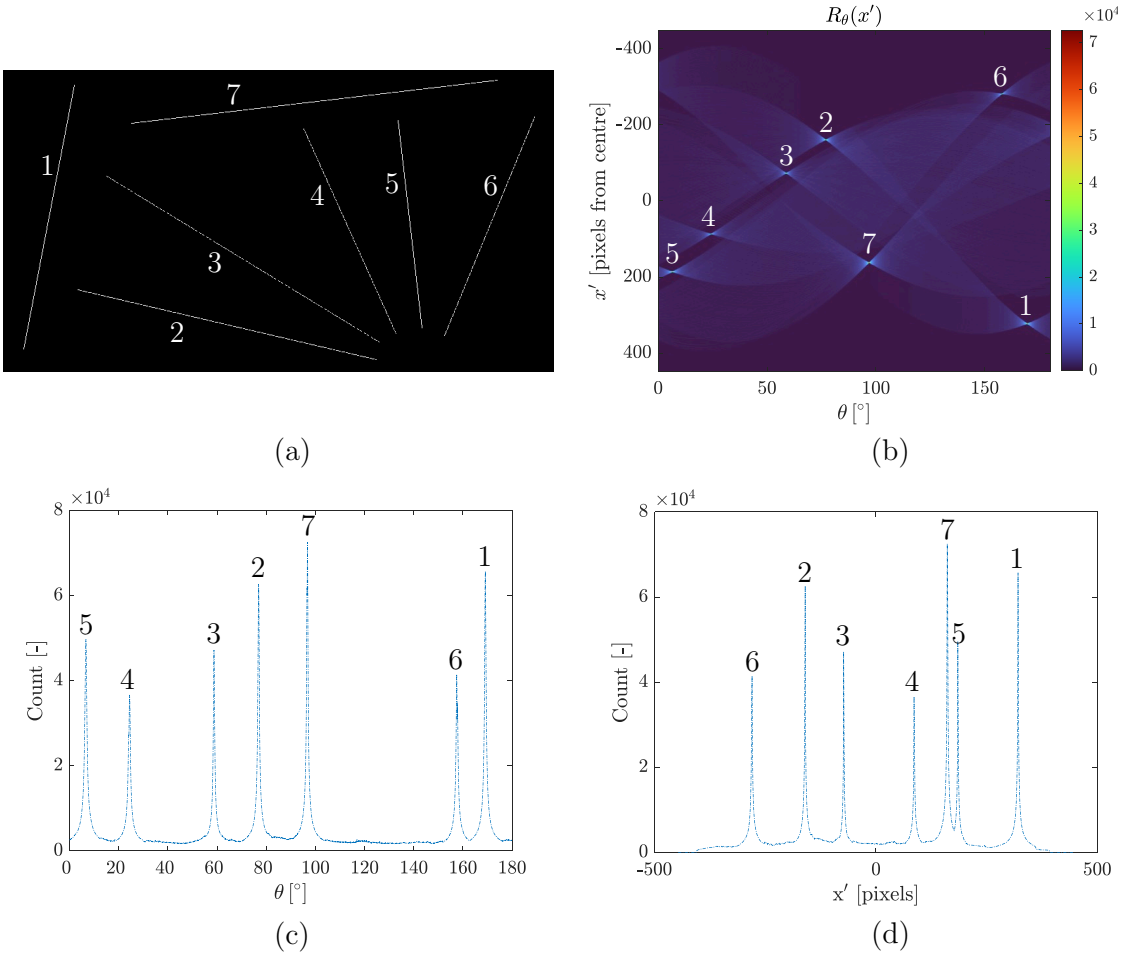

Figure A.22: Example detection of multiple lines using the Radon transform. (a) Analysed image with 7 lines, (b) Radon transform, (c) Peaks in θ vector and (d) Peaks in x' vector.

Continuation from section 6.2.3 on the topic: *Mie scattering simulations.*

This section gives further details about the Mie scattering simulation previously shown in Figure 6.7 and Figure 6.8.

The below Figure A.23 shows the calculated angle-dependent Mie scattering intensity for the individual particle mean diameters for the mean particle distribution "Juelich: median" of Figure 4.12 multiplied by the laser beam volume within the AFOV of the camera.

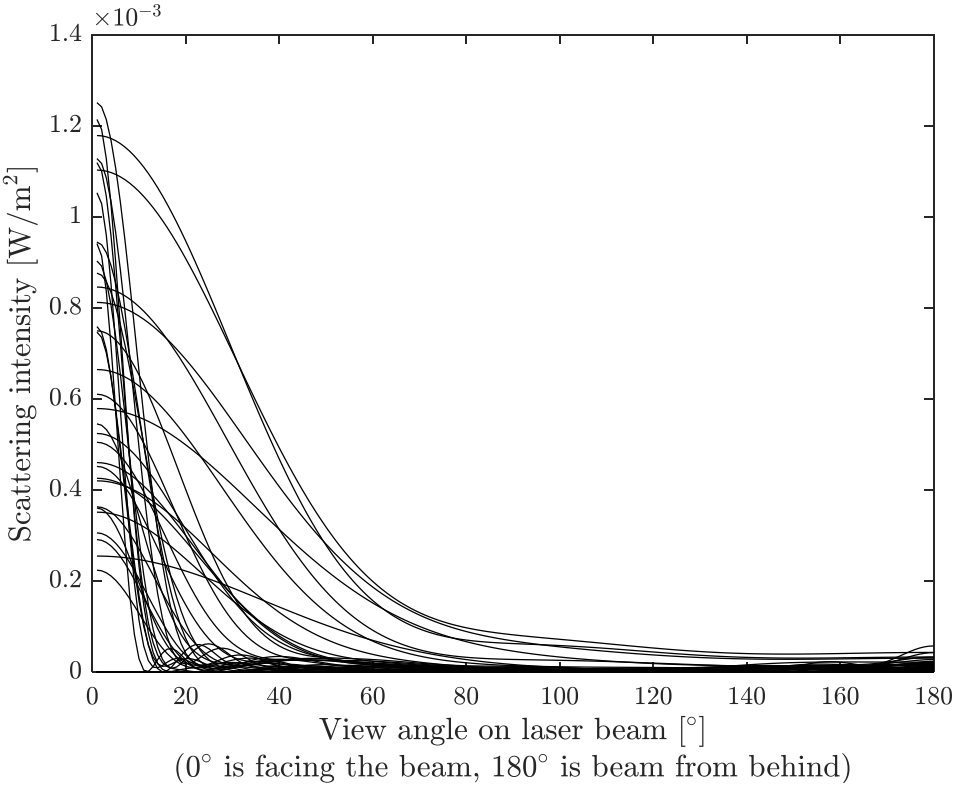

Figure A.23: Calculated angle-dependent Mie scattering intensity for the individual particle mean diameters for the mean particle distribution "Juelich: median" of Figure 4.12 multiplied by the laser beam volume within the AFOV of the camera. The particle data from the curve "Juelich: median" of Figure 4.12 was used as input.

Continuation from section 6.2.3 on the topic: *Mie scattering simulations.*

Figure A.24 shows a zoom of the calculated angle-dependent Mie scattering intensity for the individual particle mean diameters for the mean particle distribution "Juelich: median" of Figure 4.12 multiplied by the laser beam volume within the AFOV of the camera.

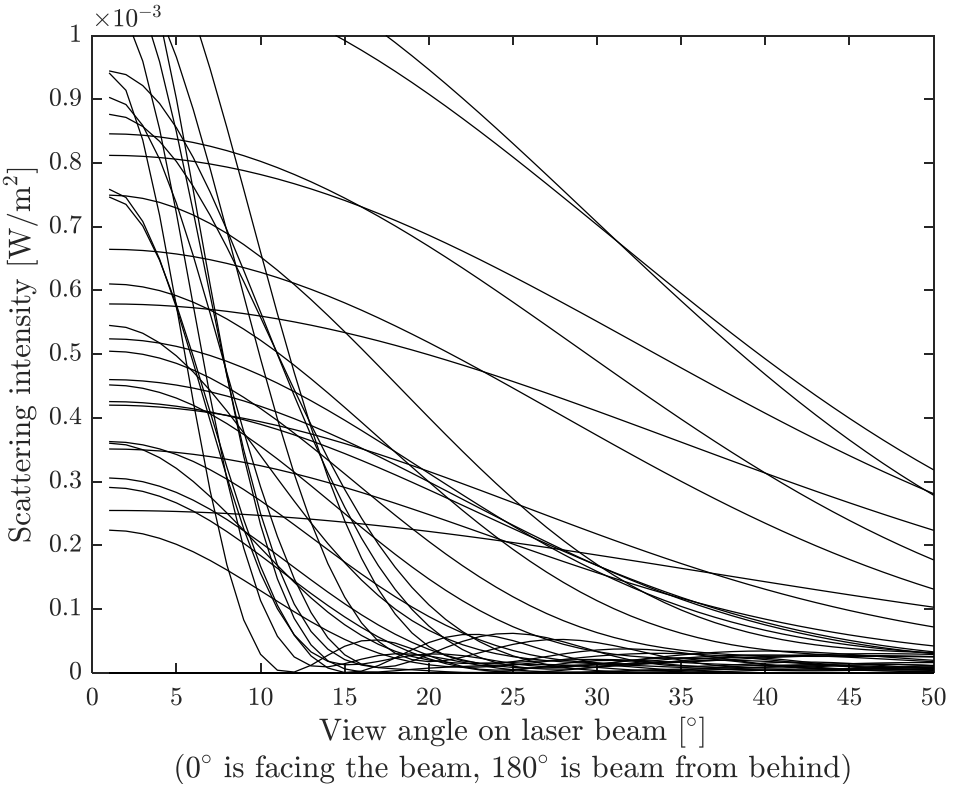

Figure A.24: Zoom of the calculated angle-dependent Mie scattering intensity for the individual particle mean diameters for the mean particle distribution "Juelich: median" multiplied by the laser beam volume within the AFOV of the camera. The particle data from the curve "Juelich: median" of Figure 4.12 was used as input.

Continuation from section 6.2.3 on the topic: *Mie scattering simulations.*

Figure A.25 shows the angle-dependent Mie scattering intensity for the individual particle mean diameters for the particle distribution "Juelich: 10 % percentile" of Figure 4.12 multiplied by the laser beam volume within the AFOV of the camera.

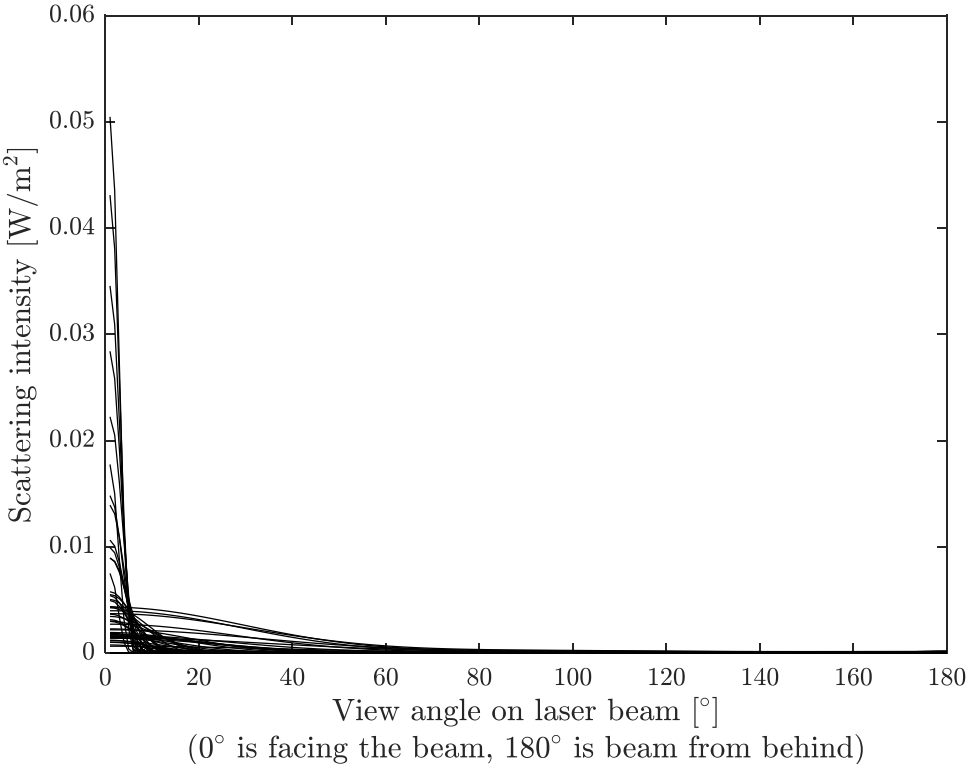

Figure A.25: Calculated angle-dependent Mie scattering intensity for the individual particle mean diameters for the particle distribution "Juelich: 10 % percentile" multiplied by the laser beam volume within the AFOV of the camera. The particle data from the curve "Juelich: 10 % percentile" of Figure 4.12 was used as input.

The below Figure A.26 shows a zoom of the angle-dependent Mie scattering intensity for the individual particle mean diameters for the particle distribution "Juelich: 10 % percentile" of Figure 4.12 multiplied by the laser beam volume within the AFOV of the camera.

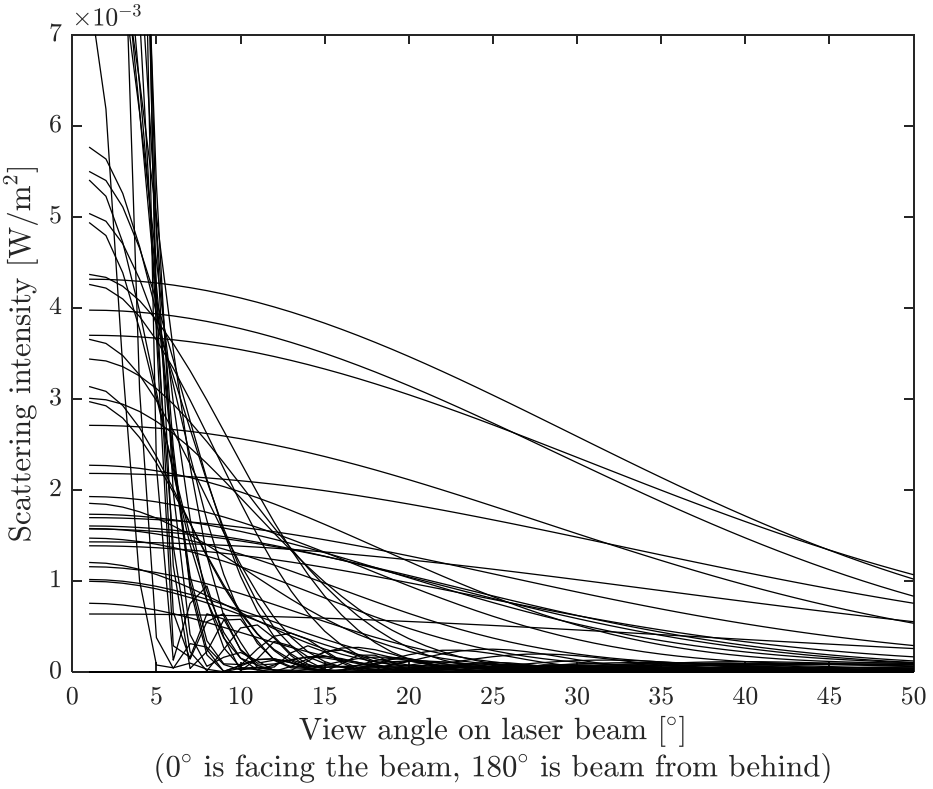

Figure A.26: Zoom of the angle-dependent Mie scattering intensity for the individual particle mean diameters for the particle distribution "Juelich: 10 % percentile" multiplied by the laser beam volume within the AFOV of the camera. The particle data from the curve "Juelich: 10 % percentile" of Figure 4.12 was used as input.

Continuation from section 6.2.3 on the topic: *Simulations for Rayleigh scattering from very small particles.*

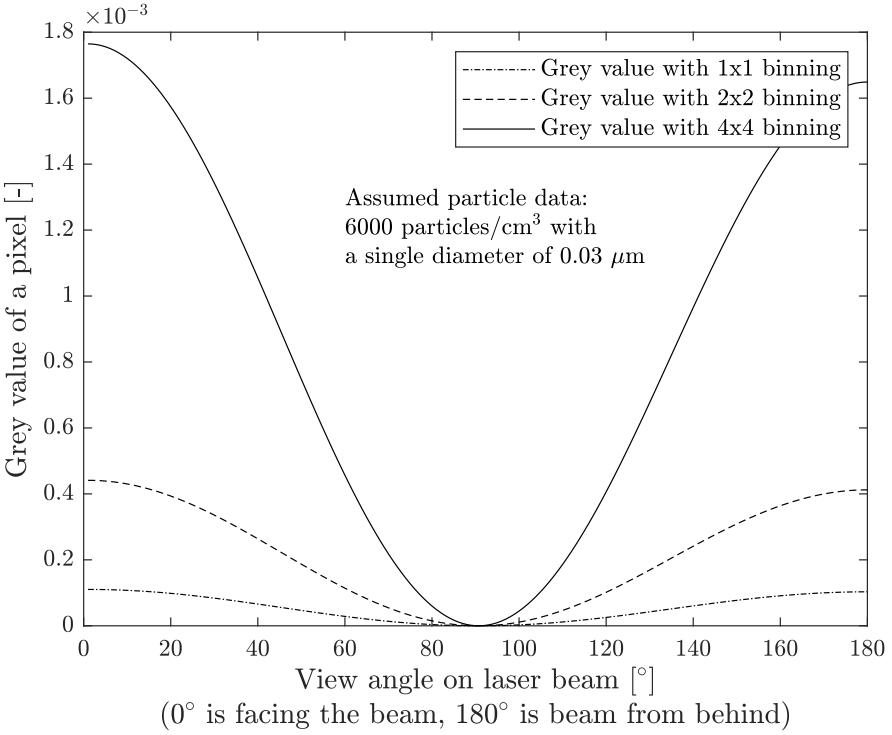

Figure A.27: Calculated grey value produced from the Mie scattering of an s-polarised laser beam captured with a monochrome scientific camera, f=25 mm lens and ultra-narrow bandpass filter with FWHM of <1.2 nm. The calculation was done for scattering angles (here called *View angle on laser beam*) from 0 to 180°. The scattering was calculated for 6,000 particles per cm^3 with a single diameter of 30 nm (i.e. 0.03 µm) used as input.

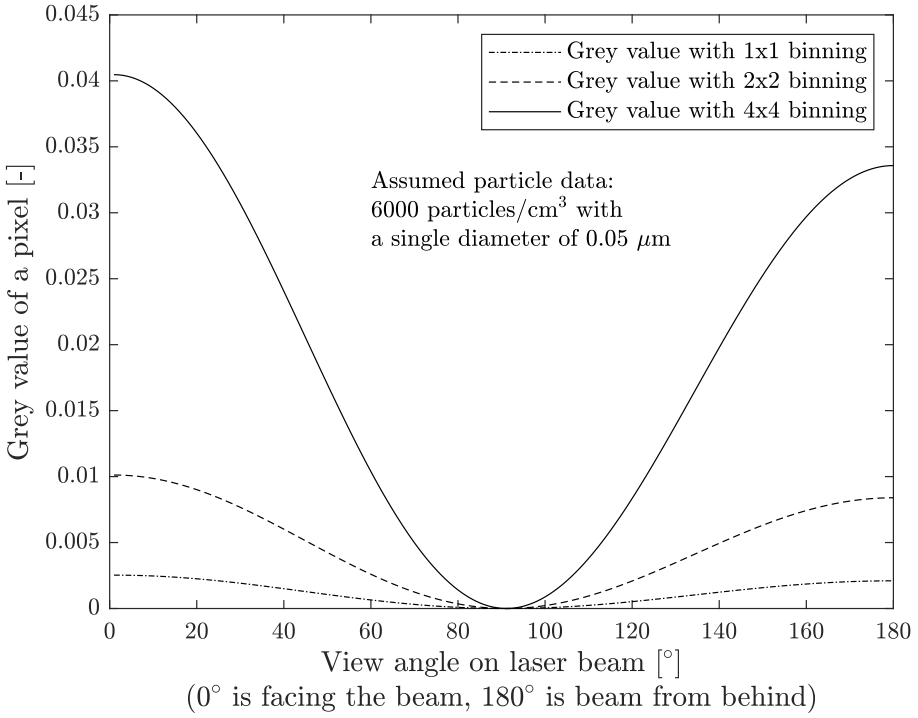

Figure A.28: Calculated grey value produced from the Mie scattering of an s-polarised laser beam captured with a monochrome scientific camera, f=25 mm lens and ultra-narrow bandpass filter with FWHM of <1.2 nm. The calculation was done for scattering angles (here called *View angle on laser beam*) from 0 to 180°. The scattering was calculated for 6,000 particles per cm^3 of 50 nm (0.05 µm) used as input.

Continuation from section 6.6 on the topic: *Image processing for images from outdoor test.*

Table A.9: Simulation study of angle detection accuracy.

Simulation Nr.	Rotation angle 1, α_1 [°]	Rotation angle 2, α_2 [°]	Angle difference, $\Delta\alpha=\alpha_2-\alpha_1$ [°]	Angle difference detected by Radon line detection, $\Delta\alpha_{Radon}=\alpha_2-\alpha_1$ [°]	Deviation $\Delta\alpha_{dev}=\Delta\alpha-\Delta\alpha_{Radon}$ [°]	Deviation $\Delta\alpha_{dev}=\Delta\alpha-\Delta\alpha_{Radon}$ [mrad]
1	-30	-20	-10	-10.0476	0.0476	0.830
2	-40	-20	-20	-20.0115	0.0115	0.200
3	-50	-20	-30	-30.0115	0.0115	0.200
4	-40	-10	-30	-29.9582	-0.0418	-0.730
5	-25	-20	-5	-4.9479	-0.0521	-0.910
6	-25	-9	-16	-15.9845	-0.0155	-0.270
7	-33	-8	-25	-25.0052	0.0052	0.090
8	-34	-8	-26	-25.9650	-0.0350	-0.610
9	-37	-12	-25	-24.9970	-0.0030	-0.052
10	-43	-12	-31	-31.0068	0.0068	0.119
11	-36	-13	-23	-23.0102	0.0102	0.178
12	-41	-11	-30	-30.0295	0.0295	0.514
13	-45	-17	-28	-27.9704	-0.0296	-0.517
14	-48	-7	-41	-41.0041	0.0041	0.072
15	-65	-7	-58	-57.9880	-0.0120	-0.209
16	-36	-25	-11	-11.0263	0.0263	0.460

Table A.10: Simulation study of angle detection accuracy after histogram manipulation.

Simulation Nr.	Rotation angle 1, α_1 [°]	Rotation angle 2, α_2 [°]	Angle difference, $\Delta\alpha=\alpha_2-\alpha_1$ [°]	Angle difference detected by Radon line detection, $\Delta\alpha_{Radon}=\alpha_2-\alpha_1$ [°]	Deviation $\Delta\alpha_{dev}=\Delta\alpha-\Delta\alpha_{Radon}$ [°]	Deviation $\Delta\alpha_{dev}=\Delta\alpha-\Delta\alpha_{Radon}$ [mrad]
1	-30	-20	-10	-10.0217	0.0217	0.3793
2	-40	-20	-20	-20.0220	0.0220	0.3846
3	-50	-20	-30	-30.0039	0.0039	0.0673
4	-40	-10	-30	-29.9861	-0.0139	-0.2433
5	-25	-20	-5	-4.9935	-0.0065	-0.1139
6	-25	-9	-16	-16.0242	0.0242	0.4228
7	-33	-8	-25	-25.0242	0.0242	0.4228
8	-34	-8	-26	-25.9450	-0.0550	-0.9596
9	-37	-12	-25	-24.9450	-0.0550	-0.9596
10	-43	-12	-31	-31.0334	0.0334	0.5833
11	-36	-13	-23	-23.0334	0.0334	0.5833
12	-41	-11	-30	-30.0344	0.0344	0.6003
13	-45	-17	-28	-27.9918	-0.0082	-0.1423
14	-48	-7	-41	-41.0043	0.0043	0.0746
15	-65	-7	-58	-58.0035	0.0035	0.0617
16	-36	-25	-11	-10.9985	-0.0015	-0.0268